Tesis Doctoral

Development of ReflEXAFS technique: atomic structure from deep surface regions

Víctor López Flores

Instituto de Ciencia de Materiales de Sevilla
Departamento de Química Inorgánica
C.S.I.C. - Universidad de Sevilla

Julio de 2008

Development of ReflEXAFS technique: atomic structure from deep surface regions

Memoria presentada por el Ldo. Víctor López Flores
para optar al grado de
Doctor por la Universidad de Sevilla

Fdo: Víctor López Flores

Los directores:

Dra. Adela Muñoz Páez

Profesora titular
Departamento de Química Inorgánica
Universidad de Sevilla

Dr. Stuart Ansell

Research fellow
ISIS Neutron Source
Rutherford Appleton Laboratory
(U.K.)

Development of ReflEXAFS technique: atomic structure from deep surface regions

Víctor López Flores

A mi familia

A Marcela

Agradecimientos

Hay una gran responsabilidad en redactar los agradecimientos de una tesis. El 99 % de las personas que va a tener este ladrillo entre sus manos va a ser sólo para leer estas líneas. Espero que los disfrutéis, ya que no os atrevéis a seguir adelante.

A Adela le debo la oportunidad de poder hacer realidad mi sueño de dedicarme a la ciencia. El que confiara en mí aún me tiene sorprendido, y el que se siga dejando engañar a pesar de todo el tiempo que ha tenido para conocerme, también. Tengo que agradecerle que me haya dejado libertad para trabajar a mi aire, y haya puesto la presión justa cuando la necesitaba. Pero sobre todo, aprecio que sea una jefa atípica, que me hable menos de trabajo y más de cualquier otra cosa; que me respete como persona y me trate como a un igual, no como a un becario más que proporciona mano de obra barata.

Stuart es quizá el peor director de tesis de la historia, pero el mejor maestro. Nunca he visto mayor esfuerzo en tratar de hacerse entender, eso sí, en su propio idioma, que dicen que es inglés. Muchos se sorprenden de que yo sea capaz de entenderlo y comprenderlo. Para mí ha sido un privilegio poder aprender de él no sólo de ciencia, sino de muchas otras cosas.

De Silvia conservo dos frases gloriosas que pocas personas entenderán, "Toma las virtudes, pero no los defectos" y "Búscate un país decente", y que resumen el nivel de realismo que tanto aprecio en sus consejos. Además, se atrevió a corregir el Capítulo 4, que tiene su miga, y es gracias a ella que ahora lo pueden entender más de 2 personas en el mundo.

Sofía y Daniel me han permitido la oportunidad de crecer como científico al lado de dos *cracks*. Si en mi vida llego a ser la mitad de bueno que ellos, me consideraré afortunado.

Todos ellos forman la que algún día llamamos la *peanut gallery*, el grupito que hicimos estos experimentos en el sincrotrón, desagradecidos y cansados a veces, pero siempre divertidos. Una experiencia que, en buena compañía, recomiendo a todo el mundo.

Ann me abrió la puerta de su casa durante mi estancia en ISIS, e hizo aún más divertida la convivencia con Stuart. Al pequeño Mark tengo que agradecerle el que probablemente fuera el catalizador que provocó la aparición de la responsabilidad que hizo que este proyecto saliera adelante.

A Jorge le agradezco que siguiera conservando la hospitalidad española, aun llevando tanto tiempo en el Reino Unido.

Al Ministerio de Ciencia y Tecnología, luego de Educación y Ciencia, y luego de Ciencia e Innovación, no le voy a dedicar agradecimientos emotivos. Pero han sido ellos los que me han permitido seguir este camino con una cierta aportación económica, por medio de la beca F.P.I. BES-2004-4904 asociada al proyecto BQU2002-04364-C02-01, y es de justicia mencionarlo.

En la fuente europea de radiación sincrotrón (E.S.R.F.) hicimos los experimentos que aquí se recogen gracias a la concesión de un proyecto de larga duración (LTP) llamado ME-737, en la estación BM29. Allí tuve la oportunidad de conocer a Gianluca Ciatto, Olivier Mathon y Sakura Pascarelli, con los que esperamos poder seguir colaborando.

Sin Merche y Carlos no hubiéramos podido hacer la mayoría de las muestras que hemos analizado en este proyecto. El ultra-optimizado laboratorio de *sputtering* del Instituto de Ciencia de Materiales de Madrid es la delicia de cualquier experimental.

Juan Pedro, en su infinito conocimiento de las láminas delgadas, fue una pieza clave en el comienzo de este proyecto.

Javier nos proporcionó valiosísimos datos sobre nuestras muestras, gracias al acelerador del Centro Nacional de Aceleradores, que tenemos tan cerca y que tan poco apreciamos.

La maestría de Jesús, Paco y Carmen en el manejo de ese pequeño gran aparato que es el AFM no sólo dotó a este libro de preciosas fotos tridimensionales, sino que ayudó en gran medida a discernir algunos de los secretos que guardaban las muestras.

Ángel y José María nos ayudaron con algo tan sencillo, pero tan importante, como son esos rayos extraños que salen de tubos y que mágicamente te dicen de qué y cómo está hecha tu muestra.

Los químico-físicos (Eli, Elisa, Elsa, Enrique, Josema, Rafapa y Regla, y seguro que me dejo a alguien) me dejaron usar su impresora en un momento crítico, me resolvieron mis primeros problemas con Linux, e impidieron que yo quemara el procesador de mi portátil durante los ajustes permitiéndome abusar de su *cluster*. Por si esto fuera poco, encima lo pasamos bien juntos en cenas y almuerzos varios a costa de los jefes.

A Flora le agradezco que fuera mi *hermana mayor* y me permitiera molestarla cuando era ella la que escribía su tesis, y yo hacía mis primeros pinitos con los ajustes EXAFS. A Lola, que sería entonces mi *hermana pequeña*, le tengo que dar las gracias por traer tan buen humor al laboratorio, y por encontrar ese maravilloso programa para simular los XRR y echarme una mano con los ajustes en estos últimos momentos que tanta falta hacía.

A Agus le debo el que rompiera con la otrora soledad del laboratorio y me trajera su amistad, que espero que dure mucho más tiempo a pesar de la distancia.

Al resto de los Fotónicos (Gabriel y Javi, Gisela y Mauricio, Hernán, Nuria H., Nuria N.–esa chica de Burgos–, Olalla y Silvia) y a Estefanía les agradezco que demostraran que compartir un laboratorio no es sinónimo de conflicto, sino que sirve para estrechar lazos y aprender unos de otros, que al final es

de lo que se trata.

A mis *compañeros de promoción*, Ana, Alberto, José Manuel y Pablo, aunque todos salieron con tanta prisa que me han dejado atrás, les agradezco muchas risas y complicidad durante el tiempo que compartimos.

A Manu, por esos buenos momentos en el sincrotrón, y al resto de la gente con la que compartimos muchos almuerzos en la *cocinita* (Marina, Pedro, Rafa, Rosa, Verónica...) por unos minutos de relajación en la mitad del día, acompañados siempre de unas lentejas.

Al *lobby* colombiano del Instituto, y a Luis, por tantos buenos momentos juntos.

A Ana, Eduardo, Javi y Luis, por obligarme a salir más temprano, y por tener siempre una sonrisa y un saludo amable dispuesto en cada momento.

A Rafa, porque siempre acoge de buen grado mis preguntas no convencionales sobre informática.

A Jose Luis, Diego, Catina y Víctor, la vieja guardia, por acogerme en su seno cuando aún era un pipiolo recien llegado.

Como seguro que estoy omitiendo a alguien, no puedo dejar de mencionar a todos los miembros tanto permanentes como itinerantes que están o han pasado por el Instituto de Ciencia de Materiales de Sevilla. Es por ellos que estos años han sido fantásticos para mi. Cada uno ha aportado algún pequeño granito de arena por el cual todo esto ha sido posible.

A Ángel le debo mucho más de lo que puedo expresar con palabras. Gracias a él estoy yo hoy aquí: "Hay un curso muy interesante en el Instituto...". A él y a Elsa les debo tanta amistad y tantos buenos consejos que jamás podré pagarles. Gracias por ser ambos un modelo a seguir.

A mi familia colombiana les agradezco el acogerme aun siendo tan diferente, sus ánimos, y el que me permitieran robarles algo tan valioso. Vladimir es otro modelo al cual algún día me gustaría parecerme.

A mi familia les debo lo que soy (tanto lo bueno como lo malo, claro). Gracias por vuestro orgullo, paciencia y por no protestar por no verme apenas en casa.

Marcela; mi linda; mi niña; mi Santa; mi fuente de inspiración. Qué te puedo decir que no sepas. Gracias por tu apoyo constante e incodicional, especialmente en los últimos días de este camino; por tu paciencia infinita, que sé que en el fondo no tienes. Gracias por tu forma de ser. Gracias por existir. Porque este fin de etapa no es más que el principio de lo que aún nos queda por vivir.

1 de Julio de 2008

"Si te caes siete veces, levántate ocho"

Proverbio chino

Contents

List of Figures

List of Tables

Chapter 1

Introduction

Tailoring the surface characteristics of materials to provide specific physical and chemical properties is a major field of industrial interest. Many methods have been developed to modify surface structures but they typically involve either (i) the deposition of an outer layer, or layers, of coating materials that intrinsically have the desired physical or chemical properties, or (ii) the direct modification of a surface using methods such as atomic bombardment or thermal cycling under controlled atmosphere [1–3].

Given our rapidly developing ability to engineer the surface properties of materials to match the requirements of their area of application, it is essential that surface characterisation techniques keep pace with these fabrication method developments [4]. By definition, the structurally modified region of a surface engineered material is smaller in thickness than its other dimensions. In addition, the surface region also does not necessarily display long range three dimensional crystalline order. The ideal characterisation techniques thus need to provide us with a means to obtain structural information that is chemically specific, depth sensitive and applicable regardless of the degree of structural or chemical order present in the surface layers.

Reflection Extended X ray Absorption Fine Structure (ReflEXAFS) spectroscopy is one such method. A detailed description of both the experimental and data analysis developments to usefully apply this technique to the characterisation of surface modified materials is the main aim of this report.

Moreover, a few examples of its application to some selected materials will be presented.

EXAFS spectroscopy provides chemically specific short range structural information and is well suited to the investigation of the local atomic environment around medium to heavy elements. There is no requirement for long range structural order and the method can equally be applied to samples of crystalline, glassy, liquid or even gaseous state [5]. In the standard set-up for an EXAFS experiment, an X ray transmission measurement is performed where the intensity of an X ray beam is measured before and after passage through a sample as a function of the incident X ray photon energy. In this experimental geometry, both surface and bulk regions of the sample are probed, since the mean free path of photons is of the order of thousands of Ångströms and the beam passes right through the bulk of the sample. The lack of sensitivity to the surface region can be overcome by changing the experimental geometry and/or the detection mode. For example, the interaction of the X ray photons with a material can induce various secondary processes with intensities that are directly proportional to the X ray absorption signal but restricted to the surface regions. The detection of the photoelectron yield at the surface of a sample as a function of the incident X ray beam energy is one such means, as the mean free path of electrons in a solid is a few tens of Ångströms [6].

An alternative means to emphasize the surface sensitivity of the technique is to adopt a glancing angle geometry that takes advantage of the fact that the refractive index of materials for X rays is slightly smaller than 1. The X ray beam can therefore undergo total reflection. The spectroscopic signal is measured by detecting the intensity of the reflected beam and and the structural properties of the sample are effectively probed by the evanescent electromagnetic wave. This technique is called ReflEXAFS.

Of particular note is the potential this gives to probe not only the structure in the outermost layer of a sample surface, like in the detection of the photoelectron yield, but also the structure in the buried layers. This is

because the detected species are the reflected photons and not the emitted electrons, which have a mean free path in the range of very few nanometers in solids. Moreover, this also means that no vacuum conditions are required for the measurement, so the samples can be studied under realistic atmospheric conditions which also simplifies the experimental setup.

In the early studies [7–14] it was important that the experiments were performed under total reflection conditions, i.e. using an incidence angle well below the critical angle. This choice was essential as it simplified the experimental requirements [15, 16], since the reflected intensity is quite high. Moreover, the data analysis is rather simple since, under this conditions, standard X ray absorption theory can be used [7, 17, 18] for analysing the spectroscopic components in the reflected beam. In these studies, the penetration depth of the beam is restricted to the order of a few tens of Ångströms.

Despite the difficulties for the direct reflection geometry experiment, a few studies [19, 20] have gone beyond the total reflection approximation but were restricted to specific angles and corresponding penetration depths, and to samples with a single local environment. Thus, no general method for a wide range of angles has yet been developed.

The generalisation of the ReflEXAFS technique to provide data at angles both below and above the critical angle is a significant development because it will enable the extraction of structural information about the shallowest region of the sample (extending a few tens of Ångströms from the surface) as well as about deep regions hundreds of Ångströms underneath. In fact, depth profiling can be achieved, as the penetration depth of the X rays increases with the incidence angle of the X ray beam on the sample.

Furthermore, in addition to the chemically specific local structure data as a function of layer depth, these types of measurements can also provide valuable information about thin multilayer structures, including thicknesses, densities and interface roughness, in a similar way to the analysis of X ray reflectometry measurements [21].

Thus, the ultimate aim of this project is to extend the ReflEXAFS technique

to the analysis of the spectra at not only below, but also above the critical angle of reflection.
This extension has to be done in two fronts:

- Experimental: optimisation of an experimental protocol using the available standard instrumentation (X ray absorption beamline with a reflectometer) to obtain X ray reflection measurements below and above critical angle conditions in both a highly quantitative and accurate fashion in three key areas, (1) angular configuration, (2) energy scale and (3) reflected beam intensity.

- Data analysis: development of the algorithms that allow to simulate, extract and analyse the EXAFS data from the raw measured ReflEXAFS spectra, not exclusively valid for the angles below the critical angle, i.e. a global method that considers all the possible angles.

To achieve and illustrate this development, a group of different sets of samples was made. The selection of the samples was motivated taking into account what seemed convenient to develop the technique as well as being themselves interesting from the materials science point of view.
This aim was fulfilled increasing the difficulty and the interest of the samples at the same time. Indeed, the first ones are quite simple, with ideal characteristics for an easy optimisation of the technique, while the last ones challenge the capabilities of the technique, pushing its limits in both the experimental requirements and the data analysis. In addition, the samples cover the fields of the multilayers, the surface reaction with reactive gasses, the hard metal nitride coatings and, finally, the surface nitriding process of steels for cutting tools.
The structure of this report is the following.
Chapter 2 describes the preparation of the samples. It also summarises the details of the characterisation techniques (other than ReflEXAFS) used for those samples.
Chapter 3 gives a detailed description on the experimental setup, the meth-

ods and, what is more important, the protocols necessary to optimise the collection of the ReflEXAFS data at these challenging experimental conditions.

Chapter 4 introduces the theory behind the ReflEXAFS process. It also describes the low angle ReflEXAFS approximation described by Martens [7, 17, 18] and the high angle approximation made by Borthen [19, 20]. Finally, it details the algorithms used to simulate and extract the EXAFS signal from the ReflEXAFS spectrum that leads to the global analysis method.

Chapters 5 to 8 presents the characterisation results, including the data simulation and analysis when necessary (like in X ray reflectometry spectra), for the different sets of samples. It also exposes the ReflEXAFS results, involving the raw experimental data, the low angle approximation EXAFS analysis if possible, the global simulation and EXAFS extraction results, and finally, the EXAFS simulation and fitting to calculate the structural parameters of the studied environments.

Finally, a Conclusions chapter summarises the main achievements of the project as well as the future work envisaged.

Chapter 2

Sample preparation and characterisation

Contents

Introduction

The X ray reflectivity of a surface decreases drastically when the incidence angle is above the critical angle, so it may drop a few orders of magnitude below the total reflection condition reflectivity. With this severe restriction, the samples should fulfill certain requirements so they can be studied with the ReflEXAFS technique.

Flatness is essential to avoid the change of the incidence angle along the sample because, in this case, a different penetration depth for different places along the surface would be reached. In addition, the lack of flatness can cause beam dispersion, resulting in a loss of intensity in the reflected beam.

As shown in Figure 2.1, the footprint of the beam has a length of $d/\sin\theta_i$, where d is the beam vertical width, usually determined by a slit, and θ_i is the incidence angle. Since the incidence angle is quite low for the ReflEXAFS experiments, usually smaller than 1°, the footprint of the beam becomes rather long (on the order of cm). For a typical vertical beam width of 100 μm and incidence angles between 0.2 and 0.6°, the footprint length varies between 29 and 10 mm, respectively. Therefore, ideal samples should have an homogeneous surface both in structure and composition at least over this length to contain the whole beam footprint.

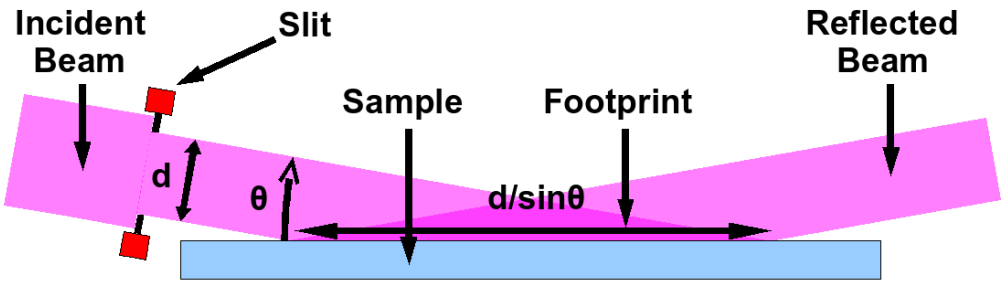

Figure 2.1: Footprint of the X ray on the sample

Since *roughness* causes beam dispersion, reducing the reflected beam intensity. Hence, samples that are as smooth as possible are desirable. Ideally roughness would be in the range of a few nanometers over the whole area of the beam footprint.

Once the samples have been prepared, some characterisation prior to the ReflEXAFS experiment is important to know whether they are suitable for the measurement, and to give some keys for the subsequent ReflEXAFS analysis. As most of the samples were made of thin film coatings, their composition and thickness of the layers was measured by different techniques. Also, it was interesting to measure the surface roughness to evaluate the possible beam dispersion.

In this Chapter, the preparation methods of the samples studied in this work are briefly described together with a list of those samples (Section 2.1), and the characterisation techniques used are summarised, and detailed when necessary (Section 2.2).

2.1 Preparation

There are several methods to prepare samples with the required properties. Most of the methods to prepare thin layered coatings fulfill these requirements. Among them, the *magnetron sputtering* (Section 2.1.1) was selected as one of the most appropriates due to its characteristics explained below.

2.1.1 Magnetron sputtering

Sputtering deposition techniques are a type of *physical vapor deposition* techniques (PVD). The process consists in the acceleration of ions against a surface, called the *target*. Upon impact, these ions tear away fragments of the target, which are transformed into vapor that can be condensed, thus deposited, afterwards in any nearby surface. Then, if a substrate is located

close to the target, it becomes coated by the target material [22].

The probability of contaminating the layer with spurious elements in the chamber is small, since no complex chemical precursors are used. Moreover, the relatively high deposition rate, compared to those of other PVD techniques like Molecular Beam Epitaxy, reduces even more this probability of contamination.

In common sputtering deposition procedure, a *plasma* is created inside a chamber between two electrodes at a high voltage. The target is located at the cathode, while the substrate is fixed to the anode. The chamber is filled with a gas (called the sputtering gas) at the desired pressure which is normally in the order of 0.5 Pa. The gas is ionized when the plasma is created, and its ions are accelerated towards the cathode, striking the target with enough energy to remove some material.

However, this *diode* configuration provides a plasma with a low degree of ionisation due to the escape of the electrons away from the plates to the deposition chamber. This causes an unstable plasma and a quite low deposition rate.

In the *magnetron sputtering* configuration [23] a set of magnets is attached underneath the cathode, so a magnetic field is created near the target. This magnetic field traps electrons, confining them close to the target, so the ionisation degree of the plasma in this region is higher, thus increasing the sputtering rate and consequently the deposition rate.

A scheme of the magnetron sputtering deposition chamber is shown in Figure 2.2. To produce an stable plasma at low voltage, the chamber must be kept at a low pressure with a series of vacuum pumps. The sputtering gas is usually Ar, so it neither gets implanted in the target nor reacts with the sputtered material, like in reactive sputtering (see section 2.1.1.1). Figure 2.3 shows a picture of the actual deposition chamber used, located in the Sputtering laboratory at the Institute of Materials Science of Madrid [3, 24].

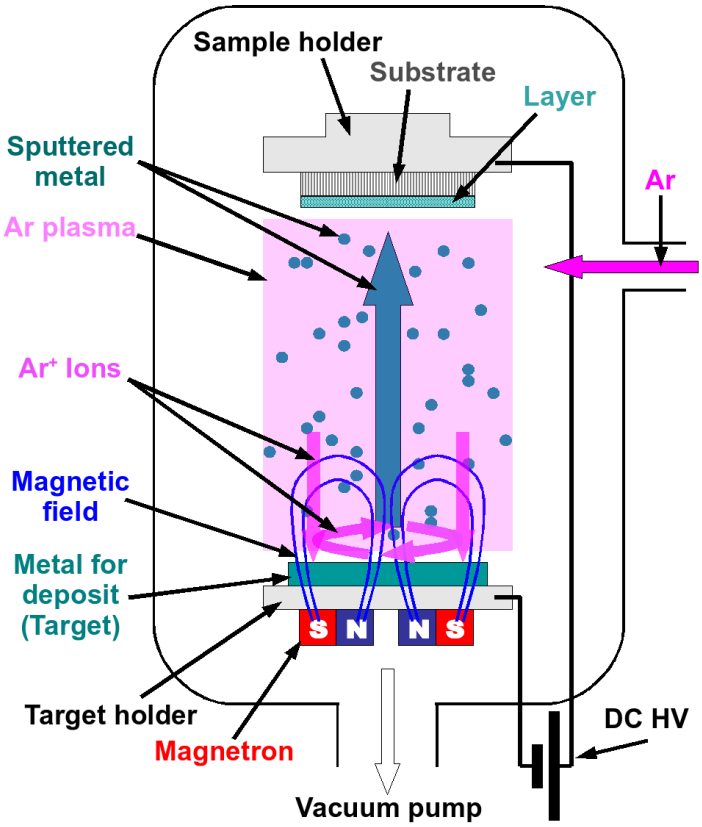

Figure 2.2: Magnetron sputtering preparation chamber scheme

Figure 2.3: Magnetron sputtering preparation chamber at the ICMM

The vacuum system consists on a rotatory pump (that gets the chamber to 0.1 Pa of pressure) attached to a turbo-molecular pump (that gets to 10^{-5} Pa). This high vacuum is the base pressure it is used before filling the chamber with the sputtering gas.

There is a pre-chamber attached to the main deposition chamber and separated by a door. An external manipulator is available to move the sample from the pre-chamber to the main one and backwards. This pre-chamber has its own vacuum system of a rotatory pump to reach 0.1 Pa of base pressure before transferring the sample to the main chamber.

The main chamber has two independent magnetron systems available that share the same anode, where the sample is located. This allows the user to fabricate layers of two different elements without exposing the sample to open air. An automated system places the sample above the magnetron to be used, at a distance of 10 cm. This system can be programmed in order to

move the sample above one or the other magnetron for a certain amount of time, and repeat this process the selected number of times. Therefore, the fabrication of multilayers using this system is straightforward. A scheme of the chambers is shown in Figure 2.4

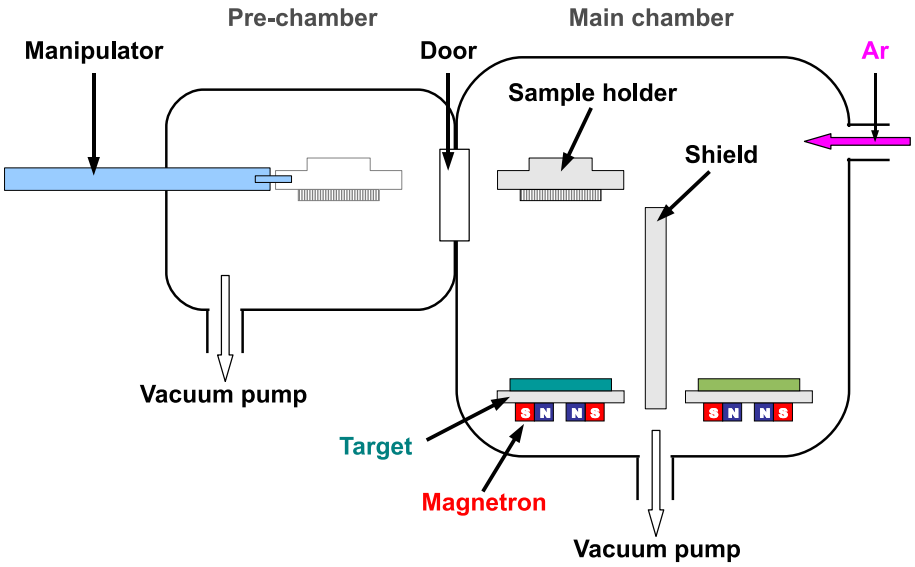

Figure 2.4: Magnetron sputtering preparation chamber scheme

To control the thickness of the deposited layers, a growth rate estimation has to be carried out prior to the actual fabrication of the samples. To do so, a thick layer of the element to be growth is deposited in the same type of substrate of the samples for a certain time. Then, an X ray reflectivity (XRR) measurement is made in a laboratory equipment, so the total thickness can be estimated from it. Thus, the mean growth rate is calculated dividing the thickness by the deposition time.

However, it must be noted that this growth rate is just an estimation that is used to get roughly the desired thickness. The actual thickness of the sample layers must be accurately determined by other methods. The only thing that can be assured is that the thickness of a layer of the same element at the

same growth conditions is the same.

2.1.1.1 Reactive sputtering

In the plasma state, the reactivity of several gasses chemically inert in standard conditions increases drastically. This enhancement is used in the sputtering techniques to prepare compounds from elemental targets by selecting the appropriate sputtering gas, e.g. O_2 or N_2, calling this technique *reactive sputtering* [22]. This technique is widely used for oxides and nitrides deposition (see, for example [3, 23, 24])

2.1.2 Samples

In this project, several samples have been prepared by reactive and non-reactive magnetron sputtering.

2.1.2.1 CuCrxN

Multilayers of metallic Cu and Cr over Si (100) wafers were grown with a periodic (CuCr)xN structure, where N = 2, 3, 4 and 8, being the period a Cu/Cr bilayer. Deposition time was controlled to keep the total thickness around 200 Å, as well as to keep the relationship between Cu and Cr thicknesses at the ratio 2:1 for N = 2, 4, 8, while the ratio for N = 3 was set to 1:1. Sample schemes are shown in Figure 2.5. Cr was used to prevent the oxidation of the Cu layers, so the Cu environment remain the same for all the layers.

The base pressure in the growth chamber was 10^{-5} Pa before the deposition. During the deposition, argon (Ar) was used as sputtering gas and its flow rate was adjusted with a mass flow controller to obtain a pressure of 5 Pa. The applied power to the magnetron cathode was kept constant at about 1 W, while the current intensity was fixed to 40 mA. The deposition was made

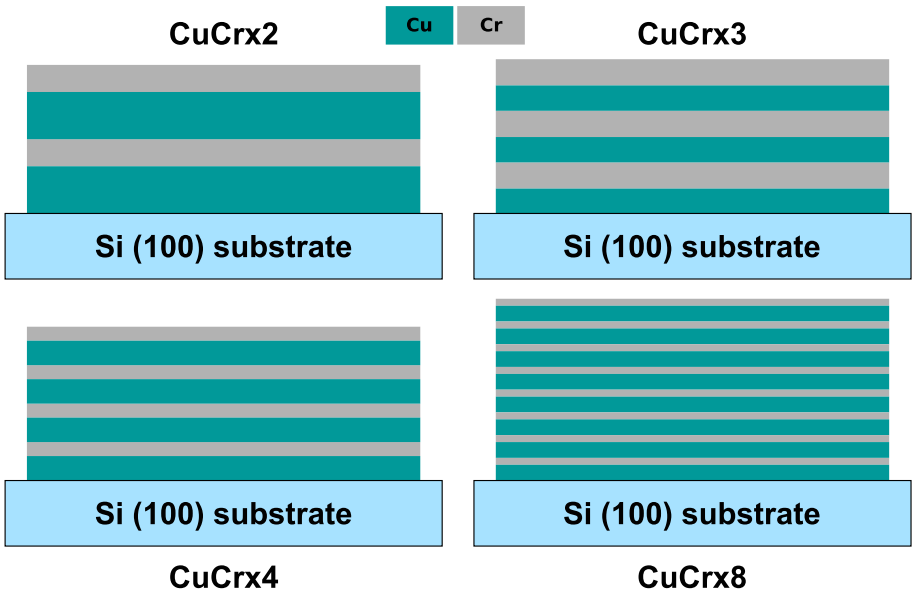

Figure 2.5: CuCrxN samples schemes

at room temperature.

Monocrystalline 0.3 mm thick Si wafers were used as substrates to obtain samples as flat as possible. The substrates were cut in rectangular shape 40 mm long, 8 mm wide, which is the longest size that can be used in the preparation chamber without producing along inhomogeneity along the sample.

2.1.2.2 CrCux3

A multilayer of metallic Cu and Cr over a Si (100) wafer was grown with a periodic (CrCu)x3 structure in the same fashion as the previous set of samples. However, the bilayers were reversed compared to the previous samples, leaving the topmost layer, made of Cu, exposed to air. Sample scheme is shown in Figure 2.6

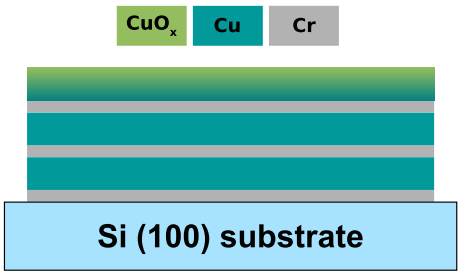

Figure 2.6: CrCux3 sample scheme

2.1.2.3 MoN/Mo

Bilayers of Mo/MoN and MoN/Mo were grown over Si (100) by non-reactive and reactive magnetron sputtering. Both bilayers were grown over a Cr coating over the Si substrate that acts as a buffer layer to enhance the adherence. Moreover, another Cr layer was grown on top of the bilayer to prevent further reaction of the Mo or MoN layers with the atmosphere. Sample schemes are shown in Figure 2.7

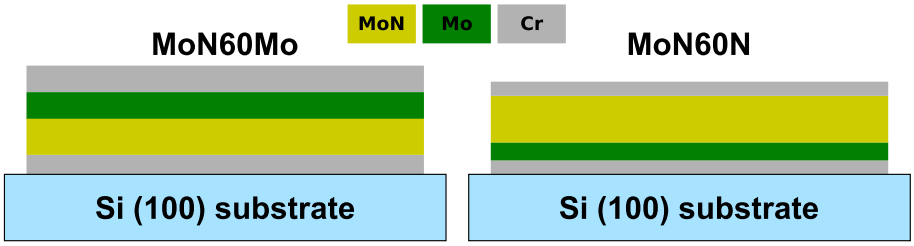

Figure 2.7: MoN/Mo and Mo/MoN samples schemes

For the metallic Mo layers, the deposition conditions were the same as for the CuCrxN multilayers. For the nitride compound, the sputtering gas was pure N_2, kept at 6.2 Pa of pressure, and the current intensity was fixed to 20 mA, being the rest of the variables the same as previously.

2.1.2.4 Nitrided steel

Gas nitriding is a standard industrial process that aims to improve the hardness and wear resistance of certain type of steels.

A piece of commercial ferritic steel with 3% Cr, 0.8% Mo, 0.3% V, 0.3% C and balance Fe, was submitted to a gas nitriding treatment. It was immersed in a N_2 and NH_3 atmosphere at 500°C for 24 hours. A second piece without the nitriding treatment was also taken for the study.

The resulting samples were polished prior to the ReflEXAFS experiments, although they were studied by X ray diffraction before and after polishing.

2.2 Characterisation

2.2.1 X Ray Diffraction

To check the existence of crystalline domains in the samples, X ray diffraction (XRD) measurements were upheld in a Siemens D-500 diffractometer, using an X ray generator with Cu anode working at 40 mV and 40 mA, using the Cu-K_α emission line. A scintillation detector with a graphite monochromator just before it was used to collect the diffraction lines. The standard diagram was made from 20 to 80° in 2θ, with a step of 0.05° at 1 s of data acquisition time per step.

2.2.2 X Ray Reflectometry

Layers thicknesses, density and roughnesses were measured by X-ray reflectometry (XRR) [25], at the XRR service of the Institute of Materials Science of Madrid (ICMM), in a Siemens D-500 diffractometer, using an X ray generator with Cu anode working at 40 mV and 25 mA, using the Cu-Kα emission line. A scintillation detector with a graphite monochromator just before the

detector was used to collect the diffraction lines avoiding fluorescence emission and other emission lines from Cu. Incidence and collection slits were chosen to be 0.3° which gave the best product signal-resolution.

As detailed in Chapter 3, XRR measurements were also upheld just before ReflEXAFS measurements for each sample. They were recorded to choose the best reflection angles for the ReflEXAFS spectra, but they can also be used to estimate the layers characteristics (thickness, density, roughness)

Both laboratory equipment and synchrotron radiation XRR diagrams were simulated and fit using the genetic algorithm provided by *GenX* program [26] to obtain the layers characteristics. Note that the analysis of the XRR curves provides direct information concerning partial thicknesses of each layer in the samples, in contrast with the results obtained by Rutherford Backscattering Spectrometry (see Section 2.2.3 below). Moreover, density can be directly obtained, so it does not have to be estimated. The variables were the interface roughnesses, and the thicknesses and densities of the layers.

2.2.3 Rutherford Backscattering Spectrometry

Sample layers composition and absolute atomic concentration were measured by Rutherford Backscattering Spectrometry (RBS) [27] at the Centro Nacional de Aceleradores (Seville-Spain), using a 3 MeV Tandem accelerator. The samples were irradiated with a 5.19 MeV $^{4}He^{++}$ beam, and the backscattered particles were detected at 165 deg using a surface barrier detector.

This technique measures the number of atoms per surface unit. Thus, if a given density is assumed, e.g. bulk density, thicknesses can be deduced.

Two methods were used to analyze the RBS spectra: (i) if the signals from the different elements were completely separated and background free, the relative composition was simply obtained by comparing the integrals of the peaks, corrected by the respective cross sections. The statistical errors were estimated to be around 2-3%. Moreover, the absolute amount of Cr and Cu

was calculated by comparison with a reference sample which contains 5.65 10^{15} atoms Bi/cm^2±1.7%. (ii) Apart form that, all spectra were analyzed using the SIMNRA simulation code [28] A very good agreement was found between these two methods for all the studied samples.

For the samples here presented the depth resolution of the RBS technique is not enough to resolve the individual thin layers. Instead, total thickness of each element was measured and equal thickness of all the layers of the same composition was assumed, as the growing conditions were the same for all of them.

RBS measurements were carried out at the centre and both extremes of each sample to show possible inhomogeneity.

2.2.4 Nuclear Reaction Analysis

As RBS is not sensitive enough for detecting light elements over heavy substrates, Nuclear Reaction Analysis (NRA) [29] technique was used to determine the abundance of N in the nitrides. This technique detects the quantity of ^{4}He^{++} emitted by the reaction:

$$^{14}N + {}^2H^+ \longrightarrow {}^{16}O \longrightarrow {}^{12}C + {}^4He^{++} \tag{2.1}$$

And it is compared with the number of ^{4}He^{++} emitted by a reference sample of Si_3N_4/Si, that has a known abundance of 1.08 x10^{18} atoms of N per cm^2. The error of this technique is estimated around 10% of the absolute values. This experiment was also performed at the CNA. The ^{2}H$^+$ beam had an energy of 1368 keV, and the detection angle was 150°. A 13 μm *mylar* filter was used to stop the backscattered ^{2}H$^+$ in front of the detector.

However, spatial resolution is not good enough to discriminate the depth at which the nitrogen is.

2.2.5 Atomic Force Microscopy

Surface roughnesses were measured by Atomic Force Microscopy (AFM) with three different microscopes: at the AFM service of the Centro de Investigación, Tecnología e Innovación de la Universidad de Sevilla (CITIUS), a Molecular Imaging Pico Plus microscope was used; at the AFM service of the Institute of Materials Science of Seville, a Topometrix TMX2000 and a Nanotec Dulcinea microscopes were used. All of them were used in contact mode with a scanner of maximum X-Y-Z ranges of $2.3 \times 2.3 \times 1$ μm.

Sample heights in different regions of the samples were measured by AFM and surface roughnesses was calculated from these results. Roughness can be defined as the root mean square (RMS) of the height deviation from the best fit line along the surface of the sample.

This roughness measured by AFM is not directly comparable to the roughness calculated by the simulation of the XRR diagrams. Roughness is a fractal phenomenon, which means that its value depends on the scale of the measurement. The AFM scale for these measurements was chosen in order to see the structure of the grains of the layers. On the other hand, XRR measurements take into account the dispersion that is caused by all the roughnesses in all the scales. What is more, their influence on the diagram depends not only on their roughness scale, but also on the incidence angle and on the energy of the radiation.

Chapter 3

ReflEXAFS experiments

Contents

Introduction

In most studies to date that have adopted the reflection geometry (Figure 3.1) for measurements of the ReflEXAFS spectra from a surface, the experimental conditions were those of the total reflection [15, 16], i.e. the incidence angles were below the critical angle. Typical examples of the values of the critical angles for a material are 0.13° for pure molybdenum to 0.33° for pure iron at about their respective K absorption edge energies.

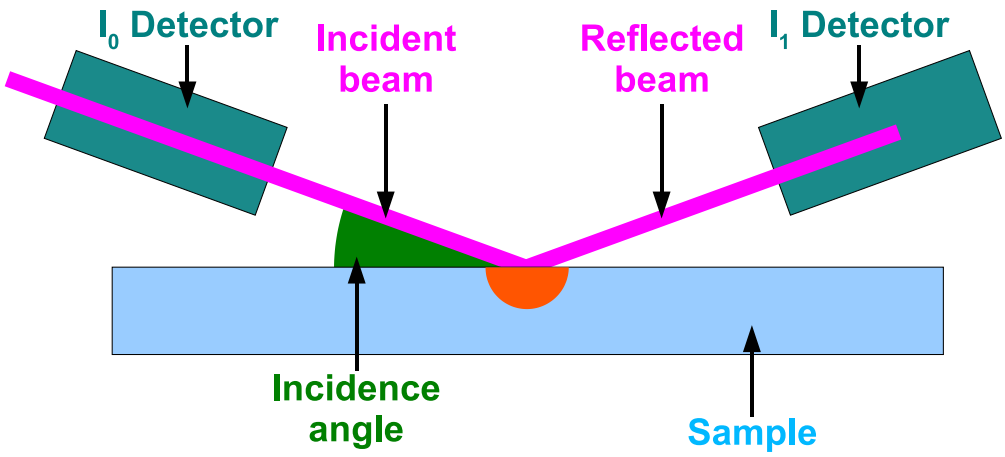

Figure 3.1: Reflection geometry for ReflEXAFS measurements

The first issue encountered when going beyond this limit is that the reflectivity intensity is extremely low. Figure 3.2 shows the reflectivity of a Cu mirror at 200 eV above the Cu-K absorption edge. It can be seen from the figure that the reflectivity drops to values a few orders of magnitude below the reflectivity for the total reflection conditions. Thus, the main experimental challenge is to design the protocols necessary to maximise the reflected beam intensity so as to get the best possible signal to noise ratio.

Furthermore, the penetration depth of the radiation also changes dramatically with the incidence angle above the critical angle. This effect, that will

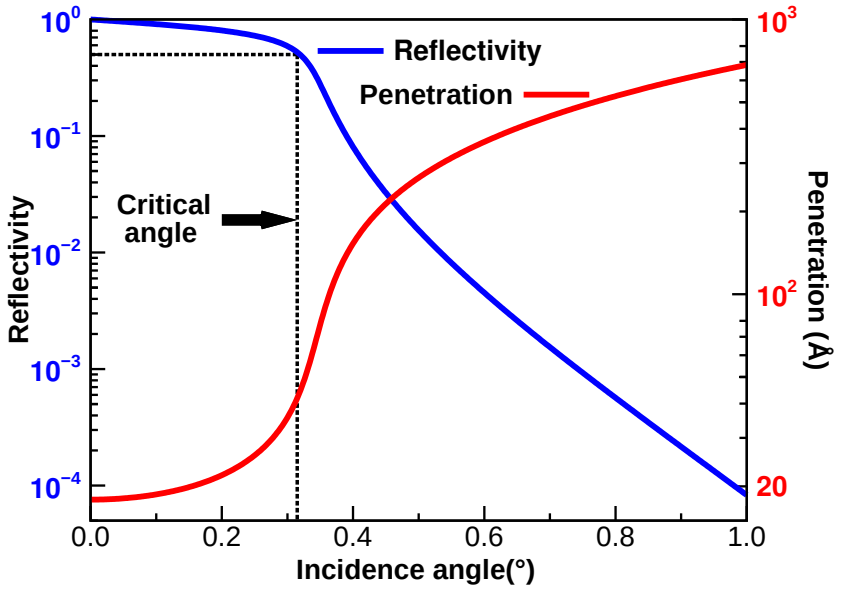

Figure 3.2: Reflectivity and penetration depth of a Cu mirror at 9.2 keV

be used for studying deeper regions on the sample surface, makes the accuracy in the determination of this angle decisive to prevent changes in probed depths in the sample for the same spectrum. In this sense, a good beam stability from the X ray source and precise instrumentation are necessary.

This Chapter summarises the instrumentation used and the protocols designed to obtain high quality ReflEXAFS data even at these difficult conditions [30].

3.1 Instrumentation

The experimental requirements for a ReflEXAFS experiment are those of a basic EXAFS measurement [31] plus some additional issues that are related to the small incidence angles of the beam impinging on the sample, that are around the critical angle of the system under study.

The beam angle stability in the synchrotron beamline is a critical parameter as explained above. Furthermore, the accurate determination of the incidence angle is also of paramount importance. Finally, as the reflected beam intensity will be quite low, a rather high X ray photon flux is needed.

3.1.1 The BM29 station at the E.S.R.F.

The experiments described in this report were performed at station BM29 of the European Synchrotron Radiation Facility (E.S.R.F.) [32, 33]. This instrument provided the desirable experimental facilities as well as the required beam flux and stability to carry out these measurements.

BM29 is the general purpose X ray absorption spectroscopy beamline at the E.S.R.F. The strengths to which BM29 operates arise from the intrinsic properties of the E.S.R.F. synchrotron, coupled with a bending magnet source and the high quality performance of the beamline monochromator.

- A large operational energy range with reasonable X ray flux: 4.5 keV to 74 keV.
- High energy resolution: typically a factor 3 to 5 better than the intrinsic spectral broadening at any K or L absorption edge.
- High spectral signal to noise ratio: in the region of $2{\times}10^4$ for well prepared samples.
- High beam stability: compatible with the demands of extreme sample environments where low beam dimensions are required.

3.1.1.1 Optics

Two monochromators were used at the BM29 beamline during these experiments. A Si(311) double crystal monochromator for the CuCrxN samples,

and a Si(111) double crystal for the rest of the samples. The main characteristics of these monochromators are summarized in Tab. 3.1.

Table 3.1: Monochromator characteristics

Mono	**Energy range (keV)**	**Energy resolution**	**Maximum flux (phot/s·mm^2)**
Si(311)	5 - 50	10^{-5}	10^{10}
Si(111)	4.5 - 24	10^{-4}	10^{11}

To reject the higher harmonics from the monochromator diffraction, the crystals were detuned (this is, moved from the parallel position) to reach 50% of the maximum intensity of the main harmonic. This way, the intensity of the 3^{rd} harmonic is reduced approximately by a factor 10^3.

The station has also the possibility of rejecting the higher harmonics using a dedicated double crystal Rh/Pt coated Si mirror. This device allowed to work with the monochromator crystals completely parallel, thus obtaining a higher stability of the beam during the measurements.

3.1.2 Reflectometer

For the reasons explained above, it is essential that the precise value of the incidence angle is determined accurately, and kept fixed during the measurements.

To meet this requirement a high quality reflectometer with at least two circles is needed on the experimental end station with a $\theta - 2\theta$ specular reflection scanning mode. In addition to the $\theta - 2\theta$ rotation axes, the sample holder must also allow movements in the x, y and z directions and in the three angular movements of *roll*, *yaw* and *pitch*. This is essential to enable an accurate alignment of the sample surface to the centre of rotation of the θ

and 2θ rotation axis of the reflectometer and with the incident beam.

A fully automated 3-circle Huber reflectometer and 3-translation axis, 3-angle goniometer were used to hold the sample and the reflected beam detector (I_1). A scheme of the reflectometer, goniometer and detectors can be seen in Figure 3.3, while a picture of the actual experimental setup at BM29 is shown in Figure 3.4. One of the circles (labeled *phi*) held the rest of the setup, allowing rotation around the vertical axis angle passing through the centre of the stage. A second circle (labeled *th1*) held the sample goniometer, seen in Figure 3.5, which was mounted concentrically with the third circle (labeled *th2*), holding the I_1 detector fixed to a bolted arm one meter long. The angular ranges and accuracy of these motors appear in Tab. 3.2. The whole system was mounted on a heavy table (for purposes of stability) that could be moved either vertically or horizontally in order to align the reflectometer with the beam position, as will be described in Section 3.2.1.2.

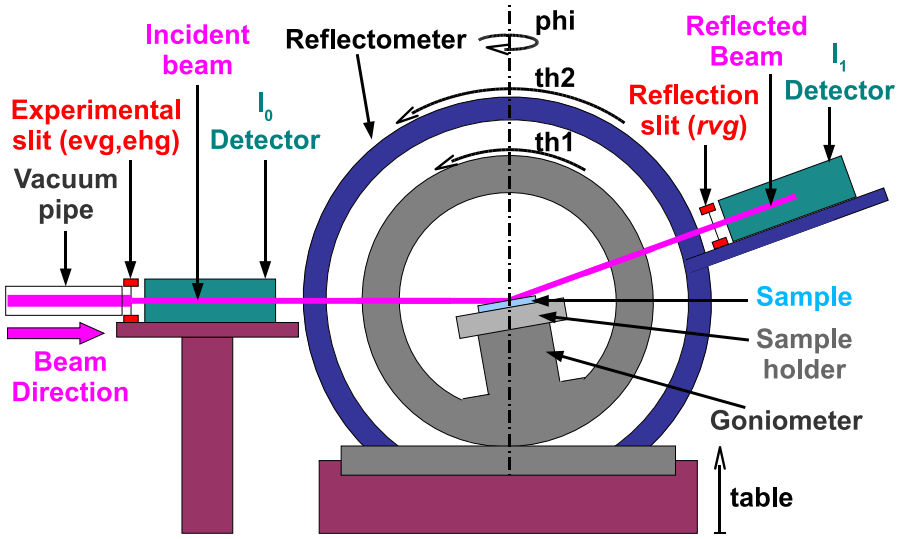

Figure 3.3: Scheme of the reflectometer used, showing the rotation circles and the slits

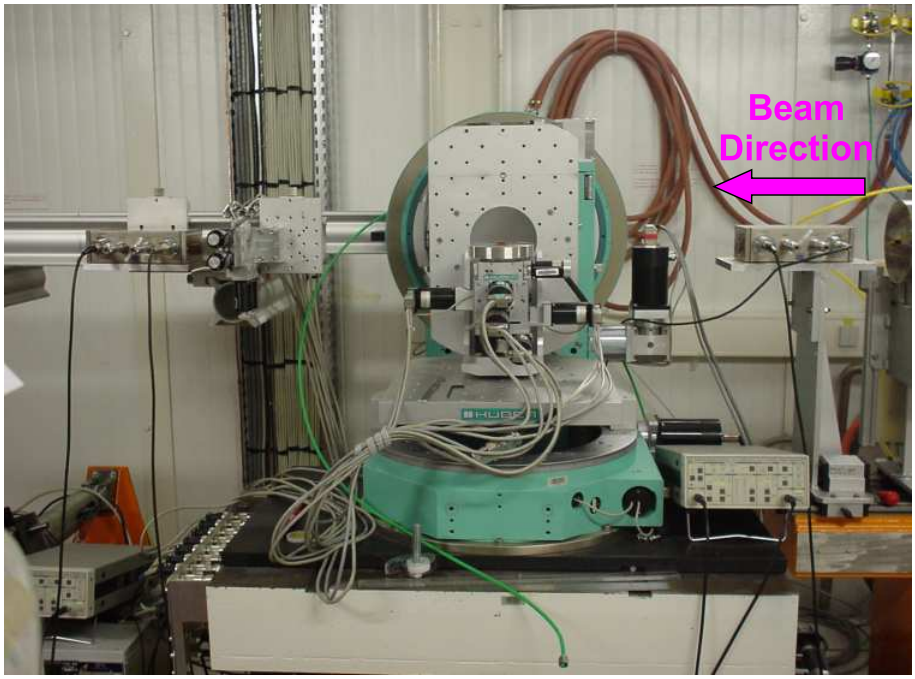

Figure 3.4: Picture of the reflectometer used at BM29

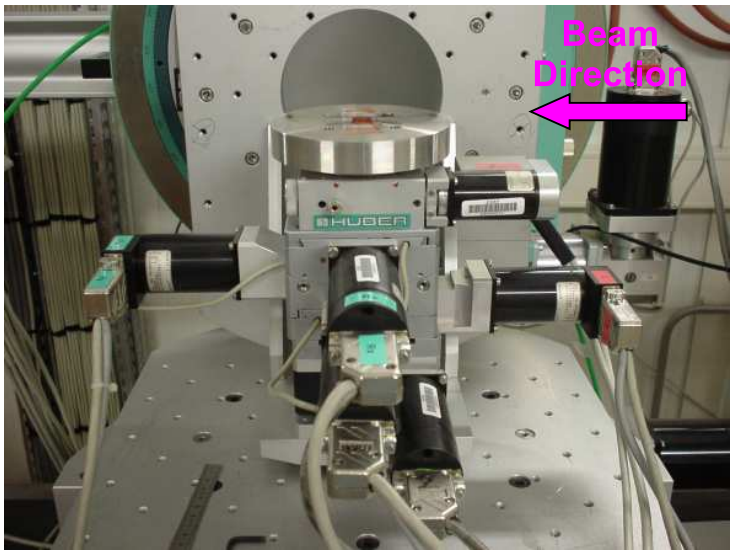

Figure 3.5: Picture of the goniometer used at BM29

Table 3.2: Reflectometer and goniometer motors range and accuracy

Motor	Range	Accuracy
th1 (deg)	(0,360)	0.001
th2 (deg)	(0,360)	0.001
x (mm)	(-12,12)	0.01
y (mm)	(-12,12)	0.01
z (mm)	(-12,12)	0.001
rx (deg)	(-15,15)	0.01
ry (deg)	(-15,15)	0.01
psi (deg)	(0,360)	0.002

3.1.3 Slits

A horizontally resizable slit, which will be called the *experimental horizontal slit gap* (*ehg*), was mounted just before the I_0 detector. This slit allows the optimization of the horizontal beam size in order to provide sufficient spatial resolution for sample alignment (as explained in Section 3.2.1) and to maximize the footprint of the beam on the sample when the actual measurements take place.

A vertically fixed slit, called the *experimental vertical slit gap* (*evg*), was mounted just after the *ehg* and determined the vertical beam size. In the experiments described here, *evg* was set to 100 μm for the Cu-K and Fe-K edge measurements, while it was fixed to 50 μm for Mo-K edge experiments. These values were found to result in a reasonable compromise between resolution and photon flux after taking into account sample size and critical angle values.

A vertically resizable slit, which will be called the *reflection vertical slit gap* (*rvg*), was mounted after the sample and just before the I_1 detector. This slit

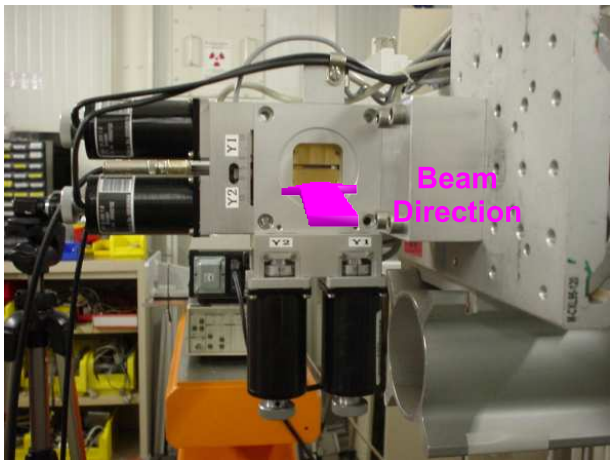

Figure 3.6: Picture of the reflection slit used at BM29

can be seen in Figure 3.6. This third slit prevents the non specular reflection components reaching the detector and determines the angular resolution for the reflection angle. A wide reflection slit increases the intensity of the reflected beam but decreases resolution, and a compromise between resolution and intensity of the reflected beam has to be reached by the experimentalist. In the experiments carried out by us, *rvg* was set to 1 mm.

3.1.4 Detectors

As in standard EXAFS experiments, a pair of beam intensity monitors, in this case ion chambers, are required to obtain an accurate, high signal-to-noise ratio for a variable energy scan. It is beneficial if these detectors are relatively light-weight since I_1 needs to be mounted on the detector arm attached to the *th2* circle. Two 15 cm long OKEN S-1194A1 ion chambers were used in the experiments presented here. These detectors were filled with appropriate gas mixtures to optimise them for the energy of the absorption edge to be studied. The optimal values are such that 20% and 80% of the beam intensity is absorbed in the I_0 and I_1 detectors, respectively.

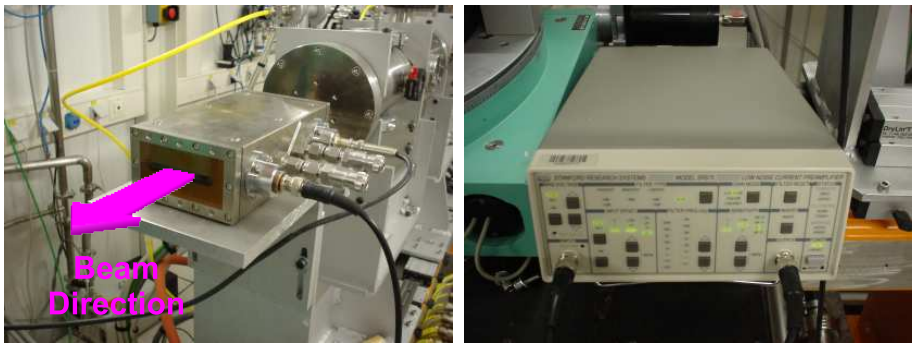

Figure 3.7: Picture of the ion chamber and its amplifier used at BM29

Each ion chamber works with a Stanford Research Systems SR570 current amplifier. Both actual devices can be seen in Figure 3.7. For noise reduction purposes, the detectors were connected using short cables and the amplifiers worked on their own batteries during ReflEXAFS scans. All non-essential electronic devices inside the experimental hutch were also turned off during the measurements to remove as many potential sources of electronic background noise as possible. This model of amplifier provides remote control of the amplification settings and this allows the recording of spectra with changes in intensity of several orders of magnitude without compromising the signal-to-noise ratio. This capability is particularly useful when measurements at incidence angles far above the critical angle are performed.

3.2 Measurement protocol

The overall procedure for carrying out the ReflEXAFS measurement is summarised in Figure 3.8. First of all, the direct beam has to be found in the *th2* circle, which holds the reflected beam detector, by scanning the *th2* motor. The sample has to be moved out of the beam path (for example by placing it about 2 mm down in z), the reflection vertical slit gap (*rvg*) is then closed down, typically to 0.2 mm, and *th2* is scanned to find the exact position of

the incident beam. This will be the origin of *th2* circle.

Once this has been done, the sample and reflectometer have to be aligned with the incidence beam. Afterwards, X ray reflectivity (XRR) curves are measured, so the angles to carry out the ReflEXAFS measurements are selected from the information contained in these curves. Then, the reflection angles have to be found for each of the incidence angles selected and finally, the energy scans are made.

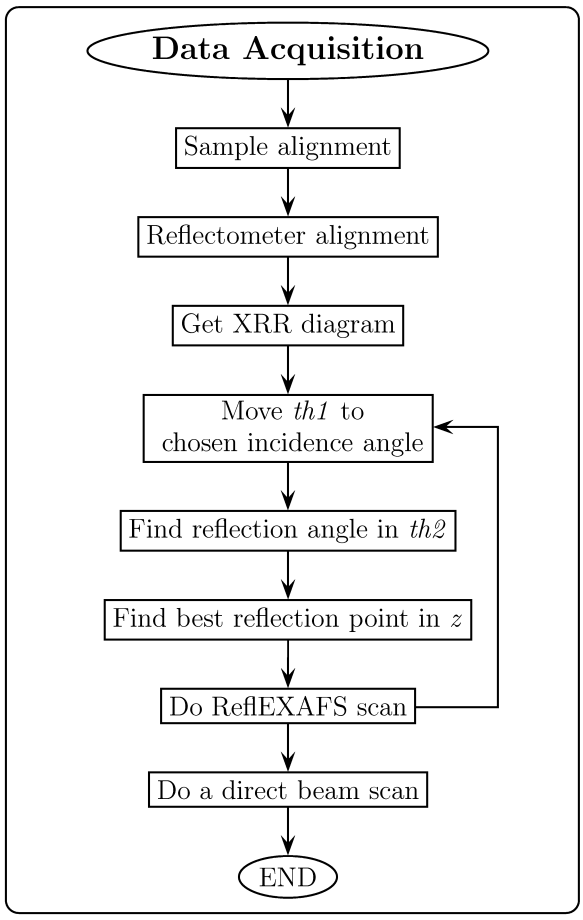

Figure 3.8: ReflEXAFS data acquisition procedure

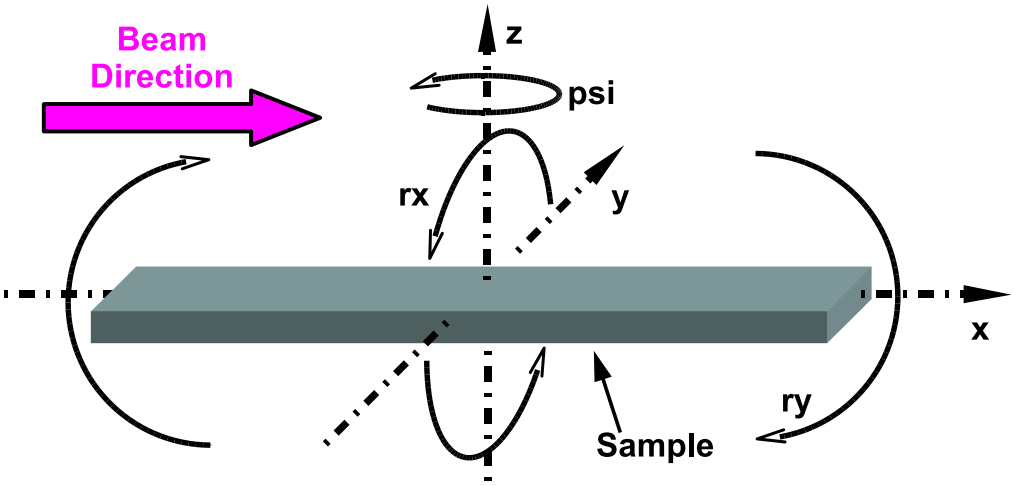

Figure 3.9: Possible movements of the sample by the goniometer

3.2.1 Alignment

The alignment is of paramount importance for two reasons: the need to maximize the intensity of the reflected beam and the need for an accurate determination of the incidence angle of the beam. To achieve this, three conditions must be fulfilled:

1. The sample must be parallel to the beam and aligned with the beam direction. Besides, the middle point of the surface of the sample must be at the center of rotation of the reflectometer circles (*th1* and *th2*) .

2. The beam must pass through the center of rotation of the reflectometer circles.

3.2.1.1 Sample alignment

The first condition is the angular and position alignment of the sample, which are done with the sample goniometer. Alignment in the z, y, ry, rx, psi, and x directions and angles, indicated in Figure 3.9, is required, and it is best

performed in this order. Decisions about additional scans or movements to be done are made on the basis of visual examination of the shape of the profile registered at the I_1 detector. This profile is made by the sample blocking the direct beam when the scan of the appropriate direction or angle is performed. All the procedures for the alignment in each direction and angle are summarized as flowcharts in Figures 3.10 to 3.15, which include the possible profiles of I_1, and how they should be optimized.

These flowcharts are illustrated with the real scans registered for a rectangular sample. Although the rectangular shape is maybe the ideal for this alignment procedure, this can be applied to any kind of shapes with little modification of the profiles shown, provided the samples fulfill the length, flatness and roughness requirements described in Chapter 2. In fact, several different samples (multilayers, surface-oxidized multilayers, metal-nitride multilayers and surface nitrided steels) have been aligned following this procedure successfully, so it has been proved to be highly reproducible.

Each alignment step has to be made independently and in the order here presented. Although some steps require a final check that apparently brings the procedure to a previous step, this does not mean that the whole procedure has to be carried out again. For instance, in the alignment of the *ry* angle, a final alignment in z has to be made. Afterwards, the next step is to align *rx*, not to re-align y.

This order has been proven not only to be sometimes essential (for instance, alignment in y direction is impossible unless the sample has been aligned in z direction previously, as y scans do not show the sample blocking the beam in this case), but also to be the most efficient in terms of the number of scans required to get the sample aligned, so it is less time consuming.

3.2.1.2 Reflectometer alignment

The second condition mentioned at the beginning of Section 3.2.1 is the alignment of the reflectometer with the beam. The rotation axis of the *th1*

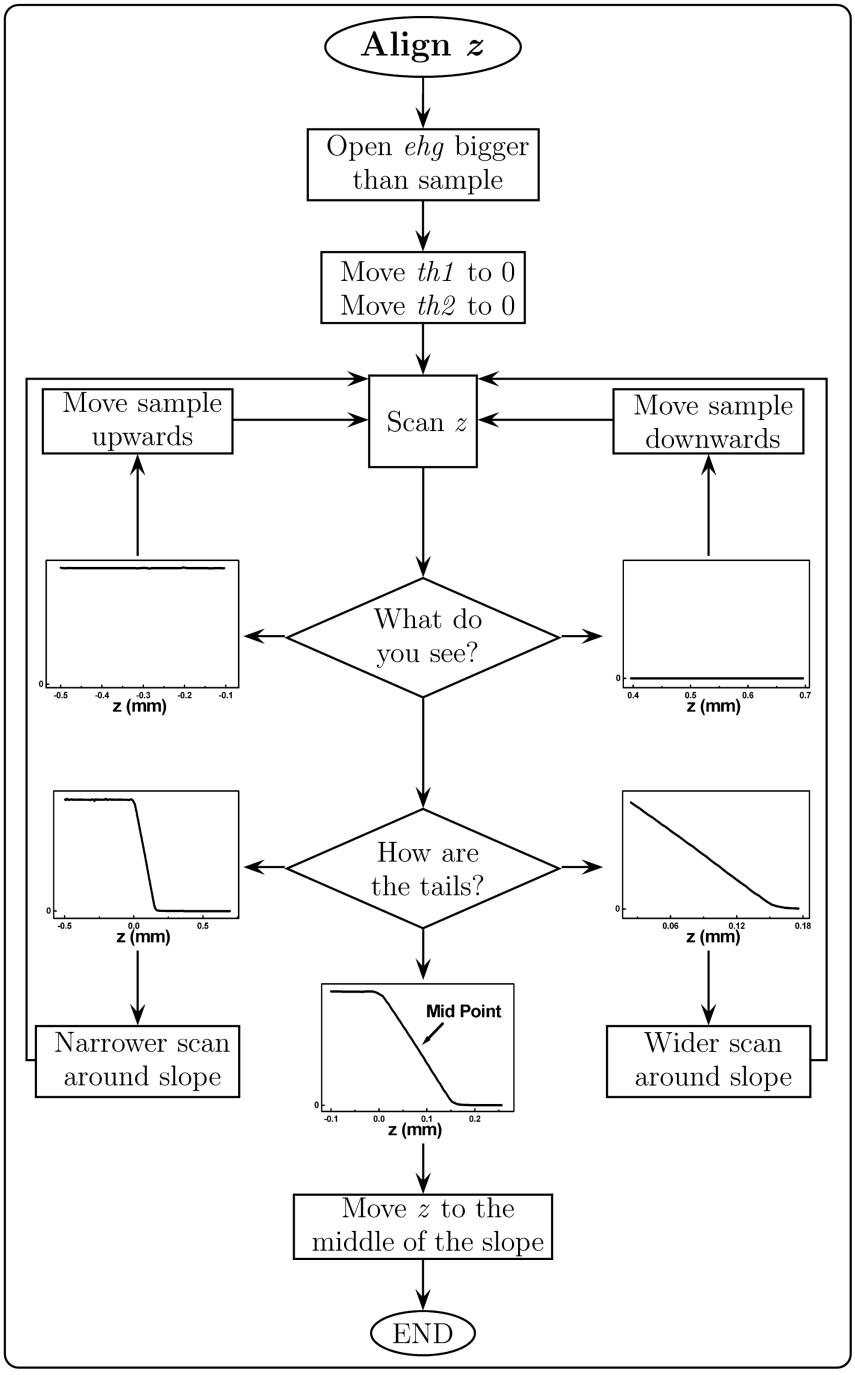

Figure 3.10: Flowchart of the alignment procedure for z direction

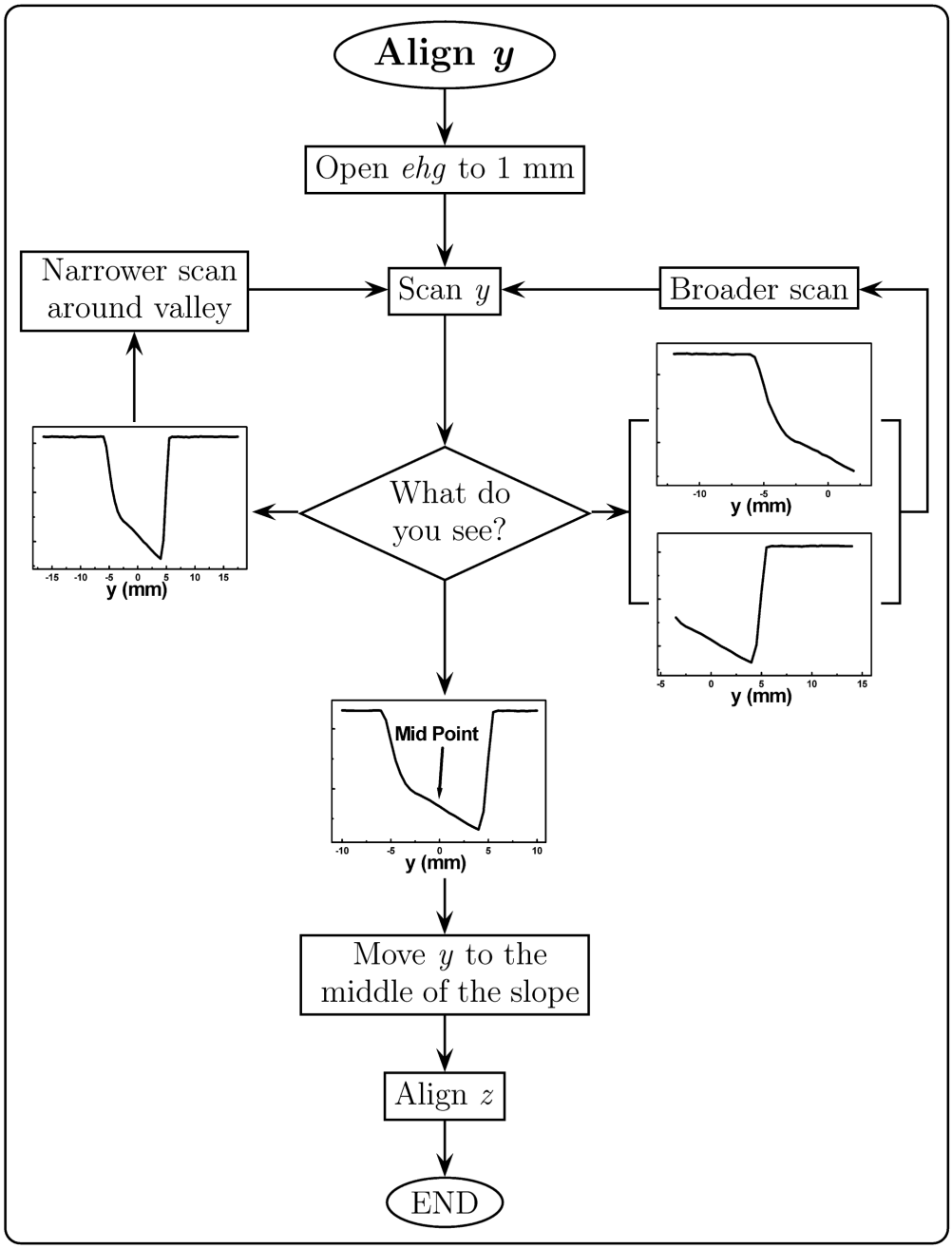

Figure 3.11: Flowchart of the alignment procedure for y direction

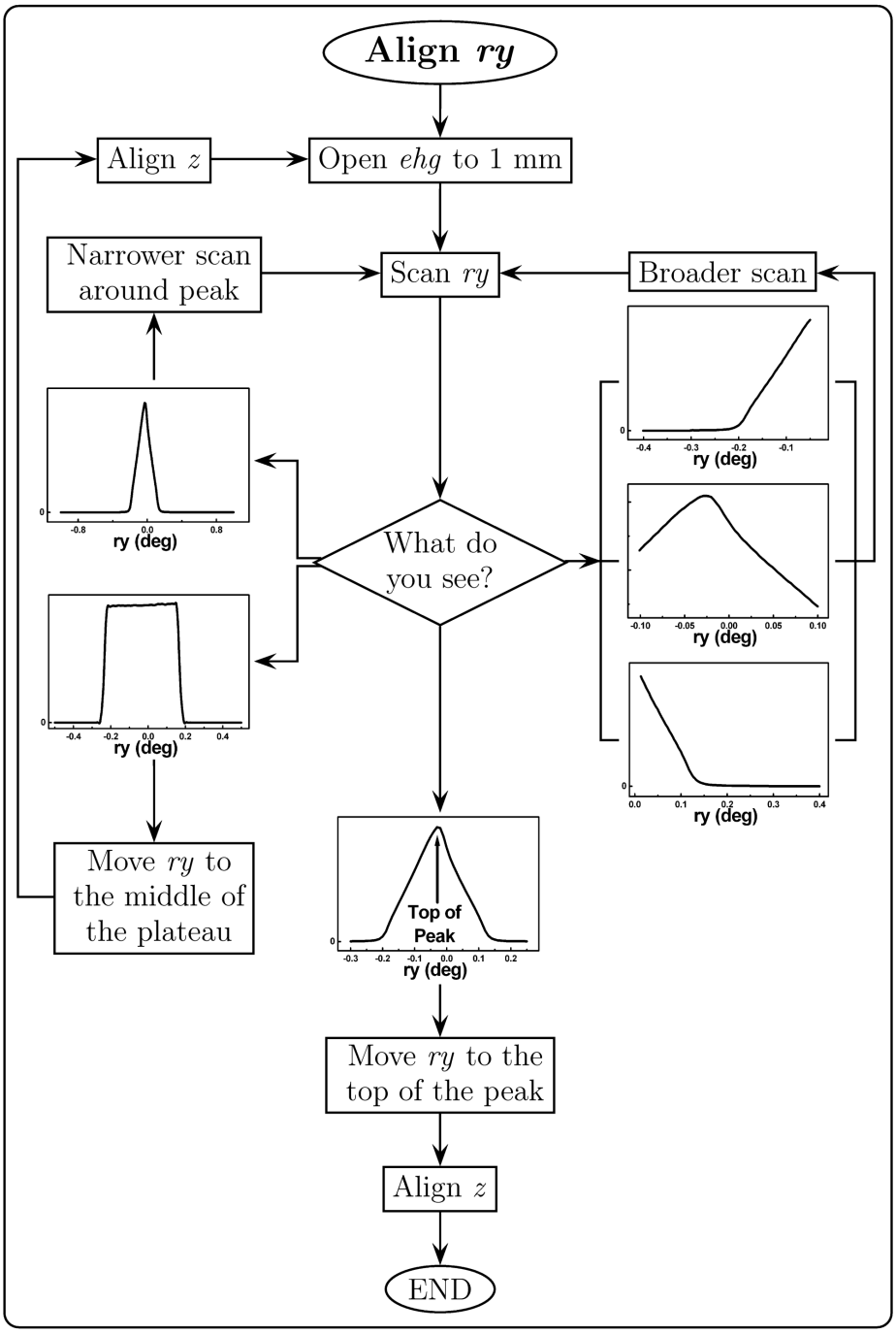

Figure 3.12: Flowchart of the alignment procedure for *ry* angle

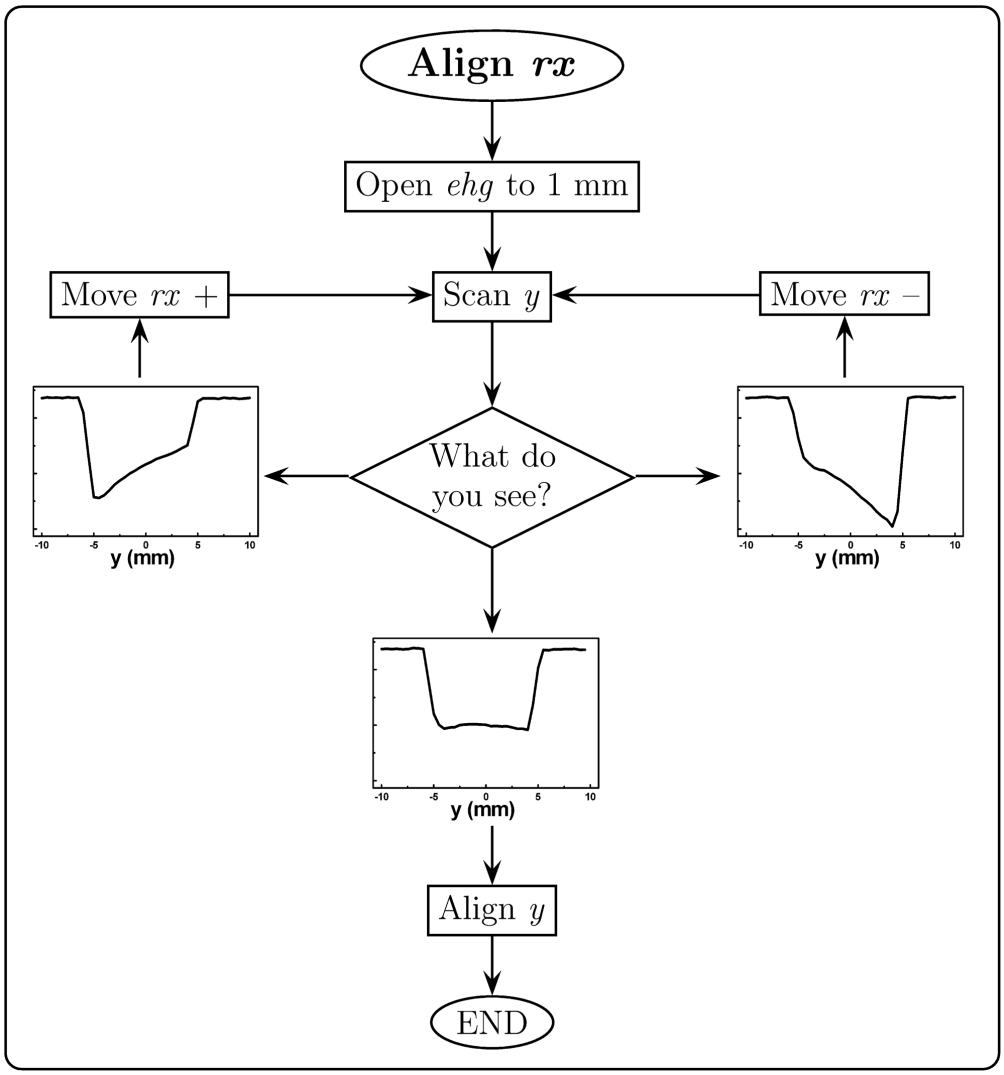

Figure 3.13: Flowchart of the alignment procedure for rx angle

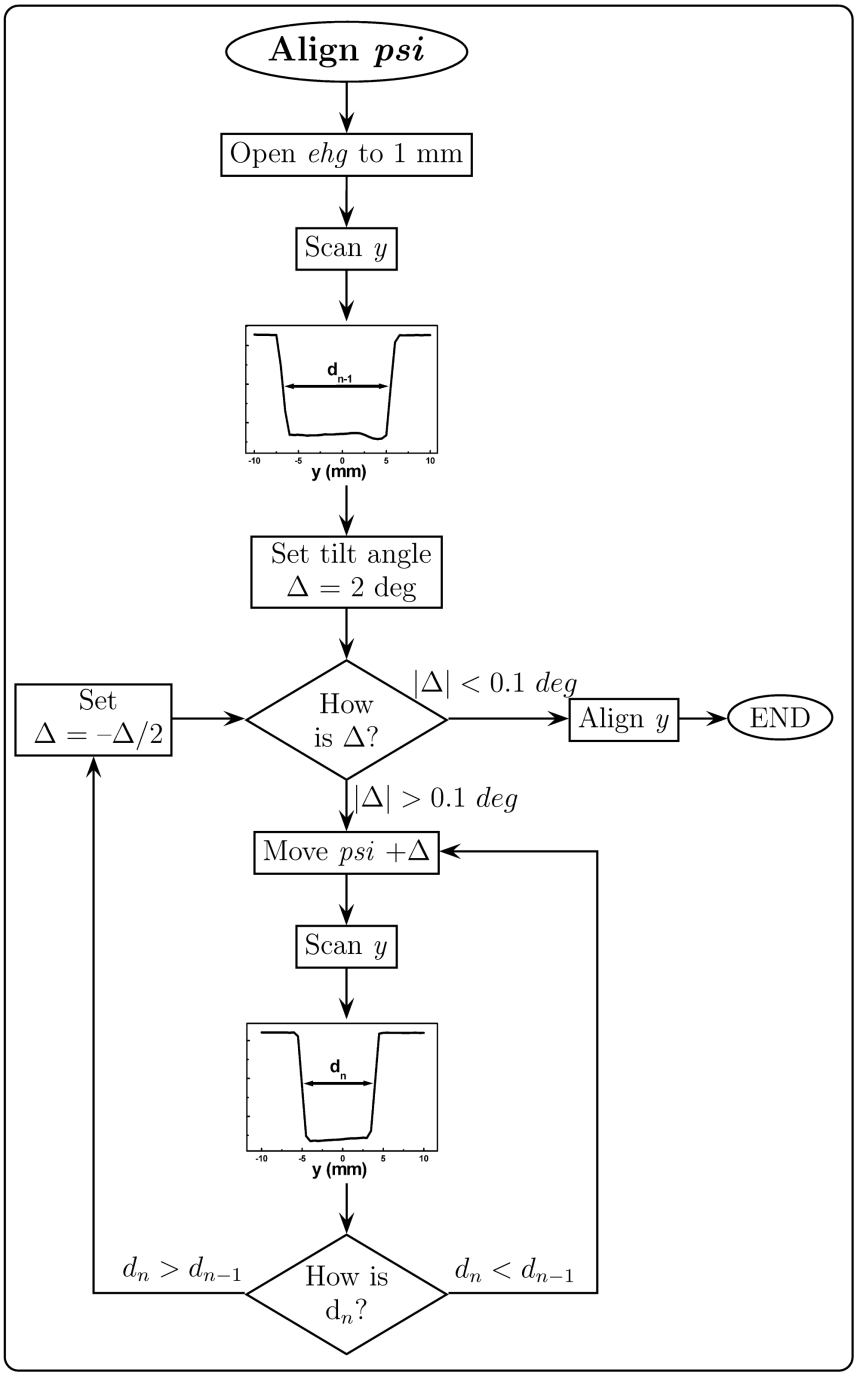

Figure 3.14: Flowchart of the alignment procedure for *psi* angle

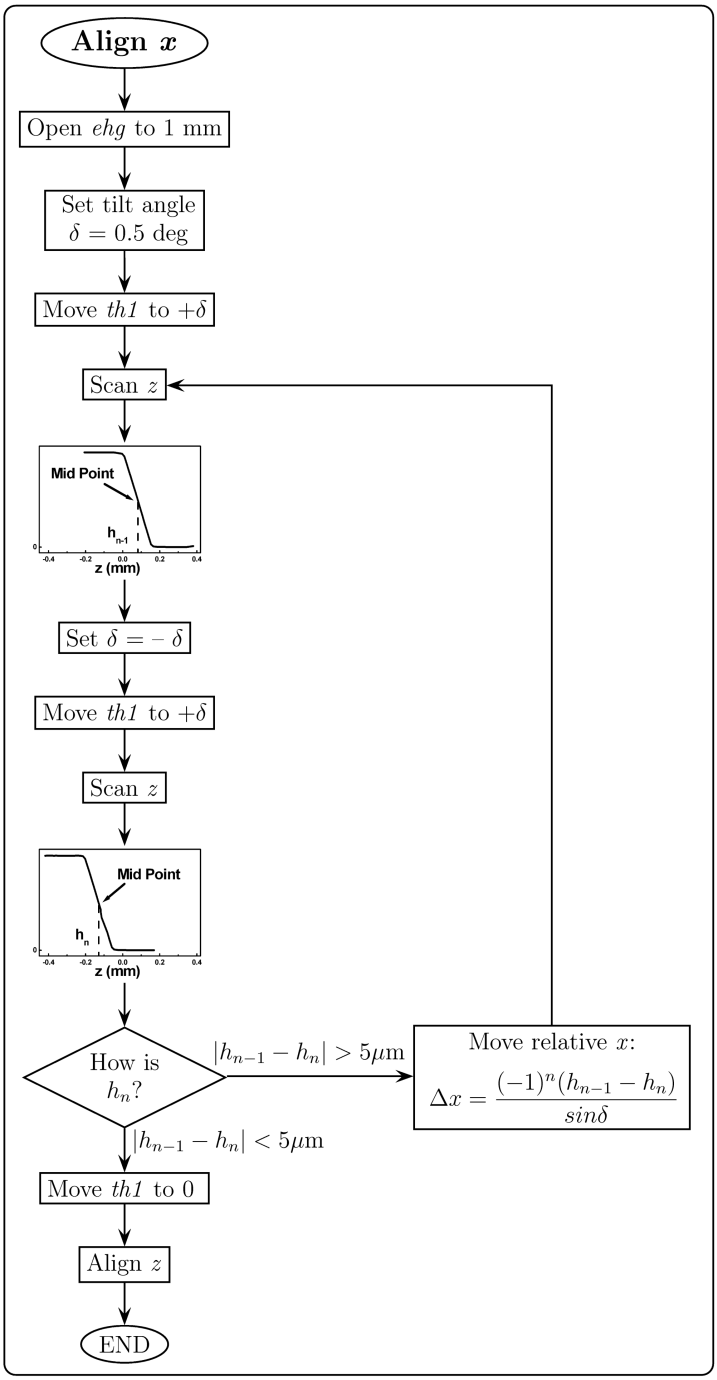

Figure 3.15: Flowchart of the alignment procedure for x direction

and *th2* circles of the reflectometer must be aligned with the beam direction, as seen in Figure 3.16. To achieve this, once the sample is aligned, a z scan has to be made and the value in the middle of the slope noted as z_0. Next, a 180° rotation in *th1* circle has to be performed, so as to invert the sample. This step must be performed with extreme care to avoid disturbance of the sample on the stage. Obviously, to undertake this alignment procedure the sample must be well fixed to the sample holder. Once the sample is upside down, another z scan is made and the value in the middle of the slope noted as z_π. The large table that holds the whole reflectometer is then moved vertically by half of the difference between the z_0 and z_π values. This places the center of the rotation axis of the reflectometer on the beam axis. Once the reflectometer has been moved, the sample is returned to $th1 = 0$. An alignment in the z direction is repeated to check the beam position is still at the mid point between z_0 and z_π.

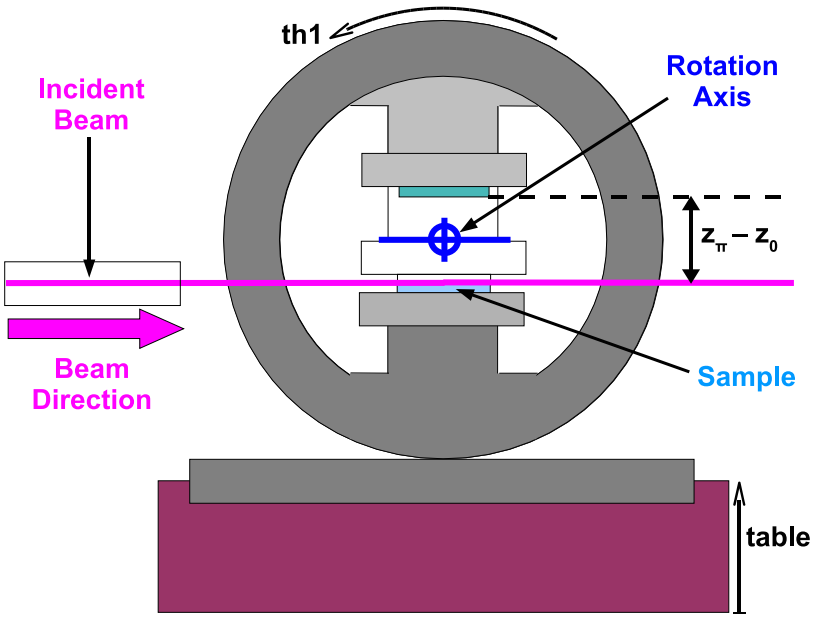

Figure 3.16: Scheme of the reflectometer alignment

As the reflectometer has moved relative to the beam position, the origin

of *th2* circle has changed, and it is thus necessary to repeat the procedure described at the very beginning of the measurement protocol. Fortunately, the reflectometer alignment has to be performed only once at the start of an experiment. As the beam should not move during the course of a series of measurements, the reflectometer should remain aligned when switching to different samples, though obviously each sample has to be aligned independently.

3.2.2 XRR measurement

The X-Ray Reflectivity (XRR) measurements provide information about the intensity of the reflected beam as a function of the incidence angle, for a given energy. In layered samples, reflectivity intensity has sudden changes due to interference effects, so it contains information concerning the thickness and composition of the layers as well as the roughness of the top surface and the interfaces. Moreover, since X ray penetration is a function of photon energy, XRR curves change with energy [21]. For this reason, to select the most appropriate angles to carry out the ReflEXAFS measurements, several XRR curves have to be recorded prior to the energy scans: one at an energy close to the edge of the atomic species to be measured and two others at the low and high energy limits of the ReflEXAFS scans. These XRR diagrams also provide an estimate of the reflected beam intensity within the energy range of the scan.

As an example, Figure 3.17 shows the XRR curve of a CuCrx2 layered sample (see Chapter 5 for composition and structure) for incidence angles between 0 and 1.5°, recorded at E=8.0 keV and at E=10.0 keV . This curve has been recorded in the same way as would be done in a laboratory equipment, including a calibration of the $\theta-2\theta$ relationship (here called $th1-th2$). Once this calibration has been done, the sample must be moved to the middle of the slope of a z scan. The scan starts at 0° and should proceed up to the value of the maximum angle that can be measured with a good signal-to-noise

ratio. In this way, the upper angular limit for the ReflEXAFS measurements can be determined.

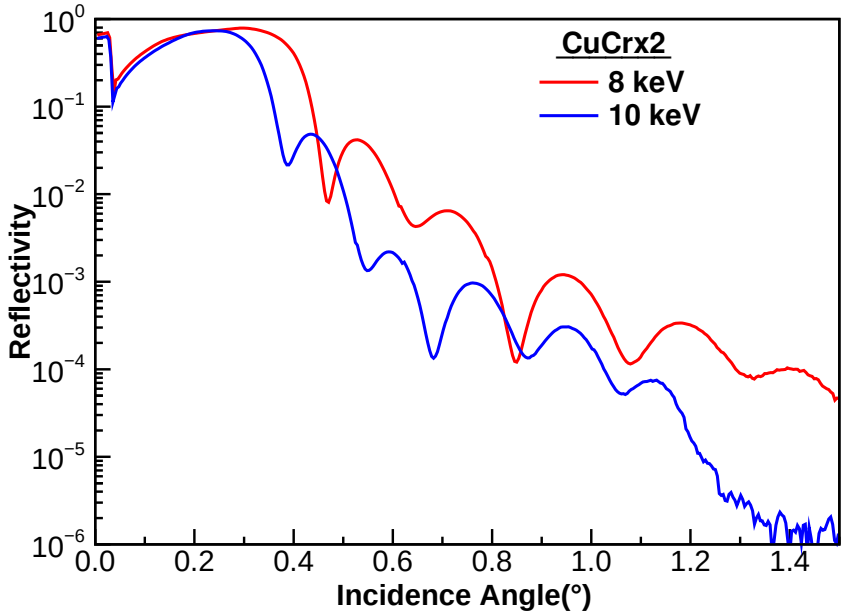

Figure 3.17: XRR diagram of sample CuCrx2

3.2.3 ReflEXAFS scans

The first step to collect a ReflEXAFS spectrum is to choose the incidence angle and determine the value of the corresponding reflection angle accurately, since the calibration curve does not yield sufficiently accurate values. To achieve this, the experimental horizontal slit gap (*ehg*) has to be opened as much as possible though avoiding the beam footprint exceeding the sample dimensions. Afterwards, a z scan has to be performed and the sample moved to the middle of the slope. The *th1* circle is then tilted to the selected incidence angle, and *th2* circle is scanned, with narrow (0.2 mm) reflection vertical slit gap (*rvg*) to find the reflection beam peak. This is explained in

Figure 3.18. Once *th2* is moved to the maximum of the peak, a scan in *z* has to be done again to find the maximum reflectivity, as explained in Figure 3.19. An EXAFS-like energy scan then has to be done around the desired absorption edge, with a starting point at least at 500 eV below the edge and an end point at least at 1000 eV above the edge. However, 1000 eV below and 1500 eV above are recommended to optimize the subsequent background subtraction procedure.

3.2.3.1 Direct beam scans

Finally, it is important to record a scan of the air absorption (direct beam scan). This is needed for data normalization purposes.

$$\left.\begin{aligned} \frac{I_1(E)}{I_0(E)} &= e^{\mu_{air}(E)x} R(E) \\ \frac{I_1^{Direct}(E)}{I_0(E)} &= e^{\mu_{air}(E)x} \end{aligned}\right\} \Longrightarrow \frac{\frac{I_1(E)}{I_0(E)}}{\frac{I_1^{Direct(E)}}{I_0(E)}} = R(E) \qquad (3.1)$$

To record this scan, the sample has to be moved out of the incidence beam, and the same range of energy of the EXAFS spectra is scanned at *th2*=0°. Direct beam scans have to be recorded under the same experimental conditions used in the ReflEXAFS scans, which means that a new direct beam scan must be performed each time the filling of the ionization chambers or the size of the slits changes. It is not necessary though to repeat them for new samples (provided the slits are not changed) of after every refilling of the synchrotron storage ring.

3.3 Automation

All steps in ReflEXAFS data collection in general and the alignment procedure in particular are time consuming. Since beam time in synchrotron radiation experiments is highly precious, a significant effort has been made

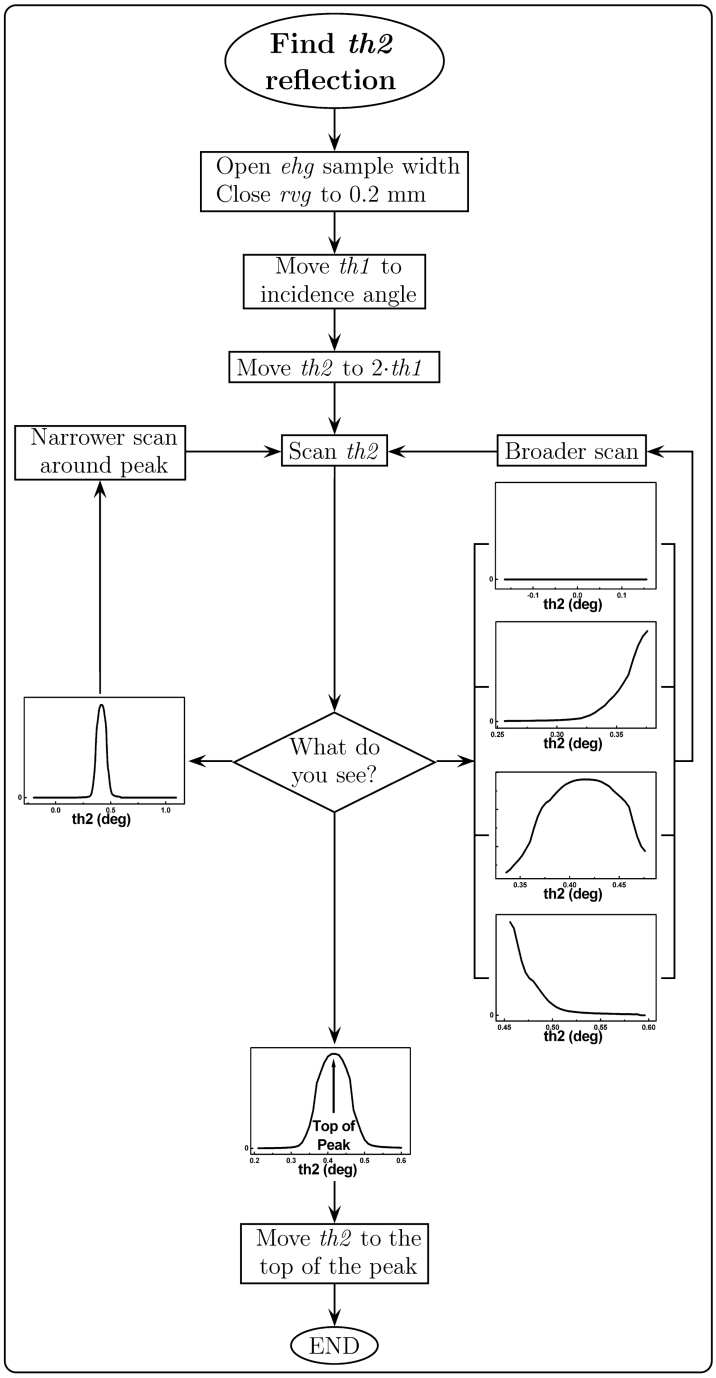

Figure 3.18: Flowchart of the reflection angle search procedure

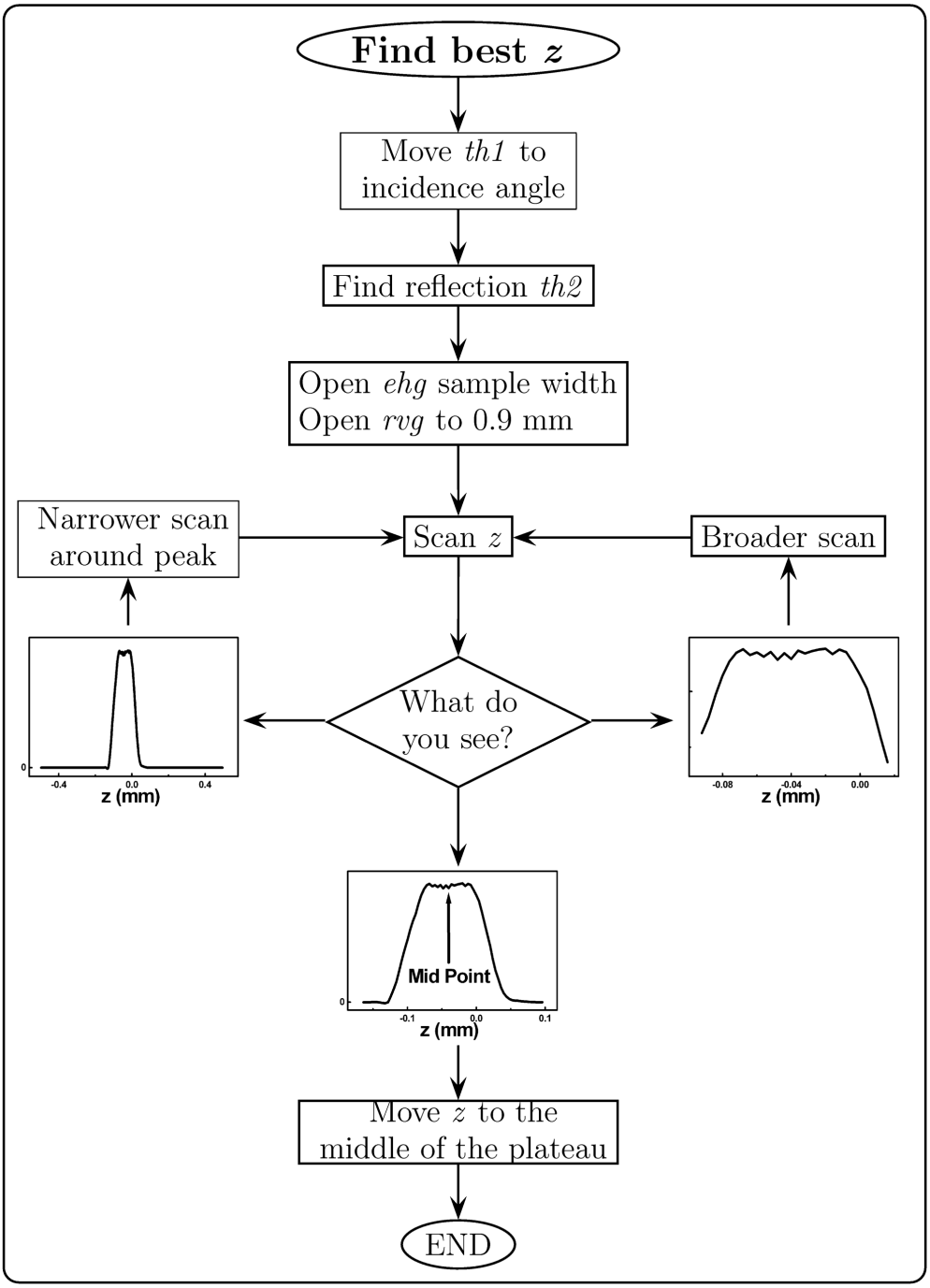

Figure 3.19: Flowchart of the best reflection z position procedure

to automate the procedures during these experiments. BM29's control software, SPEC[34], allows the remote control of the facilities in the experimental chamber as well as the extraction of mathematical information from the spectra recorded, such as position of maxima or the full width half maximum of a spectrum. Taking advantage of that, control software has been designed and written in order to evaluate the spectra and decide the steps to follow, as for instance, the decisions of the alignment procedures shown in Figures 3.10 to 3.15, 3.18 and 3.19. In fact, these flowcharts are the summary of the logical paths taken by this control software. By following this automatic procedure, the accurate alignment of the samples, which when done by hand takes several hours, can be fulfilled in less than one hour. Moreover, this automation minimizes the possibility of human errors during the procedure.

3.4 Data collection time

The typical data collection time per sample using this technique on a spectrometer such as BM29, that has a typical flux at the sample of $\sim 10^{11}$ photons per second can be outlined as follows.

The alignment procedure takes about 1 hour, plus half an hour more for the reflectometer alignment for the first sample in the experiment. Each XRR spectrum takes approximately 15 min, plus another 15 min for the calibration. These scans are repeated at least twice per energy to check reproducibility. Each ReflEXAFS spectrum lasts about 30 min, which is almost standard for an EXAFS spectrum, and three spectra per angle are typically recorded (not all in a row, but taking one spectrum per angle, and starting again three times) in order to have a better signal-to-noise ratio and to check reproducibility. Finally, two direct beam spectra are recorded per sample, that take approximately 30 min each. To characterise a standard sample eight angles are recorded, this makes a total of 16 h for a complete and accurate study of a single sample by this technique. Fortunately, by the

automation software developed, most of these steps can now be performed automatically and hence do not require the constant supervision of the user.

Chapter 4

Theory and data analysis

Contents

Introduction

The global analysis of the ReflEXAFS spectra differ considerably from the standard EXAFS analysis for several reasons: (a) there is no baseline to determine the normalization constant; (b) the penetration of the X rays changes significantly for incidence angles near the critical angle, so the energy or angle spectra that is measured has contributions from several regions of the sample; (c) the fine structure of the reflectivity is not the EXAFS $\chi(E)$ but a mixture of both the real and imaginary anomalous scattering factors. Thus, the possibility of just performing a background subtraction to the experimental reflectivity spectra in order to obtain the ReflEXAFS spectra for the different incidence angles is as attractive as mistaken.

This chapter will summarise the theory required to calculate the X ray reflectivity for multilayers as a function of energy near the absorption edge, both below and above the critical angle. This is necessary for the dedicated analysis procedure developed under this project. Furthermore, the previous attempts to analyse ReflEXAFS data will be described, showing the limitations of their approximations within the context of the theory. The last part of this chapter will describe in detail the new analysis procedure developed and followed in this work. It will also show specifically how it encompasses the previous analyses. Finally, the difficulties still to be overcome will be described.

4.1 Fundamental Theory

4.1.1 Anomalous scattering

X ray photon scattering is dominated by the bound electron-photon interaction. For this reason, it is normal to calculate the scattering processes relative to the atom centre. The electrons are not localized at the nuclear

centre, what gives rise to the atomic form factor f^0, which is the Fourier transform of the atomic electron density. Unlike nuclear cross-sections, f^0 is a function of the momentum transfer (Q). The f^0 for an atom is defined as the scattering from an atom in which all the electrons are completely bound within the non-relativistic approximation.

When the electrons are allowed to react to the incoming radiation and oscillate around the atom centre, the total atomic form factor f shows a correction as two modification terms called the anomalous scattering factors,

$$f(Q,E) = f^0(Q) + f'(E) + if''(E)\,, \tag{4.1}$$

where $f'(E)$ and $f''(E)$ are functions of incident energy and have no dependence on the momentum transfer vector. Cromer and Liberman [35] set out the basic formalism and mechanism for determining the values $f'(E)$ and $f''(E)$ by using a dipole approximation on the photon-electron interaction. They also set the limit of the valid regime when the inverse of the momentum transfer becomes comparable to orbital dimensions. When this complex form factor is used to calculate the scattering amplitude, the imaginary part of the anomalous scattering factors, $f''(E)$, effectively contributes as an absorption component.

The electric permittivity of a material, χ_e, can then be calculated by the sum of all the form factors for all the atoms present in the material per unit volume

$$\begin{aligned}\chi_e(E) &= -\frac{r_e\lambda^2(E)}{\pi}\rho_{at}f(Q,E) \\ &= -\frac{e^2\hbar^2}{\epsilon_0 m_e}\frac{1}{E^2}\rho_{at}\left[f^0(Q) + f'(E) + if''(E)\right]\,,\end{aligned} \tag{4.2}$$

where r_e is the classical electron radius, and ρ_{at} is the atomic density (number of atoms per unit volume) of the material. In the case of one material having multiple elemental components, the form factor $f(Q,E)$ is calculated from a

fractional sum of all the elements,

$$f(Q,E) = \sum_{\forall Z} c_Z f_Z(Q,E) \ , \tag{4.3}$$

where c_Z is the atomic fraction of the component Z in the material.

The refractive index of a material, n, is defined from Maxwell's equations, and is written [36]

$$n(E) = \sqrt{\epsilon_r \mu_r} \simeq \sqrt{\epsilon_r} = \sqrt{1 + \chi_e(E)} \, , \tag{4.4}$$

where the relative magnetic permeability, μ_r, is almost 1 for most non ferromagnetic materials. Within the X ray range of the electromagnetic spectrum, the electric permittivity is quite small, so the last equation may be approximated to get an expression of the refractive index in terms of the anomalous scattering factors

$$\begin{aligned} n(E) &\simeq 1 + \frac{\chi_e(E)}{2} = \\ &= 1 - \frac{e^2\hbar^2}{2\epsilon_0 m_e} \frac{1}{E^2} \rho_{at} \left[f^0(Q) + f'(E) + i f''(E) \right] \ . \end{aligned} \tag{4.5}$$

Traditionally, the refractive index of a material in the X ray region is written as [37]

$$n(E) = 1 - \delta(E) - i\beta(E) \, , \tag{4.6}$$

which yields the relationship of $\delta(E)$ and $\beta(E)$ with the anomalous scattering factors by the expressions [38]

$$\delta(E) \simeq \frac{e^2\hbar^2}{2\epsilon_0 m_e} \frac{1}{E^2} \rho_{at} \left[f^0 + f'(E) \right] \ , \tag{4.7a}$$

$$\beta(E) \simeq \frac{e^2\hbar^2}{2\epsilon_0 m_e} \frac{1}{E^2} \rho_{at} f''(E) \, . \tag{4.7b}$$

Either in a classical [38] or a quantum mechanics [39] calculation of the anomalous scattering factors, $f'(E)$ and $f''(E)$ are related by the Kramers-

Kronig ($\mathcal{KK}$) transformations, and so then $\delta(E)$ and $\beta(E)$,

$$\delta(E) = \mathcal{KK}[\beta(E)] = -\frac{2}{\pi}\int_0^\infty dE' \frac{E'}{E^2 - E'^2}\beta(E')\,, \tag{4.8a}$$

$$\beta(E) = \mathcal{KK}^{-1}[\delta(E)] = \frac{2E}{\pi}\int_0^\infty dE' \frac{1}{E^2 - E'^2}\delta(E')\,. \tag{4.8b}$$

Furthermore, $\beta(E)$ is directly related to the absorption coefficient $\mu(E)$ by the expression

$$\mu(E) = \frac{2E}{\hbar c}\beta(E)\,, \tag{4.9}$$

which will ultimately be the studied magnitude (as will be shown in Section 4.1.5).

4.1.2 X ray reflectivity

In classical optics, when a beam of light impinges on the surface between two different materials at an incidence angle θ_i (relative to the surface), the beam deviates to a refraction or transmission angle θ_t as it travels through the new material. The boundary conditions for the electromagnetic field at the interface require that the phase of the light is continuous as it travels between the materials. This leads to Snell's Law as [36]

$$\frac{\cos\theta_t}{\cos\theta_i} = \frac{n_i}{n_t}\,, \tag{4.10}$$

where n_i and n_t are the initial and the transmission materials' refractive indices respectively.

In the case of a stack of materials where the layers are labeled with the subscript j, being $j = 0$ the initial medium (normally air or vacuum) and $j{=}N+1$ the final one (normally the substrate), there are $N+2$ refractive indices (n_j) and $N+2$ angles θ_j.

The examination of Snell's Law shows that if the θ_{j-1} is small and $n_j < n_{j-1}$, then the solution for θ_j is complex. Physically, this yields the so-called total

reflection regime, with an attenuated transmission of a evanescent beam, that is a wave that travels through the transmission material with an exponential decay [36].

For most materials in the X ray region, $\delta(E)$ is positive and in the order of 10^{-5}, so the real part of n is slightly smaller than one. Therefore, X rays arriving from air or vacuum at sufficiently low incidence angle can be totally reflected. The critical angle θ_c is defined as the incidence angle at which the transmitted angle is 0. This is,

$$\cos(\theta_c) = n\cos(0) = 1 - \delta(E)\,, \tag{4.11}$$

where n is the relative refractive index between both materials. As $\delta(E)$ is small, the critical angle will also be small, so the cosine can be expanded around 0 and yield

$$\cos(\theta_c) \approx 1 - \frac{\theta_c^2}{2}\,, \tag{4.12}$$

Therefore,

$$\theta_c = [2\delta(E)]^{\frac{1}{2}}\ . \tag{4.13}$$

Any angle below θ_c will be in the total reflection regime. It has to be noted that this calculation is not accurate. The β term of the refractive index has been deliberately ignored to obtain a non complex critical angle. However, as $\beta(E) \ll \delta(E)$ for most materials at energies not too close to an absorption edge, this makes a good and simple approximate expression to identify the total reflection angular region.

The first attempt to show accurately the whole process of X ray reflectivity, including the multiple reflections in a layer of material was given by Parratt [37]. In the next section, it is shown how Parratt's approximation provides an expression for the Fresnel reflection coefficient for X rays at the interface between two media for small incidence angles.

4.1.2.1 Reflectivity from a single surface

The reflection, $r_{j-1,j}$, and transmission, $t_{j-1,j}$, coefficients at a surface between two arbitrary layers $j-1$ and j are defined as

$$r_{j-1,j} = \frac{E^r_{j-1}}{E^i_{j-1}}\,, \tag{4.14a}$$

$$t_{j-1,j} = \frac{E^t_j}{E^i_{j-1}}\,. \tag{4.14b}$$

In these equations, $r_{j-1,j}$ refers to the beam traveling downwards in the layer $j-1$ and being reflected by layer j, while $t_{j-1,j}$ refers to the beam traveling downwards in the layer $j-1$ and being transmitted through layer j. These are complex numbers in general, because the refractive index and thus the refraction angle are also complex. Then, the reflected, R, and transmitted, T, intensities from a surface are

$$R = \left|r_{j-1,j} r^*_{j-1,j}\right|\,, \tag{4.15a}$$

$$T = \left|t_{j-1,j} t^*_{j-1,j}\right|\,. \tag{4.15b}$$

The Fresnel equations [36] give the reflection and transmission coefficients in terms of the incidence and transmission angles and the refractive indices. These come from the satisfaction of the boundary condition that demands that the tangential components of the electric and magnetic vector should be continuous across the surface. For s-polarised radiation (i.e. with the electric vector perpendicular to the incidence plane, thus parallel to the *s*urface), these give

$$r_{j-1,j} = \frac{n_{j-1}\sin(\theta_{j-1}) - n_j \sin(\theta_j)}{n_{j-1}\sin(\theta_{j-1}) + n_j \sin(\theta_j)}\,, \tag{4.16a}$$

$$t_{j-1,j} = \frac{2n_{j-1}\sin(\theta_{j-1})}{n_{j-1}\sin(\theta_{j-1}) + n_j \sin(\theta_j)}\,. \tag{4.16b}$$

While for p-polarised radiation (with the electric vector parallel to the inci-

dence $p$lane), the expressions are slightly different,

$$r_{j-1,j} = \frac{n_{j-1}\sin(\theta_j) - n_j\sin(\theta_{j-1})}{n_{j-1}\sin(\theta_j) + n_j\sin(\theta_{j-1})}\,, \tag{4.17a}$$

$$t_{j-1,j} = \frac{2n_{j-1}\sin(\theta_{j-1})}{n_{j-1}\sin(\theta_j) + n_j\sin(\theta_{j-1})}\,. \tag{4.17b}$$

These equations are valid for all angles if both complex n_j and complex θ_j are used.

If the following conditions are satisfied

$$\theta_{j-1} \ll 1\,, \tag{4.18a}$$

$$\delta_j(E) \ll 1\,, \tag{4.18b}$$

$$\beta_j(E) \ll 1\,, \tag{4.18c}$$

i.e , within X ray region of the light spectrum (for most materials), and in grazing angle geometries, then it is possible to make a Taylor expansion for $\sin(\theta_{j-1})$ about $\theta = 0$, and substitute equation 4.6 to obtain [37]

$$r_{j-1,j} \simeq \frac{g_{j-1} - g_j}{g_{j-1} + g_j}\,, \tag{4.19}$$

where

$$g_j = \sqrt{\theta_{j-1}^2 - 2\delta_j - 2i\beta_j}\,, \tag{4.20a}$$

$$g_0 = \theta_0\,, \tag{4.20b}$$

where it has been assumed that the initial medium is air or vacuum, so $n_0 = 1$. At these limits, the Fresnel coefficients for both s- and p-polarisation directions are approximated to the same expression, so equation 4.19 is valid for either of them.

To obtain the reflected intensity $R_{j-1,j}$, then g_j can be split into its real and imaginary parts

$$g_j = A - iB\,, \tag{4.21}$$

where A and B are then obtained as

$$A = \frac{1}{\sqrt{2}}\left[\sqrt{\left(\theta_{j-1}^2 - 2\delta_j\right)^2 + 4\beta_j^2} + \left(\theta_{j-1}^2 - 2\delta_j\right)^2\right]^{\frac{1}{2}}, \tag{4.22a}$$

$$B = \frac{1}{\sqrt{2}}\left[\sqrt{\left(\theta_{j-1}^2 - 2\delta_j\right)^2 + 4\beta_j^2} - \left(\theta_{j-1}^2 - 2\delta_j\right)^2\right]^{\frac{1}{2}}. \tag{4.22b}$$

Usually, the definition of the critical angle helps to simplify this equation, but for this work the explicit δ terms will be kept. The reflectivity is the square modulus of the Fresnel coefficient (Equation 4.15) what, within this approximation, is given by [37]

$$R_{j-1,j} = \frac{h - \sqrt{\frac{\theta_{j-1}^2}{2\delta_j}2(h-1)}}{h + \sqrt{\frac{\theta_{j-1}^2}{2\delta_j}2(h-1)}}, \tag{4.23}$$

where

$$h = \frac{\theta_{j-1}^2}{2\delta_j} + \sqrt{\left(\frac{\theta_{j-1}^2}{2\delta_j} - 1\right)^2 + \left(\frac{\beta_j}{\delta_j}\right)^2}. \tag{4.24}$$

This exposes that the reflection intensity carries information about the absorption coefficient of the reflecting material, through the imaginary part of the refractive index, as shown in Equation 4.9.

4.1.2.2 Reflectivity on multilayers

The next question is how to expand the formalism above described to encompass the reflectivity process within a multilayered system. The objective is to calculate contribution to the top surface reflectivity from each layer in such a way as to include all the layer to layer reflections.

First consider Figure 4.1. The reflectivity from the incident beam on the surface layer is $r_{0,1}$, while the transmitted beam is $t_{0,1}$. From the figure, it can be seen that the total reflection coefficient caused by layer 1, $r'_{0,1}$, is the

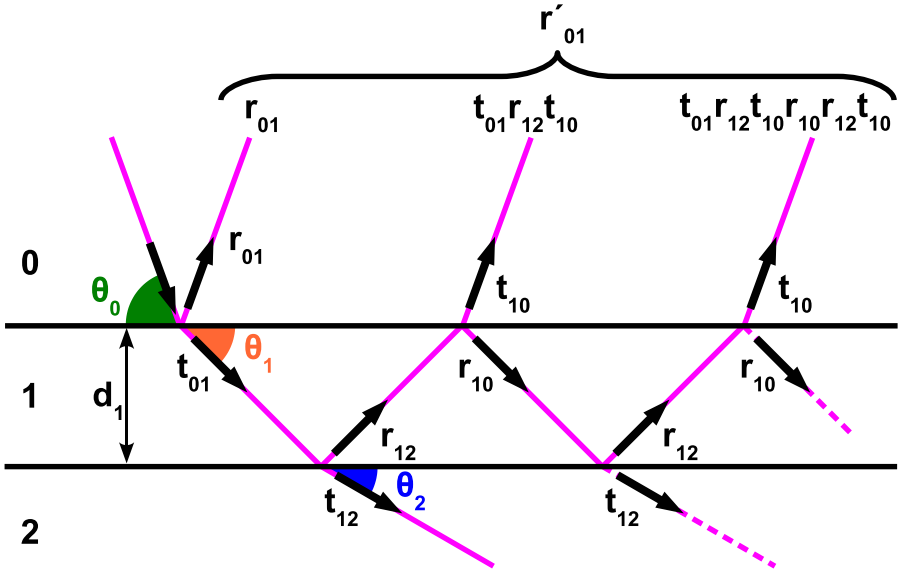

Figure 4.1: Reflectivity from the first layer

phase weighted sum of all the possible reflections in this layer. Thus [40],

$$\begin{aligned} r'_{0,1} &= r_{0,1} + t_{0,1}r_{1,2}t_{1,0}e^{-i\phi(E)}e^{-D\mu_1(E)} + \\ &\quad + t_{0,1}r_{1,2}r_{1,0}r_{1,2}t_{1,0}e^{-i2\phi(E)}e^{-2D\mu_1(E)} + \dots \\ &= r_{0,1} + \sum_{m=1}^{\infty} t_{0,1}t_{1,0}r_{1,0}^{m-1}r_{1,2}^{m}e^{-im\phi(E)}e^{-mD\mu_1(E)}\,, \end{aligned} \tag{4.25}$$

where $\phi(E)$ is the phase difference between the different reflections caused by the path length difference

$$\phi(E) = \frac{4\pi d_1 \sin(\theta_1)}{\lambda(E)} = \frac{2Ed_1 \sin(\theta_1)}{\hbar c}\,, \tag{4.26}$$

and $e^{-D\mu_1(E)}$ is the attenuation term of the wave traveling through the material whose absorption coefficient is $\mu_1(E)$. D is the total path travelled by the beam in the layer

$$D = \frac{2d_1}{\sin(\theta_1)}\,. \tag{4.27}$$

Equation 4.25 is an infinite geometric sum of ratio $r_{1,0}r_{1,2}e^{-i\phi(E)-D\mu_1(E)}$ that

fulfills the condition

$$\lim_{m\to\infty}\left[r_{1,0}r_{1,2}e^{-i\phi(E)-D\mu_1(E)}\right]^m = 0\,. \tag{4.28}$$

Thus, the sum can be calculated and gives

$$r'_{0,1} = r_{0,1} + \frac{t_{0,1}t_{1,0}r_{1,2}e^{-i\phi(E)-D\mu_1(E)}}{1 + r_{0,1}r_{1,2}e^{-i\phi(E)-D\mu_1(E)}}\,, \tag{4.29}$$

This expression is not the usual Parratt recursion formula. The difference lies in the fact that in Parratt's equation, the Stokes relationship [36], $t_{0,1}t_{1,0} = 1 - r_{0,1}^2$, is used. Unfortunately, this relationship is only valid if there is no absorption in the material, which is not the case for an X ray absorption measurement, so it could not be applied and a more general equation had to be used.

This equation can be generalized for an arbitrary layer of the stack

$$r'_{j-1,j} = r_{j-1,j} + \frac{t_{j-1,j}t_{j,j-1}r'_{j,j+1}e^{-i\phi_j(E)-D_j\mu_j(E)}}{1 + r_{j-1,j}r'_{j,j+1}e^{-i\phi_j(E)-D_j\mu_j(E)}}\,. \tag{4.30}$$

Layer $N+1$ would be the substrate or some other infinite depth material, from which no reflection would come upwards,

$$r'_{N+1,N+2} = 0 \implies r'_{N,N+1} = r_{N,N+1}\,. \tag{4.31}$$

The reflectivity coefficient of the first surface, $r'_{0,1}$, can then be calculated by iterating from the substrate upwards, replacing the $r'_{j,j+1}$ by the reflectivity calculated for the layer below. Finally, the desired reflected intensity from the top surface is given by

$$R_{0,1} = \left|r'_{0,1}r'^{*}_{0,1}\right|\,. \tag{4.32}$$

4.1.3 Roughness

The above formalism assumes a perfectly flat interface between the different layers. In real samples, there might be some intermixing of the components

of the different layers, which can be envisaged as a variable height z as a function of x and y across the surface, commonly known as surface or interface roughness. This gives rise to non-specular scattering.

If the intermixing or height variance is small relative to the beam footprint, it may be modeled statistically as a variable refractive index in the regions close to the interface, as can be seen in Figure 4.2. In this approximation, the expected specular loss can be calculated. The different statistical descriptions for the roughness has lead to a number of different models. Among them, the most used it the Nevot-Croce [41] model, which is described below.

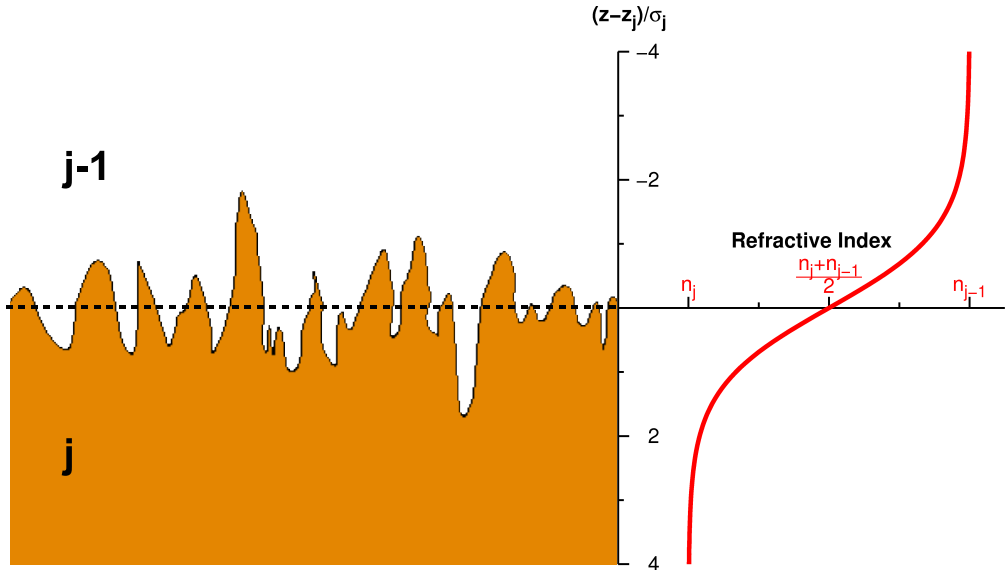

Figure 4.2: Roughness of a surface modeled statistically by a *tanh* function

The calculation of the roughness effect starts with the premise that the correlations are not in the XY plane, so the refractive index only depends on the vertical direction z, which is perpendicular to the surface.

The refractive index intermixing can be modeled by the Error function as

$$n(z) = \frac{n_{j-1} + n_j}{2} + \frac{n_{j-1} - n_j}{2} \operatorname{erf}\left(\frac{z}{\sqrt{2}\sigma_j}\right), \tag{4.33}$$

where at $z = 0$ the refractive index is the mean value of both refractive indices of both layers, i.e.

$$n(0) = \frac{n_{j-1} + n_j}{2}\,, \tag{4.34}$$

and σ_j is the roughness coefficient of the $(j-1)/j$ interface, but will be assigned to layer j. The Error function can be defined as

$$\mathrm{erf}(z) = \sqrt{\frac{2}{\pi}} \int_0^z e^{-t} dt\,. \tag{4.35}$$

This model leads to a Gaussian probability distribution of the heights of the layer surface points, which is the usual way to describe the surface roughness

$$P_j^{\mathrm{erf}}(z) = \frac{1}{\sqrt{2\pi}\sigma_j} e^{\frac{-z^2}{2\sigma_j^2}}\,. \tag{4.36}$$

This intermixed refractive index can be introduced in the Fresnel coefficient expressions given by Parratt (Equation 4.19), and in the limit where $k_j\sigma_j < 1$, the expression can be approximated to yield

$$r_{j-1,j}^{\sigma_j,\mathrm{erf}} = r_{j-1,j}\, e^{-2\sigma_j^2 k_{j-1}^2 g_{j-1} g_j}\,, \tag{4.37}$$

where k_{j-1} is the radiation wave vector at layer $j-1$.

Although this seems to be the best description of the roughness, other intermixing models can be used. For instance, a model in terms of a *tanh* function can be proposed [42, 43] as

$$n(z) = \frac{n_{j-1} + n_j}{2} + \frac{n_{j-1} - n_j}{2} \tanh\left(\sqrt{\frac{2}{\pi}}\frac{z}{\sigma_j}\right)\,, \tag{4.38}$$

This intermixing model would lead to a probability distribution of heights of the points at the surface of the form

$$P_j^{\tanh}(z) = \frac{1}{\sqrt{2\pi}\sigma_j \cosh^2\left(\sqrt{\frac{2}{\pi}}\frac{z}{\sigma_j}\right)}\,, \tag{4.39}$$

This distribution is quite similar to the one that includes the Error function, so it describes the surface roughness satisfactorily. The advantage of this model lies in the fact that the *tanh* function is integrable. For this reason, it is possible to analytically calculate the new Parratt reflection coefficient, as shown by Bahr [42], to get

$$r_{j-1,j}^{\sigma_j,\tanh} = G_{j-1,j}\frac{\sinh\left[(\pi/2)^{\frac{3}{2}}\,\sigma_j k_{j-1}\,(g_{j-1}-g_j)\right]}{\sinh\left[(\pi/2)^{\frac{3}{2}}\,\sigma_j k_{j-1}\,(g_{j-1}+g_j)\right]}\,, \tag{4.40}$$

where the parameter $G_{j-1,j}$ has the form

$$G_{j-1,j} = -\frac{\Gamma\left[2i\sqrt{\pi/2}\,\sigma_j k_{j-1} g_{j-1}\right]}{\Gamma\left[-2i\sqrt{\pi/2}\,\sigma_j k_{j-1} g_{j-1}\right]} \times \frac{\Gamma\left[-i\sqrt{\pi/2}\,\sigma_j k_{j-1}\,(g_{j-1}+g_j)\right]}{\Gamma\left[i\sqrt{\pi/2}\,\sigma_j k_{j-1}\,(g_{j-1}+g_j)\right]} \times \frac{\Gamma\left[-i\sqrt{\pi/2}\,\sigma_j k_{j-1}\,(g_{j-1}-g_j)\right]}{\Gamma\left[i\sqrt{\pi/2}\,\sigma_j k_{j-1}\,(g_{j-1}-g_j)\right]}\,, \tag{4.41}$$

where Γ is the Gamma function, defined as

$$\Gamma(x) = \int_0^\infty t^{x-1}e^{-t}dt\,, \tag{4.42}$$

For X ray energies, and roughnesses $\sigma_j < 100$ Å, the $G_{j-1,j}$ factor is approximately 1, so the calculation of this coefficient is easier. This *tanh* model has the advantage of being valid even for high roughnesses, overcoming the limit of the Error function model, $k_j\sigma_j < 1$.

4.1.4 Depth sensitivity

The information carried by the reflected radiation is weighted by the intensity of the transmitted wave at each depth in the sample.

A good approximation on the depth probed by the X rays can be the penetration depth of them. This can be defined as the depth at which the intensity of the radiation has decayed to a fraction $\frac{1}{e}$.

As an example, Figure 4.3 shows the penetration depth in a smooth and thick Cu mirror of an X ray at 9.2 keV (about 200 eV over the Cu-K absorption edge), for increasing incidence angles. It has been also plotted in the figure the reflectivity of the X ray as described by Parratt's equations.

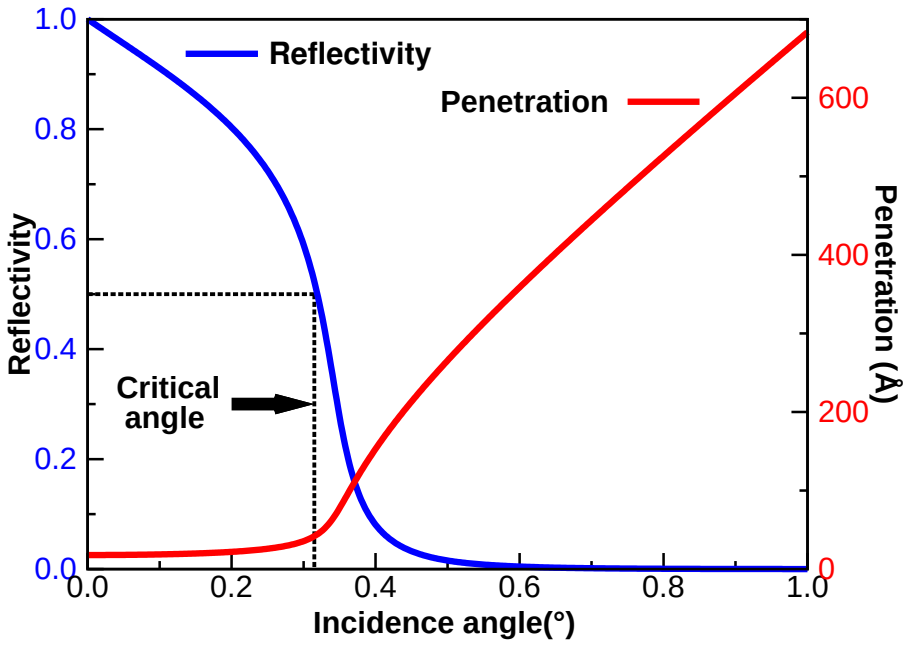

Figure 4.3: Reflectivity and penetration depth of a Cu mirror at 9.2 keV

In the total reflection regime, $\theta_i < \theta_c$, the information contained in the spectrum comes from the evanescent transmitted wave that propagates parallel to the surface and decays exponentially in the direction perpendicular to the surface. In this range of angles, this penetration depth is constant and may be then written as

$$z_{\frac{1}{e}} = \frac{\hbar c}{2E\sqrt{2\delta(E)}} = \frac{\hbar c}{2E\theta_c(E)}\,, \tag{4.43}$$

which is on the order of tens of Ångströms. As the penetration depth increases above the critical angle, in the limit $\theta_i \gg \theta_c$, it approaches to the

expression for X ray transmission,

$$I_t = I_0 e^{-\mu(E)x} = I_0 e^{-\mu(E)\frac{z}{\theta_i}} \quad \Longrightarrow \quad z_{\frac{1}{e}} = \frac{\theta_i}{\mu(E)}\,, \tag{4.44}$$

which has a linear increasing dependence with the incidence angle. Both effects can be seen in Figure 4.3

4.1.5 EXAFS

In order to understand how structural information is obtained from an X-ray absorption (XAS) spectrum, the basic process of the interaction of radiation with matter has to be considered. When an atom is irradiated with X ray photons of high enough energy to promote an internal electron to the vacuum level, these photons are absorbed and a photoelectron is ejected. The intensity of the transmitted beam, I_t, is related with the absorption coefficient μ, according to the Lambert relation [44]

$$I_t = I_0 e^{-\mu(E)z} \quad \Longrightarrow \quad \mu(E)z = \ln\left(\frac{I_0}{I_t}\right)\,. \tag{4.45}$$

Scanning energy against the absorption coefficient yields the XAS spectrum. When the energy of the incoming beam is equal to or higher than that of an inner level of the absorbing atoms, a sharp increase in the absorption coefficient takes place, and an absorption edge appears in the spectrum. If the absorbing atoms are not isolated, the X ray absorption coefficient includes an oscillatory fine structure just after the absorption edge, as can be seen in Figure 4.4. This fine structure can be described as a modification, $\chi(E)$, of the absorption coefficient as

$$\mu(E) = \mu_0(E)\left[1 + \chi(E)\right]\,, \tag{4.46}$$

where $\mu_0(E)$ is the absorption coefficient of the isolated atom. This oscillatory part of the absorption coefficient is a consequence of a variation in the atomic electron density, which is due to the interference of the wave function

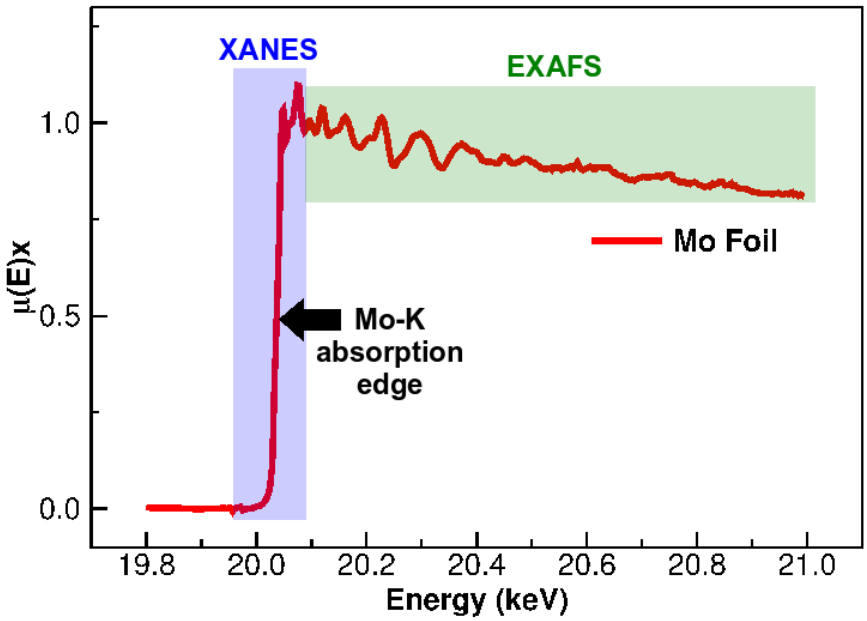

Figure 4.4: XAS spectrum for a Mo foil sample, near the Mo-K absorption edge

of the ejected photoelectron and the backscattered one from the neighbouring atoms. For this reason, function $\chi(E)$ contains local structural information and can be described as the sum extended over i neighbouring coordination shells of atoms around the absorbing atom. This fine structure is usually written as a function of the photoelectron wave vector, k,

$$k(E) = \sqrt{\frac{2m_e(E - E_0)}{\hbar^2}}, \tag{4.47}$$

where m_e is the electron mass and E_0 is the absorption edge energy. The Extended X ray Absorption Fine structure Spectroscopy (EXAFS) part of the XAS fine structure is the one that is located from 50 eV after the absorption edge to the end of the spectrum. This part can be modeled by a semi-heuristic equation that is a function of the structural parameters of the absorbing atom neighbour shells [31]

$$\chi(k) = S_0^2 \sum_i \frac{N_i}{kR_1^2} F_i(k) e^{\frac{-2R_i}{\lambda(k)}} e^{-2k^2\sigma_i^2} \sin\left[2kR_i + \phi_i(k)\right], \tag{4.48}$$

where N_i is the coordination number of the atoms in shell i at a distance R_i. S_0^2 is the amplitude reduction factor due to many body effects. F_i is the backscattering amplitude function of each kind of neighbouring atom, and the $\phi_i(k)$ the total phase shift of the photoelectron, $\lambda(k)$ is the photoelectron mean free path and σ_i^2 is the Debye-Waller factor, accounting for static and dynamic disorder. Since $F_i(k)$ and $\phi_i(k)$ are functions characteristic of each pair of absorbing and backscattering elements, the technique is element sensitive. Those functions can be calculated from *ab-initio* calculations [45], so the fit of the experimental signal with this expression yields the structural parameters R_i, N_i and σ_i^2 [46].

There is no need for long range order in the structure of the sample to be analysed. For this reason the application of EXAFS spectroscopy is widespread in the study of all kinds of systems, both liquid and solid.

Changing the standard detection system of the transmitted beam to the alternative of recording the reflected signal, the function that can be analysed is the imaginary part of the refractive index, β. This function is related to the absorption coefficient by Equation 4.9 so, if β can be calculated, the EXAFS signal can be extracted directly

$$\chi(E) = \frac{\mu(E) - \mu_0(E)}{\mu_0(E)} = \frac{\beta(E) - \beta_0(E)}{\beta_0(E)} \,. \tag{4.49}$$

4.2 ReflEXAFS partial analyses

Section 4.1 showed how to calculate the reflectivity of a sample if the complete absorption term, including the fine structure component, is known. The coupling of $\delta(E)$ and $\beta(E)$ make it difficult to deconvolve the equations in order to determine $\beta(E)$, and thus the $\chi(E)$ EXAFS signal from the fine structure of the reflectivity. Several approaches have been tried with limited success, each becoming more sophisticated with both progress in computational resources and improvements to theoretical understanding.

4.2.1 Total reflection approximation

Martens and Rabe [7, 17, 18, 47] showed that a very simple approach can be made to analyse the ReflEXAFS data in the total reflection regime.

Equation 4.23 is the reflectivity from a single surface in the low angle limit. This limit can be pushed further and study the total reflection regime, i.e. when

$$\frac{\theta}{\sqrt{2\delta}} = \frac{\theta}{\theta_c} < 1\,. \tag{4.50}$$

In this limit, R can be expanded as a Taylor series about $\frac{\theta}{\sqrt{2\delta}} = 0$,

$$R = 1 - \frac{2^{\frac{3}{2}}\sqrt{\left(1+\frac{\beta^2}{\delta^2}\right)^{\frac{1}{2}} - 1}}{\sqrt{\left(1+\frac{\beta^2}{\delta^2}\right)}}\frac{\theta}{\sqrt{2\delta}} + O\left(\frac{\theta^2}{2\delta}\right)\,. \tag{4.51}$$

The limiting value for this expansion is when $\frac{\theta}{\sqrt{2\delta}}$ (or $\frac{\theta}{\theta_c}$) approaches 1.

As the EXAFS fine structure is present in $\beta(E)$ due to Equation 4.49, and subsequently in $\delta(E)$ due to their relationship shown in Equations 4.8, both functions can be split in their isolated atom and fine structure components as

$$\delta(E) = \delta_0(E) + \Delta\delta(E) \tag{4.52a}$$

$$\beta(E) = \beta_0(E) + \Delta\beta(E) \tag{4.52b}$$

Furthermore, as the fine structure of the reflectivity is small compared to the reflectivity itself, the former can be expanded in terms of its components δ and β,

$$R(\delta,\beta) - R_0(\delta_0,\beta_0) = \Delta R \approx \left.\frac{\partial R}{\partial \delta}\right|_{\delta_0}\Delta\delta + \left.\frac{\partial R}{\partial \beta}\right|_{\beta_0}\Delta\beta\,, \tag{4.53}$$

where R_0 stands for the reflectivity without the fine structure, i.e. when $(\delta,\beta) = (\delta_0,\beta_0)$, those of the isolated atoms.

At this limits, the partial derivatives of R with respect to δ and β can be calculated and yield

$$\frac{\partial R}{\partial \delta} = \left\{ \frac{\beta^2\sqrt{2}\left[2-\left(1+\frac{\beta^2}{\delta^2}\right)^{\frac{1}{2}}\right]}{\delta^3\left(1+\frac{\beta^2}{\delta^2}\right)^{\frac{3}{2}}\sqrt{\left(1+\frac{\beta^2}{\delta^2}\right)^{\frac{1}{2}}-1}} - \right.$$
$$\left. - \frac{\sqrt{\left(1+\frac{\beta^2}{\delta^2}\right)^{\frac{1}{2}}-1}}{\delta\left(1+\frac{\beta^2}{\delta^2}\right)^{\frac{1}{2}}} \right\} \frac{\theta}{\sqrt{2\delta}} + O\left(\frac{\theta^2}{2\delta}\right), \tag{4.54a}$$

$$\frac{\partial R}{\partial \beta} = \left\{ \frac{\beta\sqrt{2}\left[\left(1+\frac{\beta^2}{\delta^2}\right)^{\frac{1}{2}}-2\right]}{\delta^2\left(1+\frac{\beta^2}{\delta^2}\right)^{\frac{3}{2}}\sqrt{\left(1+\frac{\beta^2}{\delta^2}\right)^{\frac{1}{2}}-1}} \right\} \frac{\theta}{\sqrt{2\delta}} + O\left(\frac{\theta^2}{2\delta}\right). \tag{4.54b}$$

Substituting typical values for δ and β at the X ray energies, (for instance $\delta = 10^{-5}, \beta = 10^{-6}$) show that $\frac{\partial R}{\partial \beta}$ dominates by one to two orders of magnitude. Therefore, the $\Delta\delta(E)$ component of the ReflEXAFS signal, ΔR, can be neglected, so it is almost purely proportional to $\Delta\beta(E)$, and hence proportional to the fine structure of the absorption coefficient $\Delta\mu(E)$ by Equation 4.9. Then, the EXAFS $\chi(E)$ can be determined directly as

$$\chi(E) = \frac{\mu(E)-\mu_0(E)}{\mu_0(E)} = \frac{\beta(E)-\beta_0(E)}{\beta_0(E)} = \frac{\Delta\beta(E)}{\beta_0(E)} \approx \frac{\Delta R(E)}{R_0(E)}, \tag{4.55}$$

where $R_0(E)$ can be a suitably smooth function that fits the reflectivity without the fine structure, in the same fashion as it is done for the standard EXAFS measurements.

This method is extremely easy to use, as the standard EXAFS programs can be used just after applying Equation 4.55 . However, angles higher than the critical angle, the approximation at Equation 4.51 does not hold, because the terms in $\frac{\theta^2}{2\delta}$ and higher order become important. Consequently, $\frac{\partial R}{\partial \delta}$ becomes comparable to $\frac{\partial R}{\partial \beta}$, so the $\Delta\delta$ component of the reflectivity fine structure cannot be neglected.

Furthermore, when the energy is just after and close to the absorption edge, the magnitude of β becomes significantly bigger, and close to the values of δ. This also makes the partial derivatives comparable and again the $\Delta\delta$ component of the reflectivity fine structure cannot be neglected. However, the EXAFS region of the fine structure begins far enough from the absorption edge, so it is not affected by this fact.

This approximation is then limited to the total reflection regime and hence the penetration depth is small and constant. This causes that only the top layer of the sample, within the first tens of Ångströms, can be investigated.

4.2.2 Borthen's approximation

Borthen and Strehblow [19, 20] extended the low angle limit by first calculating a linear approximation of $\Delta R(E)$,

$$R(\delta,\beta) - R_0(\delta_0,\beta_0) = \Delta R \approx \left.\frac{\partial R}{\partial \delta}\right|_{\delta_0} \Delta\delta + \left.\frac{\partial R}{\partial \beta}\right|_{\beta_0} \Delta\beta\,, \qquad [4.53]$$

The partial derivatives in this equation are functions of energy in general. However, they are slowly varying functions with energy and may be approximated by functions only dependent of the incidence angle,

$$\left.\frac{\partial R}{\partial \delta}\right|_{\delta_0} = \left.\frac{\partial R}{\partial \delta}\right|_{\delta_0}(E,\theta) \approx a(\theta)\,, \qquad (4.56a)$$

$$\left.\frac{\partial R}{\partial \beta}\right|_{\beta_0} = \left.\frac{\partial R}{\partial \beta}\right|_{\beta_0}(E,\theta) \approx b(\theta)\,, \qquad (4.56b)$$

Thus, for each incidence angle θ, the fine structure of the reflectivity is a linear combination of the fine structures of the real and imaginary parts of the refractive index as

$$\Delta R \approx a\Delta\delta + b\Delta\beta \qquad (4.57)$$

This is a reasonable approximation for a single chemical environment, when the energy range of the measurement is short, and far from the critical angle, either higher or lower angle.

A relationship between the fine structures of $\delta(E)$ and $\beta(E)$ can be established due to the linearity of the Kramers-Kronig transformations, and taking into account Equation 4.8,

$$\begin{aligned} \delta(E) &= \mathcal{KK}\left[\beta(E)\right] \\ \delta_0(E) + \Delta\delta(E) &= \mathcal{KK}\left[\beta_0(E) + \Delta\beta(E)\right] = \\ &= \mathcal{KK}\left[\beta_0(E)\right] + \mathcal{KK}\left[\Delta\beta(E)\right] = \\ &= \delta_0(E) + \mathcal{KK}\left[\Delta\beta(E)\right] \\ \Longrightarrow\ \Delta\delta(E) &= \mathcal{KK}\left[\Delta\beta(E)\right] \end{aligned} \tag{4.58}$$

This allows to take the Kramers-Kronig transformation of Equation 4.57 and use again the linearity of these transformations to get

$$\mathcal{KK}(\Delta R) \approx -a\Delta\beta + b\Delta\delta\,, \tag{4.59}$$

where a the property of the Kramers-Kronig transformations as a special case of the Hilbert transformations,

$$\mathcal{KK}\left[\Delta\delta(E)\right] = \mathcal{KK}\big\{\mathcal{KK}\left[\Delta\beta(E)\right]\big\} = -\Delta\beta(E)\,, \tag{4.60}$$

has been used. Then $\Delta\delta$ and $\Delta\beta$ can be calculated by solving these two simple simultaneous equations to yield

$$\Delta\beta(E) \approx \frac{1}{a^2+b^2}\big\{b\,\Delta R(E) - a\,\mathcal{KK}\left[\Delta R(E)\right]\big\}\,. \tag{4.61}$$

The constants a and b are generally unknown, so they have to be calculated from either a numerical simulation or from a model compound experimental data [19] in order to normalise the $\Delta\beta(E)$ function.

The problems of this method arises from the fact that $\frac{\partial R}{\partial \delta}$ and $\frac{\partial R}{\partial \beta}$ are not constant in energy. This effect is bigger when the energy is just after the absorption edge, where the variation of these functions with energy is faster. Also, the wider the energy range of the scan, the less accurate the method is,

as those functions deviate further from the constant behaviour. Moreover, if there is more than one chemical environment of the studied element at different depths in the sample, the EXAFS spectrum will have a proportion of each environment that is variable with energy. This is caused by the variation of penetration depth of the radiation with energy at incidence angles above the critical angle, and would make the spectrum extremely difficult to analyse.

4.3 ReflEXAFS global analysis

Both of the preceding methods obtain the EXAFS signal by means of an approximation of the linear expansion of the ReflEXAFS fine structure (Equation 4.53) for an individual angle. The first restricts the probe depth to the penetration of the evanescent wave in the total reflection condition, which is around tens of Ångsröms. The second, while having the ability to probe deeper depths, can be inaccurate for strongly varying $\delta(E)$ and $\beta(E)$ functions, and does not work for samples with more than a single chemical environment at different depths.

To overcome these limitations, a more general procedure was developed in this work.

The principles of the method are: (1) to work over a complete set of measurements of the same sample in the same energy range, but at different incidence angles, which will eventually reduce the number of possible solutions giving more restrictions; and (2), not to try to extract the EXAFS signal directly from the experimental ReflEXAFS, but instead, do it in a reverse way: suppose an EXAFS signal as a solution to the problem, and then try to calculate the whole experimental ReflEXAFS.

This global procedure is carried out in two stages. First, the reflectivity background (i.e. without the fine structure) is fitted for all the spectra at different angles using the reflectivity equations described in Section 4.1 for

a model of the sample. This way, the ReflEXAFS fine structure ($\Delta R(E)$) for the different spectra can be extracted. Furthermore, parameters like the real ($\delta(E)$) and imaginary ($\beta(E)$) parts of the refractive indices can be calculated, which will be necessary for the next step. Second, the ReflEXAFS fine structure set is fitted against a model function representing the EXAFS signal of the sample within the restrictions imposed.

4.3.1 Free atom reflectivity simulation and fit

The free atom reflectivity is defined as the reflectivity without the fine structure

$$R_0(E) = R_0\left[\delta_0(E), \beta_0(E)\right] , \tag{4.62}$$

where $\delta_0(E)$ and $\beta_0(E)$ are real and imaginary parts of the refractive index without the fine structure, as defined in Equations 4.52.

The objective is to calculate this free atom reflectivity. To do this, a model of the sample is built in terms of parameters that simulate the sample characteristics. As an example, consider a sample made of homogeneous layers of different materials deposited over a certain substrate (Figure 4.5. For this type of sample, Equation 4.62 can be rewritten as

$$R_{0m}(E) = R_{0m}\left[\delta_{0j}(E), \beta_{0j}(E)\right] , \tag{4.63}$$

where subindex $m \in \{1, \ldots, M\}$ will denote the spectrum of the same sample at each different incidence angle. These reflectivity spectra are functions of all the refractive indices components for the free atom, $\delta_{0j}(E)$ and $\beta_{0j}(E)$, of each j-th layer.

This sample can be determined by specifying the layers and substrate composition, density, thickness, and the interfacial roughness.

With the composition and atomic density, the refractive indices of the layers, n_{0j}, can be calculated using Equations 4.6 and 4.7, by taking the values

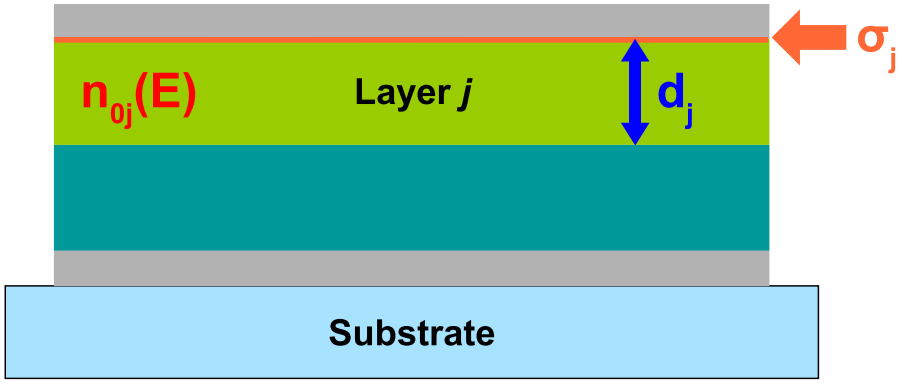

Figure 4.5: Model sample made of homogeneous layers

of $f'(E)$ and $f''(E)$ from the Cromer-Liberman [35] or Henke [38] tables of the anomalous scattering factors. In the case of a compound, its scattering factors can be calculated from those of the elements by using Equation 4.3.

The reflectivity spectrum at different energies for each incidence angle can then be calculated from Parratt's [37] recursive expression (Equation 4.30), that depends on the layers thicknesses, d_j, and the refractive indices, n_{0j}, previously obtained. These are combined with the roughness correction of the Nevot-Croce model [41] for a *tanh* type of intermixing [42] (Equation 4.40) that depends on the roughness parameters, σ_j, of the interfaces.

However, the sample characteristics and even the incidence angle are not known with enough precision to simulate accurately the reflectivity spectra. Thus, the sample parameters are set as variables in a computer program that tries to fit the calculated reflectivity against the experimental reflectivity spectra, in a similar way as the simulation and fit of X ray reflectometry measurements [26]. The fitting procedure and strategies are detailed in Section 4.3.1.1

The output of the program provides a way to extract the ReflEXAFS fine structure of each spectrum, $\Delta R_m(E)$, from the reflectivity background by

simply subtracting the simulated reflectivity from the experimental one,

$$\Delta R_m(E) = R_m^{exp}(E) - R_{0m}^{fit}(E)\,, \tag{4.64}$$

where $R_m^{exp}(E)$ is the experimental reflectivity of spectrum m, and $R_{0m}^{fit}(E)$ its corresponding best fit simulated spectrum without the fine structure.

The best fit parameters from the program output give quantitative values of the characteristics of the sample such as thickness, density and roughness of the layers. Furthermore, it gives the precise values of the refractive indices components of the layers without the fine structure, $\delta_{0j}(E)$ and $\beta_{0j}(E)$. These values will be of paramount importance for the subsequent simulation of the ReflEXAFS fine structure, as described below in Section 4.3.2.

4.3.1.1 Fitting description and strategies

The reflectivity simulation and fit tries to obtain the precise values of the variables that the reflectivity depends on, by looking for the ones that makes the simulated reflectivity closest to the experimental one. This is the solution of the fitting problem.

The fitting variables can be divided in two types: those that determine the sample to study, and those that determine each spectrum at the different incidence angles for the same sample.

For a sample made of homogeneous layers deposited over a substrate, the sample variables become the layers and substrate composition, density (to calculate the refractive indices) and roughnesses, and the layers thicknesses.

Each spectrum depends on its incidence angle, that have to be considered in the simulation in order to accurately determine its value. Besides, two more variables have to be introduced for each spectrum: (1) a linear scale factor that takes into account the possible part of the beam not impinging on the sample as well as the beam loss due to possible lack of flatness of it; and (2), an energy shift correction, that takes into account the possible miscalibration

of the monochromator.

This is an enormous amount of variables to be calculated from a small amount of experimental spectra, and besides, some of them are highly correlated. This leads to the possibility of having multiple solutions to the same fitting problem, of which there is only a real one. Thus, an effort to reduce this possibility has to be done, in terms of strategies that helps the fitting procedure. Some of the general strategies used for this work are described below.

- The spectra for the different incidence angles refer to the same sample. Hence, the simulation has to be done for all the spectra at the same time, sharing the sample variables. This give a strong restriction to the possible values of the variables, which is stronger when more spectra are measured at different incidence angles.

- The reflectivity at energies close to the absorption edge is not well simulated by the equations described in Section 4.1, because most of the approximations described are only valid when $\beta(E) \ll \delta(E)$, condition that is not fulfilled at those energies for most materials [38]. Thus, although the reflectivity is indeed calculated at that region, the fitting procedure does not consider the points within around 10 eV from the absorption edge for the calculation of the difference between experimental and simulated spectra. This removes false restrictions to the variables.

- These variables are not completely unknown. On one hand, the sample variables can be roughly inferred from the sample making, or can be estimated from previous characterization. On the other hand, the spectrum variables are approximately set at the reflectivity measurements. This allows to set some limits to the possible values of the variables, which reduces drastically the variable field to look for the best fit values.

- These variables are not always independent of each other, so they can

be coupled. For instance, a sample made of a multilayer probably have a period of layers that share their roughness and refractive indices. This reduces the number of variables to be calculated.

These strategies reduce the possibility of finding wrong solutions, but are not enough to completely ensure the finding of the true solution.

There are two additional problems that makes difficult to find the true solution. The first is that the experimental spectra are quite noisy, and can even have some singularity points due to the typical glitches that an X ray absorption measurement has. The second is that the partial reflectivities of some of the layers may be quite small for different reasons, like a high roughness or a low intensity of the beam at that depth. This can induce errors in the calculation caused by the rounding of the small quantities in the computer. In other words, the simulation is quite ill-conditioned.

For these reasons an more sophisticated algorithm that can cope with these problems was used instead of a standard Monte-Carlo fitting procedure.

The algorithm used for this fitting is called *Covariance Matrix Adaptation Evolution Strategy* or CMA-ES algorithm [48]. This is an type of evolutionary algorithm, that is specifically designed for simulations that have the following problems:

- A high dimensionality. This is, a high number of independent variables.
- Ruggedness. This is, a high amount of local possible solutions that are not the best one.
- High noise and discontinuities.
- Ill-conditioning problems.

The use of this algorithm together with the strategies above described, made the discrimination of the true solution among the local solutions possible for the samples studied in this work.

Once the simulation and fitting is done successfully, it has to be taken into account that the free atom reflectivity fit cannot be accomplished perfectly to the point that the difference between the experimental and simulated reflectivity is 0.

The origin of this experimental-simulated reflectivity mismatch lies in the effects that have not been considered in the simulation. These can be classified in two groups:

- Experimental issues like, for instance, the non linearity of the detectors signal at different detected intensities, or the possible non planarity of the sample, that causes dispersion of the reflected beam.
- Simulation model deviations from the real behaviour of the reflectivity, like the ones from the approximations in the reflectivity equations, or the roughness model used in the roughness effect calculation.

Although these differences are normally very small, they can introduce low frequency oscillations in the ReflEXAFS fine structure, which may cause errors in the subsequent EXAFS analysis. Therefore, they have to be corrected. This is done by the introduction of an additional polynomial in the simulated reflectivity, that is also fitted to get a perfect match of the experimental spectrum.

This is justified only if the polynomial correction is negligible compared to the initial fit. In other words, the difference of the fitting parameters in case a perfect fit could be achieved would be some orders of magnitude smaller than their value.

4.3.2 ReflEXAFS simulation and fit

After obtaining the free atom reflectivity fits, the fine structures of each reflectivity spectra at the different incidence angles are calculated by a simple subtraction of the best fit simulation reflectivity from the experimental

spectrum,

$$\Delta R_m(E) = R_m^{exp}(E) - R_{0m}^{fit}(E)\,. \qquad [4.64]$$

Continuing with the layered sample case, there is a total of $N+1$ layers, including the substrate. However, the number of layers that contain the absorbing element whose absorption edge is being studied, that will be denoted H, could be less than the total number of layers, i.e.

$$1 \leq H \leq N+1\,, \qquad (4.65)$$

in general. Thus, the contribution to the fine structure of the reflectivity can only come from the fine structures of those layers

$$\Delta R_m(E) = \Delta R_m\left[\Delta\delta_h(E), \Delta\beta_h(E)\right]\,. \qquad (4.66)$$

where the subindex $h \in \{1, \ldots, H\}$ denotes the layers that contain the absorbing element. Obviously by definition,

$$\Delta\delta_h(E) = \delta_h(E) - \delta_{0h}(E)\,, \qquad (4.67a)$$

$$\Delta\beta_h(E) = \beta_h(E) - \beta_{0h}(E)\,, \qquad (4.67b)$$

and each absorbing layer h may have a different fine structure spectrum.

The approximation that is used in this work has the same base as the previous works. As the reflectivity fine structure, $\Delta R(E)$ is small compared to the reflectivity itself $R(E)$, it is possible to approximate it by a linear Taylor expansion in terms of $\Delta\delta$ and $\Delta\beta$. As the reflectivity fine structure depends on all the absorbing layers, this expansion has to be made for all the possible contributions from each layer h, so

$$\Delta R_m(E) \approx \sum_{h=1}^{H}\left[\left.\frac{\partial R_m}{\partial\delta_h}\right|_{\delta_{0h}}\Delta\delta_h(E) + \left.\frac{\partial R_m}{\partial\beta_h}\right|_{\beta_{0h}}\Delta\beta_h(E)\right]\,, \qquad (4.68)$$

where each of the partial derivatives are explicit functions of E. Said in words, this means that the reflectivity fine structure at each individual energy point

can be approximated by a linear combination of the fine structures of the real and imaginary components of the refractive indices of all the absorbing layers. This equation is valid for each m spectrum, with its own partial derivative coefficients, but sharing the same $\Delta\delta_h(E)$ and $\Delta\beta_h(E)$, which are characteristic of the layers, but not the spectrum. Thus, this form a linear set of equations that can be written in a matrix form as

$$\begin{pmatrix} \Delta R_1(E) \\ \vdots \\ \Delta R_M(E) \end{pmatrix} = A(E) \begin{pmatrix} \Delta\delta_1(E) \\ \Delta\beta_1(E) \\ \vdots \\ \Delta\delta_H(E) \\ \Delta\beta_H(E) \end{pmatrix}, \tag{4.69}$$

where the coefficient matrix, A, is

$$A(E) = \begin{pmatrix} \left.\frac{\partial R_1}{\partial \delta_1}\right|_{\delta_{01}} & \left.\frac{\partial R_1}{\partial \beta_1}\right|_{\beta_{01}} & \cdots & \left.\frac{\partial R_1}{\partial \delta_H}\right|_{\delta_{0H}} & \left.\frac{\partial R_1}{\partial \beta_H}\right|_{\beta_{0H}} \\ \vdots & \vdots & \ddots & \vdots & \vdots \\ \left.\frac{\partial R_M}{\partial \delta_1}\right|_{\delta_{01}} & \left.\frac{\partial R_M}{\partial \beta_1}\right|_{\beta_{01}} & \cdots & \left.\frac{\partial R_M}{\partial \delta_H}\right|_{\delta_{0H}} & \left.\frac{\partial R_M}{\partial \beta_H}\right|_{\beta_{0H}} \end{pmatrix}, \tag{4.70}$$

which is a rectangular $M \times 2H$ matrix. It has to be taken into account that every partial derivative is a function of energy. Therefore, there is a different linear equation defined for each energy point.

There are two main ways to solve this equation. The first consists in building a parametric function that describes the expected $\Delta\mu_h(E)$, which is proportional to the EXAFS signal, and then calculate $\Delta\beta_h(E)$ by equation 4.9 and $\Delta\delta_h(E)$ by equation 4.8, which would be function of the same parameters. Then, it is possible to look for and find the values of the parameters that best fit all the $\Delta\delta_h(E)$ and $\Delta\beta_h(E)$ to all the experimental $\Delta R_m(E)$ by a least squares fitting algorithm.

However, this method has a few problems. Finding an appropriate function that describe well $\Delta\mu_h(E)$ without distorting the results may be difficult.

Besides, the equation has to be fitted for each energy point, so a function with too many parameters would lead to a huge number of calculations. Moreover, some of the elements of matrix $A(E)$ might be quite small, so the rounding errors in a computer program will scale with the number of calculations.

The second method is to assume $\Delta\mu_h(E)$ as a set of independent points, one for each energy value. Then, $\Delta\beta_h(E)$ is calculate by equation 4.9 and $\Delta\delta_h(E)$ is calculated by equation 4.8.

Once these functions have been calculated, the coefficients of matrix $A(E)$ can be calculated by a numerical derivative. With these coefficients, the equation can be solved by the evaluation of the Moore-Penrose *pseudoinverse*, $A^+(E)$ [49], of matrix $A(E)$ for each energy point. This pseudoinverse is a generalization of the inverse for a non-square matrix. The main property of this pseudoinverse is that, given a system of linear equations

$$\boldsymbol{b} = A\boldsymbol{x}\,, \tag{4.71}$$

where A is the coefficient matrix, not necessarily square, the vector $\boldsymbol{x_0}$ that is the closest solution, i.e. the least squares solution, or in other words, the one that minimises the Euclidean norm

$$\min |A\boldsymbol{x} - \boldsymbol{b}|^2 = |A\boldsymbol{x_0} - \boldsymbol{b}|^2\,, \tag{4.72}$$

is the one that fulfills [50]

$$\boldsymbol{x_0} = A^+\boldsymbol{b}\,, \tag{4.73}$$

where A^+ is the Moore-Penrose pseudoinverse of matrix A.

The solution of the equation thus obtained for each energy point is a new and different set of points that describe $\Delta\delta_h(E)$ and $\Delta\beta_h(E)$. These new functions can be used again to calculate the coefficients of matrix $A(E)$ by a numerical derivative, so the process can start again. This process is then done iteratively until the difference between the $\Delta\delta_h(E)$ and $\Delta\beta_h(E)$ functions between two consecutive steps is small.

The problem of this method is again that, if some of the matrix elements of $A(E)$ are too small, they will have rounding errors in a computer that will be magnified in the calculation of the pseudoinverse.

To overcome these problems, it is convenient to use an orthogonal decomposition method for the calculation of the pseudoinverse. Specifically, the *Singular Value Decomposition* or *SVD* method was used in this work.

Matrix $A(E)$ of Equation 4.69 can decomposed as

$$A = UDV^* \,, \tag{4.74}$$

where U is a $M \times M$ unitary matrix, V^* is the conjugate transpose matrix of V, which is a $2H \times 2H$ unitary matrix, and D is a $M \times 2H$ diagonal matrix of positive (or zero) values. Then, the pseudoinverse of A can be easily calculated as

$$A^+ = (V^*)^{-1} D^+ U^{-1} = V D^+ U^* \,, \tag{4.75}$$

where it has been applied the property that defines the unitary matrices

$$U^{-1} = U^* \quad , \quad V^{-1} = V^* \,. \tag{4.76}$$

The inverse of the diagonal matrix D is calculated just inverting its diagonal matrix elements

$$(D)_{ij} = d_{ii} \implies (D^+)_{ij} = \frac{1}{d_{ii}} \quad , \quad \forall i \,. \tag{4.77}$$

A property of the SVD method is that, if a certain matrix element d_{aa} of the diagonal matrix D is small compared to the $Tr(D) = \sum_{\forall i} d_{ii}$, then this matrix element and its corresponding inverse $1/d_{aa}$, in the inverse matrix, can be neglected. This leaves truncated matrices $\widetilde{D}$ and $\widetilde{D}^+$ where

$$\widetilde{A} = U \widetilde{D} V^* \,, \tag{4.78a}$$

$$\widetilde{A}^+ = V \widetilde{D}^+ U^* \,, \tag{4.78b}$$

where the truncated pseudoinverse matrix, $\widetilde{A}^{+}$, is as a very good approximation of A^{+}. Thus, this property overcome the problem of the rounding errors of the small matrix elements, as they can be neglected.

In many cases, the above approach did not converge and oscillated. Fortunately, there is an additional constraint that can be used, which is the Kramers-Kronig relationship between $\Delta\delta(E)$ and $\Delta\beta(E)$ of Equation 4.58. This has to be applied at every iteration so as to assure that Equation 4.58 is fulfilled every time. This way, the equation has a double constraint.

The resulting $\Delta\beta_h(E)$ are normalised to the $\beta_{0h}(E)$ jump so, finally, each $\chi_h(E)$ can be calculated using equation 4.49, and may be analysed using the standard EXAFS analysis programs [45, 46]

Chapter 5

CuCrxN multilayers

Contents

Introduction

The motivation for the preparation of the first set of samples is to have a known system to test the experimental issues of the technique so as to optimise the experimental method. Indeed, a set of somehow ideal samples was made. More specifically, these samples should be as flat and smooth as possible to avoid beam dispersion, and rather long and homogeneous in the beam direction to maximise the reflectivity. Also they should be rather simple from the analysis point of view.

As described in Section 2.1.2.1, a set of multilayered samples with a (CuCr)xN structure was prepared to study the Cu local environment by analysing the ReflEXAFS spectra around the Cu-K absorption edge. Cr was chosen as the outermost layer to prevent the oxidation of the Cu layers to avoid having two different EXAFS spectra at the same sample, that was not (yet) the aim of this set of measurements.

The monocrystalline Si wafers gave the layers a extremely flat substrate to grow. The *magnetron sputtering* deposition technique described in Section 2.1.1 provided a straightforward method to obtain relatively dense and smooth layers.

The samples were of approximately the same total thickness, but increasing the number of periods: N = 2, 3, 4 and 8. This allows the possibility of investigating the local structure of metallic Cu for different thicknesses of the layers.

5.1 Characterization results

5.1.1 X Ray Reflectometry

As explained in Section 2.2.2, X Ray Reflectometry measurements were recorded both in a laboratory X ray diffractometer and at the synchrotron

radiation beamline BM29. All these diagrams were simulated and fit using the program *GenX* [26] to obtain the layers characteristics of the samples.

The variables of the XRR diagram simulation were the interface roughnesses, and the thicknesses and relative densities (to the bulk crystalline density of each material) of the layers. Crystal densities are ρ_{Cu}=0.0847 at/Å^3 and ρ_{Cr}=0.0833 at/Å^3. To reduce the number of free parameters, the thicknesses and relative densities of the same layer (Cu or Cr) of each period of the multilayer were linked, as they were grown in the same conditions. The interface (either Cr/Cu or Cu/Cr) roughnesses were also linked, leaving the substrate (Si/Cu) and the surface (Cr/air) roughnesses free.

The results of the fitting are summarised in Table 5.1. The experimental and best fit simulated XRR diagrams and are shown in Figures 5.1, to 5.13.

Table 5.1: XRR simulation results for samples CuCrxN

Sample	**Energy**	**Thickness (Å)**		**Relative Density**		**Roughness (Å)**		
		Cu	Cr	Cu	Cr	Sub.	Intf.	Sur.
CuCrx2	**8 keV**	54	35	1.00	0.90	5	16	11
	10 keV	54	35	1.00	0.90	5	15	12
	Cu-K$_\alpha$	54	35	1.00	0.90	5	16	11
CuCrx3	**8 keV**	28	32	1.00	0.94	8	12	12
	8.8 keV	28	34	1.00	0.88	10	16	14
	10 keV	25	33	1.00	0.98	11	13	16
	Cu-K$_\alpha$	25	35	1.00	0.92	4	12	9
CuCrx4	**8 keV**	34	15	1.00	0.94	5	13	18
	10 keV	30	17	1.00	0.95	7	16	14
	Cu-K$_\alpha$	28	19	0.99	0.92	12	11	9
CuCrx8	**8 keV**	19	10	0.98	1.00	8	17	8
	10 keV	19	9	0.99	1.00	7	3	16
	Cu-K$_\alpha$	18	12	1.00	1.00	5	10	19

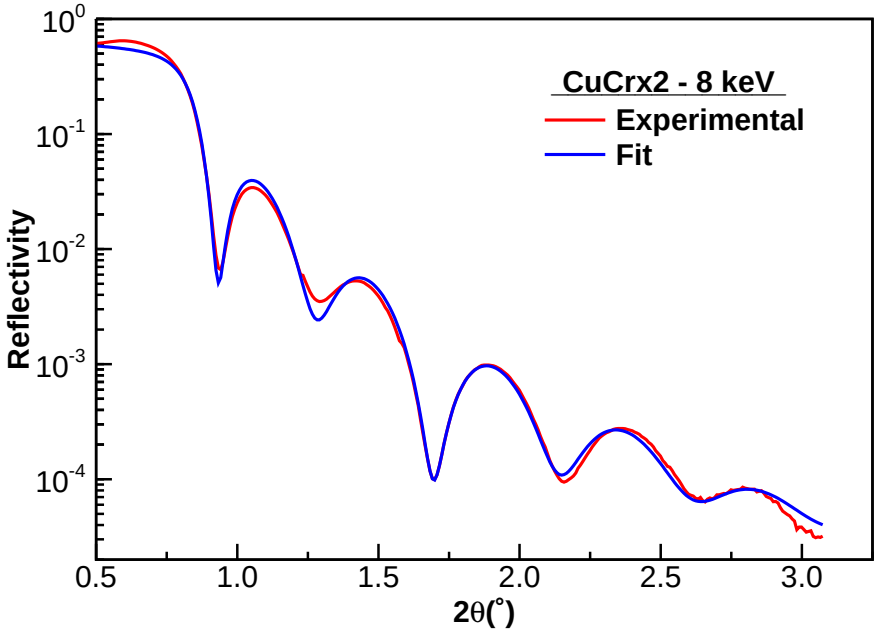

Figure 5.1: XRR at 8 keV experimental diagram and best fit for sample CuCrx2

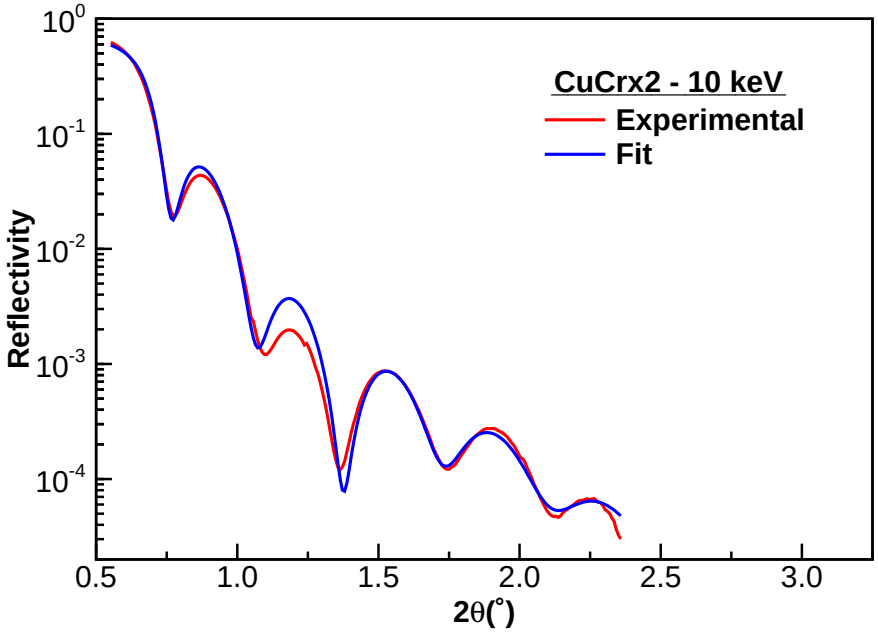

Figure 5.2: XRR at 10 keV experimental diagram and best fit for sample CuCrx2

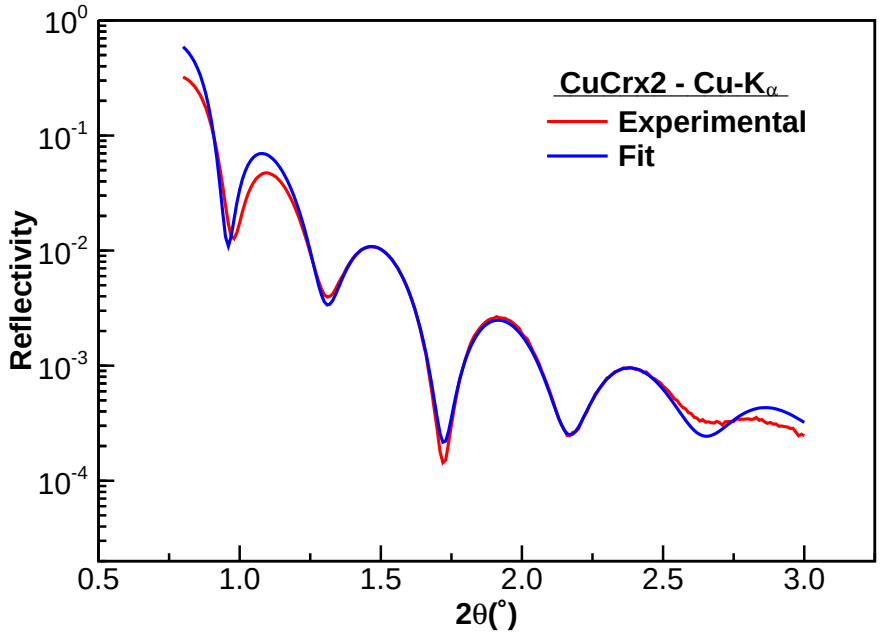

Figure 5.3: XRR at Cu-K_α experimental diagram and best fit for sample CuCrx2

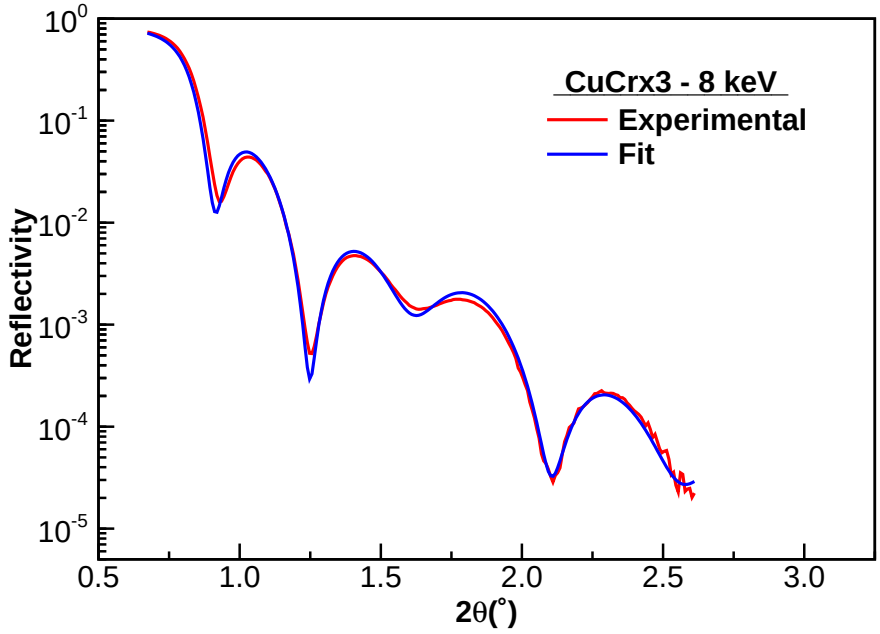

Figure 5.4: XRR at 8 keV experimental diagram and best fit for sample CuCrx3

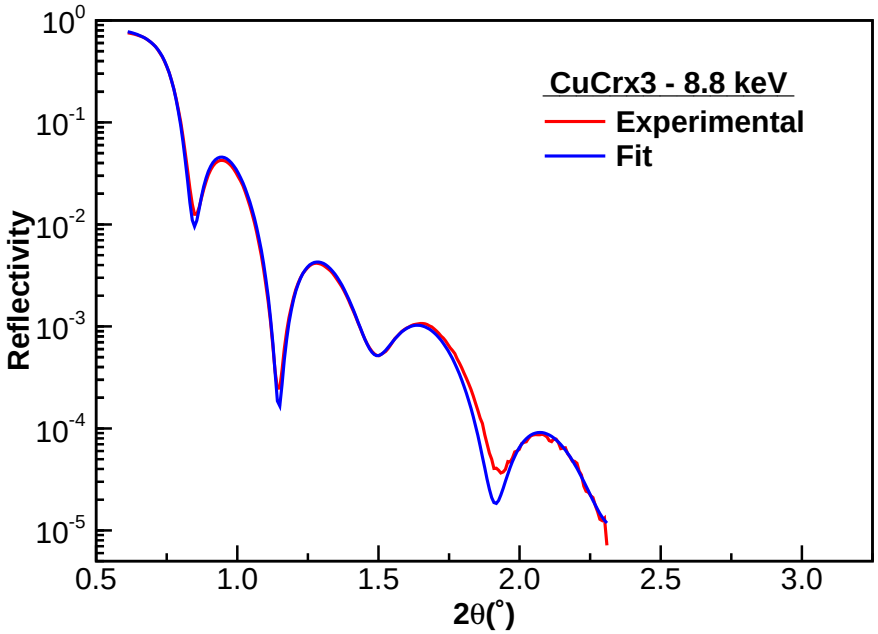

Figure 5.5: XRR at 8.8 keV experimental diagram and best fit for sample CuCrx3

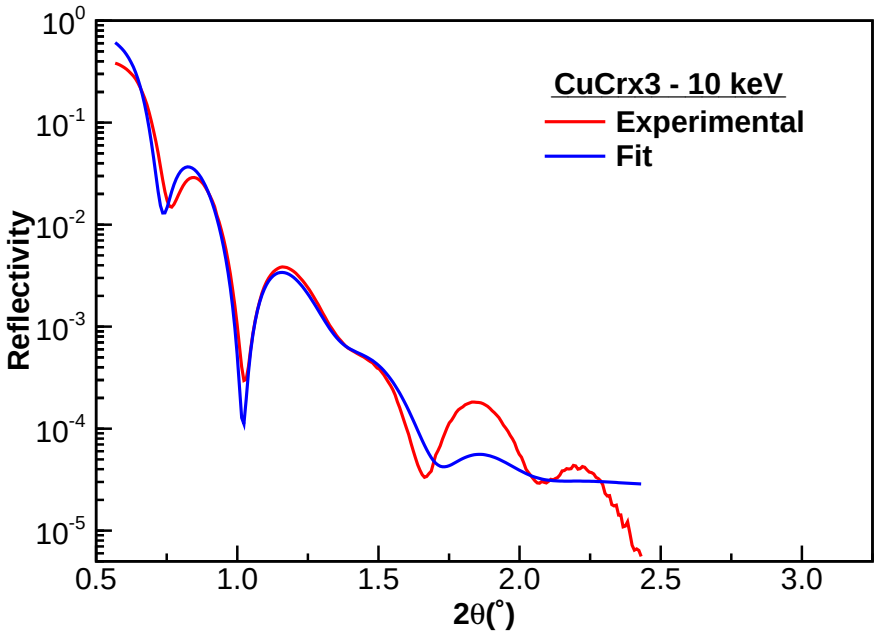

Figure 5.6: XRR at 10 keV experimental diagram and best fit for sample CuCrx3

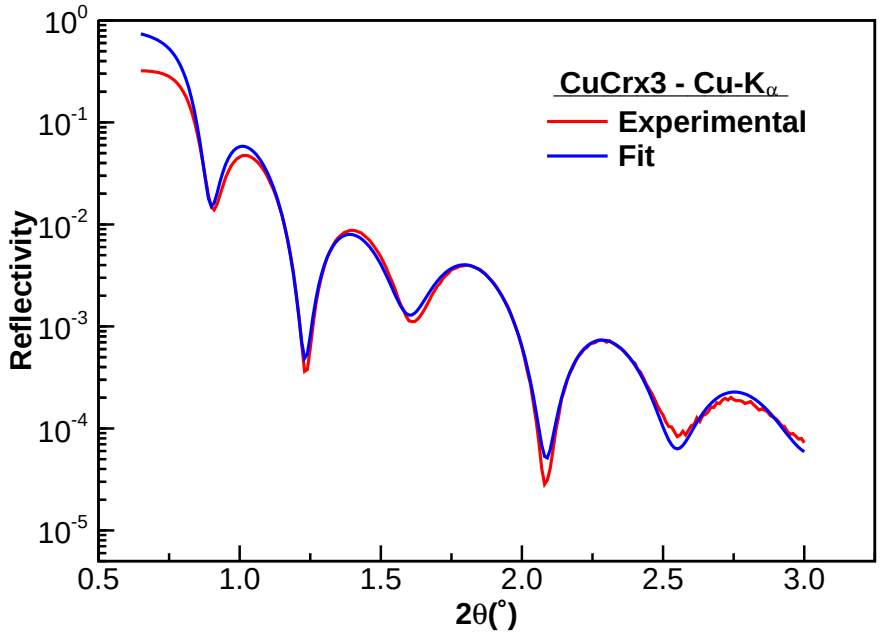

Figure 5.7: XRR at Cu-K_α experimental diagram and best fit for sample CuCrx3

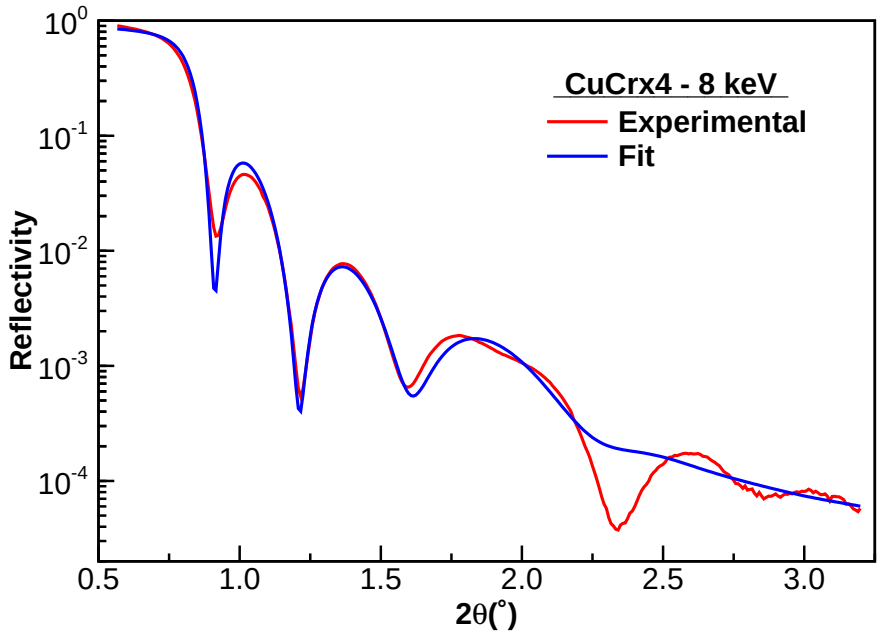

Figure 5.8: XRR at 8 keV experimental diagram and best fit for sample CuCrx4

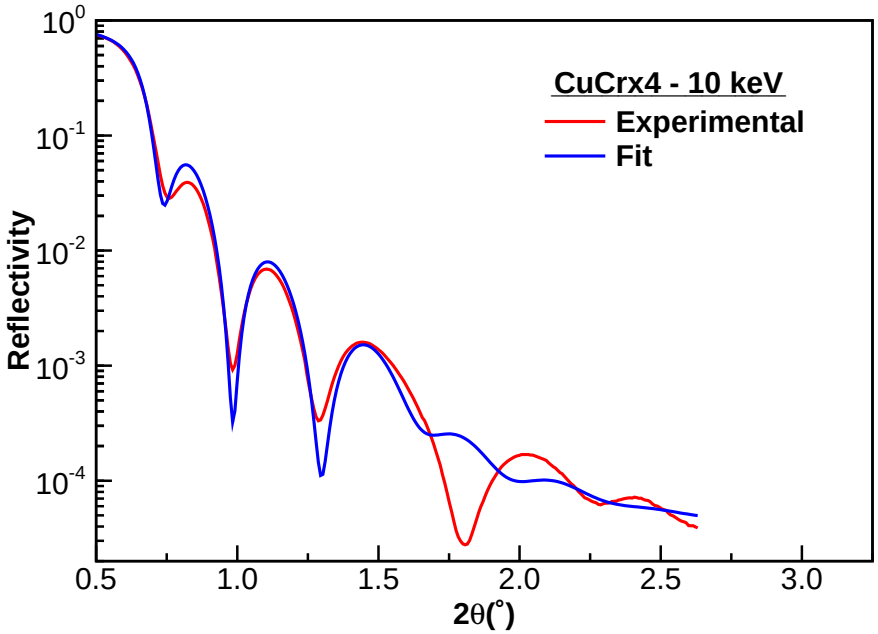

Figure 5.9: XRR at 10 keV experimental diagram and best fit for sample CuCrx4

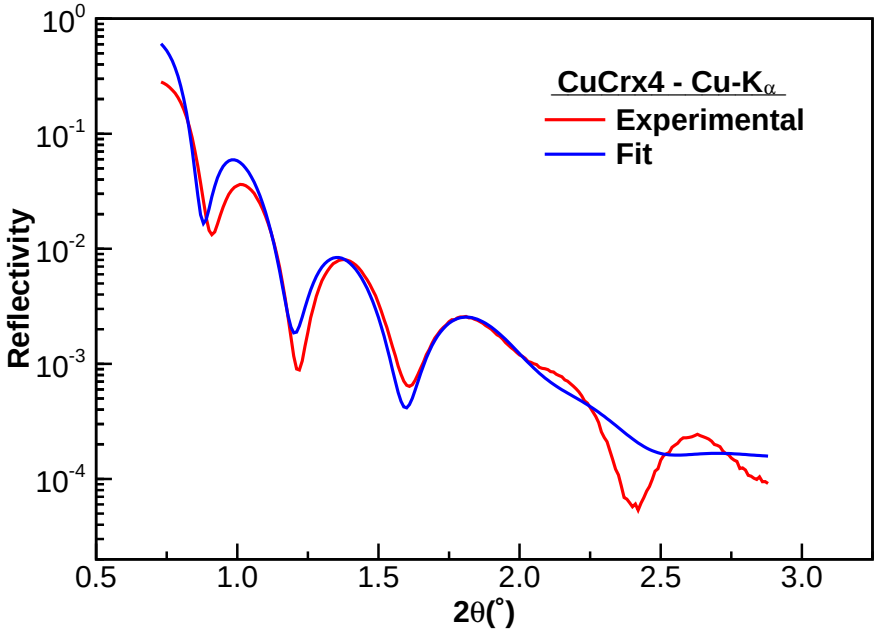

Figure 5.10: XRR at Cu-K_α experimental diagram and best fit for sample CuCrx4

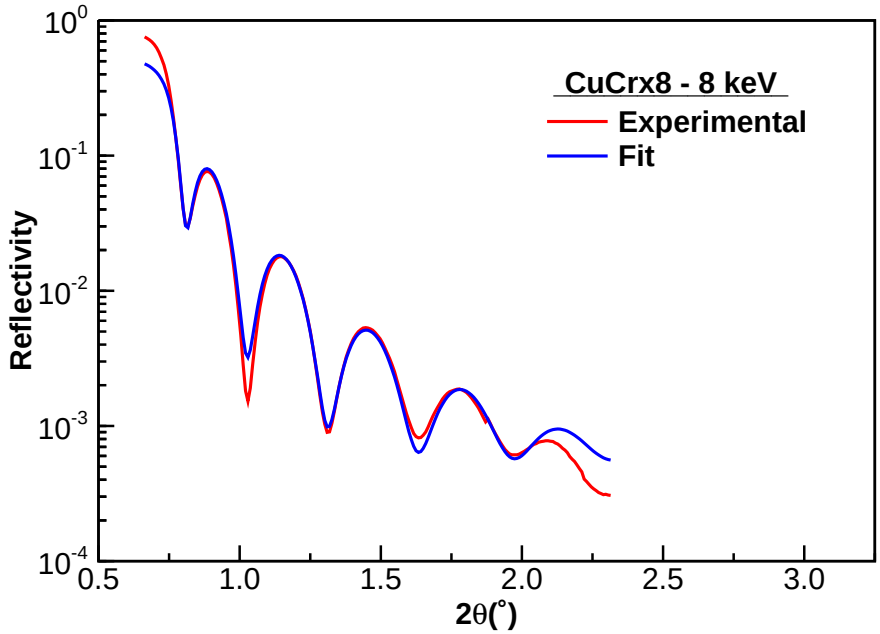

Figure 5.11: XRR at 8 keV experimental diagram and best fit for sample CuCrx8

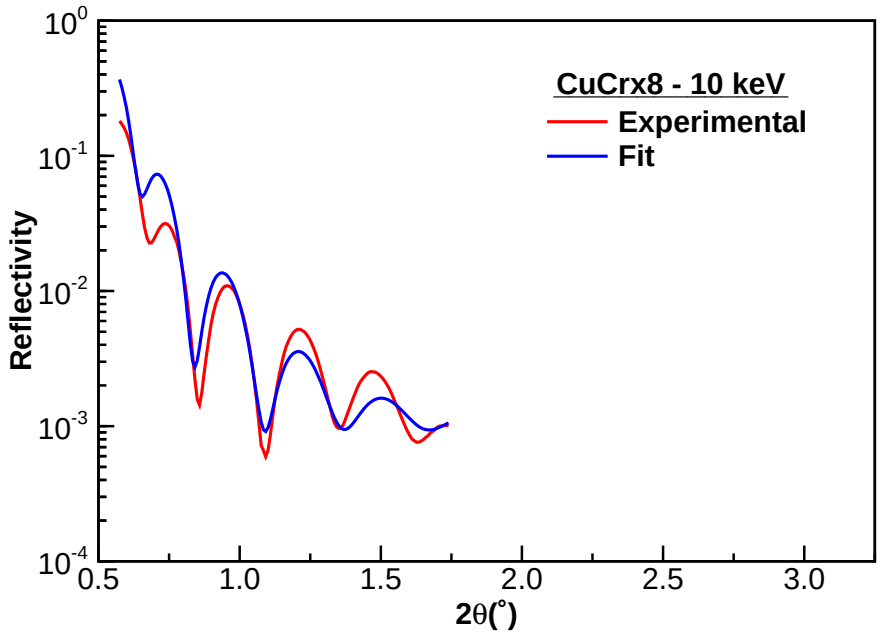

Figure 5.12: XRR at 10 keV experimental diagram and best fit for sample CuCrx8

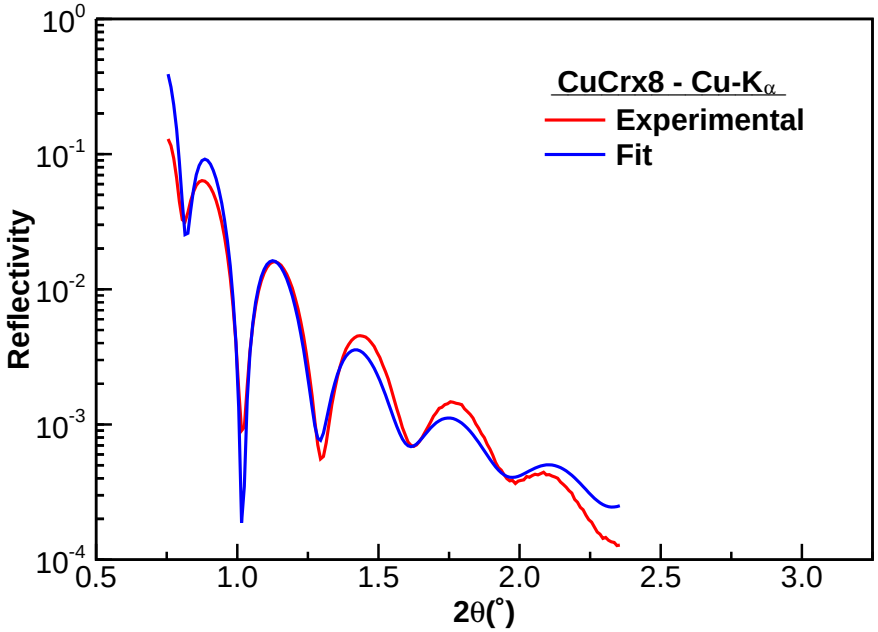

Figure 5.13: XRR at Cu-K_α experimental diagram and best fit for sample CuCrx8

The XRR diagrams present a typical interference pattern of a layered system, being quite similar for all the samples due to the similar total thickness.

Rather good fits were obtained in all cases, reading consistent values of thicknesses and densities. Nevertheless, a variety of values was obtained for roughnesses, ranging within a factor 2 or even 3 for some cases and the results are less consistent for the samples with thinner layers. For this reason, it seems that this indetermination can come from the fact that the approximations in the theory involved in the roughness simulation [26, 41] fail for too high roughness compared to the thickness of the layers.

5.1.2 Rutherford Backscattering Spectrometry

RBS measurements were carried out using the linear accelerator of the Centro Nacional de Aceleradores (Seville), and analised as explained in Section 2.2.3.

RBS data give the amount of material per surface unit, so the thickness of a

layer can be calculated by assuming a density of the layers. The density can be assigned as the bulk density of the material, or as the density calculated from the XRR measurements. The thicknesses determined using both bulk density and the XRR calculated density are shown in Table 5.2

Table 5.2: RBS results

Sample	**Thickness (Å) (Crys. Dens.)**		**Thickness (Å) (XRR Dens.)**		**×N**
	Cu	Cr	Cu	Cr	
CuCrx2	54	31	54	34	×2
CuCrx3	35	35	35	37	×3
CuCrx4	28	16	28	17	×4
CuCrx8	18	8	18	8	×8

The RBS thickness results are in good agreement with the XRR ones, given the fact that the data come from completely different physical processes. The measurements at different parts of the samples showed that they are homogeneous in all the length within the accuracy of the technique.

5.1.3 Atomic Force Microscopy

Sample surface topography images were taken with a Topometrix TMX2000 microscope, and roughnesses were calculated as explained in Section 2.2.5.

The surface topography images of CuCrx2 to CuCrx8 samples are shown in Figures 5.14 to 5.17. Table 5.3 summarises the roughness calculated from the RMS values of these measured for each sample.

CuCrx2, CuCrx3 and CuCrx4 samples have similar topography and the variance of heights are near the instrument noise level. It can then be concluded that they are quite smooth and homogeneous in the scale selected. However, this also means that the calculation of the roughness is a convolution between

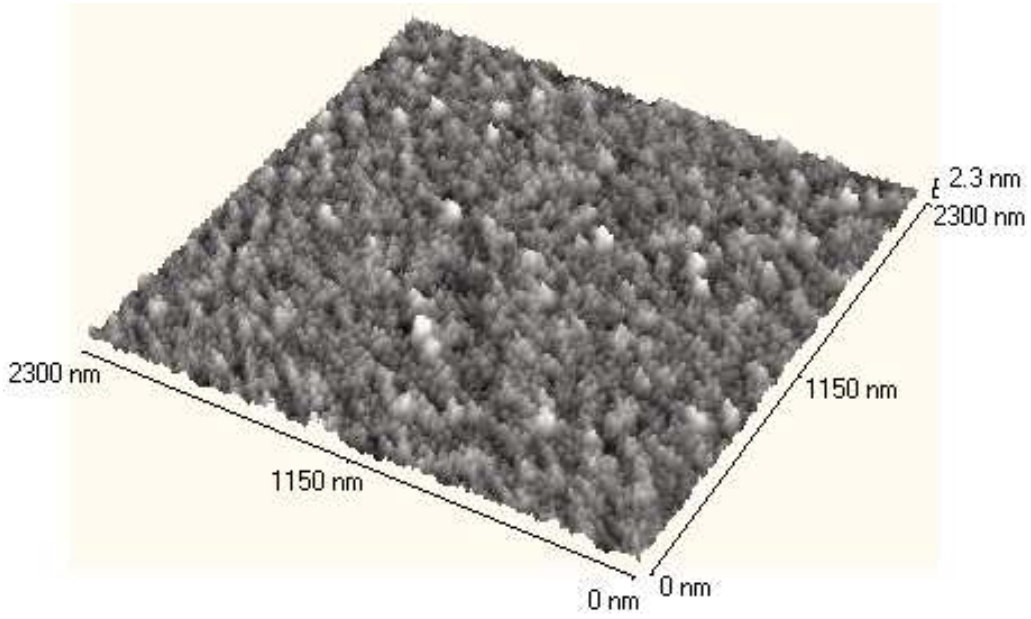

Figure 5.14: AFM surface topography for sample CuCrx2

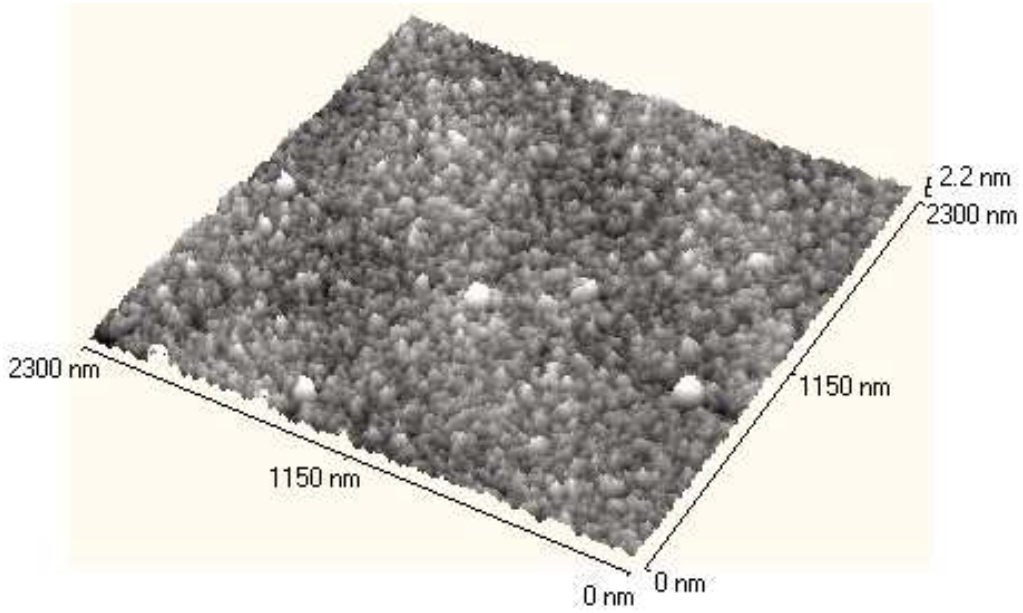

Figure 5.15: AFM surface topography for sample CuCrx3

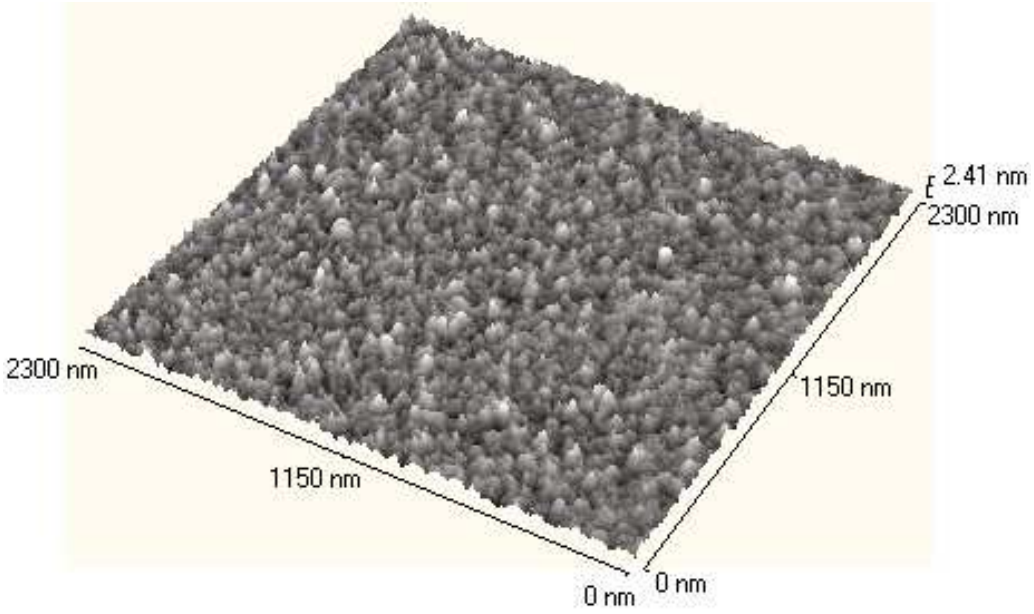

Figure 5.16: AFM surface topography for sample CuCrx4

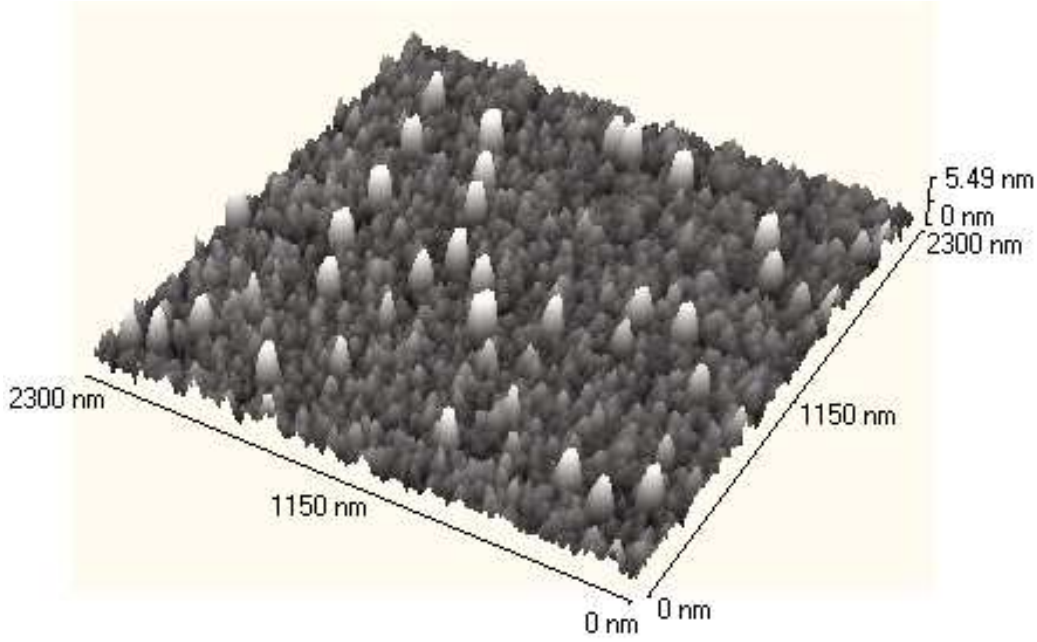

Figure 5.17: AFM surface topography for sample CuCrx8

Table 5.3: AFM surface roughness for samples CuCrxN

Sample	Roughness (Å)
CuCrx2	3
CuCrx3	3
CuCrx4	4
CuCrx8	9

the instrument noise and the actual roughness which results in a slight over estimation.

On the other hand, CuCrx8 sample topography shows a set of emerging columns of similar shape and height which are randomly distributed. Due to the extremely thin thickness of the outermost Cr layer, this might show a grow of Cu oxide from the second layer. The preferential spots can be a consequence of the variance on the Cr layer thickness, so the oxygen only penetrates at the places where the Cr layer is thin enough.

For these reasons, CuCrx2, CuCrx3 and CuCrx4 samples have a similar roughness in this scale, while CuCrx8 roughness is higher due to the columns seen in the topography figure.

5.2 ReflEXAFS experiments

5.2.1 Angle selection

As explained in Section 3.2.2, X ray reflectivity diagrams were recorded at the synchrotron beamline, at different energies, to show the reflectivity behaviour, so as to choose the most convenient angles for the ReflEXAFS scans.

The reflectivity patterns are shown in Figures 5.18 to 5.21. The figures are marked with the angles where the ReflEXAFS measurements were made. Since the ReflEXAFS measurements are at fixed angles and move in energy

from 8 to 10.5 keV, they effectively move from the 8 keV curve position to the same point on the rest of the energies.

These particular angles were chosen with the aim to have a wide range of different patterns in ReflEXAFS scans. This allows a test of the fitting procedure of the global analysis on a number of different baseline curve types, including a valley point (at 10 keV for approximately 0.38°) and a rising peak (at 10 keV for approximately 0.43°). This gives a good validation scope for the subsequent analysis.

5.2.2 ReflEXAFS scans

ReflEXAFS scans were performed as explained in Section 3.2.3 at the angles selected with the aid of the XRR curve. After that, each spectrum was divided by the direct beam scan to remove the absorption component of the air between the detectors and get a normalised spectrum.

The set of the experimental normalised spectra for each sample are shown in Figures 5.22 to 5.25.

Both the background with the typical interference pattern due to the multilayers reflection and the EXAFS fine structure can be seen in all the samples spectra.

The background of the spectra show the expected interference pattern due to the multilayered structure of the samples, which is obviously different for each of them due to the different multilayered structure. This pattern changes as the angle change and also decreases its overall intensity for higher incidence angles, due to the loss of the total reflection condition and the increase of the transmission coefficient.

Superimposed to the background, it can clearly be seen the absorption edge at the Cu-K absorption edge energy (8.979 keV), along with an EXAFS-like pattern just after it. This pattern is better resolved at intermediate angles. On one hand, the lowest angle spectrum interacts very little with the Cu

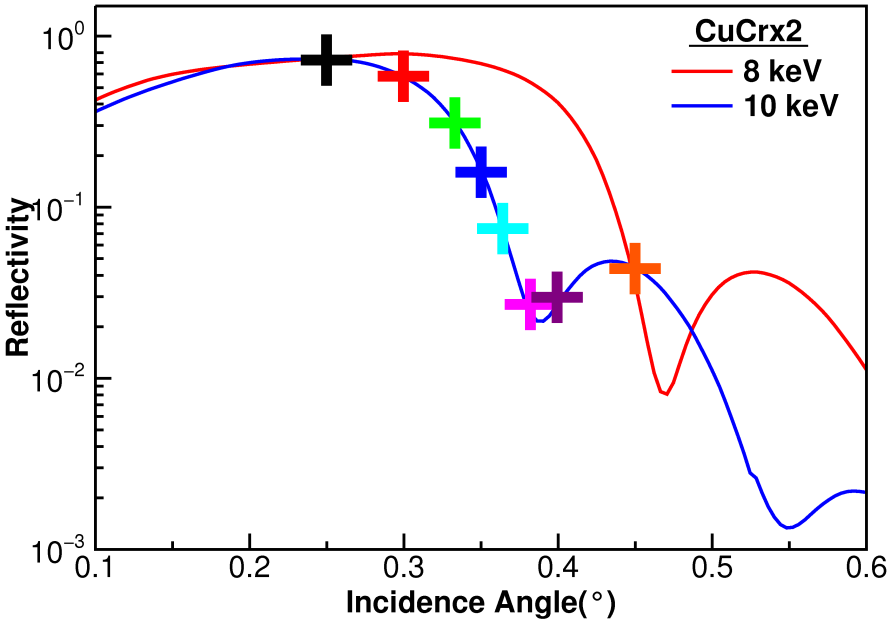

Figure 5.18: XRR experimental diagrams and ReflEXAFS selected angles for CuCrx2

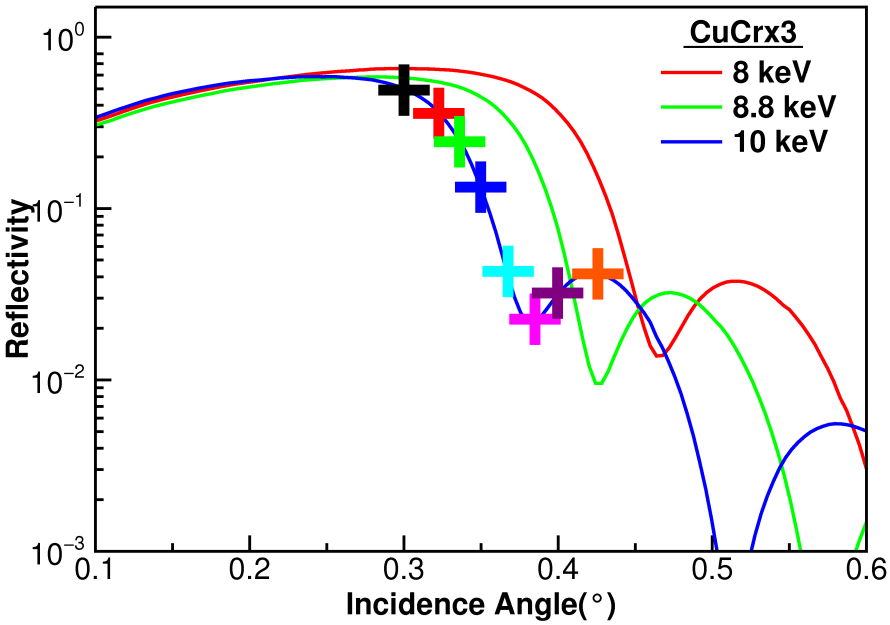

Figure 5.19: XRR experimental diagrams and ReflEXAFS selected angles for CuCrx3

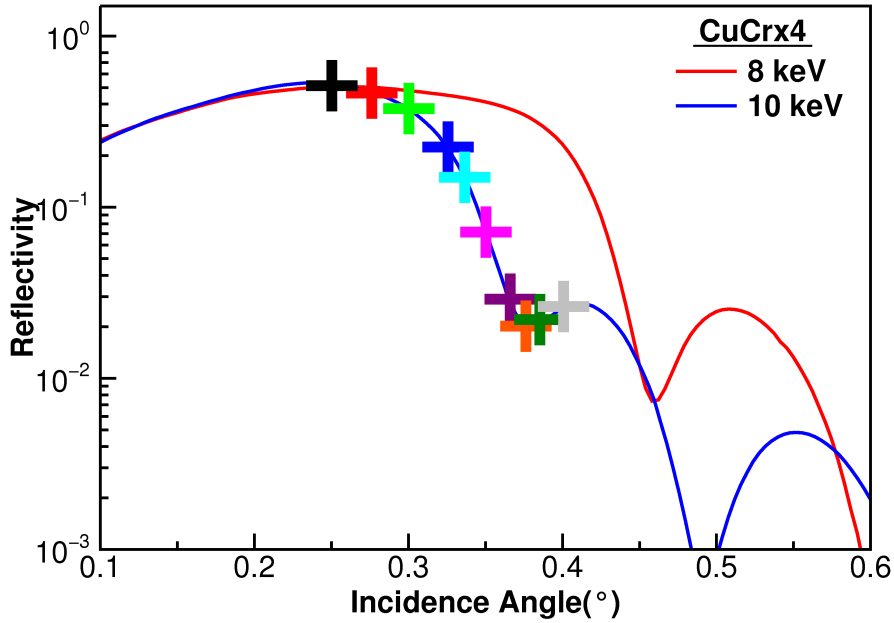

Figure 5.20: XRR experimental diagram and ReflEXAFS selected angles for CuCrx4

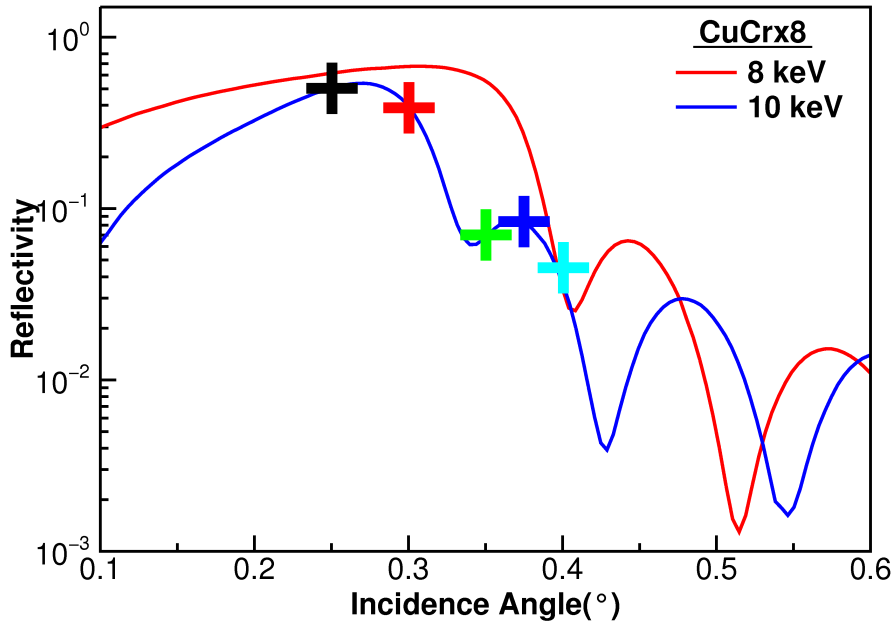

Figure 5.21: XRR experimental diagram and ReflEXAFS selected angles for CuCrx8

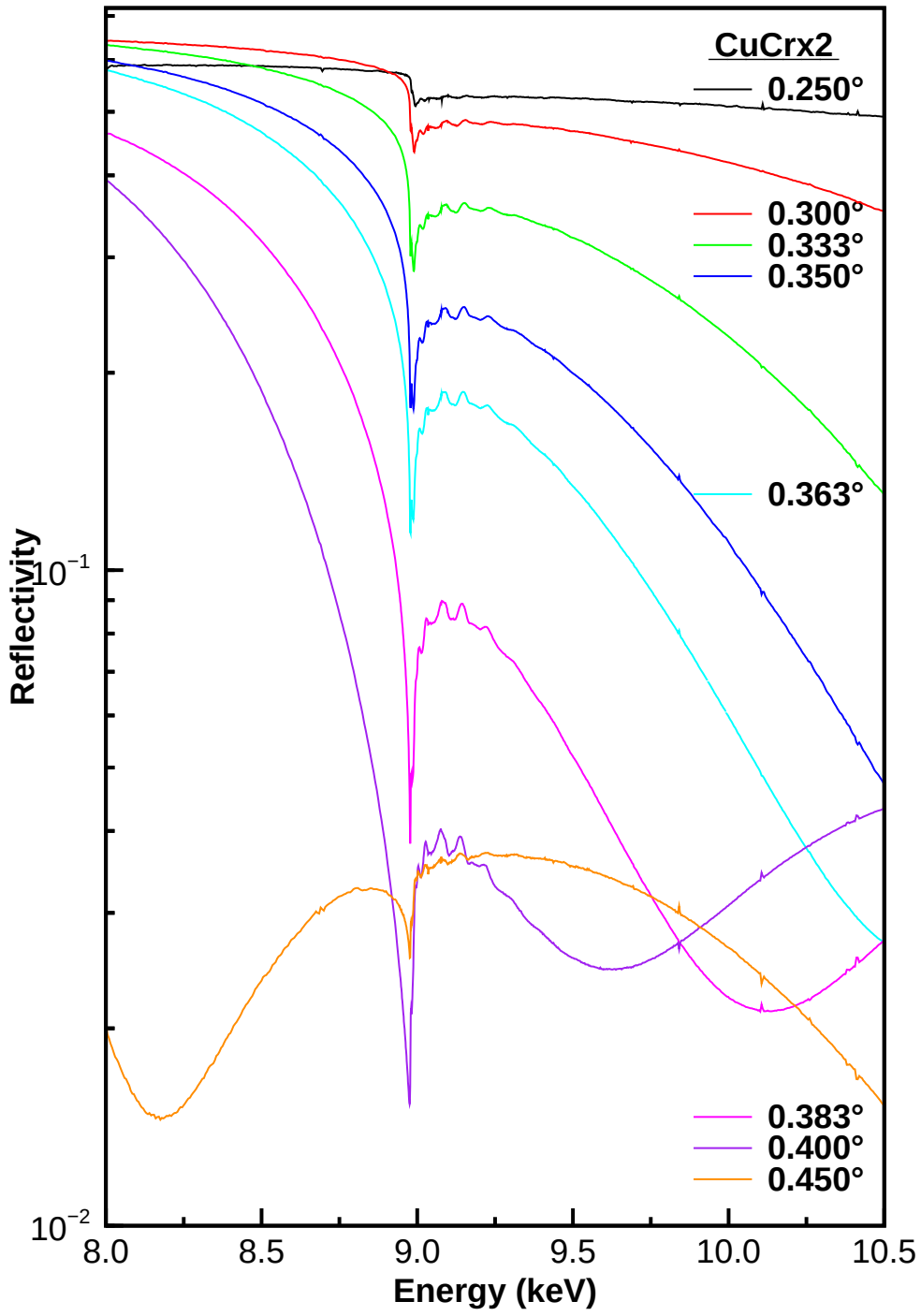

Figure 5.22: ReflEXAFS normalised experimental spectra for sample CuCrx2

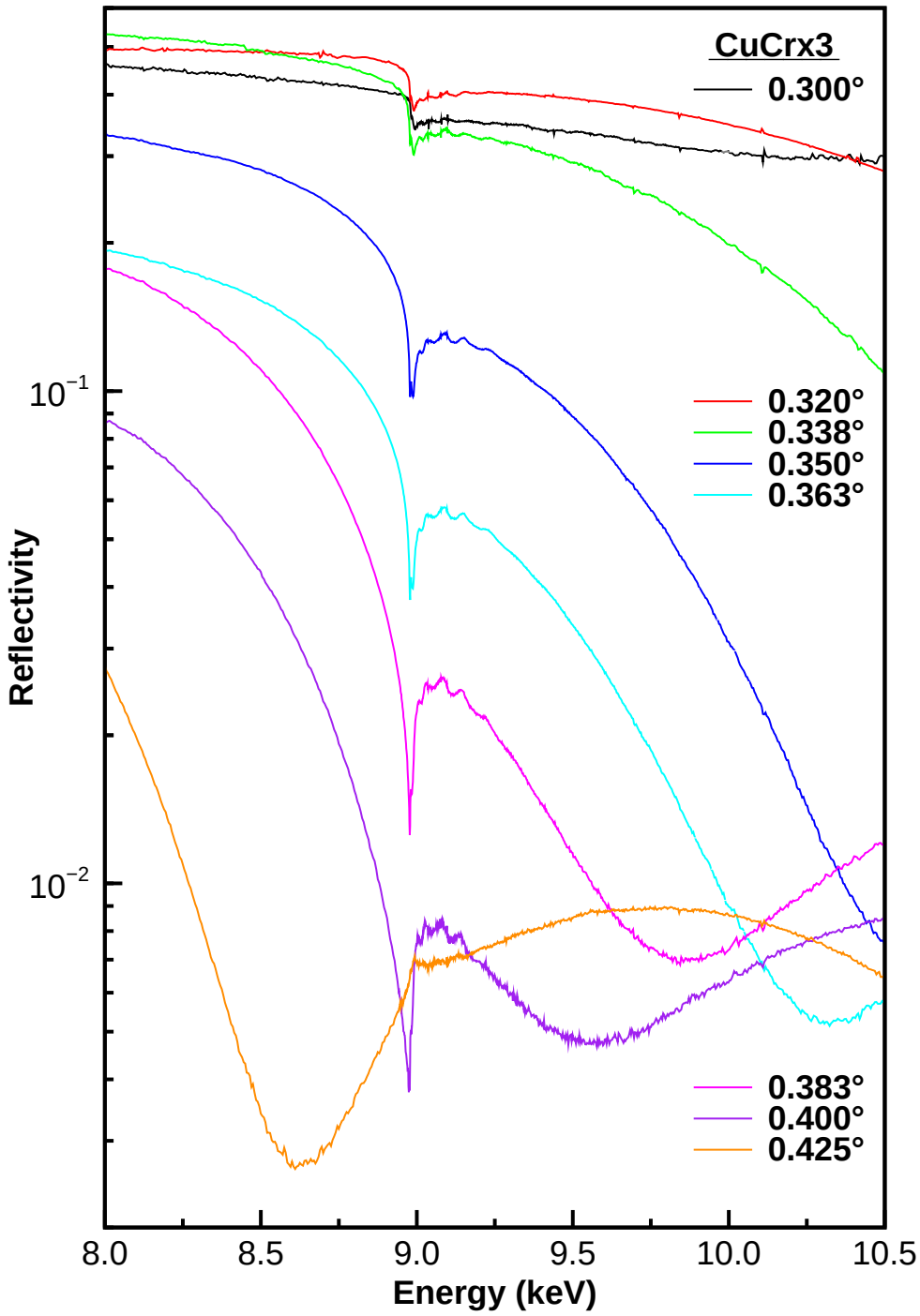

Figure 5.23: ReflEXAFS normalised experimental spectra for sample CuCrx3

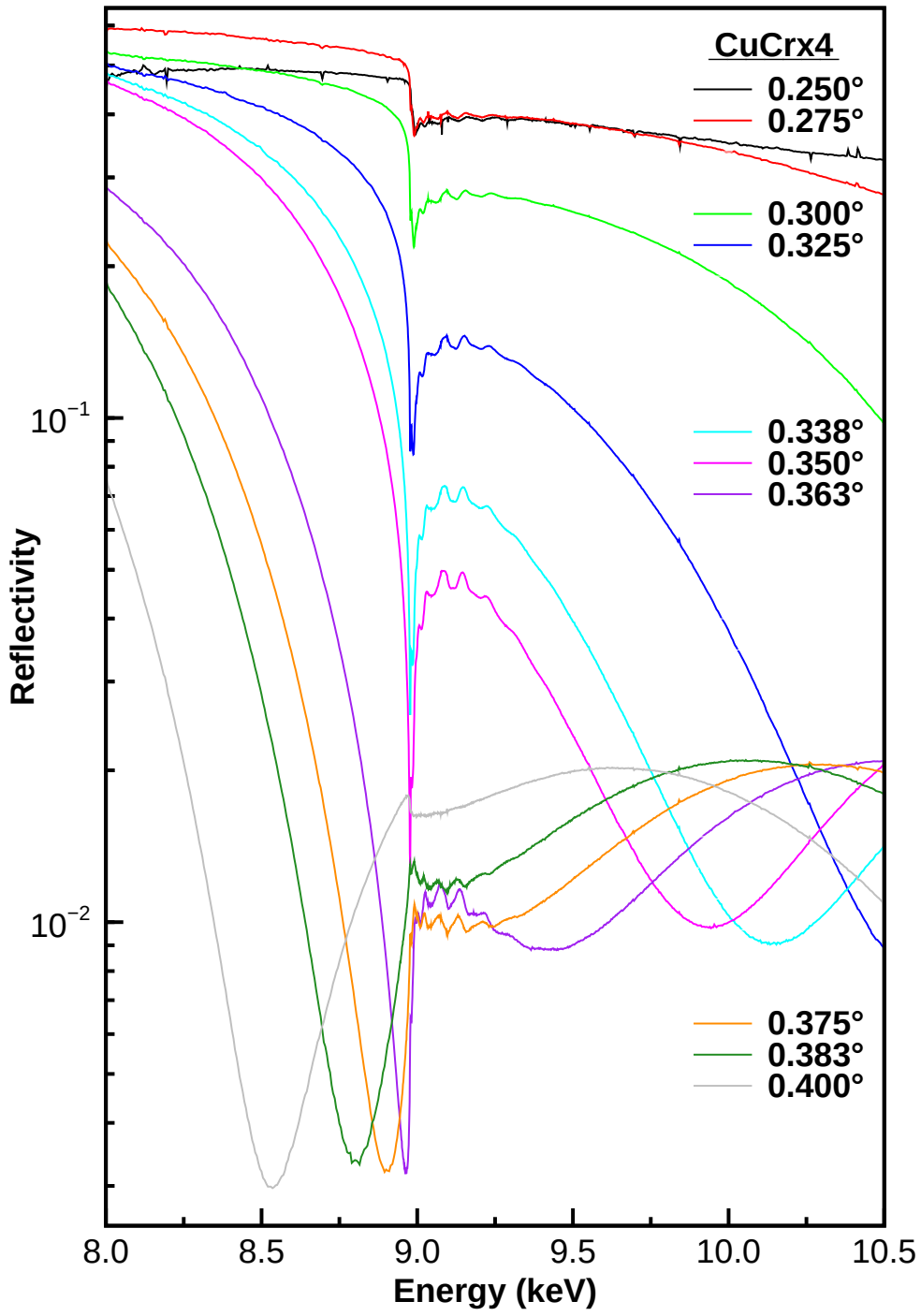

Figure 5.24: ReflEXAFS normalised experimental spectra for sample CuCrx4

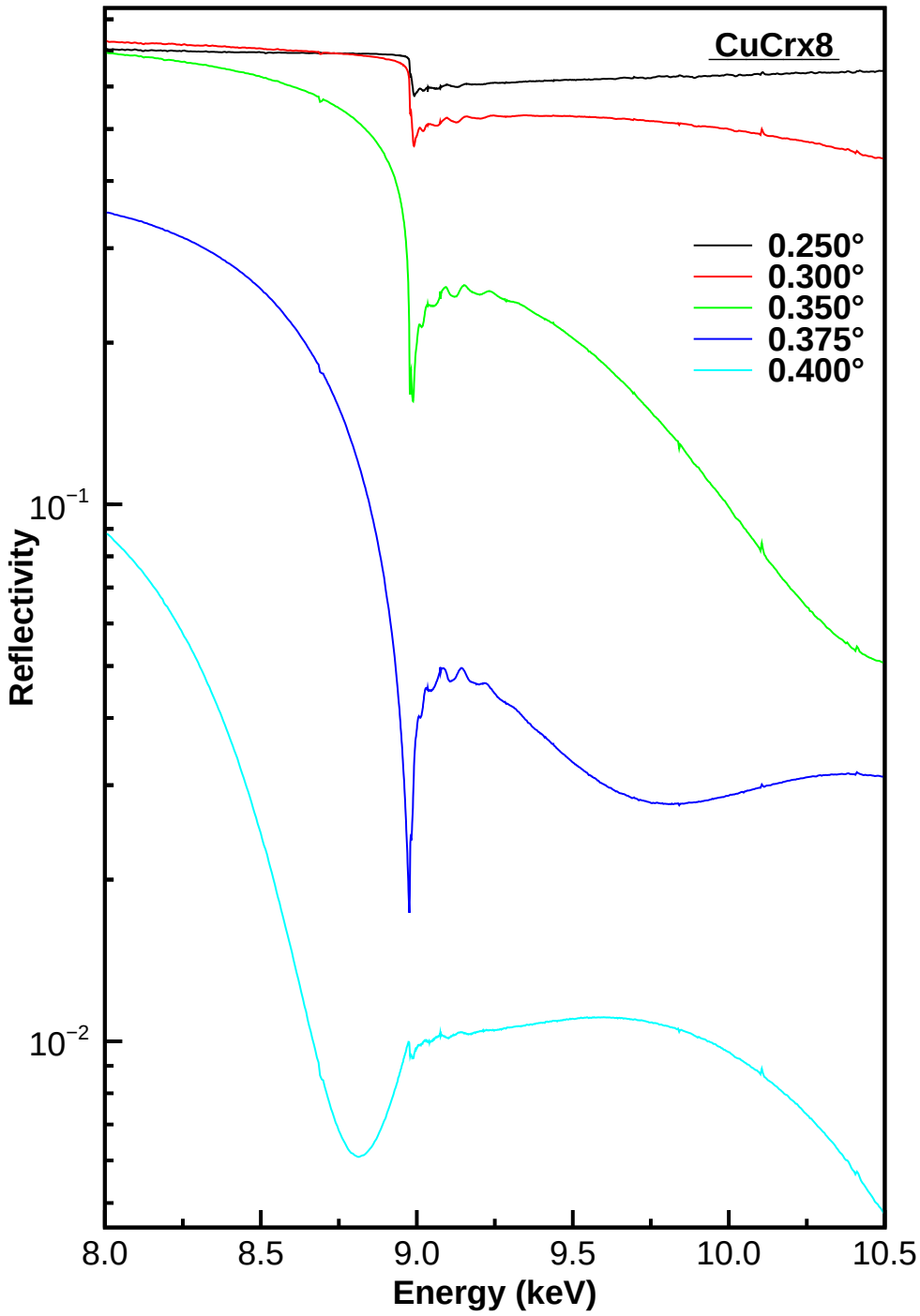

Figure 5.25: ReflEXAFS normalised experimental spectra for sample CuCrx8

absorbing atoms due to the low penetration depth of the radiation; in fact, the total reflection condition is fulfilled at those angles. On the other hand, the highest angle spectrum has a worse signal-to-noise ratio due to the low reflectivity coefficient at those angles.

5.3 Analysis

The ReflEXAFS spectra may be analised by using any of the approximations described in Chapter 4. For this work, the total reflection approximation analysis and the developed global analysis will be used, and the results will be compared.

5.3.1 Total reflection approximation analysis

Using Martens [18] approximation, the EXAFS signal can be extracted directly from a spectrum of incidence angle below the critical angle. Thus, the lowest angle workable spectrum for each sample was analysed.

However, a close inspection of the 0.250° spectra for CuCrx2 and CuCrx4 samples, and 0.300° spectrum for sample CuCrx3, reveals that their signal-to-noise ratio is quite poor. This fact made the attempt to analyse these spectra a failure. Thus, the next angle for those samples was analised, i.e. 0.300° for CuCrx2, 0.320° for CuCrx3, and 0.275° for CuCrx3. Spectrum 0.250° for sample CuCrx8 does have enough signal to noise ratio, so it could be analised.

The EXAFS function obtained from these ReflEXAFS scans were fitted by using a Cu metal model structure with coordination numbers fixed to the crystal values. A single free parameter, Δa, varying the lattice parameter from the Cu bulk value (3.61 Å) was used to allow the variation of coordination distances coherently for all the coordination shells of the model. Moreover, the Debye-Waller factors, that take into account the dynamic (mainly

thermal) and the static disorder, were allowed to vary independently for each shell.

The scattering paths used for this model were the single scattering paths for each shell, plus the co-linear multiple scattering paths with the fourth coordination shell, as these have a high contribution to the EXAFS signal [51]. S_0^2 was set to 0.81, which is a value within the range of values reported in the literature [52], that rarely varies for the same element at different chemical environments. Then, six free independent parameters were used in each fit.

The software used for the analysis was the UWXAFS software package [46, 53, 54].

The results of the fitting are summarised in Table 5.4. Figures 5.26, 5.28, 5.30 and 5.32 show comparative plots of the extracted experimental EXAFS data, $\chi(k)$, with the best fit obtained with the model described above, for all the samples. Figures 5.27, 5.29, 5.31 and 5.33 show a comparative plot of the Fourier transform magnitudes of the EXAFS signals, $\chi(R)$, with their respective fits, and with a Cu foil reference from the IXAS database [55].

Table 5.4: Total reflection angle EXAFS results for CuCrxN samples

Sample	**Shell**	**1**st	**2**nd	**3**rd	**4**th	**5**th	**a (Å)**
	N	12	6	24	12	24	**[Δa (Å)]**
CuCrx2	**R (Å)**	2.56	3.61	4.43	5.11	5.72	3.61
	σ^2 **(Å^2)**	0.010	0.014	0.017	0.018	0.020	[+0.00]
CuCrx3	**R (Å)**	2.53	3.57	4.38	5.06	5.65	3.57
	σ^2 **(Å^2)**	0.012	0.012	0.022	0.023	0.025	[-0.04]
CuCrx4	**R (Å)**	2.53	3.58	4.39	5.07	5.67	3.58
	σ^2 **(Å^2)**	0.012	0.015	0.021	0.023	0.030	[-0.03]
CuCrx8	**R (Å)**	2.51	3.55	4.35	5.03	5.62	3.55
	σ^2 **(Å^2)**	0.015	0.018	0.026	0.026	0.030	[-0.06]

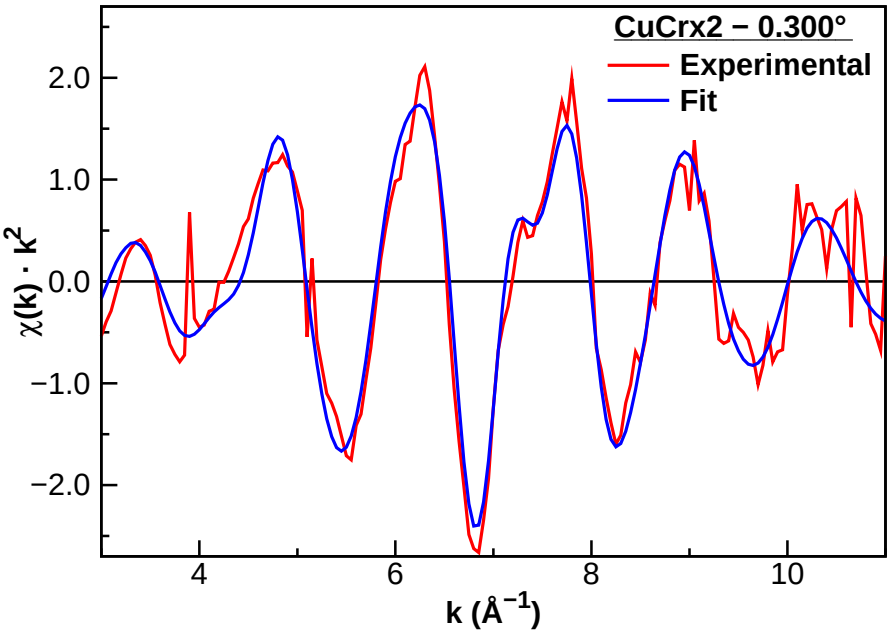

Figure 5.26: EXAFS experimental χ(k) and best fit for sample CuCrx2

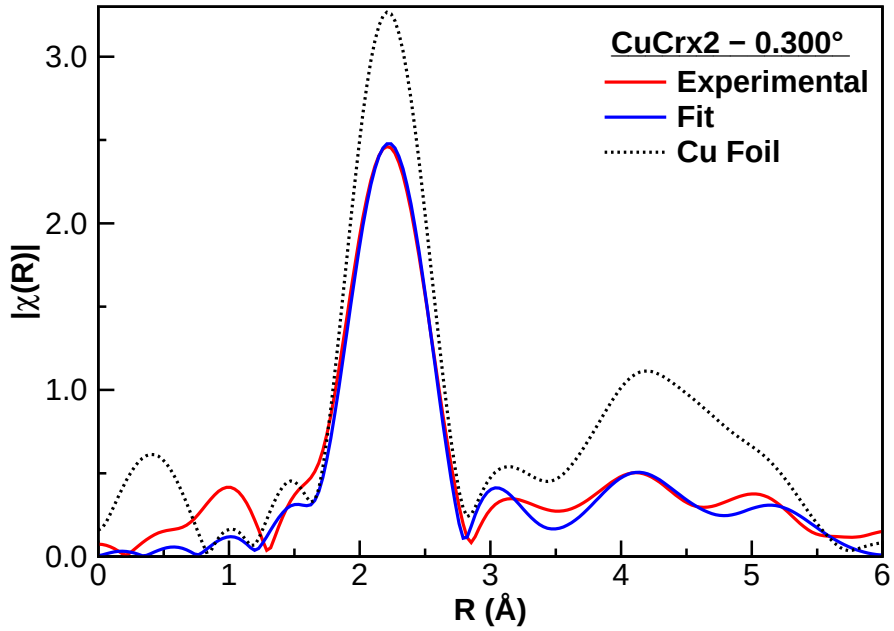

Figure 5.27: EXAFS experimental χ(R) and best fit for sample CuCrx2

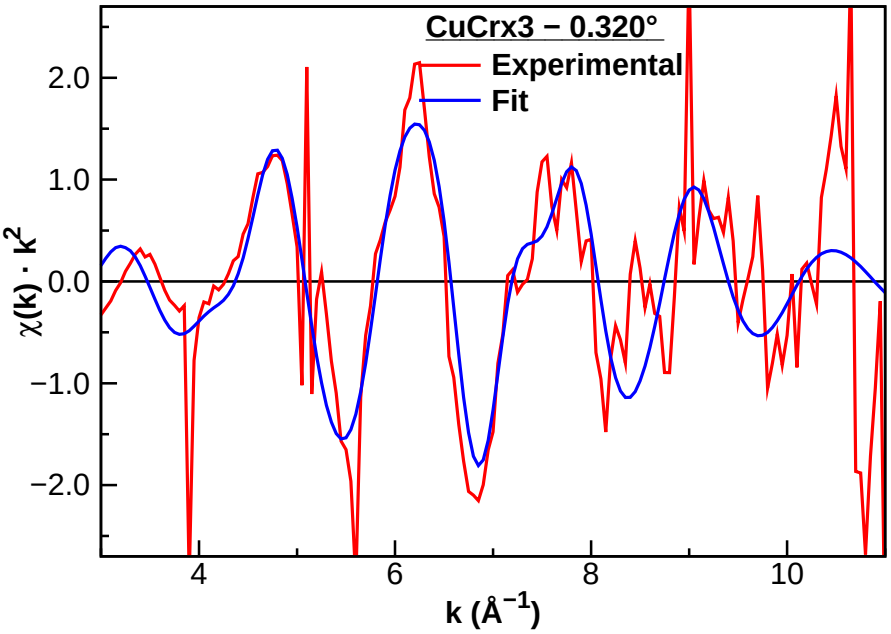

Figure 5.28: EXAFS experimental χ(k) and best fit for sample CuCrx3

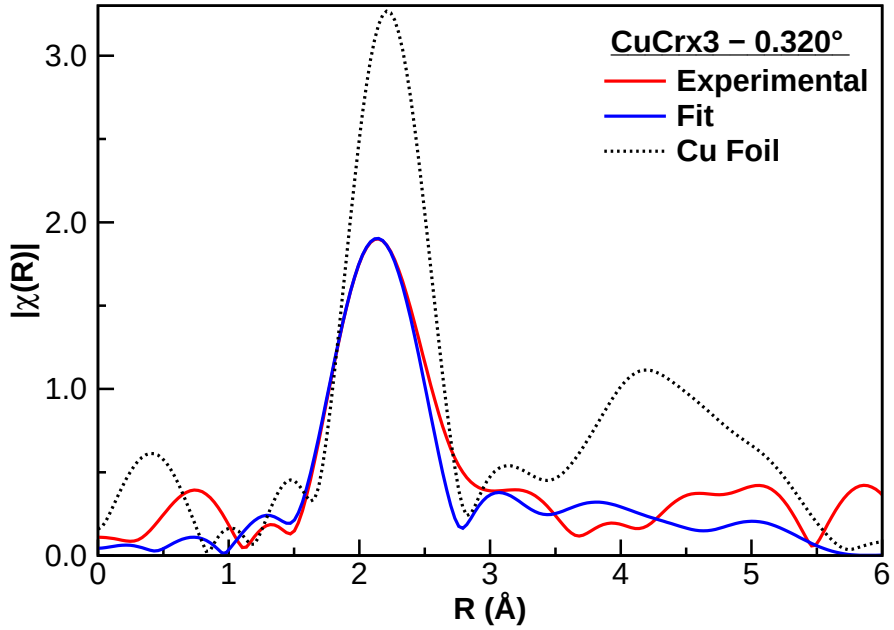

Figure 5.29: EXAFS experimental χ(R) and best fit for sample CuCrx3

At first sight, the pattern of both the EXAFS signal and the Fourier transform magnitude are all quite similar to the Cu foil reference. However, there is an evident decrease on the intensity of both the EXAFS signal and the Fourier transform magnitude not only with regard to the Cu foil reference, but also when the thickness of the layers decrease.

The results of the analysis show an increasing disorder in the local structure around the absorbing Cu in the layers when their thicknesses decrease. This is deduced from the values Debye-Waller factors for all the shells of the model for the different samples. This may be caused because the deposition method sputters almost atom by atom the material from the target, and cannot relax to the crystal structure when it condenses on the substrate at room temperature. Besides, the extremely low thickness of the layers prevent further reorganization of the atoms, as the lack of long range element purity in one dimension plus the possible interdiffusion of the Cr atoms are strongly distorting the crystal lattice. Similar results have been obtained for similar multilayers [56].

The results also show a slight compression of the lattice parameter of the model from the Cu metal bulk value. The thinner the layers are, the more compressed the lattice parameter is. This may be explained in two ways: The Cr-Cr distance is lower than the Cu-Cu distance in the respective bulk metals, so Cu-Cr distance in a metallic bonding should be lower than Cu-Cu distance. As the number of layers increase (higher N), the number of Cu atoms in contact with Cr atoms increase. Then, the number of Cr backscattering atoms per Cu atom increase, so the average distance of the backscattering atoms decrease. What is more, if the interfacial roughness is not neglected, so the interfaces show some interdiffusion, the Cu-Cr bonding has a higher probability of occurring than in a ideal smooth interface. At the same time, the crystal lattice of Cr may be distorting the Cu lattice [57].

A hint of a peak at approximately the Cu-O distance can be seen in the

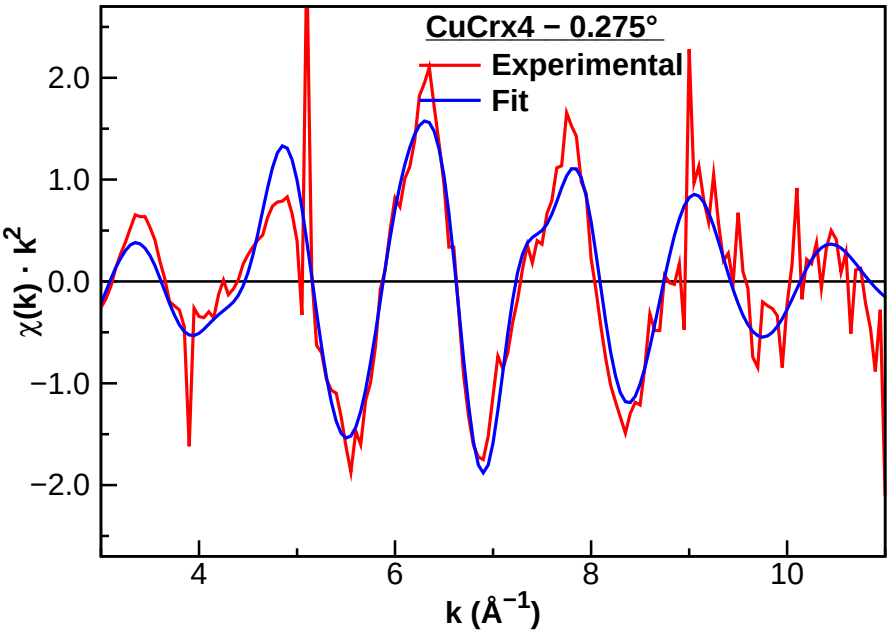

Figure 5.30: EXAFS experimental χ(k) and best fit for sample CuCrx4

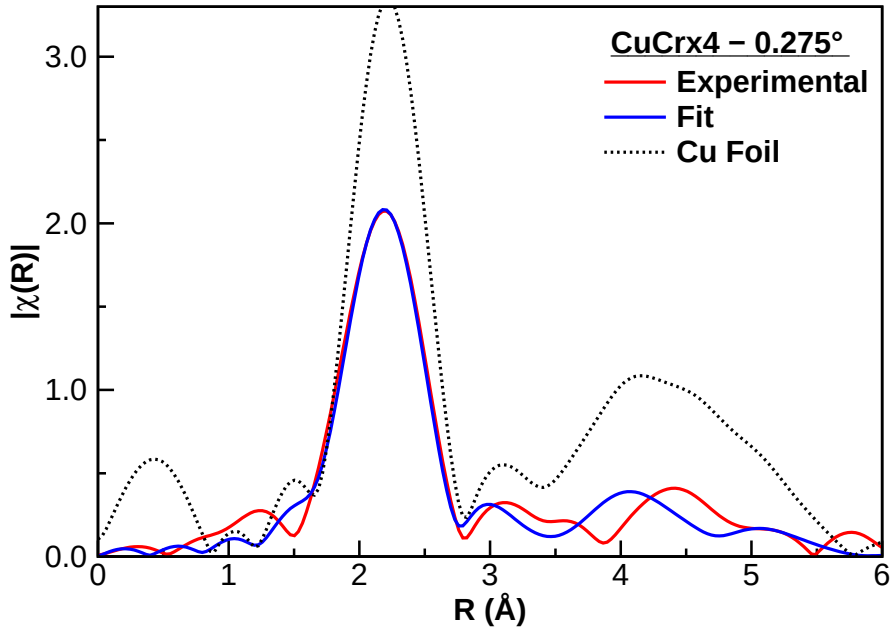

Figure 5.31: EXAFS experimental χ(R) and best fit for sample CuCrx4

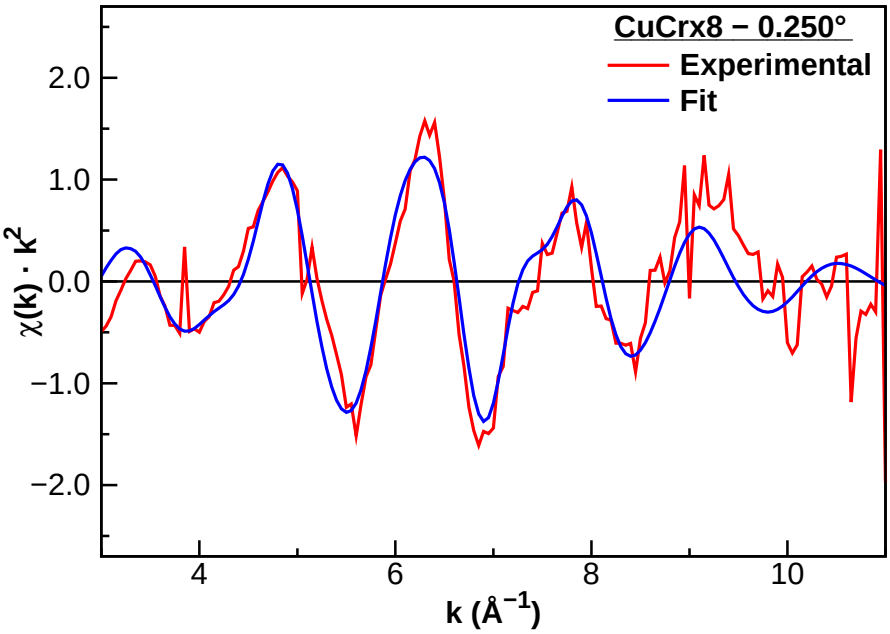

Figure 5.32: EXAFS experimental χ(k) and best fit for sample CuCrx8

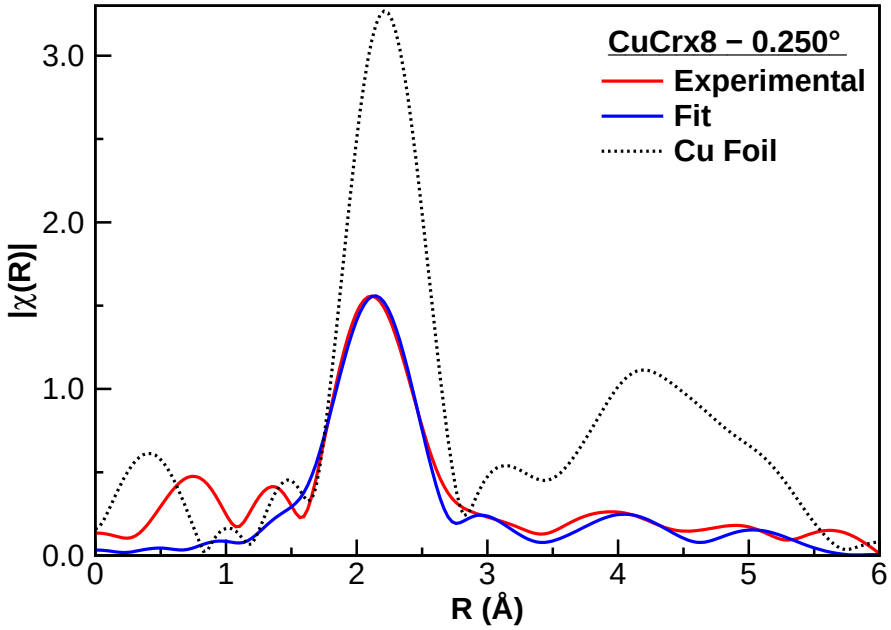

Figure 5.33: EXAFS experimental χ(R) and best fit for sample CuCrx8

Fourier Transform spectra for N = 4 and 8 samples, although not resolved enough to be analyzable. This suggests a second explanation for the lattice parameter compression that involves the oxidation of the Cu layers. If the Cr protective layer is not thick enough to protect the first Cu layer, oxygen can penetrate and oxidise it. This oxidation may be almost negligible and remain unnoticed in an EXAFS spectrum, not showing a Cu-O well resolved first shell peak. However, there could be enough Cu oxide to distort the first Cu-Cu (or Cu-Cr) peak, moving it to lower R values, and interfering with it so the amplitude might be lower.

This phenomenon can also explain the higher surface roughness of sample CuCrx8 measured by AFM. The first Cu layer can be non-uniformly oxidised due to the local variation of thicknesses that can occur in the first Cr layer. Then, the Cu oxide grows preferentially in some spots, so the average surface roughness consequently rises. These spots can be seen in fact in the AFM topography image in Figure 5.17.

5.3.2 Global analysis

5.3.2.1 Free atom reflectivity simulation and fit

Background simulation was performed with the dedicated developed program described in Chapter 4

The common variables of the fit were the same as those of the XRR spectra simulation, i.e. the thicknesses and densities of the layers and the roughnesses of the interfaces, linked in a similar manner to that described above: the thicknesses and densities of the same type of layer (Cr or Cu) are forced to be the same, as the growing conditions are the same; the roughnesses of the Cr/Cu and Cu/Cr interfaces are also the same, leaving both the substrate (Si/Cu) and the surface (Cr/air) roughnesses independent. The composition of the layers are fixed to pure Cr or Cu.

Each spectrum has also its own variables: the incidence angle, the scale

factor, and the shift in the energy values. These variables can be linked as well. In fact, the energy shifts for these spectra were forced to be the same, because the measuring conditions do not change among them.

The normalised experimental ReflEXAFS spectra for all the samples together with the corresponding best fit are shown in Figures 5.34 to 5.37. The parameters resulting from the best fit are summarised in Tables 5.5 (sample parameters), 5.6 (angles) and 5.7 (shift in energy of the spectra).

Table 5.5: ReflEXAFS free atom reflectivity fit results (Sample)

Sample	**Thickness (Å)**		**Relative Density**		**Roughness (Å)**		
	Cu	Cr	Cu	Cr	Sub.	Intf.	Sur.
CuCrx2	50	32	1.00	0.90	18	17	10
CuCrx3	24	36	0.98	0.88	15	20	13
CuCrx4	27	17	0.99	0.97	14	21	18
CuCrx8	18	10	0.98	1.00	20	17	14

The figures show the fit for all the angles except for those lower angles discarded previously due to the low signal to noise ratio.

In most of the spectra, it can be seen that the fit is better after the absorption edge that before it. This is caused by the polynomial refinement described in Chapter 4, that is anyway so small that does not give any significant additional error to the analysis. For the same reason, a step just after the edge in the fitting curve may be seen in some of the spectra, which marks the lower limit of the polynomial refinement.

The variables that measure the sample layers thicknesses, densities and roughnesses best fit roughly agree with the results coming from RBS measurements. The main difference lies on the decreasing Cr layers density with increasing thickness of this layer, what RBS cannot distinguish.

This can be explained by the increasing porosity of layers coming from sput-

Table 5.6: ReflEXAFS free atom reflectivity fit results (Angles)

CuCrx2		**CuCrx3**		**CuCrx4**		**CuCrx8**	
Angle	**Fit**	**Angle**	**Fit**	**Angle**	**Fit**	**Angle**	**Fit**
0.250	0.254	**0.300**	0.286	**0.250**	0.284	**0.250**	0.225
0.300	0.302	**0.320**	0.290	**0.275**	0.304	**0.300**	0.263
0.333	0.331	**0.338**	0.317	**0.300**	0.326	**0.350**	0.309
0.350	0.347	**0.350**	0.343	**0.325**	0.354	**0.375**	0.332
0.363	0.358	**0.363**	0.351	**0.338**	0.370	**0.400**	0.355
0.383	0.376	**0.383**	0.369	**0.350**	0.378		
0.400	0.395	**0.400**	0.380	**0.363**	0.396		
0.450	0.458	**0.425**	0.414	**0.375**	0.405		
				0.383	0.413		
				0.400	0.430		

Table 5.7: Shift in energy of the spectra

Sample	**ΔE (eV)**
CuCrx2	−2.8
CuCrx3	−2.5
CuCrx4	−3.1
CuCrx8	−3.1

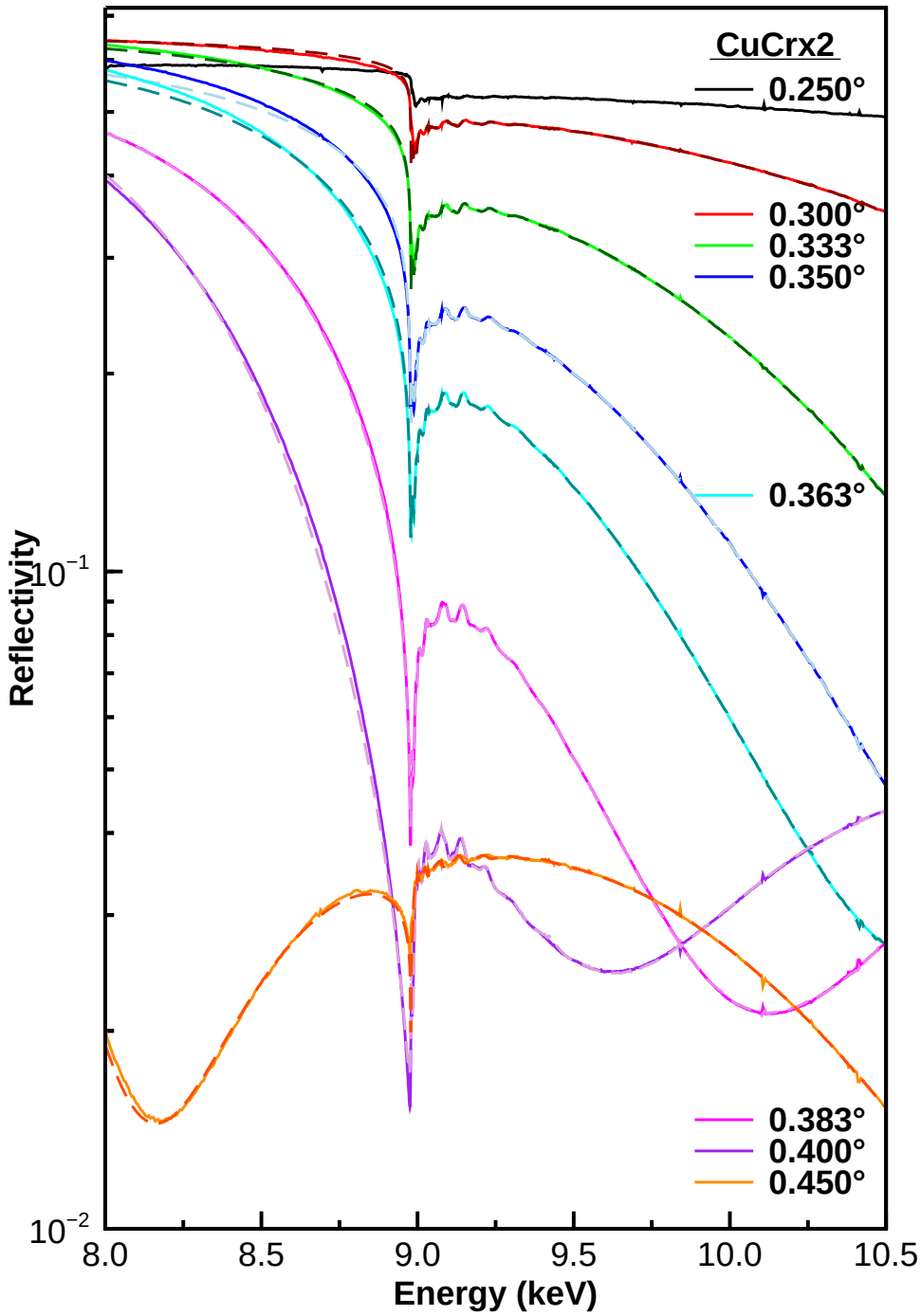

Figure 5.34: ReflEXAFS experimental spectra (solid) and best background fit (dashed) for sample CuCrx2

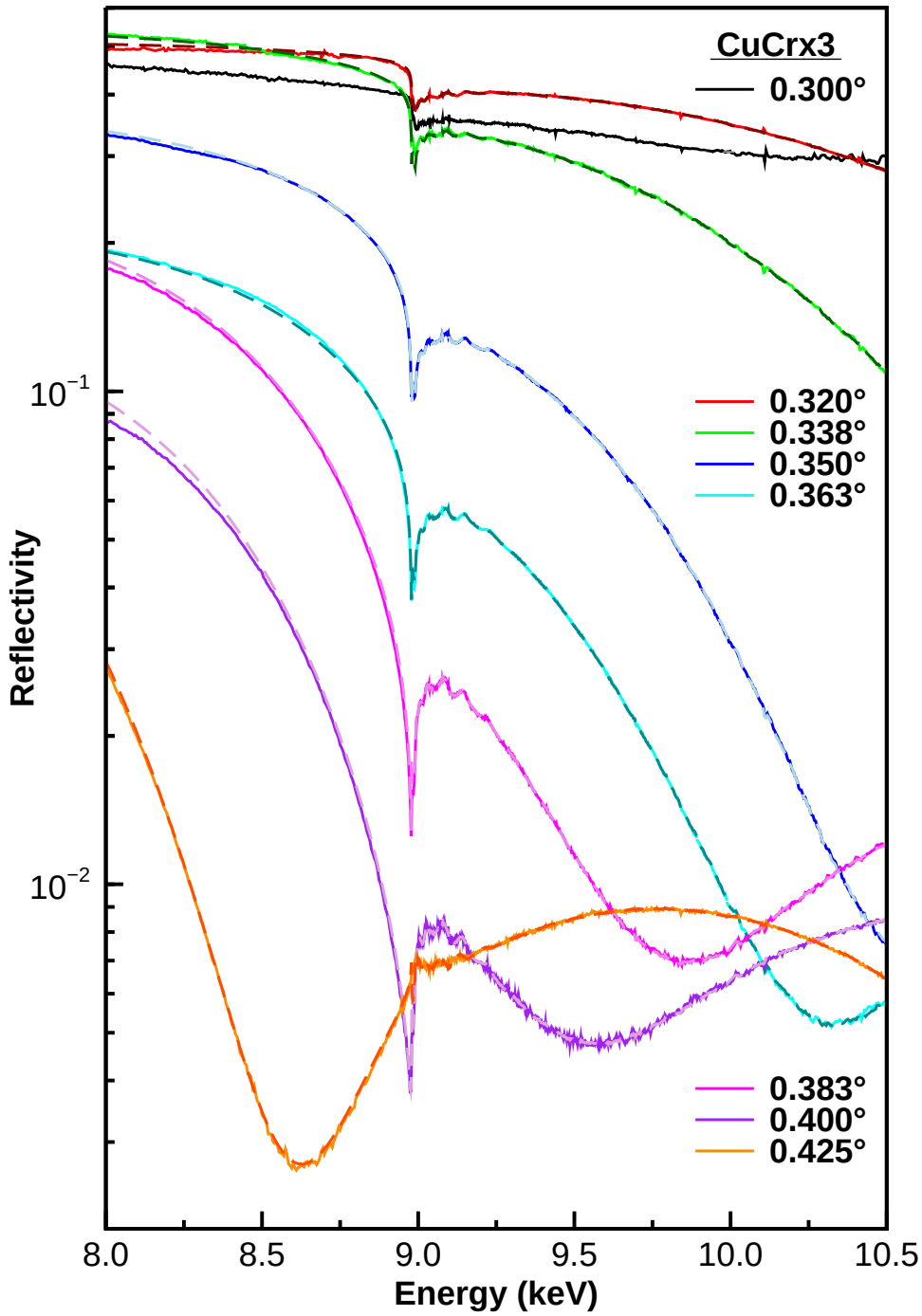

Figure 5.35: ReflEXAFS experimental spectra (solid) and best background fit (dashed) for sample CuCrx3

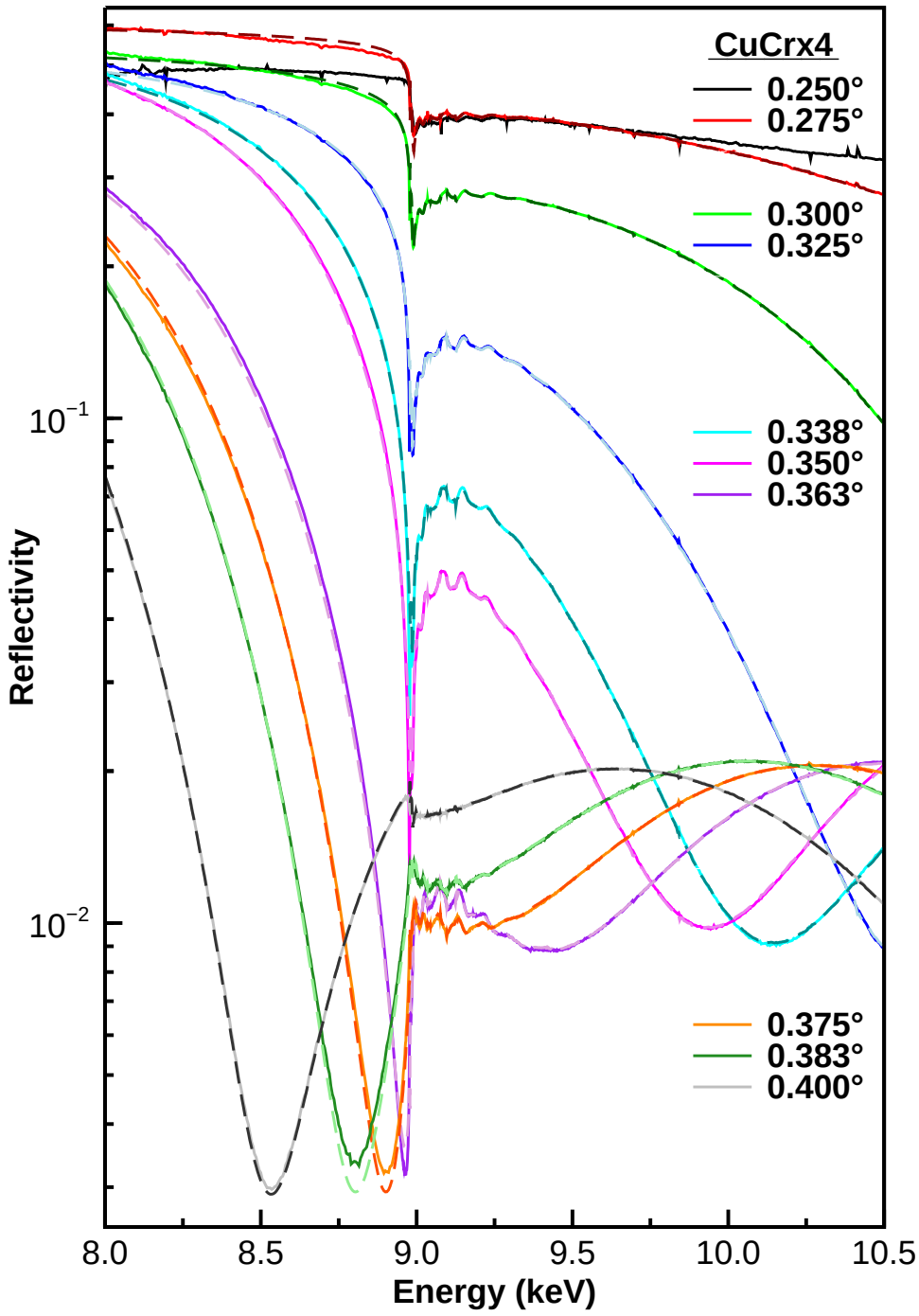

Figure 5.36: ReflEXAFS experimental spectra (solid) and best background fit (dashed) for sample CuCrx4

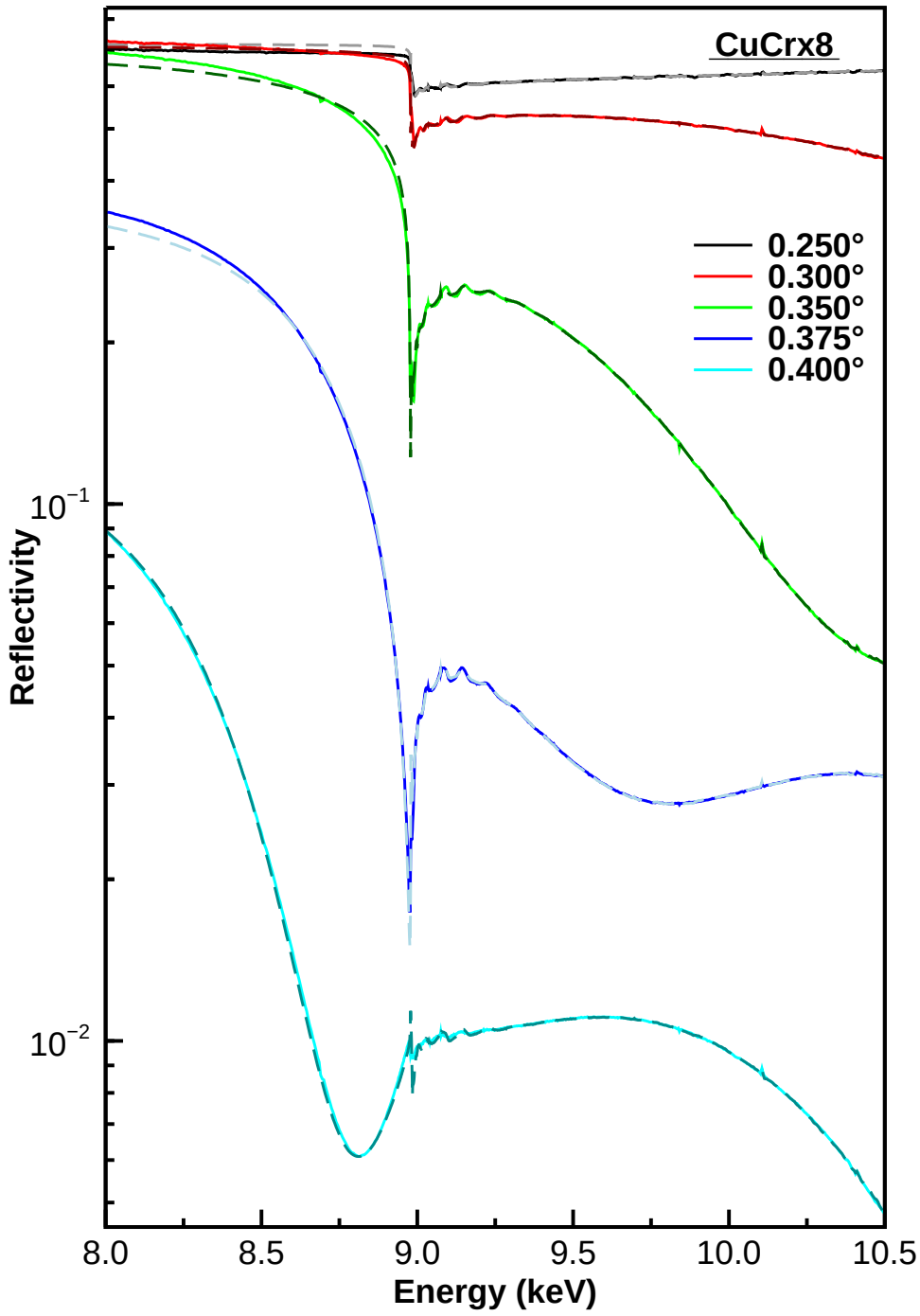

Figure 5.37: ReflEXAFS experimental spectra (solid) and best background fit (dashed) for sample CuCrx8

tering. As the growth of these materials is not layer by layer, but rather an island-type one, the first islands may cast shadows to the forthcoming atoms. This would make the layer rather porous, with increasing porosity for the first stages of the growth, but tending towards a constant value [58]. The reason for the Cu layers not following this tendency may be a different sticking coefficient that allows a better mobility of the atoms at the surface after the deposition [59].

Roughnesses are quite high respect to the layers thicknesses. Unfortunately, these roughnesses cannot be directly related to the RMS roughness values calculated from the AFM measurements due to the fractal behaviour of this phenomenon. In fact, the roughness increase due to the columns that appear on the CuCrx8 sample surface is unnoticed. Furthermore, various other effects of beam loss may be modifying these values, such as non perfect planarity of the sample, or beam angular dispersion.

However, these roughnesses results allows a relative evaluation of the different layers. For instance, both the substrate and the surface seem to be slightly smoother than the interfaces. The initial smooth monocrystalline surface of the Si can explain the former effect, while the possible reorganization of the Cr atoms due to surface oxidation could explain the latter one.

The angles values obtained in the fits show a certain consistency. Although the fitted values are not the same as the measured *th1* for most of the samples, they all remain consistently lower of higher than the expected, what can be explained by a possible misalignment of *ry* angle. This would cause an equal shift in the experimental incidence angles for all the spectrum, but different for each sample, as the alignment procedure was done for each one independently.

Finally, the energy shift values are almost the same for all the samples, what denotes that this parameter effectively does not depend on the sample but on the measurement conditions, most probably the monochromator calibration.

5.3.2.2 Global EXAFS analysis

The local environment of the Cu atoms in each of these samples must be the same, as the growing conditions of all the different layers were identical. Then, the EXAFS function was set to be the same for all the Cu layers of each sample.

This function thus obtained was simulated and fit using a Cu metal model with variable lattice parameter and Debye Waller factors, in the same fashion as described above for the total reflection approximation analysis (Section 5.3.1)

The best fit results are summarised in Table 5.8. Figures 5.38, 5.40, 5.42 and 5.44 show the extracted experimental EXAFS data, $\chi(k)$, compared with the best fit function obtained with the model, for all the samples. Figures 5.39, 5.41, 5.43 and 5.45 show the Fourier transform magnitudes of the EXAFS signals, $\chi(R)$, together with their respective best fits, with the corresponding total reflection angle experimental data, and with a Cu metal foil reference taken from the IXAS database [55].

Table 5.8: Global analysis EXAFS results for CuCrxN samples

Sample	**Shell**	**1st**	**2nd**	**3rd**	**4th**	**5th**	**a (Å)**
	N	12	6	24	12	24	**[Δa (Å)]**
CuCrx2	**R (Å)**	2.56	3.61	4.43	5.11	5.72	3.61
	σ^2 **(Å^2)**	0.011	0.017	0.019	0.020	0.030	[+0.00]
CuCrx3	**R (Å)**	2.53	3.57	4.38	5.06	5.65	3.57
	σ^2 **(Å^2)**	0.011	0.015	0.023	0.023	0.024	[-0.04]
CuCrx4	**R (Å)**	2.53	3.58	4.39	5.07	5.67	3.58
	σ^2 **(Å^2)**	0.013	0.017	0.023	0.024	0.027	[-0.03]
CuCrx8	**R (Å)**	2.55	3.60	4.42	5.09	5.70	3.60
	σ^2 **(Å^2)**	0.008	0.019	0.021	0.021	0.022	[-0.01]

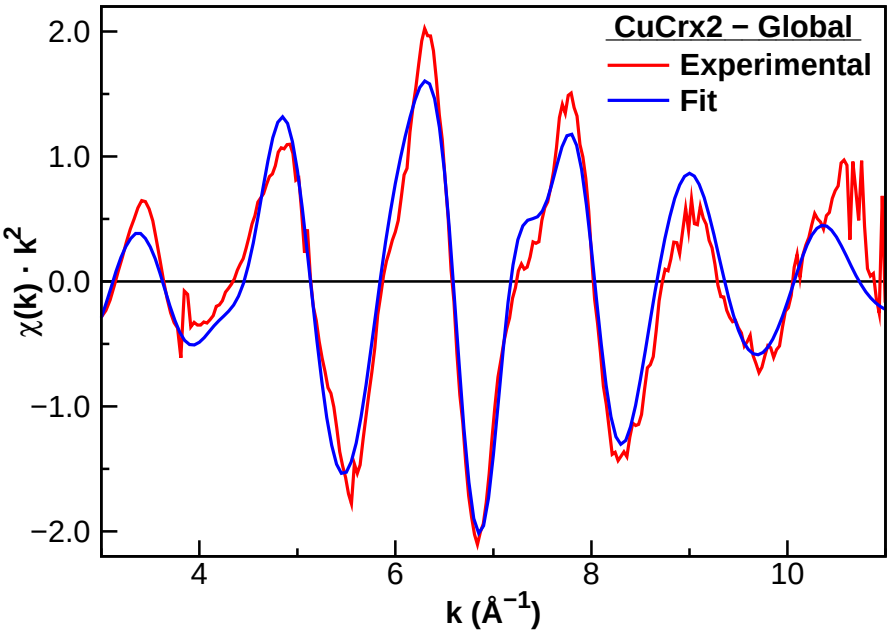

Figure 5.38: EXAFS experimental χ(k) and best fit for sample CuCrx2

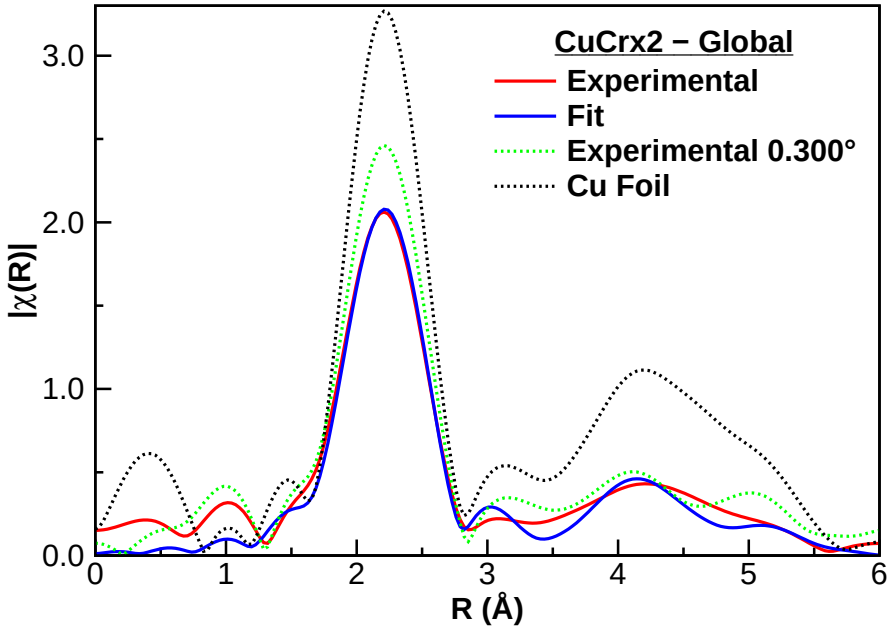

Figure 5.39: EXAFS experimental χ(R) and best fit for sample CuCrx2

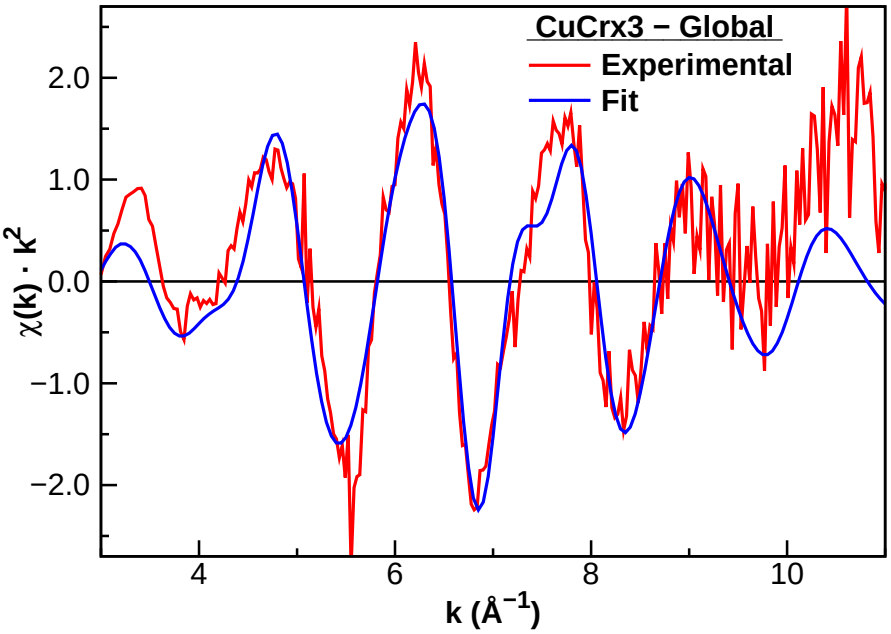

Figure 5.40: EXAFS experimental χ(k) and best fit for sample CuCrx3

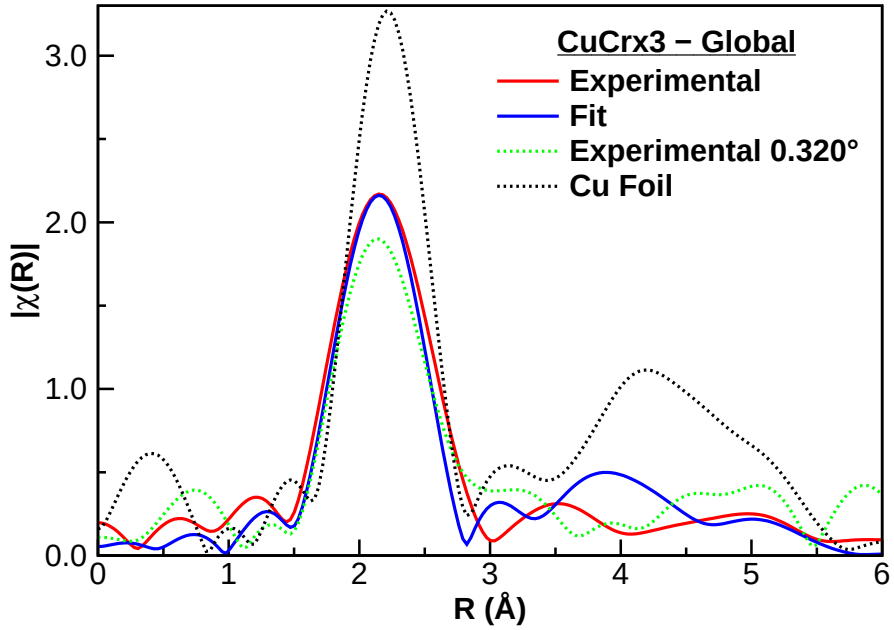

Figure 5.41: EXAFS experimental χ(R) and best fit for sample CuCrx3

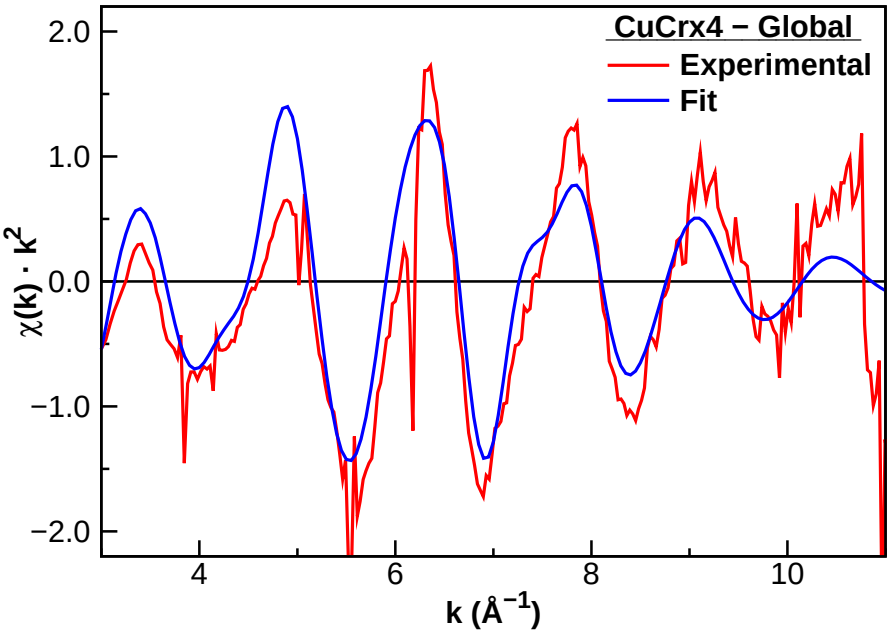

Figure 5.42: EXAFS experimental χ(k) and best fit for sample CuCrx4

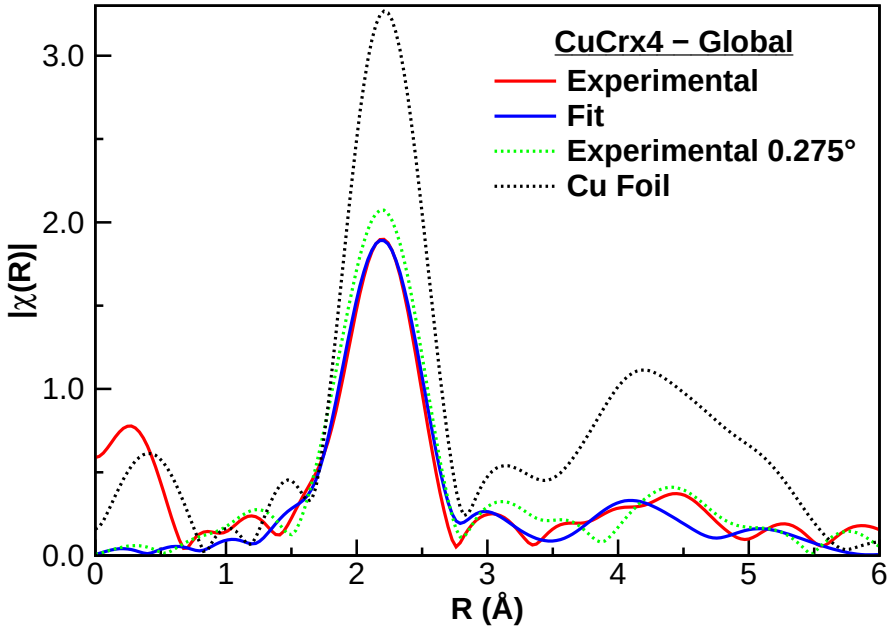

Figure 5.43: EXAFS experimental χ(R) and best fit for sample CuCrx4

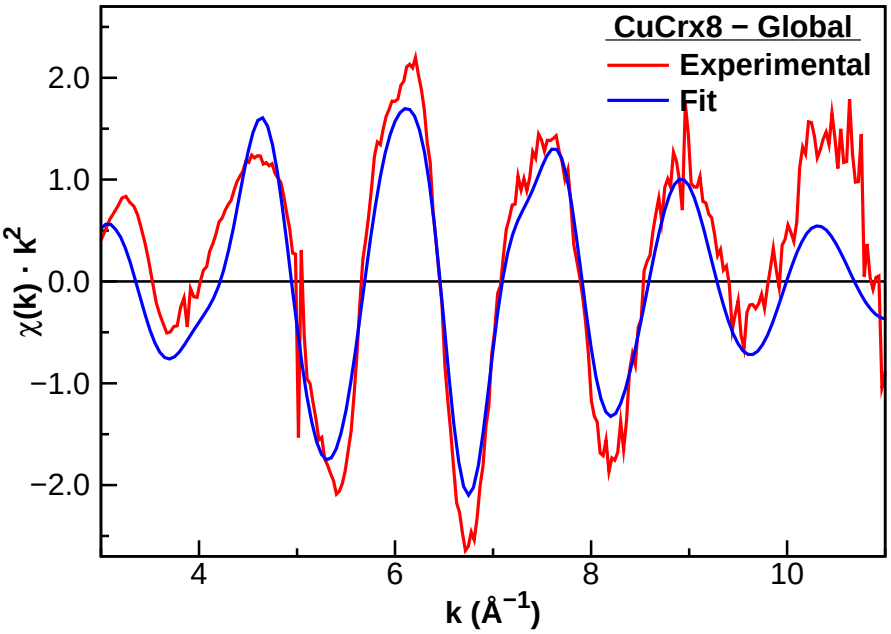

Figure 5.44: EXAFS experimental χ(k) and best fit for sample CuCrx8

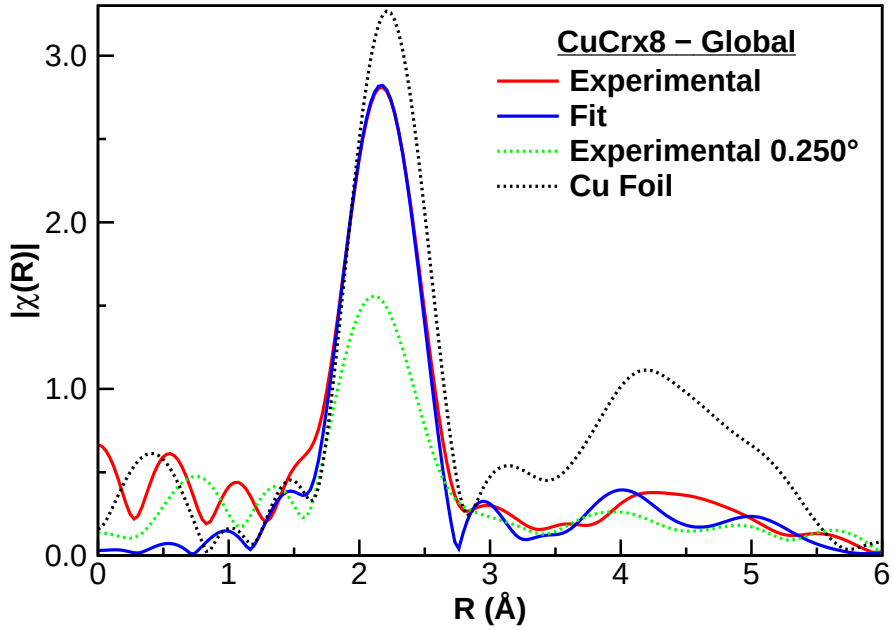

Figure 5.45: EXAFS experimental χ(R) and best fit for sample CuCrx8

The low angle and global analysis seem to give roughly the same results within the accuracy of the technique. CuCrx8 is an exception to this, so the big difference between the low angle approximation and the global spectrum has to be caused by the nature of the sample itself.

It has been suggested with the aid of the low angle analysis and the AFM images, that the topmost Cu layer of the CuCrx8 sample may have undergone a partial oxidation due to the extremely low thickness of the Cr protective layer. This oxidation would give a new local environment of CuO_x, that would result in a new EXAFS function added to the Cu metal environment one.

The addition of a new function in a low proportion can reduce drastically the intensity of the EXAFS signal if the phases interfere destructively. This may be the case of the CuCrx8 sample low angle analysis results, where this interference had to be simulated with an abnormally high Debye-Waller factor.

However, when the whole sample is probed at the global analysis, the proportion of CuO_x decreases so much that it remains unnoticed. This also explains why the lattice parameter at the global analysis is much closer to the Cu metal value.

Chapter 6

Copper oxide multilayers

Contents

Introduction

One of the capabilities of the extension of the ReflEXAFS technique described in this work is to distinguish between different local environments at different depths in the sample. To empirically demonstrate this, a particular set of samples was prepared.

As described in Chapter 2, a sample was prepared consisting of a CrCux3 multilayer, so the top layer is made of Cu. This would allow the oxidation of this layer naturally just exposing the sample to open air. Thus, the sample will have two different EXAFS environments (Cu oxide and Cu metal) that, what is more important, are at different depths and can be easily distinguished due to the Cr layer between them.

However, although the top Cu layer was thin enough to be oxidised completely, the possibility of having a partial oxidation thus a top layer split in two (Cu metal / Cu oxide) has to be considered and will be investigated in terms of growth of the oxide and diffusion of the oxygen into the layer.

Furthermore, this will allow the study of the surface oxidation process from the structural point of view without the aid of XRD, that is difficult to use in these very thin layers due to the lack of long range order in at least one of the space directions. In fact, not only the structure may be deduced, but also the reorganisation process due to the oxidation reaction may be shown by the EXAFS disorder quantification with the Debye-Waller factors.

6.1 Characterisation results

6.1.1 X Ray Reflectometry

As explained in Section 2.2.2, X Ray Reflectometry measurements were recorded at the synchrotron radiation beamline BM29. All these diagrams were simulated and fit using the program *GenX* [26] to obtain the layers

characteristics of the samples.

The model used for the simulation is a multilayered model as seen in Figure 2.6, where the layers are made of metallic Cu or Cr except for the top layer, that is made of CuO (copper oxide (II)). This choice was made because Cu_2O (copper oxide (I)) is less stable at standard conditions.

Similarly to the previous samples, the variables of the XRR simulations were the interface roughnesses and the thicknesses and relative densities (to the bulk crystalline density of each material) of the layers. Crystal densities are ρ_{Cu}=0.0847 at/Å^3, ρ_{Cr}=0.0833 at/Å^3 and ρ_{CuO}=0.0956 at/Å^3.

Again, to reduce the number of free parameters, the thicknesses and densities of the same type of layer (Cu or Cr) were linked, as they were grown in the same conditions. In this case, these links can only be applied to the three Cr and two Cu layers closest to the substrate, so the top CuO layer has its own thickness and density. The interface (both Cr/Cu or Cu/Cr) roughnesses were also linked, while the top surface, the Cr/CuO interface and the substrate roughness are all independent variables.

However, this model did not work well and a good fit was not possible. Thus, a model where the top Cu layer had undergone a partial oxidation, so it is split in two different environments (Cu metal / CuO) was set. Thus, the thickness and density of the un-oxidised top Cu layer was added to the variables explained above, along with a new roughness of the Cu/CuO interface. This way, the roughness of the interface shows the interdiffusion between both species.

Furthermore, as the growing conditions are the same, the total amount of Cu atoms in each layer should be the same, so the top CuO and top un-oxidised Cu atoms together add up the same amount as the rest of the Cu layers. Thus, this further restriction can be set at the XRR simulation.

The experimental and best simulated fit XRR diagrams are shown in Figures 6.1 and 6.2. The results of the fitting are summarised in Table 6.1

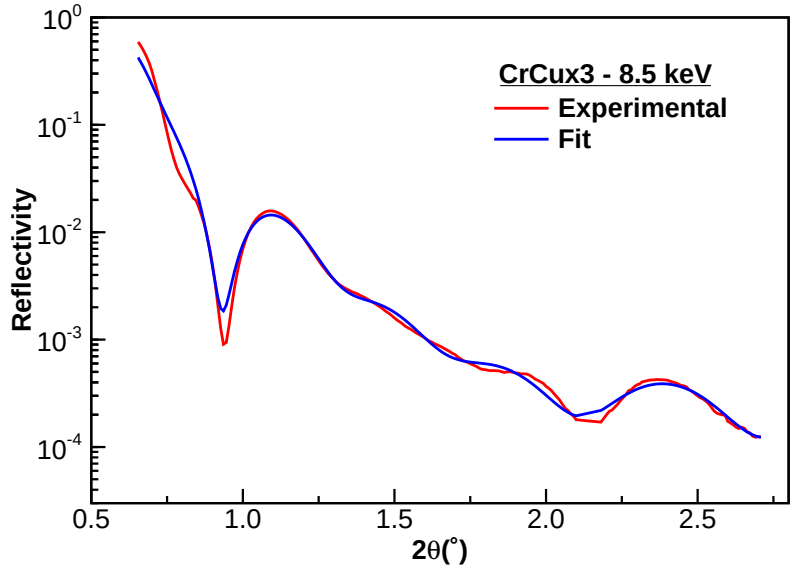

Figure 6.1: XRR at 8.5 keV experimental diagram and best fit for sample CrCux3

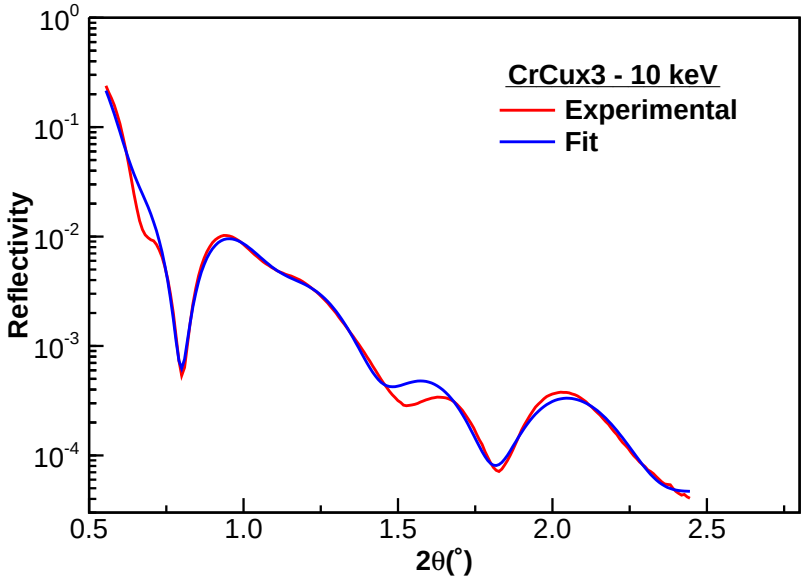

Figure 6.2: XRR at 10 keV experimental diagram and best fit for sample CrCux3

Table 6.1: XRR simulation results for sample CuCrx3

Energy	Thickness (Å)				Relative Density			
	Cr	Cu	Top Cu	Top CuO	Cr	Cu	Top Cu	Top CuO
8.5 keV	16	38	30	47	0.98	0.97	0.61	0.66
10 keV	17	37	30	50	0.91	0.99	0.66	0.64

Energy	Roughness (Å)			
	Sub.	Cr/ Cu	Cu/ CuO	Surf.
8.5 keV	3	7	3	19
10 keV	3	3	4	18

The XRR diagrams present a typical interference pattern of a layered system. Contrary to those of the previous samples in Chapter 5, these patterns are smoother, showing less defined peaks and valleys. This may be caused by the broken symmetry of the layers due to the surface oxidation.

Rather good fits were obtained for both energies, with fairly consistent values of thicknesses, densities and roughnesses. A detailed interpretation of these results will be presented in Section 6.3.2.1 together with the free atom simulation results.

6.1.2 Rutherford Backscattering Spectrometry

RBS measurements were carried out using the linear accelerator of the Centro Nacional de Aceleradores (Seville), and analysed as explained in Section 2.2.3.

RBS data give the amount of material per surface unit, so the thickness of a layer can be calculated by assuming a density of the layers. The density can

be assigned as the bulk density of the material, or as the density calculated from the XRR measurements.

These measurements are not sensitive to the chemical environment of the studied atoms, so they cannot distinguish between the top CuO layer and the rest Cu atoms. Using the proportion of un-oxidised Cu / CuO of the first layer from the mean value of the XRR simulations, the thickness of the top Cu / CuO layer can be calculated from the RBS measurements.

This cannot be applied to the calculation of the equivalent thickness using the bulk crystal density, as the Cu / CuO proportion of the first layer is unknown. Thus, this top layer will be presented as it was not oxidised, but taking into account that this is just a measurement of the amount of Cu atoms in each layer.

The thicknesses determined using both bulk density and the XRR calculated parameters are shown in Table 6.2.

Table 6.2: RBS results for sample CrCux3

Thickness (Å) (Crys. Dens.)		**Thickness (Å) (XRR Dens.)**			
Cr	Cu	Cr	Cu	Top Cu	Top CuO
13	36	14	37	29	47

The RBS thickness results are found to be in good agreement with the XRR ones. The measurements at different parts of the samples showed that they are homogeneous in all the length within the accuracy of the technique.

6.1.3 Atomic Force Microscopy

Sample surface topography image was taken with a Nanotec Dulcinea microscope, and the roughness was calculated as explained in Section 2.2.5.

Figure 6.3 shows the surface topography image of sample CuCrx3.

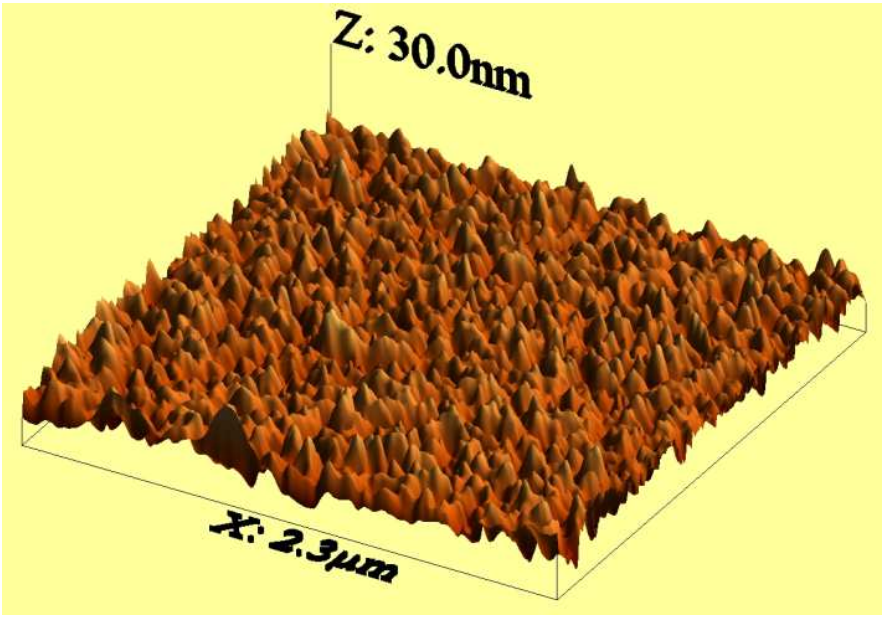

Figure 6.3: AFM surface topography for sample CrCux3

The roughness calculated from the RMS value is 23 Å.

The surface topography of this sample is quite homogeneous, from which it might be deduced that the surface oxidation process has occurred at all the surface homogeneously, in contrast with what happened in sample CuCrx8 from the previous set of samples (Chapter 5). The RMS roughness is higher than those calculated for the previous samples. This is due to the oxidation of the top layer, that may happen preferentially in some spots (like the grain boundaries) and then grow more efficiently from those first spots, as the surface is not a perfect crystalline plane.

6.2 ReflEXAFS experiments

6.2.1 Angle selection

XRR measurements were performed at 8.5 keV and 10 keV at the synchrotron radiation beamline in order to show the behaviour of the reflectivity at different angles. This aids the selection of the most convenient angles for the ReflEXAFS measurements.

Figure 6.4 shows the reflectivity patterns, which are marked with the angles chosen for the ReflEXAFS measurements. These angles were selected in order to have different penetration depths, so as to probe not only the upper surface regions of the sample, but also the deep Cu layers buried below.

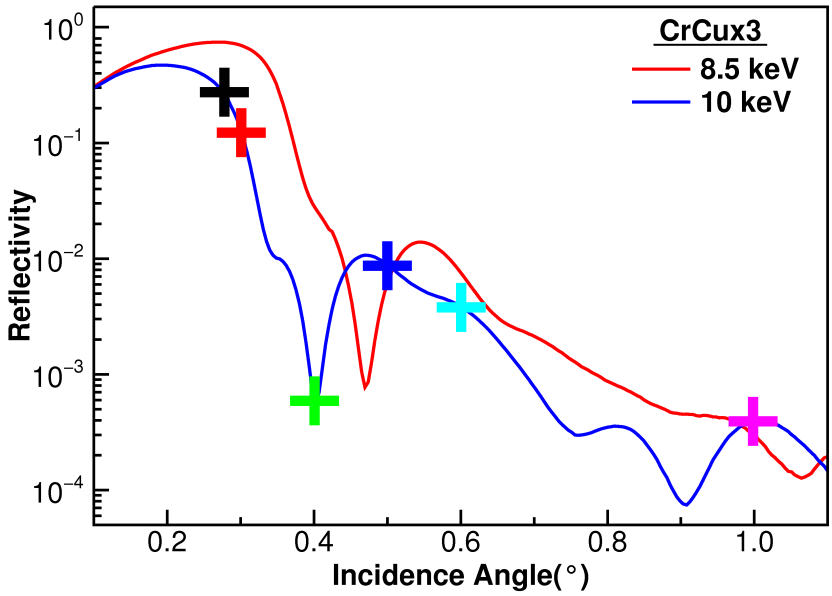

Figure 6.4: XRR experimental diagram showing ReflEXAFS chosen angles for sample CrCux3

6.2.2 ReflEXAFS scans

ReflEXAFS scans were performed as explained in Chapter 3 at the angles chosen with the aid of the XRR curve. After that, each spectrum was divided by the direct beam scan to remove the absorption component of the air between the detectors and get a normalised spectrum.

The set of normalised spectra for the sample is shown in Figure 6.5.

Both the background with the expected interference pattern due to the multilayers reflection and the EXAFS-like fine structure can be seen in all the spectra. The background pattern changes as the angle change and decreases its overall intensity for higher incidence angles in general, due to the loss of the total reflection condition and the increase of the transmission coefficient. However, for some angles, the reflectivity does increase again, following the XRR pattern as shown in Figure 6.4. This allows the possibility of having spectra measured at high angles, thus with a high penetration depth, but with a relatively high reflected intensity, thus with a good signal to noise ratio.

Superimposed to the background, it can clearly be seen the absorption edge at the Cu-K absorption edge energy (8.979 keV), along with an EXAFS-like pattern just after it. This pattern is better resolved at intermediate angles as the the lowest angle spectrum interacts very little with the Cu absorbing atoms and the highest angle spectrum has a worse signal-to-noise ratio due to the low reflection intensity at that angle.

It can also be seen that the fine structure of the lowest angle spectrum is significantly different from the rest of the spectra. This is because this spectrum is the only one in the total reflection regime, so it only probes the first tens of Ångströms. Then, the highest contribution to the EXAFS fine structure should be from the Cu oxide environment, while for the rest of the spectra, the Cu metal environment is predominant.

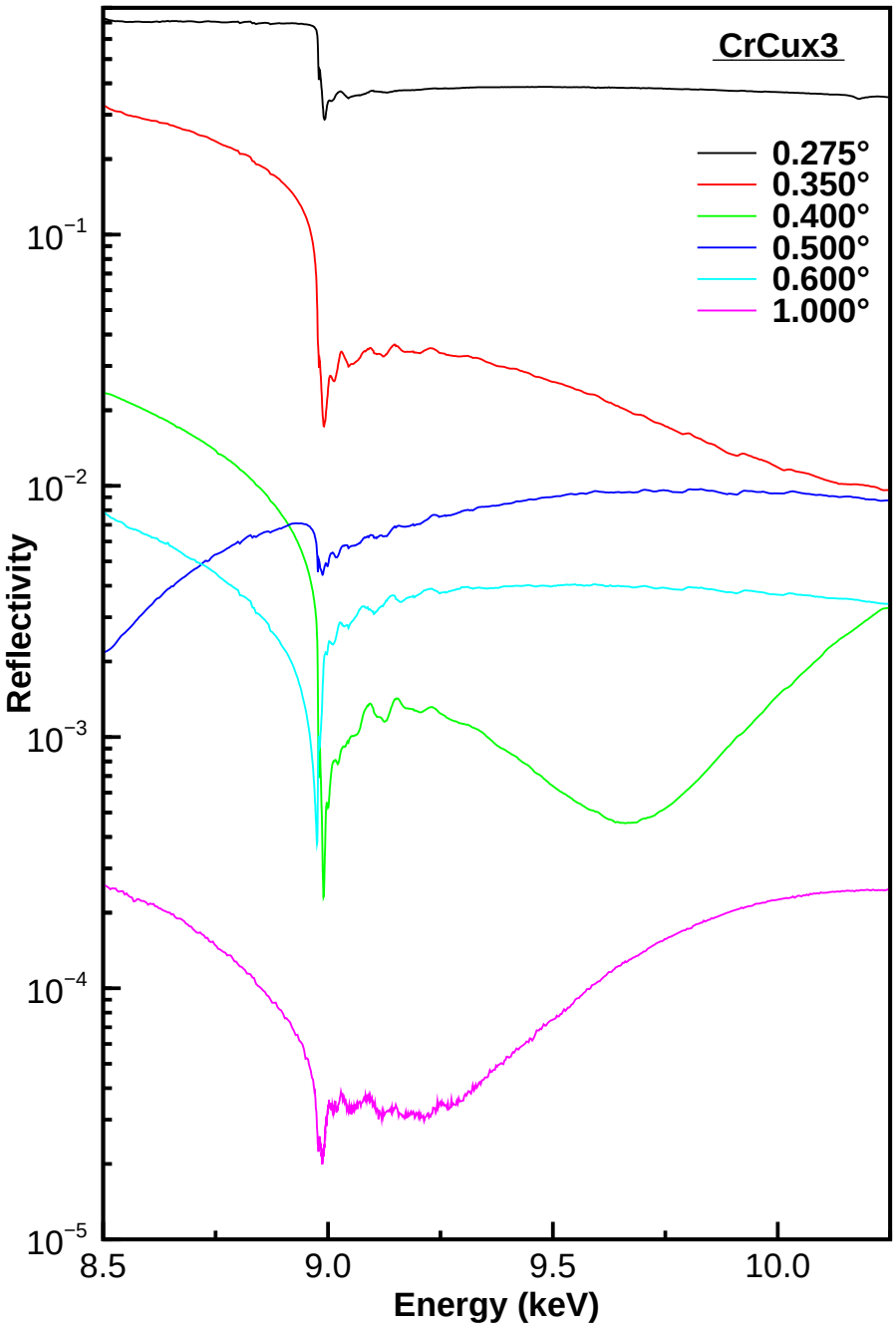

Figure 6.5: Normalised ReflEXAFS spectra for sample CrCux3

6.3 Analysis

For this sample, the ReflEXAFS spectra was analysed by both the total reflection approximation (Section 4.2.1) for the spectrum of the lowest angle recorded, and by the developed global analysis (Section 4.3).

6.3.1 Total reflection approximation analysis

Using Martens [18] approximation, the EXAFS signal may be extracted directly from a spectrum of incidence angle below the critical angle. The critical angle of a CuO surface of a relative density of 0.65, which is the average of the XRR results, is approximately 0.237° for an incident beam of 9.2 keV (just above the Cu-K absorption edge). Unfortunately, the spectrum of the lowest angle was registered at 0.275°, so it does not fulfill the total reflection condition.

The analysis of this spectrum would firstly cause the signal to be wrongly normalised, as the absorption step is no longer proportional to the imaginary part of the refractive index, $\beta(E)$, and have a term in $\delta(E)$ that cannot be neglected. Furthermore, the fine structure is a mixture of the $\Delta\delta(E)$ and $\Delta\beta(E)$ as explained in Section 4.2.1.

The Kramers-Kronig transform does not change the frequencies of the functions it transforms. Then, the $\Delta\delta(E)$ component of this mixed spectrum will have the same frequencies as $\Delta\beta(E)$ and thus the EXAFS signal [47]. This makes the Fourier transform magnitude peak positions and relative amplitude to be the same of those of the EXAFS signal, although nothing can be said about the phase and the overall amplitude. Thus, the spectrum is not valid to be simulated, but at least the Fourier transform magnitude can give a *qualitative* idea of what is present at the surface of the sample.

Figure 6.6 shows a comparative plot of the Fourier transform magnitude, $|\chi(R)|$, of the extracted spectrum recorded at 0.275°, together with a Cu

metal foil, a CuO and a Cu_2O references taken from the IXAS database [55] for comparison. These references have been scaled down to better compare the plots.

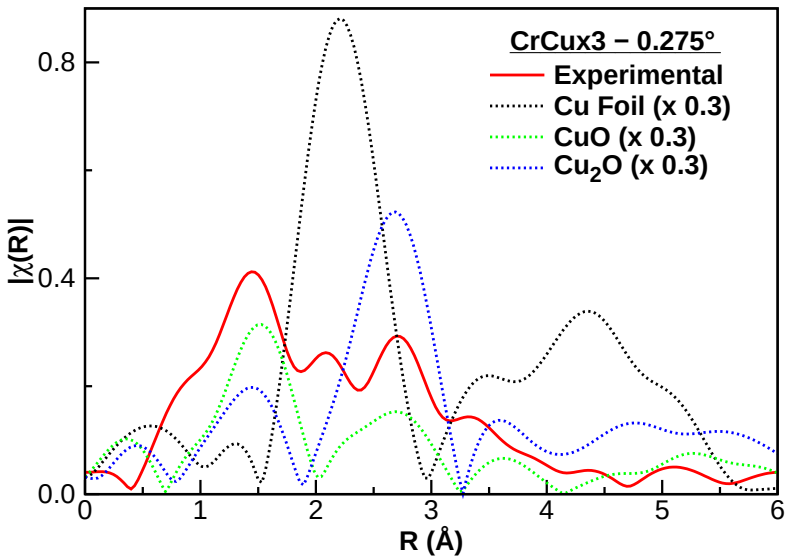

Figure 6.6: EXAFS experimental χ(R) for sample CrCux3 and Cu meta, CuO

The Fourier transform magnitude of the spectrum with the lowest incidence angle seems to be quite similar to the CuO reference, which is consistent with the XRR calculations. However, an intermediate peak at approximately 2 Å suggests that some Cu metal environment should be added to the spectrum. This is also consistent with the fact that the penetration depth of the beam at this incidence angle just above the critical angle is high enough to probe the un-oxidised part of the first layer and even some of the next Cu layer.

In principle, the spectrum seems to lack of a Cu_2O environment, but this cannot be assured until a complete analysis of the ReflEXAFS spectra is made.

6.3.2 Global analysis

6.3.2.1 Free atom reflectivity simulation and fit

Background simulation was performed with the dedicated developed program described in Chapter 4.

The common variables of the fit were the same as those of the XRR spectra simulation, i.e. the thicknesses and densities of the layers and the roughnesses of the interfaces, linked in a similar manner to that described in Section 6.1.1. Each spectrum has also its own variables, which are: (1) the incidence angle; (2) a scale factor that takes into account the possible part of the beam not impinging on the sample as well as the possible lack of flatness of it; and (3) a shift in the energy values, that takes into account a possible miscalibration of the monochromator.

Figure 6.7 show the normalised experimental ReflEXAFS spectra for all the samples together with the corresponding best fit spectra. Tables 6.3 and 6.4 summarise the best fit values calculated for the sample variables and the incidence angles of the spectra respectively. The shift in energy was +4.1 eV for these spectra.

Table 6.3: ReflEXAFS free atom reflectivity fit results for sample CuCrx3

Thickness (Å)				**Relative Density**				**Roughness (Å)**			
Cr	Cu	Top Cu	Top CuO	Cr	Cu	Top Cu	Top CuO	Sub.	Cr/ Cu	Cu/ CuO	Sur.
16	37	29	44	0.92	1.00	0.68	0.60	4	3	7	13

As shown in Figure 6.7, the spectra are better fitted after the absorption edge, what is a consequence of the polynomial fitting described in Section 4.3.1.1, which is made only after the absorption edge. For the same reason, a small step may be seen just after the edge, which is the starting point of

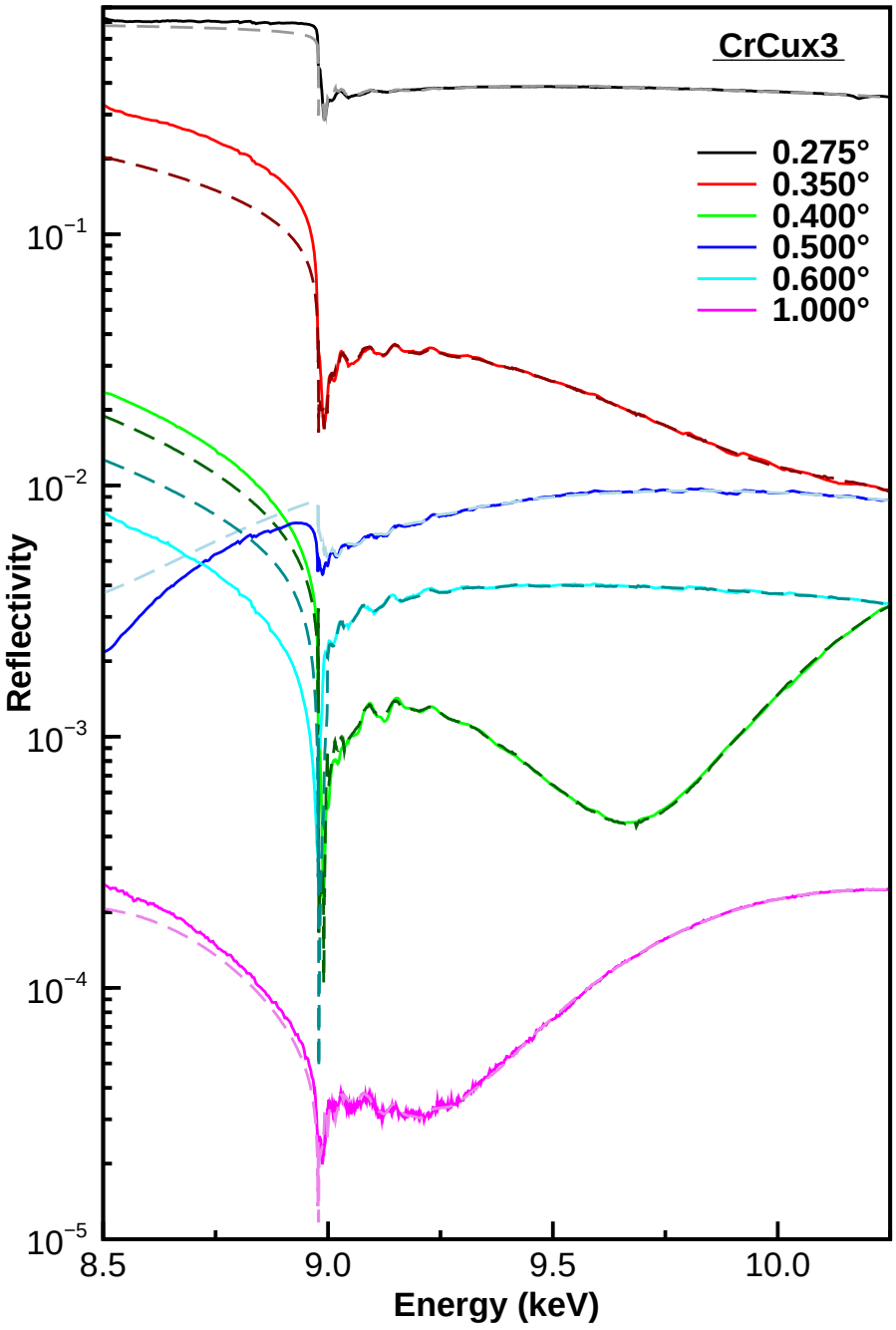

Figure 6.7: ReflEXAFS experimental spectra (solid) and best background fit (dashed) for sample CrCux3

Table 6.4: ReflEXAFS background simulation results

Angle	Fit
0.275	0.285
0.350	0.360
0.400	0.463
0.500	0.535
0.600	0.677
1.000	1.039

the polynomial refinement. This step is well below the EXAFS region, so it will not disturb the subsequent analysis.

The sample best fit parameters are consistent with the results of the XRR diagrams simulation and fit. Both show firstly an increase of the surface roughness compared with the interface roughnesses. This is consistent with the oxidation process that may happen preferentially in the grain boundaries, and then grow more efficiently from those first spots, which is confirmed by the AFM results.

Secondly, there is a slight reduction in density of the Cr layers compared with the crystalline value, also seen in the previous CuCrxN samples, as described in Section 5.3.2.1. This may be caused by an increasing porosity of Cr layers due to shadow effects during sputtering deposition.

Thirdly, a strong decrease of the density of the un-oxidised Cu region of the top layer compared to the rest of the Cu layers. This layer was grown in the same manner as the inner ones, so this difference must be caused by the subsequent oxidation process of this first layer with the oxygen from the air. The oxidation may be preferential in some places of the surface such as the grain boundaries. This may cause the later migration of Cu atoms to the initial oxide spots [60, 61], leaving the Cu metal layer with a high porosity.

Finally, the low density of the CuO top layer compared with the bulk value

is a consequence of the same process of preferential oxidation that increases the roughness, leaving a highly porous oxide layer with a low density.

6.3.2.2 Global EXAFS analysis

For this sample, a model with two different local environments was used. The top Cu oxide layer was set to have one EXAFS function, while the un-oxidised top Cu layer and the rest of the Cu layers below were constrained to have the same EXAFS but different from the previous one.

The EXAFS function extracted from the top Cu oxide layer had some low-R (below 1.2 Å) peaks in the Fourier transform magnitude function. These peaks do not have any physical meaning, so they must be a consequence of an inaccurate background subtraction, that had introduced some low frequency oscillations. A Fourier filtering of the signal was performed to remove these peaks. Unfortunately, the first real peak of a coordination shell was rather close to one of the low-R peaks, so a remaining of them was left unfiltered in order not to distort the real one.

This EXAFS function from the top Cu oxide layer was simulated by using a CuO structure model. This is a monoclinic structure that leads to a complex set of coordination shells and a high number of possible scattering paths. In principle, this fact seems to make difficult the use of this model. However, this amount of shells and scattering paths tend to interfere and finally compensate among themselves when the number of paths at similar distances is high. This happens at a relatively short scattering length for this structure, so eventually only the closest (below 3.5 Å) few coordination shells are relevant.

This model had the coordination numbers fixed to the crystal values. A single free parameter, which was set as the variation of the coordination distance from the crystal value of the first Cu-Cu coordination shell, was used to allow the variation of coordination distances proportionally in all the structure.

The shells were grouped according to their coordination distances, so a single

Debye-Waller factor was assigned to those shells that are relatively close to each other. All these factors were then allowed to vary independently.

The scattering paths used were just the single scattering paths. The amplitude reduction factor, S_0^2, was set to 0.81, which is a value within the range of values reported in the literature [52], that rarely varies for the same element at different chemical environments.

Unfortunately, after performing a first fitting attempt with this model, the fit unsatisfactory.

The examination of the shape of the experimental $|\chi(R)|$ magnitude showed that the region above the first coordination shell is slightly different from the usual CuO one. Then, the possibility of having a different local environment added to the CuO one was taken into account.

The oxidation process of a Cu surface is known to consider the formation of a metastable Cu oxide (I) phase, Cu_2O, which may dismute afterwards in metal Cu (0) and CuO [62]. The EXAFS spectrum of the Cu_2O phase includes a Cu-O first coordination shell at a similar distance as the CuO one, and a Cu-Cu second coordination shell that produces a peak of a high intensity at about 3 Åin the phase uncorrected $|\chi(R)|$ plot, as can be seen in Figure 6.6. Thus, if there were some remains of this phase in this top oxidised layer of the sample, it would mostly perturbs precisely this region.

This Cu_2O phase would probably be located mostly at the interface between the un-oxidised top Cu layer and the Cu oxide layer, as the process of the formation of the surface Cu oxide involves the first oxidation to Cu_2O and then, when the oxygen at the surface is unable to diffuse trough the Cu_2O layer, CuO appears.

Thus, the Cu_2O environment was added to the model, in the same fashion as the previous one, i.e. with coordination number fixed to the crystalline values, a single free parameter, Δa, that accounts for the variation of the first Cu-Cu coordination distance, and allows the coordination distances to have

a proportional variation within the structure, and an independent Debye-Waller factor for each single scattering path. The first four coordination shells of this model were considered.

Both environments were weighted by a linear factor that take into account the proportion of each in the spectrum. However, it must be noted that this factor cannot be directly related to the thickness ratio between the CuO layer and a possible Cu_2O layer, as both species might be highly intermixed.

Also, the energy shift of the Cu_2O environment was set as -2 eV from that of the CuO environment. This is to simulate the energy shift of the absorption edge due to the change on the oxidation state of the element.

The software used for the simulation and fit of these data was the UWXAFS software package [46, 53, 54].

The results of the fitting are summarised in Table 6.5. Figure 6.8 shows a comparative plot of the extracted experimental EXAFS data, $\chi(k)$, with the best fit obtained with the models described above. Figures 6.9 shows a comparative plot of the Fourier transform magnitude, $|\chi(R)|$, with its respective fit, and with a Cu foil reference taken from the IXAS database [55].

The EXAFS function obtained for the Cu metal layers was simulated and fit using a Cu metal model with variable lattice parameter and Debye Waller factors, in the same fashion as described for the simulation of the EXAFS signal of the CuCrxN samples, as described in Section 5.3.1.

The results of the fitting are summarised in Table 6.6. Figure 6.10 shows a comparative plot of the extracted experimental EXAFS data, $\chi(k)$, with the best fit obtained with the models described above. Figure 6.11 shows a comparative plot of the Fourier transform magnitude, $|\chi(R)|$, with its respective fits, and with a Cu foil reference taken from the IXAS database [55].

The fitting results show a noticeable difference of the lattice parameters of the Cu oxide environments compared to the bulk values. Specifically, both the CuO and Cu_2O environments show a high compression of the lattice.

Table 6.5: Global EXAFS results for top Cu oxide layer

CuO							
Proportion	86 %						
a [Δa] (Å)	2.80 [−0.10]						
Shell (Element)	**1 (O)**	**2 (O)**	**3.1 (Cu)**	**3.2 (Cu)**	**3.3 (Cu)**	**4.1 (O)**	**4.2 (Cu)**
N	4	2	4	4	2	2	2
R (Å)	1.89	2.69	2.80	2.98	3.06	3.29	3.30
σ^2 (Å^2)	0.005	0.006	0.007			0.008	

Cu_2O				
Proportion	14 %			
a [Δa] (Å)	2.99 [−0.12]			
Shell (Element)	**1 (O)**	**2 (Cu)**	**3 (O)**	**4 (Cu)**
N	2	12	6	6
R (Å)	1.78	2.99	3.40	4.10
σ^2 (Å^2)	0.005	0.007	0.008	0.010

Table 6.6: Global EXAFS results for Cu metal layers

Cu Metal					
a [Δa] (Å)	3.60 [−0.01 Å]				
Shell	**1**	**2**	**3**	**4**	**5**
N	12	6	24	12	24
R (Å)	2.55	3.60	4.41	5.10	5.70
σ^2 (Å^2)	0.012	0.016	0.018	0.019	0.025

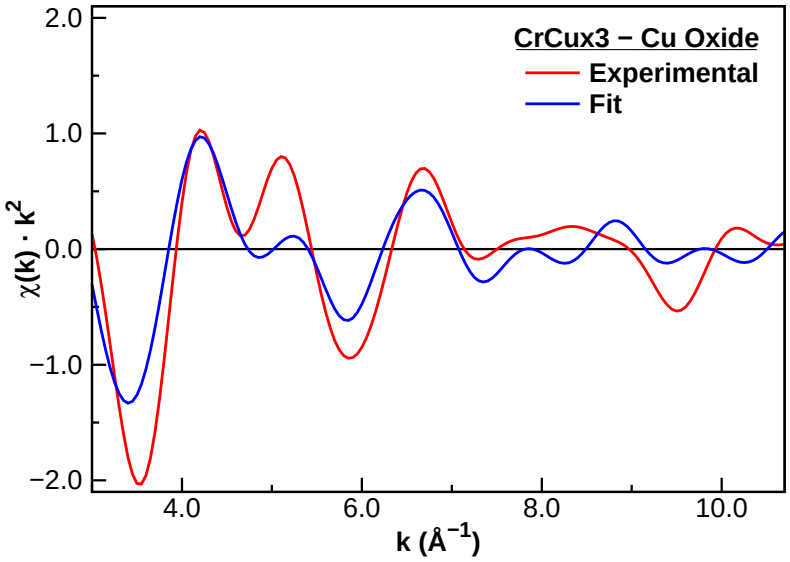

Figure 6.8: EXAFS experimental χ(k) and best fit for Cu oxide layer

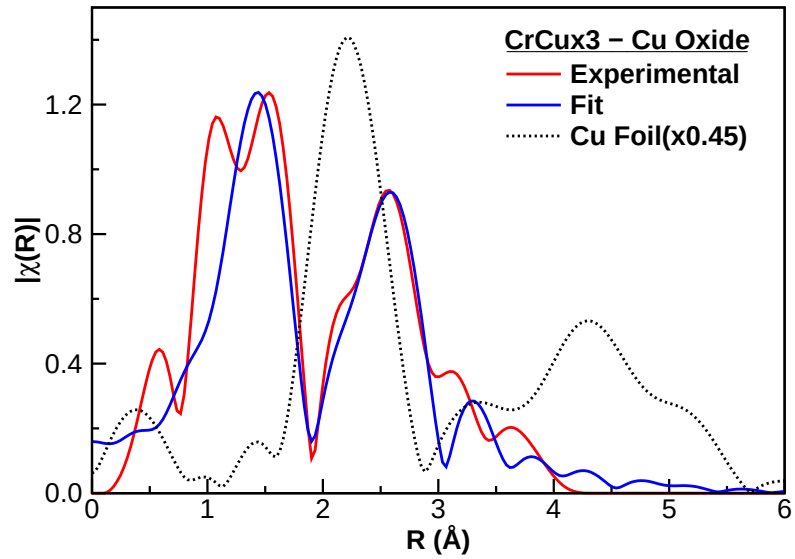

Figure 6.9: EXAFS experimental χ(R) and best fit for Cu oxide layer

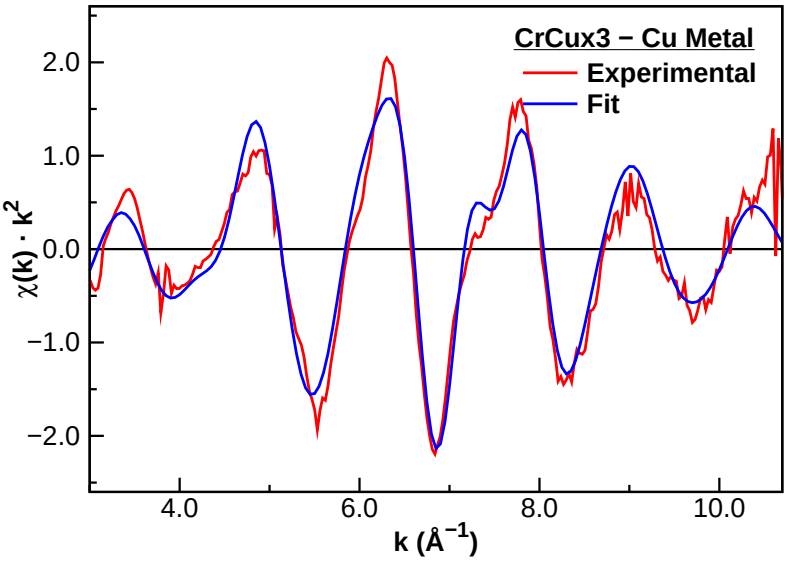

Figure 6.10: EXAFS experimental χ(k) and best fit for Cu metal layers

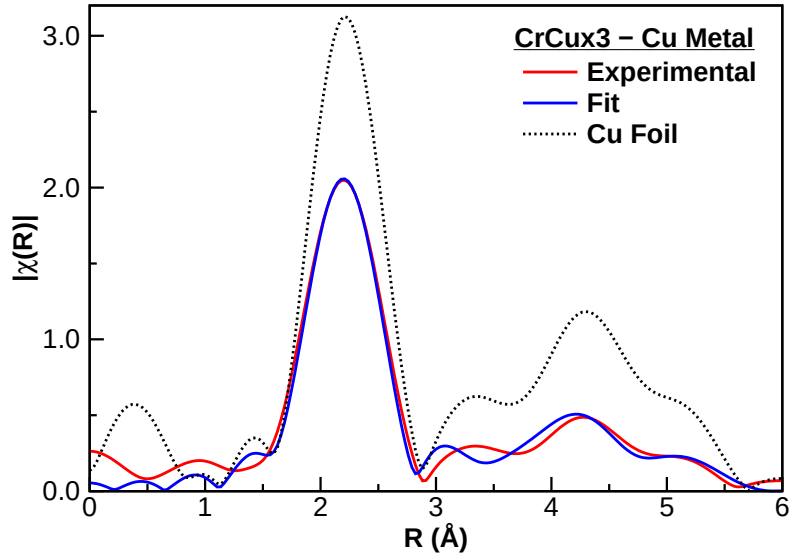

Figure 6.11: EXAFS experimental χ(R) and best fit for Cu metal layers

This might be caused by two main processes. First, the surface formation of oxides implies a bond with the metal matrix that compresses the upper oxide lattice parameter when the oxide layer is still relatively thin (below 100 Å) [60]. Second, the initial stage of the formation of the oxides can accommodate a high number of O vacants that may distort the lattice by reducing its average lattice parameter.

The Cu metal environment also shows a slight compression that may be explained by the same reasons as for the CuCrxN multilayer samples, as described in Section 5.3.1. However, this compression is in the limit of the sensitivity of the EXAFS analysis for this parameter, so it may be neglected.

The Debye-Waller factors are also relatively high compared to those typical for a bulk crystalline sample. This is also consistent with the results for the previous samples, which were made by the same deposition method, so the same explanation can be applied (Section 5.3.1).

In contrast, the Debye-Waller factors of both the CuO and Cu_2O are relatively low, approaching the typical values of crystalline species. As these phases come from a rather disordered Cu metal layer, this implies that there is an atomic reorganisation [60] with a consequent reduction of the disorder.

Chapter 7

Molybdenum nitride multilayers

Contents

Introduction

Transition metal nitrides such as VN, Zr-N, Hf-N, Ta-N, W-N and most prominently TiN have been extensively studied for their interesting electronic and mechanical properties that give multiple applications. For instance, they have been used as diffusion barriers for semiconductor metallisation and as superconducting materials, while their wear and corrosion resistance makes them useful for protective coatings [63].

These properties are influenced by their chemical composition, crystallographic phase and morphology. Most of them crystallise in the *fcc* NaCl type structure. Hexagonal close-packed (*hcp*) or simple hexagonal (with non-metal atoms in interstitial sites) structures are also stable [64].

Relatively small number of studies have been devoted to group 6 elements. Molybdenum nitride phases include two non-stoichiometric compounds, cubic γ-Mo_2N and tetragonal β-Mo_2N, and the stoichiometric , hexagonal compound δ-MoN [65]. γ-Mo_2N is known to be a superconductor with a T_c of 5.2K; δ-MoN is a hard material with a low compressibility, showing a superconducting transition in the 4−12K range [66]. A theoretical study has predicted that a γ-MoN with a cubic NaCl type structure would have a superconducting T_c at 29K [67].

Various methods have been used to synthesize molybdenum nitrides, being the reactive sputtering one of the most used for thin film deposition [63, 68, 69].

When they have one dimension much smaller than the other two, as in the form of thin films for surface protective coatings, this material tends to adopt structures different than in crystalline bulk, getting sometimes unusual ones or even amorphous phases. A common feature is that they lack long range order, most frequently when films are thinner, so XRD techniques are difficult to use. That makes EXAFS and the ReflEXAFS technique particularly suitable for the determination of the structures of these kind of materials.

The election of Mo from the technique development point of view was motivated by the high energy of the Mo-K absorption edge (20000 eV) to be studied, which makes the measurements challenging for several reasons. At this energy, the critical angle of reflection is approximately 0.12° for a Mo metal surface, so the incidence angles to be studied are rather small and its range is narrower.

Besides, the penetration depth of the radiation is quite high at this energy, and changes dramatically with it. This makes sometimes unavoidable the mixing in the same spectrum the EXAFS signal of different local environments of the same element that are located at different depths of the sample. Thus, the total reflection approximation, described in Section 4.2, is difficult to apply for these kind of measurements. However, the layer by layer discrimination of the global analysis method of the ReflEXAFS technique can provide the EXAFS signal of each layer, i.e. a solution to this problem.

Two different samples were prepared to study MoN thin films grown by reactive sputtering, as described in Section 2.1.2.3. This samples are bilayers of MoN/Mo or Mo/MoN that have two additional layers of Cr: one of them as a buffer layer for the Si substrate, and the other as a top layer to prevent oxidation. These samples add the difficulty of having a second Mo structure (in this case Mo metal) at a different depth in the sample.

7.1 Characterisation results

7.1.1 Atomic Force Microscopy

Sample surface topography images were taken with a Molecular Imaging Pico Plus microscope, and roughnesses were calculated as explained in Section 2.2.5.

Figures 7.1 and 7.2 show the topography images of the samples. Table 7.1 summarises the roughness calculated from the RMS values of these measured

for each sample.

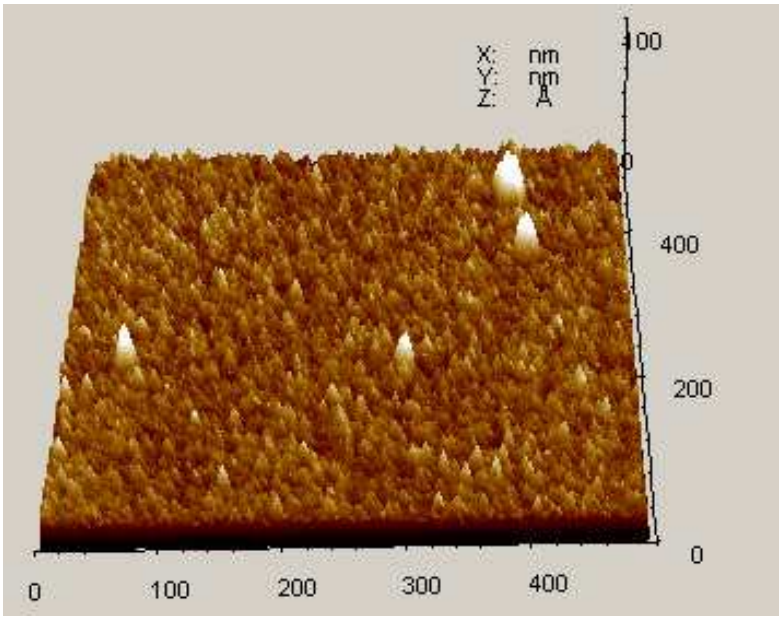

Figure 7.1: AFM surface topography for sample MoN60Mo

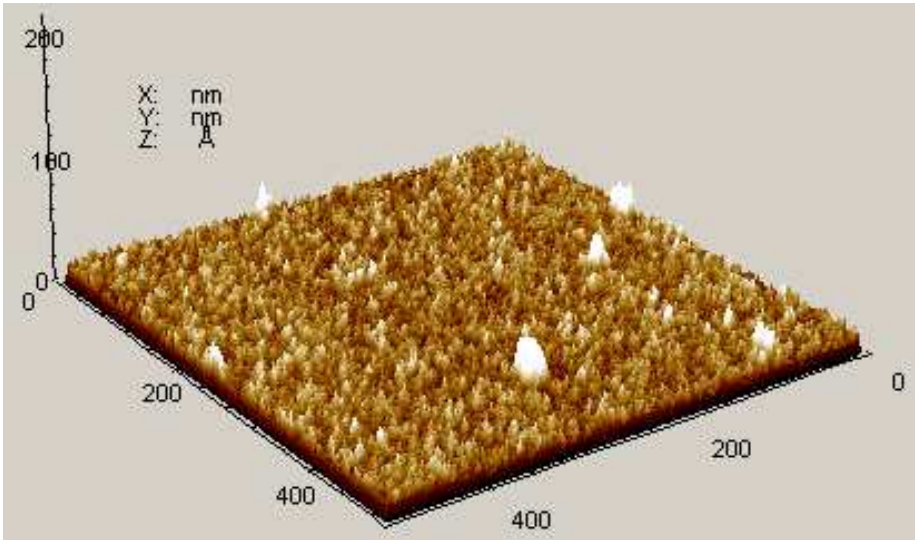

Figure 7.2: AFM surface topography for sample MoN60N

Table 7.1: AFM roughness for samples CuCrx3

Sample	Roughness (Å)
MoN60Mo	5
MoN60N	7

Both samples have similar topography and the variance of heights are close to the microscope noise level. It can then be concluded that they are quite smooth and homogeneous in the scale selected.

7.1.2 Rutherford Backscattering Spectrometry and Nuclear Reactions Analysis

RBS and NRA measurements were performed for all the samples at the Centro Nacional de Aceleradores, and analysed as explained in Section 2.2.3 in order to quantify the amount of Mo and N per surface unit of the samples.

It has to be taken into account that RBS measurements cannot distinguish between Mo in the metal or in the nitride layers, as the depth resolution of the technique is not enough to discriminate between layers as thin as these.

Thus, a reference sample of pure MoN, grown in the same conditions as all the MoN layers in the other samples was prepared. Afterwards, both the amount of Mo by RBS and N by NRA were measured. This way, the Mo/N atomic ratio was calculated and this ratio was assumed to be the same in all the MoN layers. Then, being the N abundance measured for all the layers by NRA, and also assuming that it is only present in the MoN layer, the amount of Mo in the MoN layer can be calculated with the aid of the Mo/N ratio calculated, so that the remaining Mo would be the one in the metal layer.

Table 7.2 shows the results of the measurements for the MoN reference sample. According to this results, the N/Mo ratio is 1.7.

Table 7.2: RBS and NRA results for reference sample

Sample	**Abundance (at/Å^2)**		**Ratio**
	Mo	N	
MoN-Ref	5.9	10.1	1.7

As explained in Section 2.2, both RBS and NRA measurements gives the amount of material per surface unit, and this is converted to thickness by assuming a density of the layers.

RBS and NRA thickness results assuming bulk density of the layers are shown in Table 7.3. Crystal densities are ρ_{Mo}=0.0643 at/Å^3 and ρ_{MoN}=0.0504 molec/Å^3. Note that the table has been simplified, so the columns do not show the order of the layers. Sample MoN60Mo has a Mo metal layer on top of the MoN layer, while sample MoN60N has the MoN layer on top of a Mo metal layer.

Table 7.3: RBS and NRA results

Sample	**Thickness (Å)**			
	Bot Cr	MoN	Mo	Top Cr
MoN60Mo	22	42	30	30
MoN60N	16	53	20	16

7.2 ReflEXAFS experiments

The measurement the spectra at the range of angles that the Mo-K absorption edge to be studied adds a experimental difficulty, as the angles have to be

quite lower than the ones for the previous samples, so the footprint at the sample become quite large. For instance, with a 100 μm experimental vertical slit gap, the footprint on the sample for the critical angle of a Mo surface at 20 keV (0.120°) would be about 48 mm. A sample of this size would be inhomogeneous for most laboratory thin film deposition methods.

Thus, the beam vertical size was reduced to 50 μm by using a narrower experimental vertical slit gap. The intensity of the beam is then reduced as well, but BM29 beamline bending magnet provides its highest flux at around the Mo-K absorption edge energy, so the reduction is partially compensated.

7.2.1 Angle selection

XRR measurements were performed at 19 keV and 21 keV in order to show the behaviour of the reflectivity at different energies, so as to choose the most convenient angles for the ReflEXAFS measurements.

Figures 7.3 to 7.4 show the reflectivity patterns at both energies, and are marked with the angles chosen for the ReflEXAFS measurements. These angles were chosen in order to have different penetration depths, so as to probe all the regions to be studied of the sample, that are buried below the protective Cr layer.

7.2.2 ReflEXAFS scans

ReflEXAFS scans were performed as explained in Chapter 3 at the angles chosen with the aid of the XRR curve. After that, each spectrum was divided by the direct beam scan to remove the absorption component of the air between the detectors and get a normalised spectrum.

The set of normalised spectra for each sample are shown in Figures 7.5 and 7.6.

Both the background with the expected interference pattern due to the mul-

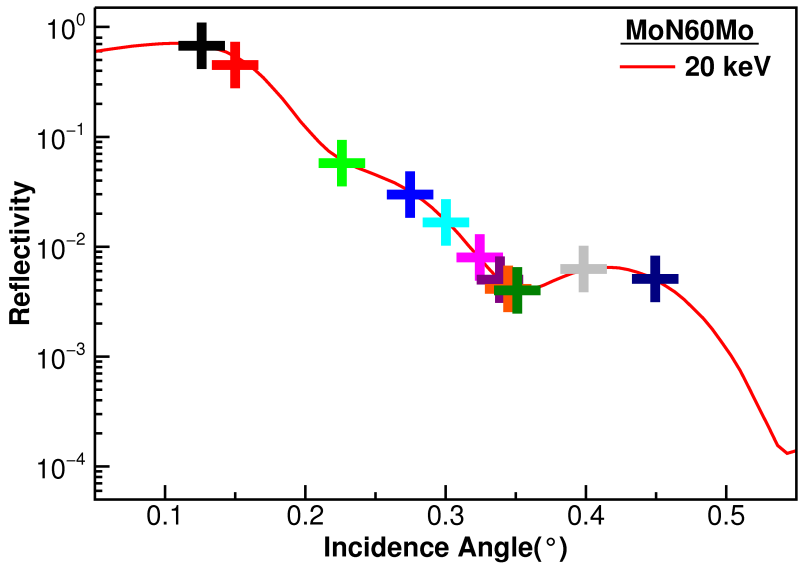

Figure 7.3: XRR experimental diagram and ReflEXAFS selected angles for MoN60Mo

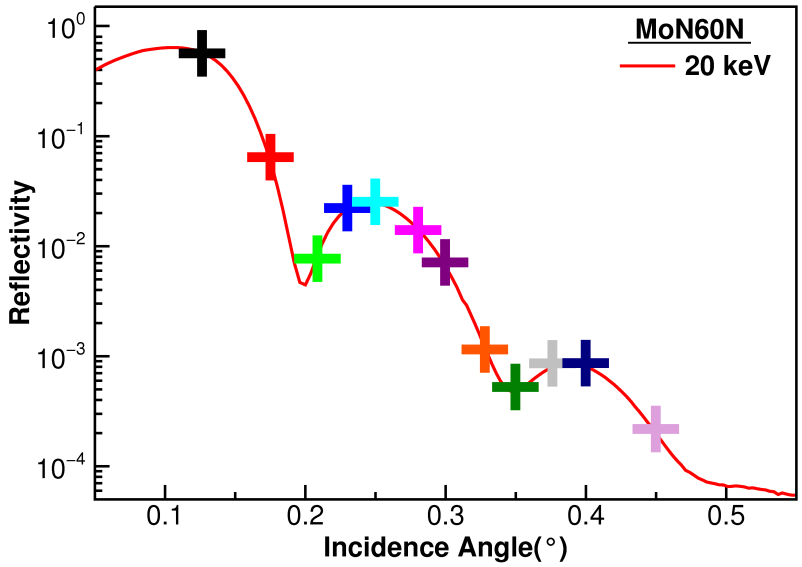

Figure 7.4: XRR experimental diagram and ReflEXAFS selected angles for MoN60N

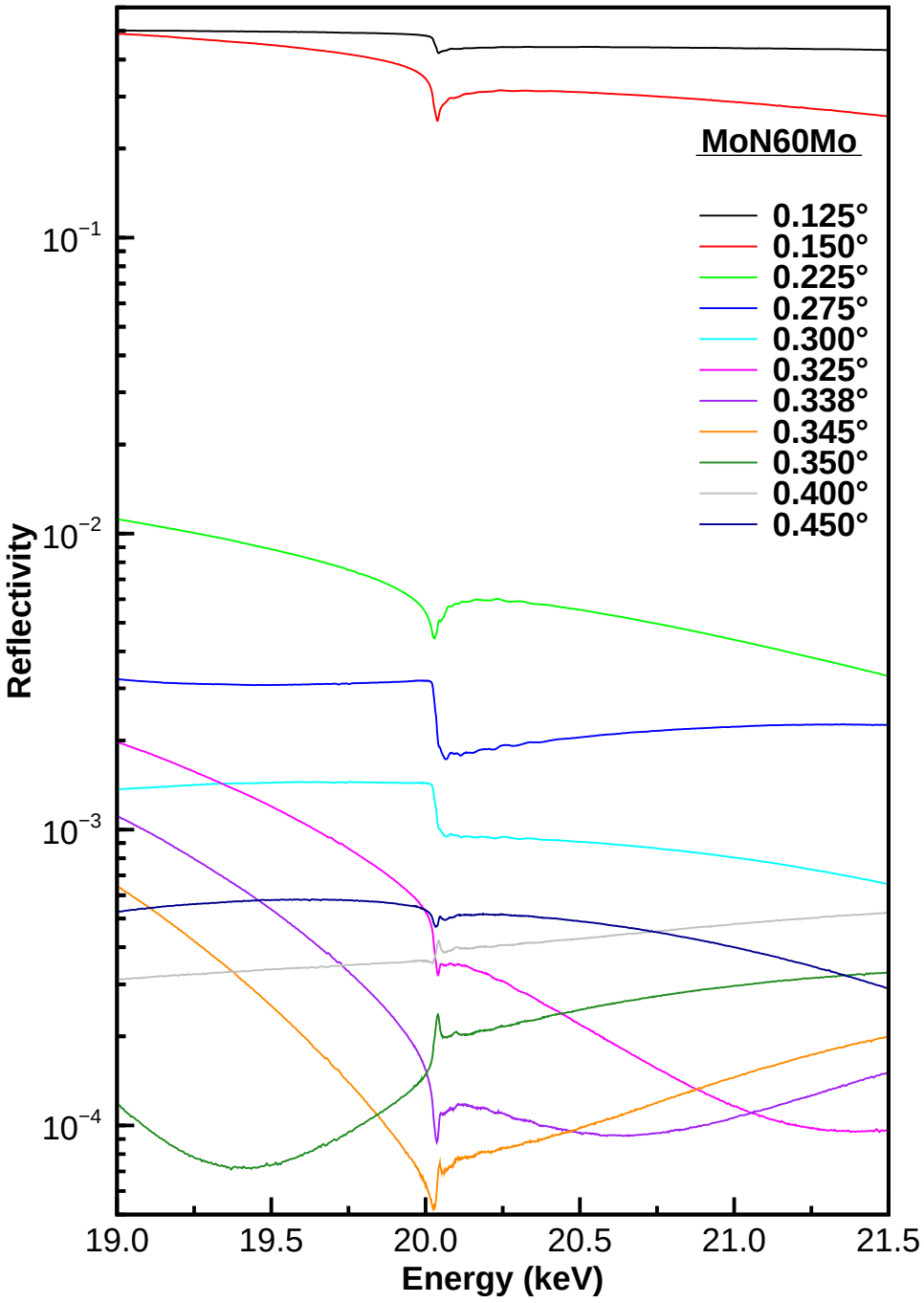

Figure 7.5: Normalised ReflEXAFS spectra for sample MoN60Mo

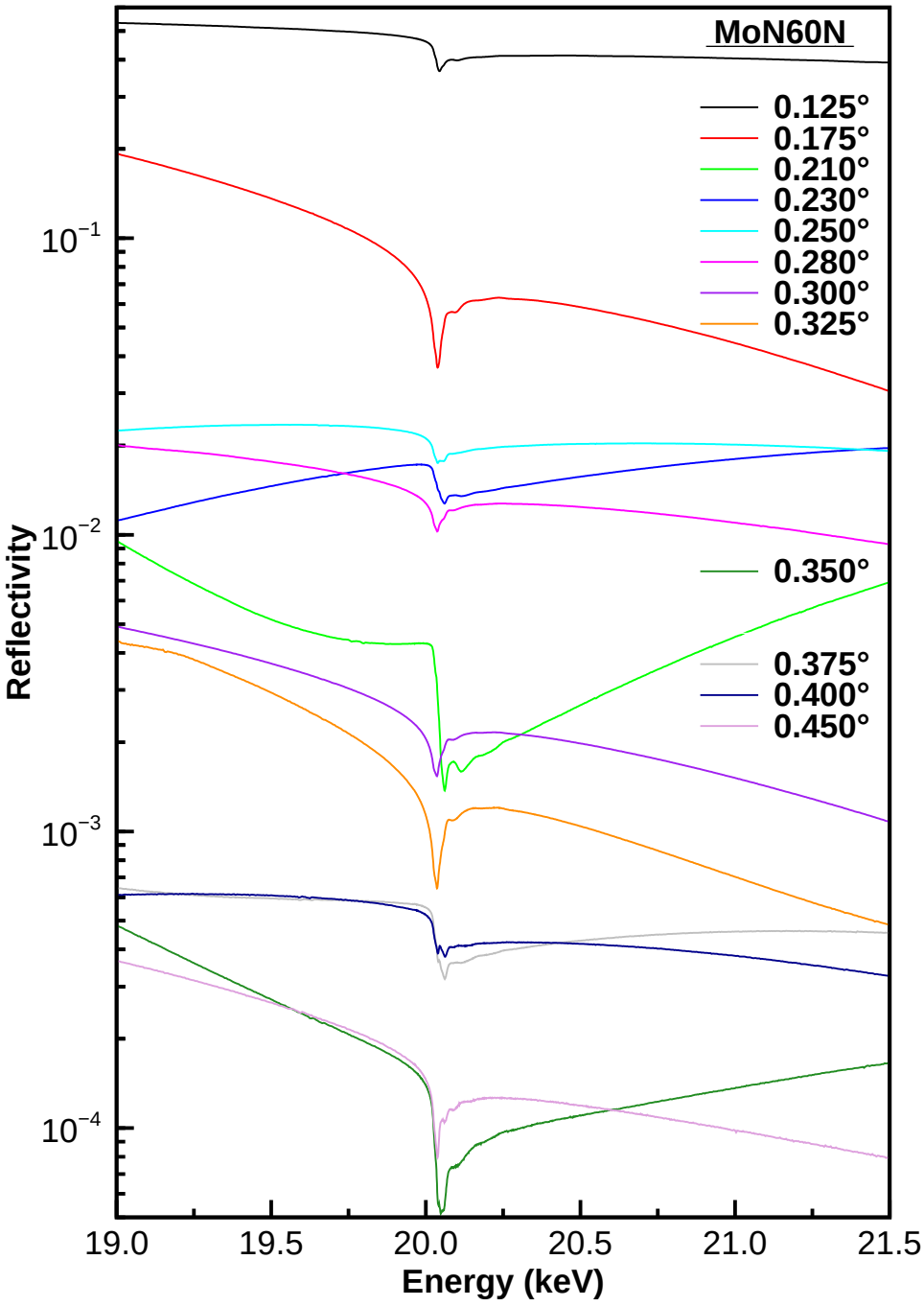

Figure 7.6: Normalised ReflEXAFS spectra for sample MoN60N

tilayers reflection and the EXAFS-like fine structure can be seen in all the spectra. The background pattern changes as the angle change, following the XRR diagram. This can be seen better in a 3D plot where the x, y and z axes are energy, incidence angle and reflectivity, as shown in Figure 7.7 for sample MoN60N. In this plot, the projection of the interpolated surface on the YZ plane would yield the XRR diagrams for the different energies, while the projection on the XZ plane gives back the energy-reflectivity plot shown in Figure 7.6

At first, it decreases its overall intensity for increasing incidence angles due to the loss of the total reflection condition, but then the reflectivity does increase and decrease again due to the interferences of the layers. This allows the possibility of having spectra measured at high angles, thus with a high penetration depth, but with a relatively high reflected intensity, thus with a good signal to noise ratio.

Superimposed to the background, it can clearly be seen the absorption edge at the Mo-K absorption edge energy (20.000 keV), along with an EXAFS-like pattern just after it. This pattern is better resolved at intermediate angles as the the lowest angle spectrum interacts very little with the Cu absorbing atoms and the highest angle spectrum has a worse signal-to-noise ratio due to the low reflection intensity at that angle. It is noticeable that such thin layers (less than 75 Åof Mo species) may be probed so a good and well resolved absorption edge may be registered.

It can also be seen that the fine structure of the lower angles spectra is significantly different from the rest of the spectra. This is because those spectra have a penetration depth relatively low, so they probe mostly the first environment in the first layer, either Mo metal for sample MoN60Mo or MoN for sample MoN60N, while the rest of the angles probe both of the environments in a more balanced proportion.

These experimental spectra show how the experimental method developed is able to obtain high quality data on these challenging conditions. The signal

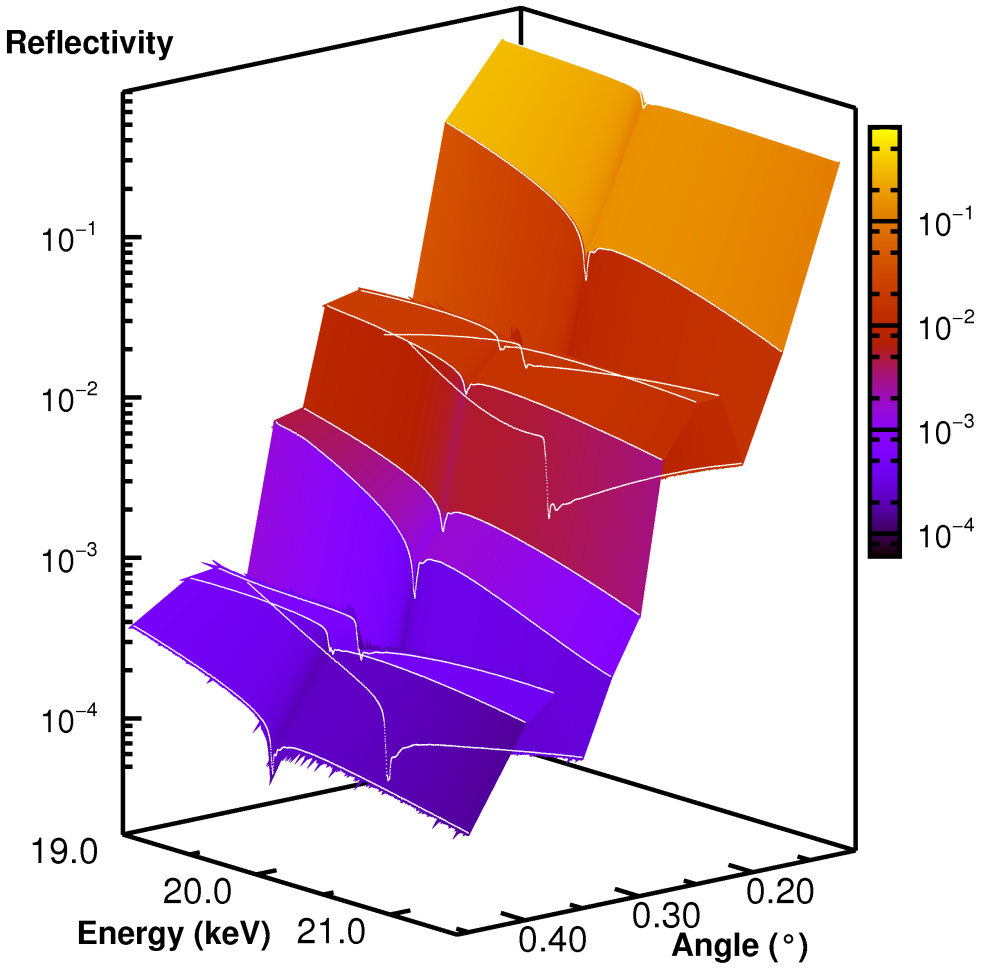

Figure 7.7: 3D plot of the normalised ReflEXAFS spectra for sample MoN60N, as function of energy and incidence angle

to noise ratio is excellent for almost all the spectra, where these cover a range of 4 orders of magnitude. The fine structure can be seen even for an incidence angle as high as four times the critical angle.

7.3 Analysis

The ReflEXAFS spectra may be analysed by using any of the approximations described in Chapter 4.

Unfortunately, none of the experimental spectra reached the total reflection condition angle, which is 0.120° for Mo metal at 20 keV, and even lower for MoN at the same energy. Anyway, a qualitative description of the Fourier transform magnitudes for the lowest incidence angle spectrum of each sample will be detailed below.

Furthermore, the global analyses of these spectra are currently in progress at the time of the writing of this report. The expected results would discriminate the Mo metal and MoN EXAFS signal, and would analyse the MoN phase generated with the reactive sputtering deposition. These results will be published elsewhere.

7.3.1 Total reflection approximation

As already explained in Chapter 4, using Martens [18] approximation, the EXAFS signal may be extracted directly from a spectrum of incidence angle below the critical angle.

However, these samples have such a low critical angle for the energies involved, that a spectrum of an angle low enough to surely fulfill the total reflection condition was impossible to record.

Anyway, the spectrum corresponding to the lowest angle was extracted by the standard EXAFS analysis programs, and its Fourier transform magnitude

was calculated.

As explained in Chapter 6, the Kramers-Kronig transform does not change the frequencies of the functions it transforms [47]. Thus, the spectrum is not valid to be simulated, but the Fourier transform magnitude can give a *qualitative* idea of the local environment at the surface of the sample.

Figures 7.8, and 7.9 show comparative plots of the Fourier transform experimental magnitudes with a Mo metal foil and a δ-MoN references taken from the IXAS database [55].

The Fourier transform magnitude of sample MoN60Mo shows a main peak at the position of the first peak of the Mo metal environment. It also shows a pair of peaks at higher R distances that may correspond to the further Mo metal shells. This result seems consistent with the fact that, at this angle, the penetration depth of the radiation is still relatively small, so the main contribution to the EXAFS signal must come from the most shallower layers, which is Mo metal in this case.

However, an additional smaller peak at about 1.5 Å denotes that a light backscattering atom exists at a lower distance. This peak is at a close position of the first Mo-N shell peak from the δ-MoN environment, so there must be some EXAFS signal coming from the MoN layer below the Mo metal layer added to the spectrum. As the Mo metal layer is relatively thin, the radiation penetrates enough to probe efficiently that second layer.

On MoN60N sample, the Fourier transform magnitude is quite different. This has a main peak at the distance of the first coordination shell of the δ-MoN environment. This result seems consistent, as the first layer the radiation encounters is the MoN layer, so the highest contribution to the EXAFS signal must come from there. The second peak of the experimental spectrum seems to be either a highly distorted second coordination shell of the MoN environment, or the result of the destructive interference of this peak with the first shell peak of the Mo metal environment below.

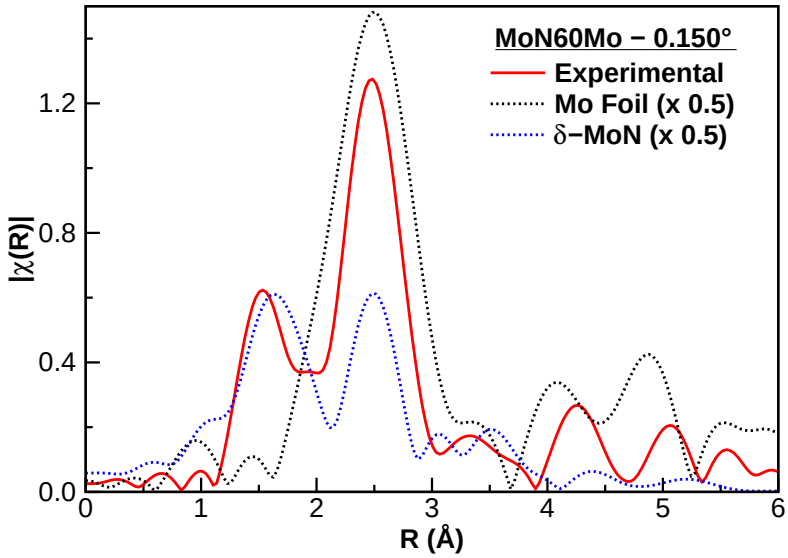

Figure 7.8: EXAFS experimental χ(R) for sample MoN60Mo, and references

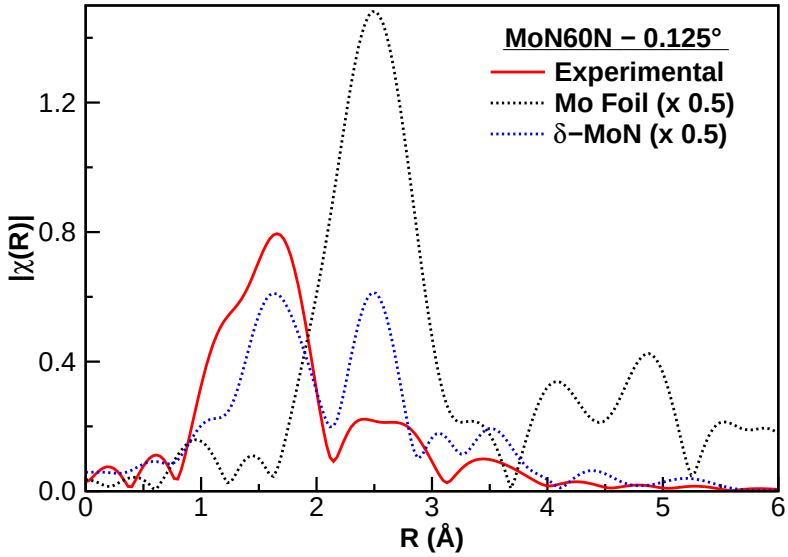

Figure 7.9: EXAFS experimental χ(R) for sample MoN60N, and references

In any case, the MoN contribution seems to be much stronger than the possible Mo metal contribution, contrary to what happens in the previous sample, where both contributions seems to be rather balanced. This is because the MoN layer in MoN60N sample is quite thicker than the Mo layer in MoN60Mo sample, so the radiation can penetrate better to the second layer in the latter sample.

These results show that, at these energies, the penetration depth of the radiation is so high that even in the lowest incidence angles the samples are probed further than the shallowest layers. The discrimination of the contributions at different depths can only be done by the global analysis method.

Chapter 8

Surface modified steels

Contents

Introduction

Steels are present in most of the industrial fields as well as in everyday life. Their versatility coming from the many different compositions and treatments makes them the most widely used material for its excellent mechanical properties.

Among the various treatments to modify the surface properties of the steel, nitriding is a treatment that aims for an improvement of the mechanical properties such as hardness, wear resistance and fatigue resistance.

Gas nitriding is the traditional method of performing this treatment. It consist on a heating to a temperature between 450 and 550°C, while NH_3 and H_2 are flowing in the preparation chamber. These conditions are maintained for a time that depends on the type of nitriding wanted, but can last from a few hours to some days. At those temperatures involved, the iron is in the ferrite phase (α-Fe, *bcc* structure) and does not change it.

The mechanism of nitriding is generally known, but the specific reactions that occur in different steels and with different nitriding processes are not always the same. Nitrogen atoms are introduced into the structure of the surface of a steel. These have partial solubility in iron, so it forms a solid solution with ferrite reaching nitrogen contents up to about 6%. At that N proportion, a compound called γ', with a composition of Fe_4N is formed.

The outermost layer formed by this compound is commonly referred to as the *white layer*. This layer is normally harder than the base steel, although is so brittle and shows such a low adherence to the steel that it is usually removed in the common industrial procedures.

However, under this layer, a compound with a composition of Fe_3N is formed and called ϵ. This phase is still quite hard while not so brittle, giving some improved hardness and wear resistance. Moreover, below this layer there is some solid solution from the nitrogen diffusion that swells the Fe structure. This makes the Fe structure rather distorted, what induces it to be much

more resistant.

Improved mechanical properties may be achieved when the steel contains small amounts of Al and/or of transition metals such as Cr, V, and Mo. The nitrides of these elements that show a rock salt structure are among the hardest compounds, achieving hardnesses similar to that of diamond.

When the steel is submitted to the nitriding treatment, the alloyed elements tend to form their respective nitrides on the surface of the steel, improving its properties [2].

The nitriding process induces strong improvements in the mechanical properties, but very subtle changes in the structure and chemical composition. Highly specific techniques are needed to detect them.

- The nitrides from the minor elements can be studied by EXAFS in the fluorescence mode [2].
- The enlargement of the Fe lattice close to the surface can be measured by recording X ray diffractograms in glancing angle geometry.
- The tiny amount of nitrogen in the surface can only be detected by X ray photoelectron spectroscopy due to its strong surface sensitivity, after the sputtering of the outer layers to remove the oxygen contamination.

By conventional fluorescence EXAFS, the Fe local structure seems to be the same in the surface and in the bulk, as the probe depth of this technique is in range of thousands of Ångströms. However, the changes should appear in a shallower region.

Its higher surface sensitivity makes ReflEXAFS a suitable technique to study the changes in the Fe local structure, with the added advantage of getting a depth profile of it.

From the ReflEXAFS technique development point of view, the nitrided steels are one of the most interesting and difficult scenarios. As explained above,

there is a continuous change in the local structure of the Fe of the steel that depends on the depth from the surface. Firstly Fe_xN phases should appear at the surface; then, a distorted *bcc* Fe structure with N atoms in it appears; and finally, the original ferrite *bcc* Fe of the steel is found at the bulk.

Discriminating among the different EXAFS of these phases is a real possibility with the global analysis method since they should appear at different depths.

Thus, two samples were prepared to study the structure of the nitrided steels, as explained in Chapter 2: two pieces of commercial ferritic steel with 3% Cr, 0.8% Mo, 0.3% V, 0.3% C and balance Fe, before and after being submitted to a gas nitriding treatment.

8.1 Characterisation results

8.1.1 X Ray Diffraction

X ray diffraction diagrams were measured for both samples at glancing angle regime in order to enhance the structures present near the surface. There were two measurements for each of them: one before polishing the samples (Figure 8.1), right after the nitriding treatment for the nitrided sample, and one after the polishing (Figure 8.2), so as to remove the white layer of the nitrided sample.

The diagram for the un-nitrided steel show the typical pattern of a *bcc* structure for the Fe lattice, with no difference before and after polishing.

The nitrided steel diagram before polishing shows not only this structure, but also peaks corresponding to the Fe_4N phase. However, the peaks of this structure disappear at the diagram for the polished sample. On the other hand, the remaining Fe-*bcc* peaks are wider and shifted towards lower angles when compared to those of the un-nitrided sample. This points to the

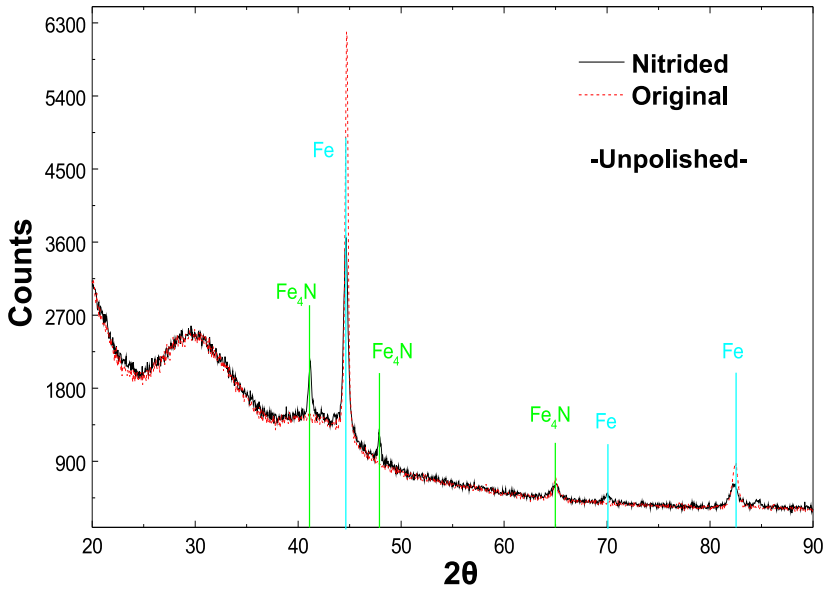

Figure 8.1: XRD diagram for un-nitrided and nitrided steel before polishing

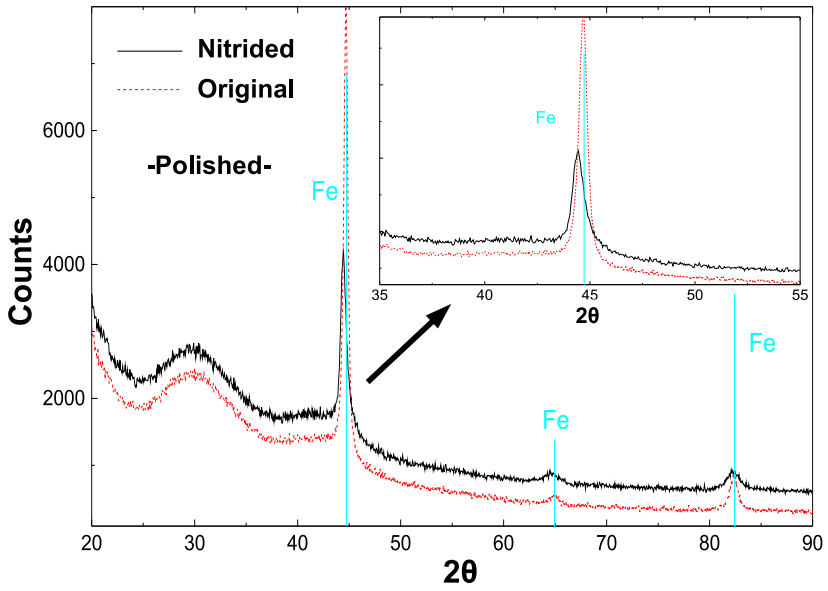

Figure 8.2: XRD diagram for un-nitrided and nitrided steel after polishing

deformation of the Fe structure above mentioned in the regions close to the surface.

8.1.2 Scanning Electron Microscopy

The samples surfaces were treated with a mixture of nitric acid and ethanol for a few second in order to reveal the grain structure by attacking preferentially the grain borders.

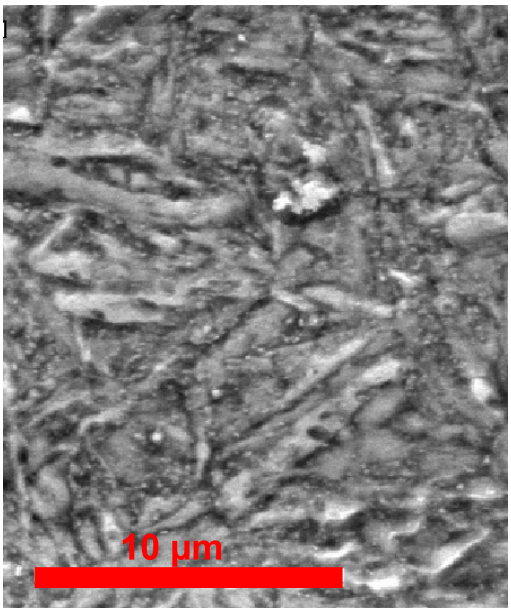

Figure 8.3: SEM micrograph of the surface of the nitrided steel

The SEM micrograph of the surface (Figure 8.3) show the grains that have a needle shape, typical from ferrite precipitation in the steel fabrication.

8.2 ReflEXAFS experiments

8.2.1 Angle selection

XRR measurements were performed at 8 and 8.9 keV in order to show the behaviour of the reflectivity at different energies, so as to choose the most convenient angles for the ReflEXAFS measurements.

Figures 8.4 and 8.5 shows the reflectivity patterns for the un-nitrided and nitrided steel, and are marked with the angles chosen for the ReflEXAFS measurements. These angles were selected in order to have different penetration depths, so as to probe a wide region in depth in the sample.

These XRR diagrams are quite different from the previous samples ones. As the steels surfaces do not have a defined layered structure, its reflectivity patterns are a monotonous decay without any maxima due to interferences between the layers.

8.2.2 ReflEXAFS scans

ReflEXAFS scans were performed as explained in Chapter 3 at the angles chosen with the aid of the XRR curve. After that, each spectrum was divided by the direct beam scan to remove the absorption component of the air between the detectors and get a normalized spectrum.

The set of normalised spectra for each sample are shown in Figures 8.6 and 8.7.

Contrary to the layered samples spectra, this ones do not show interference patterns with maxima and minima of reflectivity changing their positions with energy and incidence angle. This is because no layers are present. Instead, the spectra follow the XRR diagram with a monotonous decrease of the reflectivity, from 1 to 10^{-3}, with angle range from 0.20 to 0.65°.

The changes of the shape while moving to higher angles comes from the

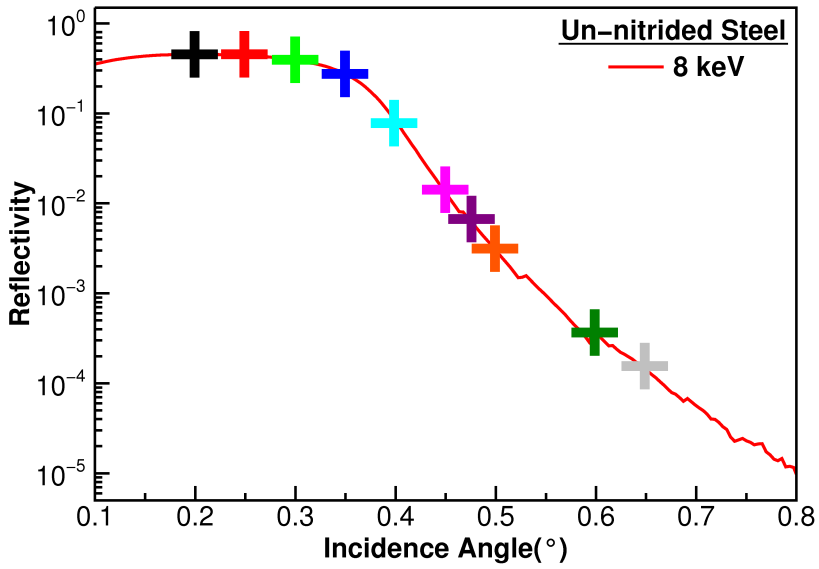

Figure 8.4: XRR experimental diagram showing ReflEXAFS chosen angles for un-nitrided steel

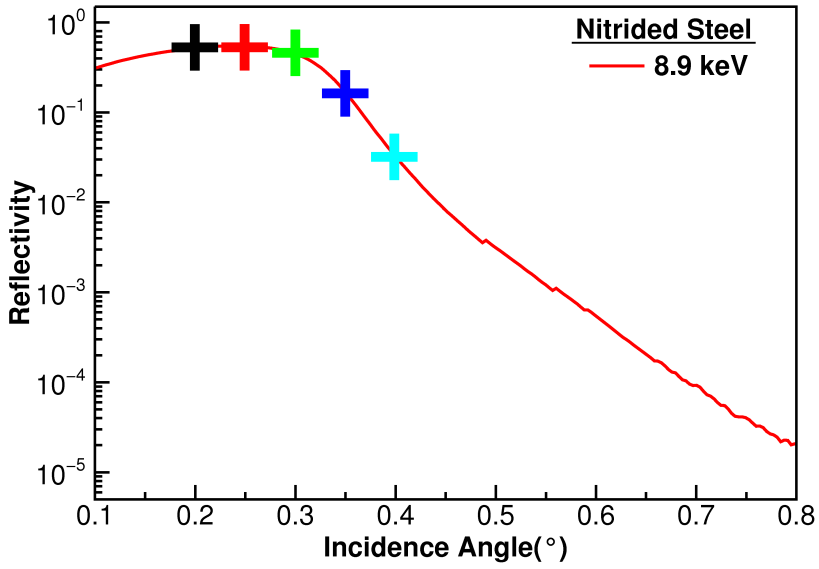

Figure 8.5: XRR experimental diagram showing ReflEXAFS chosen angles for nitrided steel

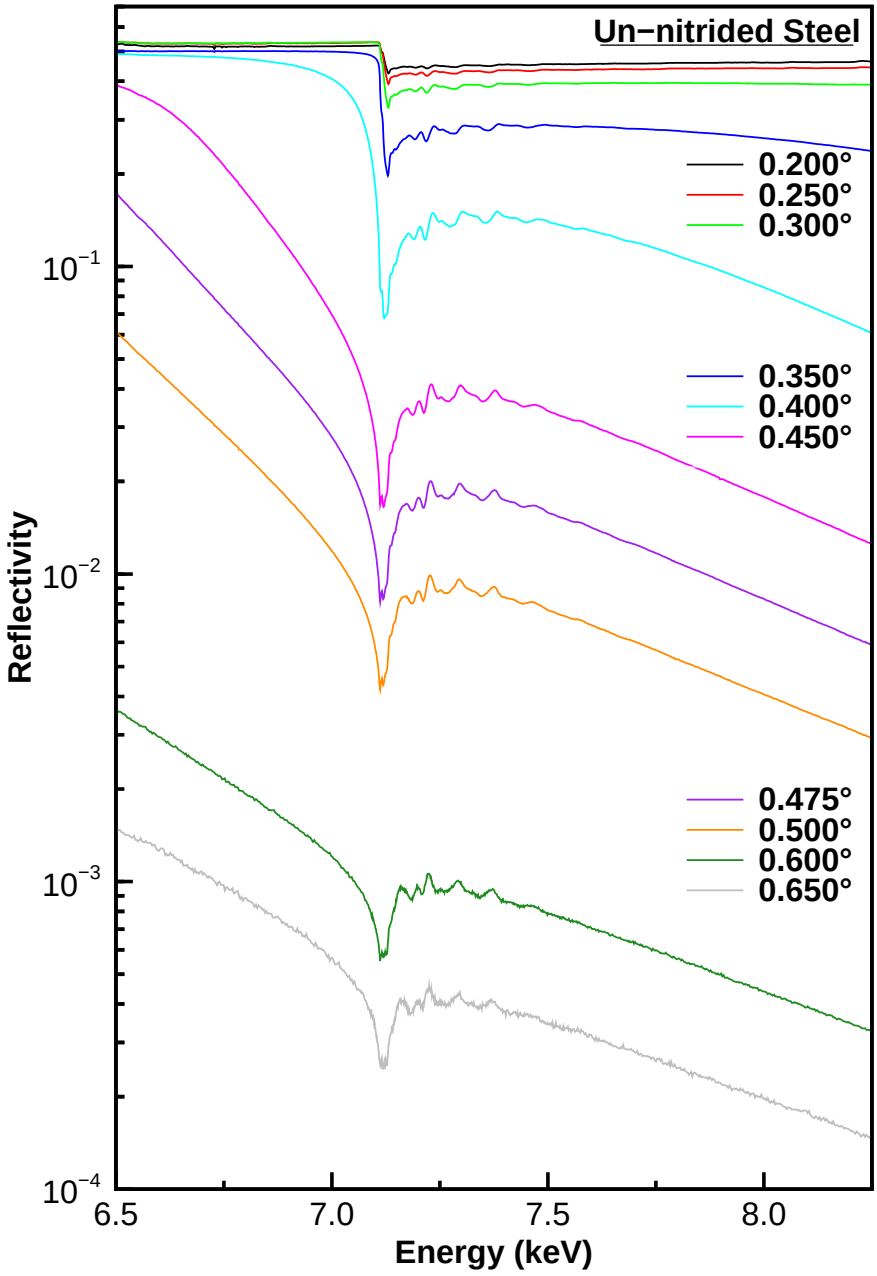

Figure 8.6: Normalised ReflEXAFS spectra for the un-nitrided steel

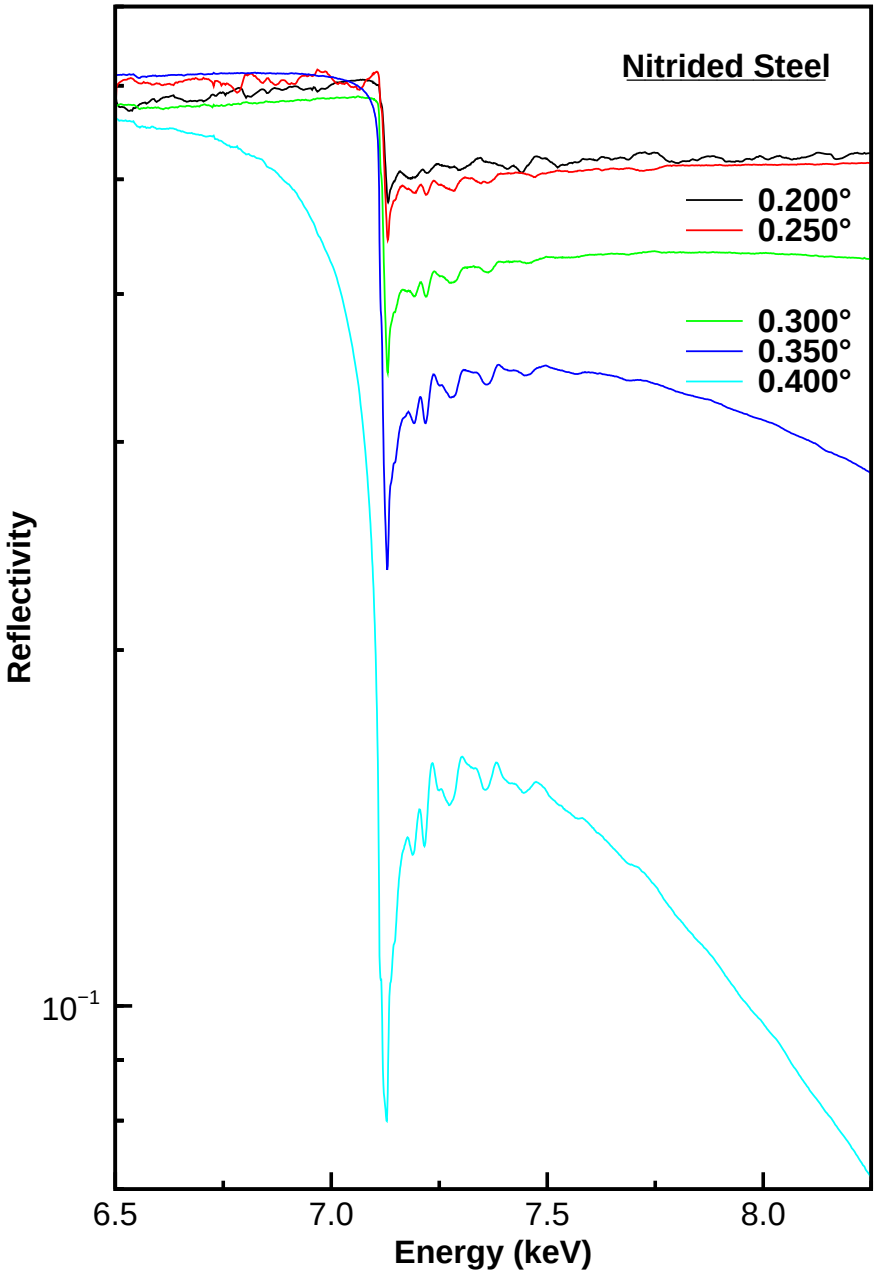

Figure 8.7: Normalised ReflEXAFS spectra for the nitrided steel

different proportions of the δ and β of the refractive index for the different angles.

At first glance, the spectra of the un-nitrided steel is quite similar to the nitrided ones. The main difference lies in the lower signal to noise ratio for the lowest angle of the latter. Being both surfaces different, the oxidation process may have originated a different roughness, in fact higher for the nitrided steel.

Superimposed to the background, the fine structure associated with the absorption can clearly be seen. At first sight, there is no difference between the un-nitrided and nitrided steel, although a further analysis must be performed. In both cases the intensity and frequency of the oscillations suggest that the main contribution to the fine structure should came from a heavy backscatter, most probably Fe.

8.3 Analysis

The ReflEXAFS spectra may be analysed by using any of the approximations described in Chapter 4.

8.3.1 Total reflection approximation

As already explained in Chapter 4, using Martens [18] approximation, the EXAFS signal can be extracted directly from a spectrum of incidence angle below the critical angle.

The spectra recorded at 0.250° for both samples fulfill the total reflection condition. Figure 8.8 show a comparative plot of the extracted experimental EXAFS data of this angle for both the samples. Figure 8.9 show a comparative plot of the Fourier transform magnitudes of the same spectra.

A difference in the Fourier transform magnitude can be seen between both

samples spectra. While the shape of the un-nitrided steel $|\chi(\mathrm{R})|$ suggest a metal *bcc* structure, the nitrided steel one seems to have some other contributions at lower R. This may come from either a N or an O backscattering shell, which may be disclosed with the quantitative analysis.

8.3.2 Global analysis

The global method cannot be applied to these kind of samples. The current form of the analysis program is optimised for the analysis of a sample made of a finite number of homogeneous layers. A sample like the nitrided steel have a continuous change on the EXAFS spectrum with the depth from the surface. In principle, a model with a high number of layers could be tested, but the errors would scale with the number of calculations, and the results would be meaningless. At the moment, the development of the method is heading towards the analysis of this type of samples.

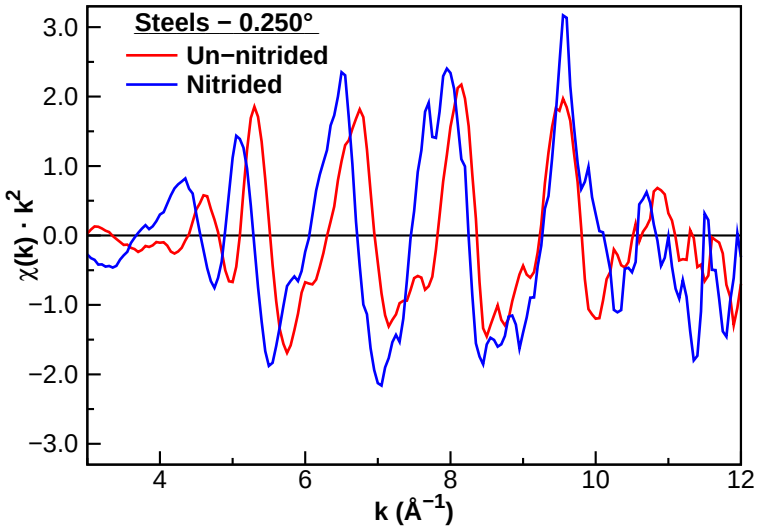

Figure 8.8: EXAFS experimental χ(k) for the total reflection angle of the un-nitrided and nitrided steel

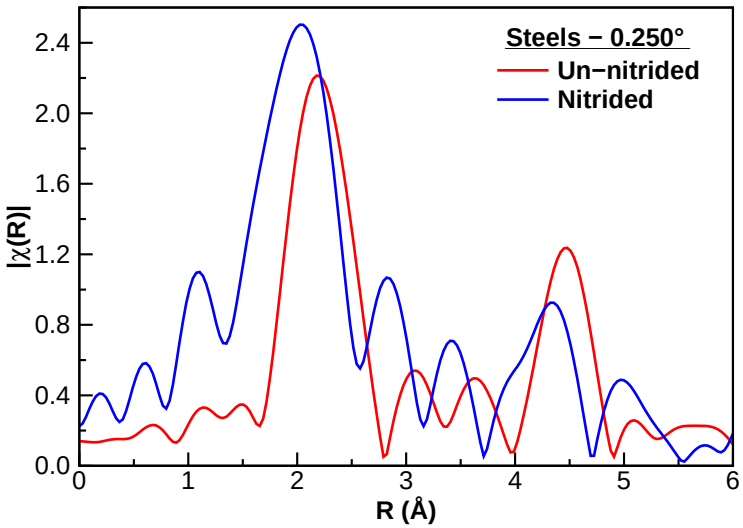

Figure 8.9: EXAFS experimental $|\chi(R)|$ for the total reflection angle of the un-nitrided and nitrided steel

Chapter 9

Conclusions

When the recording of an XAS spectrum is carried out by detecting the intensity of the reflected instead the transmitted beam, the technique is called ReflEXAFS. With this experimental arrangement the structural properties of near surface regions in the sample are effectively probed by the evanescent electromagnetic wave. This arrangement provides information not only the structure in the outermost layer of a sample surface but also the structure in the buried layers, since the detected species are the reflected photons and not the emitted electrons.

The aim of this project was to extend the ReflEXAFS technique to the analysis of the spectra not only below, as it had been made up to now, but also above the critical angle of reflection. This was of interest since it should enable the extraction of structural information not only about the shallowest region of the sample (extending a few tens of Å from the surface) but also about deep regions hundreds of Å underneath To achieve such an aim, he generalisation of the ReflEXAFS technique had to be done in the experimental and theoretical fronts.

In the Experimental one it was carried out the development of an experimental protocol using the available standard instrumentation (X-ray absorption beamline with a reflectometer) to obtain X-ray reflection measurements be-

low and above critical angle conditions. It has to be carried out in a highly accurate way to optimized angular configuration, energy scale and reflected beam intensity. The protocol was optimized at beamline BM29 (European Synchrotron Radiation Facility) in such a way that it could be done in a rather efficient and automatic way. It was tested in several types of samples designed to fulfill special requirements concerning surface structure, planarity and roughness. Moreover it was applied to commercial samples, such as surface modified steels.

In the theoretical front, a global method that considered all the angles below the critical angle was developed. This was achieved by developing the algorithms that allowed to simulate, extract and analyze the EXAFS data from the raw measured ReflEXAFS spectra. It was showed how the global analysis method here presented could be reduced, within the appropriate conditions, to the low and high angle approximations ReflEXAFS approximations carried out previously by other authors (Martens [7, 17, 18] and Borthen [19, 20]).

The selection of the samples was made in such a way that they not only fulfilled the requirements of the technique, but were by themselves interesting from the materials science point of view. The samples covered the fields of the multilayers, modified surfaces by controlled atmosphere, hard metal nitride coatings and, finally, the nitride-modified steels for cutting tools. In all cases, complementary information concerning both layers structure and interface properties on one hand, obtained from the reflectivity patterns, and short range order structure, obtained from the fine structure, was obtained. To obtain the second type of information the full analysis of ReflEXAFS results has to be carried out. It involved the treatment of the raw experimental data, the low angle approximation EXAFS analysis when possible, the global simulation and EXAFS extraction results, and finally, the EXAFS simulation and fitting to calculate the structural parameters of the studied environments

The first type of samples had the ideal characteristics for an easy optimisation

of the technique. They were bimetallic Cu-Cr layers deposited over Si(100) wafers by magnetron sputtering techniques. In these systems the variables were the thickness of the metal layers (8-40 Å). It was found that for all the samples the Cu layer showed the structure of crystalline copper, although an increase in the disorder and a decrease in the lattice parameter appeared for the smaller thicknesses.

In the second type of samples, Cr-Cu layered samples with similar characteristics but with copper layer exposed to the air, the process of copper oxidation was followed. Apart from crystalline metallic copper, the main phase found was Cu(II) oxide together with a small amount of Cu(I) oxide in the first layer. A significant increase of copper layer thickness, roughly by a factor of two, was a found as a consequence of copper oxide formation.

The third type of samples had the experimental difficulty of the measurement in a high energy. This made the value and the range of angles to be measured quite small compared to previous samples, so a smaller beam size had to be used. However, high quality data was obtained with these adverse, conditions, so the experimental method was found to be rather robust.

Finally, a set of commercial steels (nitrided and un-nitrided) was studied. This give the chance of testing the ReflEXAFS technique with a sample that not fulfilled completely the requirements for obtaining good measurements. Fortunately, the method developed was robust enough to get spectra of high quality even in these adverse conditions. Regarding the samples, it was found that, contrary to that observed by fluorescence EXAFS, changes in Fe environment are detected after the nitriding treatments. This mean that the changes in the Fe environment that give the useful properties to nitrided steels occur in a shallower region than the detection depth of fluorescence EXAFS (in the order of 1000 Å). ReflEXAFS was able to see these changes.

Appendix A

Resumen

Contenido

Introducción

Hoy en día, los materiales con propiedades superficiales singulares distintas de las del resto del material son del máximo interés a escala industrial. Existen principalmente dos tipos: los recubrimientos en forma de láminas delgadas, por ejemplo, los usados en los sistemas ópticos para mejorar su reflectancia o transparencia, o los recubrimientos duros que protegen ciertas piezas industriales del desgaste, y los tratamientos superficiales que modifican las propiedades del material como la nitruración de aceros para herramientas de corte. Debido a que el espesor de esta capa o zona superficial suele ser mucho más pequeño que sus otras dos dimensiones, no suelen presentar un buen orden a largo alcance, con lo que su carácter es mayoritariamente amorfo. Esto hace que las técnicas de caracterización estructural tradicionales, fundamentalmente la difracción de rayos X, no proporcionen datos concluyentes.

Las técnicas de absorción de rayos X en general y la espectroscopía EXAFS (Extended X-ray Absorption Fine structure Spectroscopy) en particular suministran información sobre los parámetros estructurales de los entornos cercanos de los átomos estudiados, como las distancias de enlace y los números de coordinación, que pueden ser fundamentales en la comprensión de ciertos fenómenos macroscópicos. Estas técnicas se basan en el análisis de la estructura fina presente en la señal de absorción de rayos X de energía variable, consecuencia de la retrodispersión de los fotoelectrones producidos en el proceso de absorción, provocada por los átomos vecinos al absorbente.

El modo de detección en transmisión, el más usual en los experimentos EXAFS, no distingue entre la superficie y el resto del sistema estudiado, con lo que los resultados contienen información mezclada de ambas partes del sistema. Además, como la cantidad de material en la superficie suele ser tan pequeña, la intensidad de la señal registrada no es suficiente como para obtener resultados fiables.

La sensibilidad a la superficie se puede conseguir usando otros modos de

detección. Por ejemplo, en lugar de detectar la radiación transmitida por la muestra se pueden detectar los electrones emitidos por el material como consecuencia de las transiciones energéticas relacionadas con el proceso de absorción de la radiación. Como el recorrido libre medio de los electrones en un sólido a estas energías suele ser de unos cuantos nanómetros, la información obtenida procede únicamente de las capas superficiales del material.

Otra forma de obtener sensibilidad superficial en esta técnica es usar una geometría diferente, incidiendo en la muestra a un ángulo muy pequeño con respecto a la superficie y detectando la onda reflejada. A este modo de detección se le denomina ReflEXAFS.

Los primeros trabajos que consiguieron analizar la estructura fina de la onda reflejada los realizó Barchewitz [70], aunque la primera aproximación importante al problema tanto desde el punto de vista teórico como experimental se debe a Martens [7, 17, 18]. Heald [8], Pizzini [9, 15, 71, 72] y D'Acapito [12, 13, 16] también han hecho experimentos con un ángulo de incidencia rasante, pero detectando la emisión de fluorescencia en lugar de la onda reflejada. Todos estos estudios se han realizado en condiciones de reflexión total, por debajo del ángulo crítico, donde las condiciones experimentales son buenas debido al alto flujo de rayos X reflejado, y las condiciones teóricas permiten aproximaciones que permiten analizar los datos con los programas comunes de análisis de datos EXAFS, como FEFF / FEFFIT [45, 46].

Los trabajos de Borthen [19, 20] significaron un avance al encontrar una forma de analizar la señal de estructura fina para espectros registrados a ángulos por encima del crítico. Sin embargo, este método sólo es válido en ciertos casos muy concretos. Hasta ahora no ha habido una aproximación general al problema.

El avance principal de este trabajo de investigación consiste en extender la aplicación de esta técnica al análisis de espectros con ángulos de incidencia por encima del ángulo crítico para obtener información sobre el entorno local de los átomos de zonas próximas a la superficie a distintas profundidades

en la muestra estudiada. Esta extensión debe hacerse en dos frentes: el experimental, diseñando los protocolos de toma de datos adecuados dadas las condiciones de baja reflexión para ángulos altos; y el de análisis de datos, desarrollando los algoritmos que permitan extraer y tratar la estructura fina de espectros medidos.

A.1 Preparación y caracterización de muestras

Las muestras que se pueden caracterizar mediante ReflEXAFS deben poseer una serie de características para poder obtener la máxima reflexión posible.

La planaridad es esencial para tener un buen rayo reflejado. Para un tamaño de rendija en el detector de reflexión de 1 mm y una distancia muestra-detector de 1 m, la apertura del haz no debe ser superior a 0.06° para que pueda entrar por completo en el detector. Por tanto, éste es el límite angular de curvatura de la muestra para no perder señal en la reflexión. También la rugosidad causa dispersión del rayo, por lo que interesa que la muestra sea lo menos rugosa posible.

La huella del rayo X sobre la muestra tiene una longitud de $d/sin\theta$, donde d es el tamaño vertical del rayo determinado por la rendija y θ es el ángulo de incidencia (ver Figura A.1). Así pues, las muestras deben ser de este tamaño y homogéneas en toda su longitud para poder contener toda la huella y así tener una alta reflectividad. Como el ángulo suele ser pequeño, esta huella es grande. Para tamaños típicos de rendija de 100 μm, y ángulos de incidencia de entre 0.2 y 0.6 grados, la huella está entre 29 y 10 mm respectivamente.

Sin embargo, una muestra de poca calidad puede ser compensada por una mejor calidad de fuente de rayos X. Por ejemplo, se puede contrarrestar una alta rugosidad en la muestra con un mayor flujo de rayos X, o una muestra pequeña se puede medir a bajo ángulo con una rendija más estrecha y también mayor flujo de radiación.

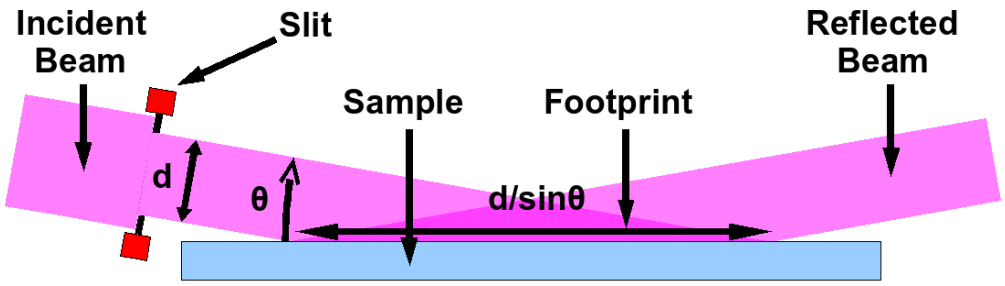

Figura A.1: Huella del rayo X sobre la muestra

Con estos requerimientos, las muestras típicas que se pueden estudiar son, por ejemplo, las láminas delgadas, pues suelen depositarse sobre sustratos planos, y las superficies tratadas siempre que estén planas y bien pulidas. Los líquidos, que tienen una superficie plana natural, pueden estudiarse siempre que se tenga un método para desviar el rayo incidente hacia la muestra.

A.1.1 Preparación

Se usó la técnica *Magnetron Sputtering Physical Vapor Deposition* para fabricar multicapas, pues este método proporciona las características necesarias a las capas para poder ser medidas fácilmente mediante ReflEXAFS.

Esta técnica consiste en crear un plasma de Ar y dirigir los iones de Ar^+ hacia el cátodo, donde se encuentra una diana del metal a depositar, que se ve pulverizada por el impacto de estos iones. Para aumentar la velocidad de evaporación, se genera un campo magnético permanente de forma toroidal cerca del cátodo que concentra los iones y electrones en las cercanías de la diana. Un esquema de este sistema se puede ver en la Figura A.2.

Cuando se trata de fabricar compuestos binarios como nitruros u óxidos, se puede usar como gas de trabajo N_2 u O_2, de forma que el plasma producido reacciona con el metal pulverizado y se depositara el compuesto resultante

sobre el sustrato. Esta técnica se denomina *Reactive Sputtering*.

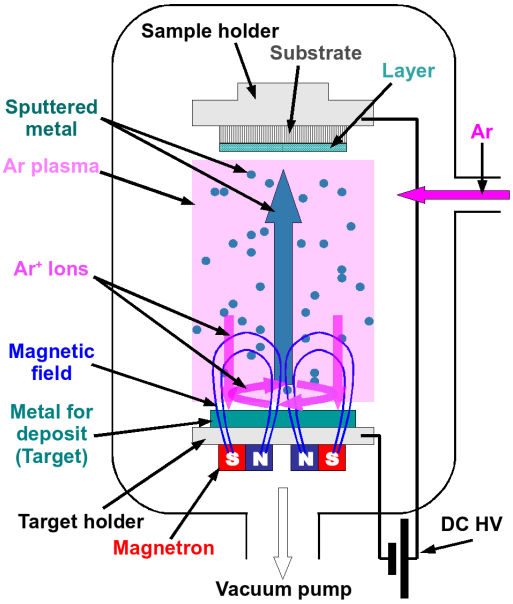

Figura A.2: Esquema de la cámara de Magnetron Sputtering

El espesor se controló haciendo pruebas previas con los mismos parámetros en la cámara que permitieron medir la velocidad de deposición y se supuso la misma velocidad al fabricar las muestras mencionadas. Aun así, se midió el espesor de las muestras *a posteriori* con otras técnicas.

Para los primeros experimentos se usaron una serie de muestras sencillas, de composición y estructura conocidas formadas por multicapas metálicas de (CuCr)xN, de diversos espesores y número de periodos, que permitieron la puesta a punto de los protocolos y métodos experimentales de la técnica para luego poder aplicarla a muestras más complejas.

Éstas se depositaron sobre sustratos de Si (100) de 4 x 1 cm de superficie para asegurar la planaridad. Se depositó la última capa de Cr en la superficie para prevenir la oxidación de las capas de Cu. Un esquema de las muestras puede verse en la Figura A.3

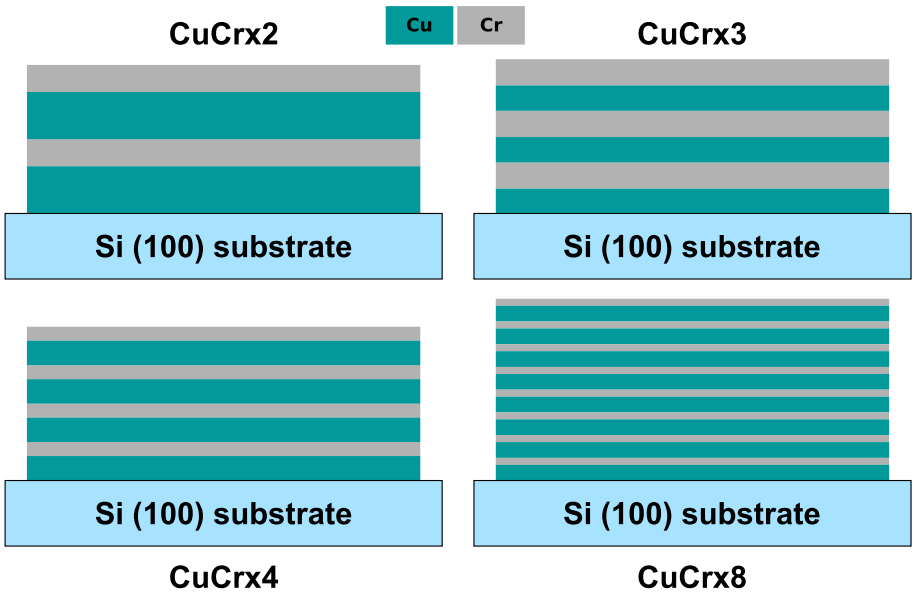

Figura A.3: Esquema de las muestras CuCrxN

Otra serie de muestras consistió en multicapas similares a las anteriores, pero con el periodo invertido, (CrCu)xN, de forma que la capa más externa fuera Cu. De esta forma, esa capa se oxidaría con la atmósfera y se tendría el mismo elemento (Cu) con dos entornos de coordinación diferentes (óxido y metal) para distintas profundidades en la muestra.

La siguiente serie de muestras consta de una multicapa de Mo y nitruro de Mo producida por *Reactive Sputtering*. Estas muestras también tienen dos entornos diferentes a distintas profundidades en la muestra. Además, el estudio del borde de absorción K del Mo, a una energía mucho más alta (20 keV), lo que implica permite probar la técnica en distintas condiciones experimentales.

La última serie de muestras están compuestas de un acero comercial. Una de las muestras ha sido sometida a un proceso de nitruración gaseosa, mientras que la otra permanece sin nitrurar. Estas muestras permiten analizar la apli-

cación de la técnica a muestras más "reales" (menos planas y más rugosas), y con una dificultad añadida al análisis de datos.

A.1.2 Caracterización

Las muestras se estudiaron empleando distintas técnicas para obtener información sobre su estructura y composición antes de efectuar los experimentos ReflEXAFS, para comprobar si eran adecuadas.

Se comprobó la cristalinidad de las muestras mediante Difracción de Rayos X (XRD). Mediante Reflectometría de Rayos X (XRR) se calcularon los espesores, densidades y rugosidades de las capas. Se midió la cantidad de los distintos elementos que contienen las muestras, mediante Espectrometría de Retrodispersión Rutherford (RBS), en el Centro Nacional de Aceleradores (CNA, Sevilla) La Microscopía de Fuerzas Atómicas (AFM) proporcionó una medida de la rugosidad como la dispersión estadística (RMS) de las alturas en una superficie de 23 x 23 micras sobre las muestras.

A.2 Experimentos ReflEXAFS

Esta técnica tiene ciertos requerimientos experimentales. Primero, como en cualquier experimento EXAFS, se necesita una estación de absorción de rayos X en una fuente de radiación sincrotrón que proporcione una buena resolución en energía en las proximidades del borde de absorción que se vaya a estudiar. Además, al caer rápidamente la reflectividad para ángulos por encima del crítico, se necesita un flujo de rayos X especialmente alto para poder tener una buena relación señal-ruido a estos ángulos que permita obtener una señal de estructura fina suficientemente limpia.

Una alta estabilidad angular es imprescindible para poder medir con precisión los ángulos de incidencia. Este tipo de inestabilidad provocaría un cambio en la profundidad de penetración estudiada, que si ocurriera en el transcurso

de una medida, nos daría una estructura fina cambiante con el tiempo muy complicada de estudiar.

La estación debe poseer la instrumentación necesaria que permita montar la muestra y tomar los datos necesarios para los distintos ángulos con precisión. Para ello, se necesita un reflectómetro de al menos 2 círculos para colocar la muestra al ángulo requerido respecto del haz incidente y orientar el detector en el correspondiente ángulo del rayo reflejado.

El alineamiento de la muestra es extremadamente importante como se explica más adelante, por tanto el reflectómetro debe estar equipado con un goniómetro que permita mover la muestra en los 3 ángulos y 3 direcciones del espacio con gran precisión.

Los experimentos se realizaron en la fuente de radiación sincrotrón europea E.S.R.F., en el marco de un proyecto cuyo propósito ha sido desarrollar esta técnica en la estación BM29. Esta estación dispone de las características necesarias para cumplir con los requerimientos.

A.2.1 Instrumentación

El reflectómetro usado en estos experimentos es un Huber de 3 círculos completamente automatizado cuyo esquema se puede observar en la Figura A.4. Uno de ellos (llamado *th1*) sostiene el goniómetro en el que se monta la muestra y rota en un eje horizontal, en la dirección perpendicular al rayo X. Otro de ellos (llamado *th2*) es concéntrico a *th1* y lleva adosado el detector de reflexión y una rendija motorizada. Ambos tienen una precisión de 0.001 grados para pequeños movimientos.

El goniómetro permite movimientos en las tres direcciones del espacio y en tres ángulos de ejes perpendiculares entre sí. La precisión de los motores lineales es de 0.001 mm para la dirección z y 0.01 mm para las direcciones x e y. La precisión de los motores angulares es de 0.01 grados para todos ellos.

El tamaño del haz que incide sobre la muestra viene determinado por una

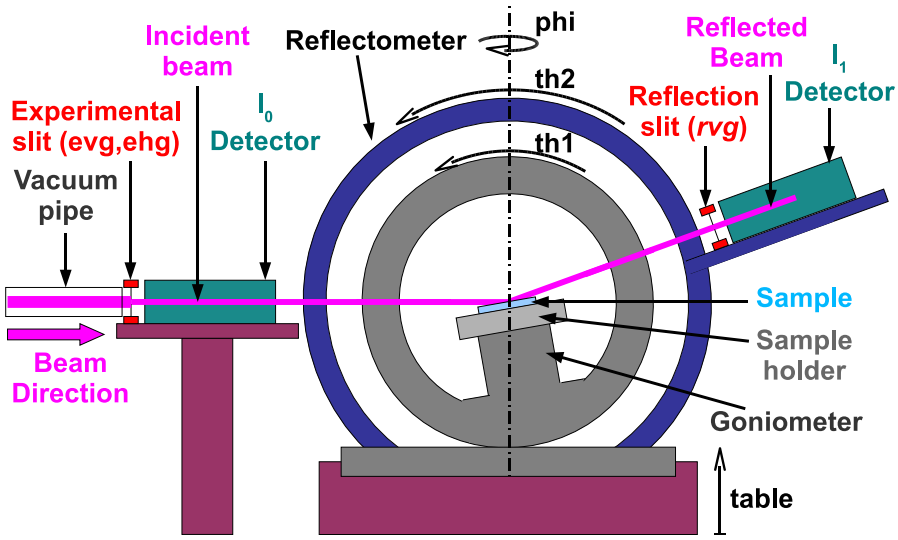

Figura A.4: Esquema del reflectómetro

rendija horizontal, que se abre hasta ocupar algo menos que el ancho de la muestra, y otra vertical que debe ser de una apertura pequeña para poder acceder a ángulos de incidencia pequeños sin que la huella del rayo X se salga de la muestra. La rendija vertical utilizada en estos experimentos es de 50 micras para las medidas en el borde de absorción del Mo, y de 100 micras para el resto de las medidas.

Como en cualquier experimento EXAFS, se necesita una pareja de cámaras de ionización iguales para detectar el haz incidente I_0 y el reflejado I_1 de forma precisa y con baja relación señal-ruido para un espectro variable en energía. Además, es necesario que sean pequeñas y ligeras con el objetivo de no dañar el círculo *th2* al montar la segunda cámara sobre el brazo antes mencionado.

Las cámaras usadas en estos experimentos fueron unas OKEN S-1194A1 de 15 cm de largo, fácilmente rellenables con la apropiada mezcla de gases en función del borde de absorción del elemento que se vaya a estudiar. Como es usual, la primera (I_0) y la segunda (I_1) cámara se llenarán de forma que

absorban un 20 % y un 80 % del rayo incidente, respectivamente.

Cada cámara de ionización lleva asociado un pre-amplificador de corriente Stanford Research Systems SR570. Estos pueden trabajar con sus propias baterías para minimizar el ruido electrónico, y permiten un control remoto de las ganancias desde un ordenador.

A.2.2 Protocolo experimental

A.2.2.1 Alineamiento

El alineamiento es un proceso esencial en estos experimentos por dos motivos: la necesidad de una reflectividad máxima y la necesidad de medir el ángulo de incidencia con precisión. Por ello, se ha desarrollado un procedimiento estándar durante los experimentos.

El objetivo de este procedimiento es conseguir, por un lado, orientar la muestra con su lado mayor paralelo a la dirección del rayo, plana con respecto a la rendija y por otro, colocar el centro de rotación del círculo *th1*, que nos da el ángulo de incidencia, en el centro de la muestra y en la dirección del rayo. Así, un giro de este círculo dará el ángulo de incidencia con exactitud y no se iluminará más que la muestra a partir del ángulo mínimo.

A.2.2.2 Medidas de Reflectometría de Rayos X

Al intentar medir con ángulos de incidencia superiores al ángulo crítico, la reflectividad cae drásticamente. En ciertos casos, como en muestras formadas por láminas delgadas, los efectos de interferencia ocasionados por las distintas interfases pueden aumentar o disminuir la reflectividad para algunos ángulos. Por tanto, es aconsejable registrar algunos espectros de reflectometría de rayos X (XRR) para así poder elegir los ángulos más convenientes para tomar los datos ReflEXAFS. Esta técnica consiste simplemente en registrar la reflectividad de una muestra a una energía de rayos X fija para un cierto

rango de ángulos de incidencia θ. Lo que se mide es la intensidad de radiación detectada en 2θ (ángulo de reflexión) para cada θ.

Lo más útil es registrar un espectro XRR a una energía cercana al borde de absorción que se va a estudiar para saber qué reflectividad se tendrá cerca de ese borde de absorción para todos los ángulos. El rango debe ser desde 0°, hasta el máximo ángulo para el cual la relación señal ruido sea satisfactoria, y así saber el límite al cual se puede llegar.

A.2.2.3 Medidas ReflEXAFS

El procedimiento para registrar los espectros ReflEXAFS sigue los siguientes pasos. Se mueve el círculo *th1* hasta el ángulo de incidencia elegido. Después, se busca el rayo reflejado con el círculo *th2* y se coloca *th2* en ese punto. Seguidamente se escanea el motor z del goniómetro para encontrar el máximo de reflexión, que corresponderá a la posición ideal de la huella del rayo X en la muestra, consiguiendo así que toda esta huella esté contenida en ella. En este momento se está en condiciones ideales para medir espectros ReflEXAFS.

Se hace un barrido en energía y se registra la señal en los detectores I_0 e I_1 a la vez, tal como se hace en una medida EXAFS convencional. Los límites de este espectro deben ser, como mínimo, 500 eV por debajo y 1000 eV por encima del borde de absorción estudiado, pero es recomendable registrar 1000 eV por debajo y 1500 eV por encima para facilitar el posterior tratamiento de datos.

Con la ayuda de las curvas XRR, se eligen varios ángulos de incidencia para los cuales se registran los espectros para cada muestra. Es aconsejable tener espectros que cubran todo el rango de reflectividad, y se deben aprovechar los efectos de interferencia (si los hay) para registrar espectros con alta reflectividad a ángulos altos.

Se deben registrar un total de 6 a 10 ángulos distintos, dependiendo de la muestra, con el objetivo de tener suficientes datos para el posterior análisis

de datos. También es importante tener varios espectros del mismo ángulo para comprobar la reproducibilidad y mejorar la relación señal ruido de los mismos.

Adicionalmente, se deben registrar datos de los fondos de radiación para normalizar los espectros y así obtener datos de reflectividad absolutos que se puedan ajustar mediante un modelo teórico. Para ello, simplemente se aparta la muestra, se coloca el detector en la dirección del rayo directo, y se registra un espectro en el mismo rango de energía que se ha estado usando.

A.2.2.4 Automatización

Cuando se desarrolla una nueva técnica de caracterización, es importante tener en cuenta que debe ser fácil de usar y que debe tener un protocolo rutinario. Por tanto, se debe hacer un esfuerzo en sistematizar y automatizar en la medida de lo posible el uso de la misma. El desarrollo de programas que controlan automáticamente el alineamiento y la toma de datos ha sido fundamental en el desarrollo de este proyecto.

Tanto el alineamiento que se ha descrito más arriba como otros procesos (la búsqueda del ángulo de reflexión, por ejemplo) son procesos iterativos en la mayoría de los casos, pues se deben hacer barridos en las posiciones de los motores del goniómetro y el reflectómetro y comprobar las representaciones gráficas de la intensidad en el segundo detector hasta que se encuentra el punto adecuado. En algunos casos, esto puede ser automatizado en forma de programas informáticos para que a lo largo de la medida sólo se tengan que controlar los resultados. De esta forma se logra una sistematización del proceso, reduciendo el número de errores humanos y aumentando la velocidad de toma de datos. Se pueden representar estos procesos mediante diagramas de flujo que pueden servir luego como base para escribir los correspondientes programas en el lenguaje necesario. Como ejemplo, se presenta uno de los diagramas de flujo en la Figura A.5, que corresponde al alineamiento del ángulo *psi* del eje vertical a la muestra. En total, el alineamiento requiere de

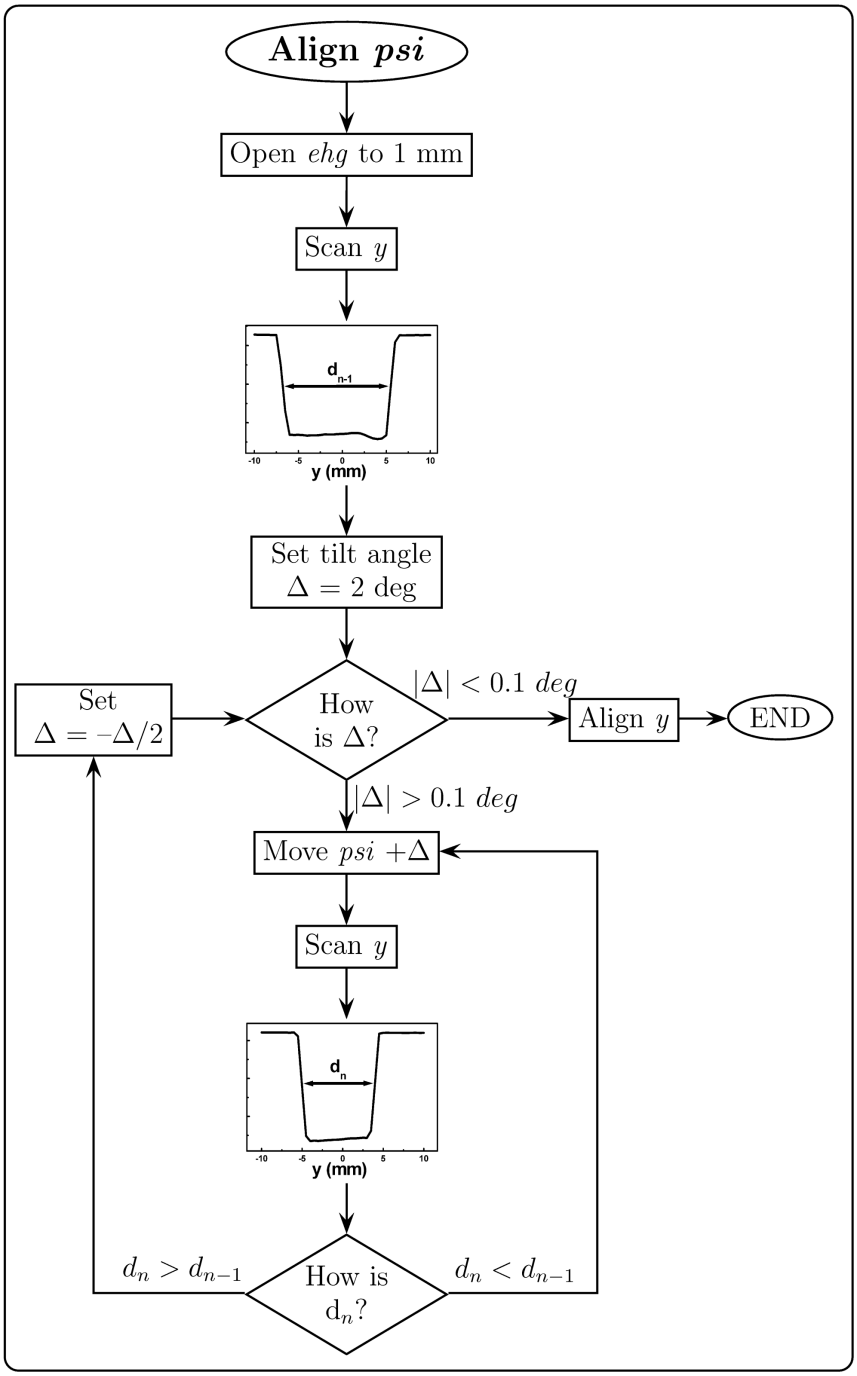

Figura A.5: Ejemplo del proceso de alineamiento

ocho de estos procesos.

A.3 Teoría y análisis de datos

El análisis de datos ReflEXAFS difiere enormemente del análisis de los espectros EXAFS tradicionales por varias razones. En la mayoría de los casos no es posible hacer simplemente una sustracción del fondo para extraer la estructura fina de los espectros a distintos ángulos. Por ello, se ha desarrollado un procedimiento de análisis específico para este proyecto.

A.3.1 Base teórica

A.3.1.1 Reflectividad

Tradicionalmente, el índice de refracción de un material en la región de los rayos X se escribe [37]

$$n(E) = 1 - \delta(E) - i\beta(E)\,, \tag{A.1}$$

donde $\delta(E)$ y $\beta(E)$ se pueden relacionar con los factores de dispersión anómala, $f'(E)$ y $f''(E)$ mediante [38]

$$\delta(E) \simeq \frac{e^2\hbar^2}{2\epsilon_0 m_e}\frac{1}{E^2}\rho_{at}\left[f^0 + f'(E)\right]\,, \tag{A.2a}$$

$$\beta(E) \simeq \frac{e^2\hbar^2}{2\epsilon_0 m_e}\frac{1}{E^2}\rho_{at} f''(E)\,, \tag{A.2b}$$

los cuales se pueden calcular a partir de una descripción clásica [38] o mecanocuántica [35] de la interacción fotón-electrón en el átomo absorbente. Además, $\delta(E)$ y $\beta(E)$ están relacionados por las transformaciones de Kramers-Kronig

($\mathcal{KK}$)

$$\delta(E) = \mathcal{KK}[\beta(E)] = -\frac{2}{\pi}\int_0^\infty dE' \frac{E'}{E^2 - E'^2}\beta(E')\,, \tag{A.3a}$$

$$\beta(E) = \mathcal{KK}^{-1}[\delta(E)] = \frac{2E}{\pi}\int_0^\infty dE' \frac{1}{E^2 - E'^2}\delta(E')\,, \tag{A.3b}$$

$$= -\mathcal{KK}[\delta(E)]\,. \tag{A.3c}$$

Además, $\beta(E)$ está relacionado directamente con el coeficiente de absorción $\mu(E)$ por la expresión

$$\mu(E) = \frac{2E}{\hbar c}\beta(E)\,, \tag{A.4}$$

El formalismo de la reflectividad de una superficie para ángulos bajos y en el rango de los rayos X fue propuesto por Parratt [37]. En él, el coeficiente de reflexión de Fresnel, $r_{j-1,j}$ en la intercara entre dos materiales $j-1$ y j, con índices de refracción n_{j-1} y n_j, puede aproximarse en la forma

$$r_{j-1,j} \simeq \frac{g_{j-1} - g_j}{g_{j-1} + g_j}\,, \tag{A.5}$$

donde

$$g_j = \sqrt{\theta_{j-1}^2 - 2\delta_j - 2i\beta_j}\,, \tag{A.6a}$$

$$g_0 = \theta_0\,, \tag{A.6b}$$

siendo θ_j el ángulo del rayo en el material j, y θ_0 el ángulo en el material inicial, que se considera aire o vacío ($n_0 = 1$).

En el mismo formalismo, se puede obtener una expresión del coeficiente de reflexión completo, $r'_{j-1,j}$, de una intercara cualquiera de una muestra hecha de N capas sobre un sustrato (que sería la capa $N+1$), que proviene de la suma de las múltiples reflexiones entre las intercaras [37]

$$r'_{j-1,j} = r_{j-1,j} + \frac{t_{j-1,j}t_{j,j-1}r'_{j,j+1}e^{-i\phi_j(E)-D_j\mu_j(E)}}{1 + r_{j-1,j}r'_{j,j+1}e^{-i\phi_j(E)-D_j\mu_j(E)}}\,. \tag{A.7}$$

Ésta es una expresión recursiva, ya que depende del coeficiente para la intercara inferior. Como desde el sustrato se considera infinito, no proviene de él ninguna reflexión,

$$r'_{N+1,N+2} = 0 \implies r'_{N,N+1} = r_{N,N+1}\,. \tag{A.8}$$

por lo que los $r'_{j-1,j}$ pueden calcularse iterando desde el sustrato hacia arriba para al final obtener el coeficiente para la superficie, $r'_{0,1}$, y así calcular la reflectividad,

$$R_{0,1} = \left|r'_{0,1}r'^{*}_{0,1}\right|\,. \tag{A.9}$$

A.3.1.2 Rugosidad

Este formalismo supone unas intercaras perfectamente planas. En muestras reales existe una interdifusión de material que se suele expresar como una rugosidad. Si esta rugosidad se modela estadísticamente, se puede llegar a una expresión de la reflectividad en función de un parámetro de rugosidad σ_j, de la intercara superior de la capa j.

El modelo más usado para la rugosidad es el de Nevot [41], que considera una rugosidad como una función gaussiana de las alturas en la intercara. En este trabajo, se ha usado una modificación de este modelo, que considera una interdifusión modelada por una función *tanh* [42], de forma que el índice de refracción en la intercara $j-1, j$ es

$$n(z) = \frac{n_{j-1}+n_j}{2} + \frac{n_{j-1}-n_j}{2}\tanh\left(\sqrt{\frac{2}{\pi}}\frac{z}{\sigma_j}\right)\,, \tag{A.10}$$

donde $z = 0$ es el punto donde el índice de refracción es la media aritmética entre los de ambas capas. Esta función da como resultado una distribución de alturas (rugosidad) con la forma

$$P_j^{\tanh}(z) = \frac{1}{\sqrt{2\pi}\sigma_j\cosh^2\left(\sqrt{\frac{2}{\pi}}\frac{z}{\sigma_j}\right)}\,, \tag{A.11}$$

que es muy parecida a la distribución gaussiana. La ventaja de escoger esta función es que es integrable, por lo que podemos introducirla en la ecuación del coeficiente de reflectividad de Parratt (Ecuación A.5) para obtener la reflectividad real

$$r_{j-1,j}^{\sigma_j,\tanh} = G_{j-1,j}\frac{\sinh\left[(\pi/2)^{\frac{3}{2}}\,\sigma_j k_{j-1}\,(g_{j-1}-g_j)\right]}{\sinh\left[(\pi/2)^{\frac{3}{2}}\,\sigma_j k_{j-1}\,(g_{j-1}+g_j)\right]}\,, \tag{A.12}$$

donde el parámetro $G_{j-1,j}$ tiene la forma

$$\begin{aligned} G_{j-1,j} = -\frac{\Gamma\left[2i\sqrt{\pi/2}\,\sigma_j k_{j-1} g_{j-1}\right]}{\Gamma\left[-2i\sqrt{\pi/2}\,\sigma_j k_{j-1} g_{j-1}\right]} &\times \frac{\Gamma\left[-i\sqrt{\pi/2}\,\sigma_j k_{j-1}\,(g_{j-1}+g_j)\right]}{\Gamma\left[i\sqrt{\pi/2}\,\sigma_j k_{j-1}\,(g_{j-1}+g_j)\right]} \\ &\times \frac{\Gamma\left[-i\sqrt{\pi/2}\,\sigma_j k_{j-1}\,(g_{j-1}-g_j)\right]}{\Gamma\left[i\sqrt{\pi/2}\,\sigma_j k_{j-1}\,(g_{j-1}-g_j)\right]}\,, \end{aligned} \tag{A.13}$$

A.3.2 Análisis ReflEXAFS

A.3.2.1 Aproximación de reflexión total

Martens [7, 18] propuso un modo de analizar un espectro ReflEXAFS en el caso de un ángulo de reflexión total.

Como la estructura fina de cada espectro ReflEXAFS es pequeña comparada con el fondo de reflectividad, se puede aproximar en primer orden en función de las estructuras finas de $\delta(E)$ y $\beta(E)$ en la forma

$$R(\delta,\beta) - R_0(\delta_0,\beta_0) = \Delta R \approx \left.\frac{\partial R}{\partial \delta}\right|_{\delta_0}\Delta\delta + \left.\frac{\partial R}{\partial \beta}\right|_{\beta_0}\Delta\beta\,, \tag{A.14}$$

donde

$$\delta(E) = \delta_0(E) + \Delta\delta(E) \tag{A.15a}$$

$$\beta(E) = \beta_0(E) + \Delta\beta(E) \tag{A.15b}$$

siendo R_0, δ_0 y β_0 las funciones sin la estructura fina, es decir, las funciones que habría si los átomos estuvieran aislados. En el caso de reflexión total, es decir, cuando en ángulo de incidencia es inferior al ángulo crítico,

$$\frac{\theta}{\sqrt{2\delta}} = \frac{\theta}{\theta_c} < 1\,. \tag{A.16}$$

ocurre que $\frac{\partial R}{\partial \beta}$ es varios órdenes de magnitud superior a $\frac{\partial R}{\partial \delta}$ para valores típicos de δ (10^{-5}) y β (10^{-6}). Por tanto, $\Delta R(E)$ es proporcional a $\Delta\beta(E)$ y se puede calcular la estructura fina EXAFS $\chi(E)$ de forma sencilla

$$\chi(E) = \frac{\mu(E) - \mu_0(E)}{\mu_0(E)} = \frac{\beta(E) - \beta_0(E)}{\beta_0(E)} = \frac{\Delta\beta(E)}{\beta_0(E)} \approx \frac{\Delta R(E)}{R_0(E)}\,, \tag{A.17}$$

A.3.2.2 Análisis global

Para un análisis global de los espectros ReflEXAFS es necesario el cálculo completo de los términos de la ecuación A.14. Para ello, primero debe calcularse los coeficientes δ_0 y β_0 mediante una simulación y ajuste de la reflectividad sin la estructura fina. Luego, se simulan las estructuras finas de la reflectividad para cada ángulo en términos de las funciones EXAFS presentes en la muestra.

Simulación y ajuste de la reflectividad de átomo aislado

Los espectros de reflectividad sin la estructura fina dependen de los índices de refracción de cada elemento presente en la muestra. En el ejemplo particular de una multicapa, con capas $j \in \{1, \ldots, N\}$, cada espectro de reflectividad se puede escribir como

$$R_{0m}(E) = R_{0m}\left[\delta_{0j}(E), \beta_{0j}(E)\right]\,, \tag{A.18}$$

donde $m \in \{1, \ldots, M\}$ denota cada ángulo diferente al que se ha recogido el espectro.

Cada muestra puede identificarse por los espesores, composición y densidad de cada una de sus capas, así como por la rugosidad de sus intercaras. Me-

diante las ecuaciones presentadas en la Sección A.3.1, se pueden calcular las reflectividades.

Como ni parámetros que definen la muestra ni los parámetros experimentales (ángulos de incidencia precisos, desplazamiento en energía de los espectros) se pueden determinar con total exactitud, estos se introducen como variables en un programa de simulación que busca los valores a partir de los cuales se genera el espectro de reflectividad que mejor reproduce el experimental.

Al haber una gran cantidad de variables, es necesario diseñar estrategias que faciliten la localización de la solución óptima, así como usar un algoritmo de optimización del tipo evolutivo llamado *Covariance Matrix Adaptation Evolutionary Strategy* o *CMA-ES* [48]

El resultado de la simulación proporciona por un lado la posibilidad de extraer la estructura fina $\Delta R_m(E)$ de cada espectro, y además, calcula los valores de δ_{0j} y β_{0j}, que serán necesarios para el siguiente paso.

Simulación y ajuste ReflEXAFS

Una vez extraída la estructura fina de cada espectro, ésta se puede suponer como función de las estructuras finas de los índices de refracción correspondientes sólo a las capas que generen una señal EXAFS, es decir

$$\Delta R_m(E) = \Delta R_m\left[\Delta\delta_h(E), \Delta\beta_h(E)\right] , \tag{A.19}$$

donde $h \in \{1, \ldots, H\}$ es el índice que cuenta las capas que contribuyen a la señal EXAFS, es decir que contienen el átomo cuyo borde de absorción se está estudiando, de forma que $1 \leq H \leq N+1$ en general. Como $\Delta R_m(E)$ es pequeño, se puede desarrollar en primer orden en función de las estructuras finas de $\delta_h(E)$ y $\beta_h(E)$ en la forma

$$\Delta R_m(E) \approx \sum_{h=1}^{H} \left[\left.\frac{\partial R_m}{\partial \delta_h}\right|_{\delta_{0h}} \Delta\delta_h(E) + \left.\frac{\partial R_m}{\partial \beta_h}\right|_{\beta_{0h}} \Delta\beta_h(E) \right] , \tag{A.20}$$

Estas ecuaciones se deben satisfacer simultáneamente y para todos los posibles espectros m a cada ángulo de incidencia diferente, pero compartiendo los

$\Delta\delta_h(E)$ y $\Delta\beta_h(E)$, pues la muestra es la misma. Entonces podemos escribir todas las ecuaciones en forma matricial

$$\begin{pmatrix} \Delta R_1(E) \\ \vdots \\ \Delta R_M(E) \end{pmatrix} = A(E) \begin{pmatrix} \Delta\delta_1(E) \\ \Delta\beta_1(E) \\ \vdots \\ \Delta\delta_H(E) \\ \Delta\beta_H(E) \end{pmatrix}, \tag{A.21}$$

donde la matriz de coeficientes, $A(E)$, es

$$A(E) = \begin{pmatrix} \left.\frac{\partial R_1}{\partial \delta_1}\right|_{\delta_{01}} & \left.\frac{\partial R_1}{\partial \beta_1}\right|_{\beta_{01}} & \cdots & \left.\frac{\partial R_1}{\partial \delta_H}\right|_{\delta_{0H}} & \left.\frac{\partial R_1}{\partial \beta_H}\right|_{\beta_{0H}} \\ \vdots & \vdots & \ddots & \vdots & \vdots \\ \left.\frac{\partial R_M}{\partial \delta_1}\right|_{\delta_{01}} & \left.\frac{\partial R_M}{\partial \beta_1}\right|_{\beta_{01}} & \cdots & \left.\frac{\partial R_M}{\partial \delta_H}\right|_{\delta_{0H}} & \left.\frac{\partial R_M}{\partial \beta_H}\right|_{\beta_{0H}} \end{pmatrix}, \tag{A.22}$$

Este sistema de ecuaciones lineales se puede resolver. Para ello, se generan funciones aleatorias $\Delta\delta_h(E)$ y $\Delta\beta_h(E)$, para las cuales se calculan los coeficientes de la matriz para cada punto de energía. Seguidamente, se calcula la matriz *pseudoinversa* de Moore-Penrose $A^+(E)$ de $A(E)$, ya que ésta da la solución de mínimos cuadrados de este sistema sobredeterminado [49, 50].

Esta solución es otro conjunto de funciones $\Delta\delta_h(E)$ y $\Delta\beta_h(E)$ en general diferente de la anterior, que se pueden volver a introducir en la ecuación en un proceso iterativo hasta que la diferencia entre las funciones en dos pasos consecutivos sea pequeña.

Para el cálculo de la matriz *pseudoinversa*, es conveniente usar una descomposición ortogonal de la matriz $A(E)$. Específicamente, se usó el método de descomposición en valores singulares (SVD), ya que permite la posibilidad de despreciar los valores pequeños en esta matriz, que provocarían errores de redondeo en el cálculo de la matriz pseudoinversa por un ordenador.

A.4 Resultados

En este resumen se han seleccionado sólo algunas muestras representativas. El resto de los resultados puede verse en los capítulos 5 a 8

A.4.1 Muestra CuCrx2

A.4.1.1 Caracterización

La curva XRR fue simulada usando el algoritmo del programa GenX [26], para obtener el espesor, densidad y rugosidad de las capas en la muestra. La Figura A.6 muestra la curva experimental y la simulada, mientras que la Tabla A.1 incluye los parámetros de mejor ajuste de la simulación.

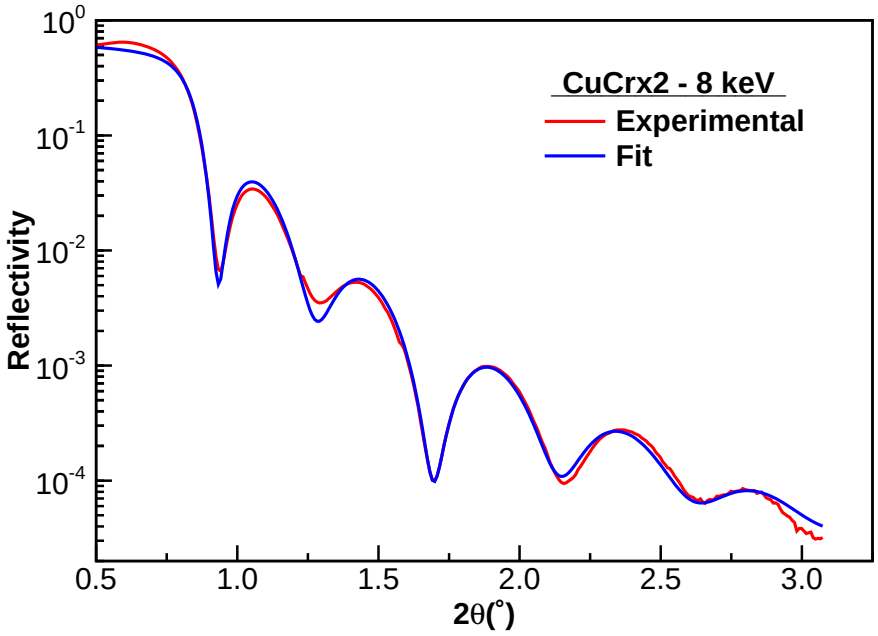

Figura A.6: Curva XRR experimental a 8 keV y menor ajuste para la muestra CuCrx2

Los resultados de RBS se muestran en la Tabla A.2, donde se ha supuesto que la densidad de las capas es igual a la densidad del metal en estado cristalino,

Tabla A.1: Parámetros de mejor ajuste de la curva XRR para la muestra CuCrx2

Energía	**Espesor (Å)**		**Densidad Relativa**		**Rugosidad (Å)**		
	Cu	Cr	Cu	Cr	Sus.	Int.	Sup.
10 keV	54	35	1.00	0.90	5	16	11

o bien a la densidad calculada en la simulación de la curva XRR, y que todas las capas de la misma composición tienen el mismo espesor, ya que han sido depositadas en las mismas condiciones.

Tabla A.2: Espesor de las capas de la muestra CuCrx2 medidas por RBS

Muestra	**Espesor (Å) (Dens. Crist.)**		**Espesor (Å) (Dens. XRR)**		**×N**
	Cu	Cr	Cu	Cr	
CuCrx2	54	31	54	34	×2

La Figura A.7 muestra la topografía superficial de la muestra CuCrx2 medida por AFM. La rugosidad superficial calculada como la dispersión de las alturas en el rango de la medida da un resultado de 3 Å.

A.4.1.2 Experimento ReflEXAFS

La Figura A.8 muestra la curva XRR, donde se han marcado los ángulos escogidos para registrar los espectros ReflEXAFS. Estos ángulos se seleccionaron porque cubren un rango suficientemente amplio tanto en la profundidad de penetración de los rayos X, como en las distintas formas que pueden tomar los espectros debido a las interferencias entre las capas.

La Figura A.9 muestra el conjunto de espectros ReflEXAFS (en línea continua), normalizados por el espectro de haz directo. Por un lado, se observa la rápida caída de la intensidad de la onda reflejada por encima del ángulo

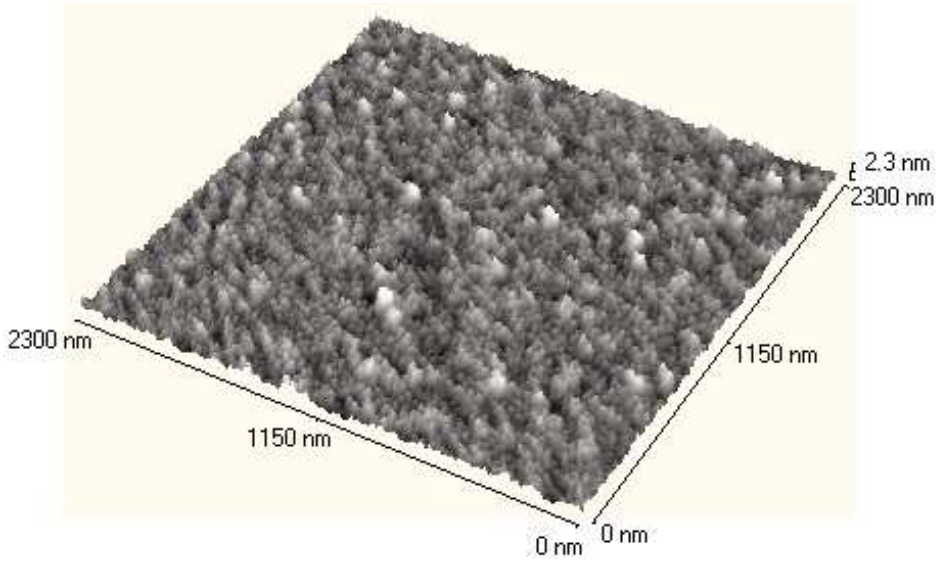

Figura A.7: Topografía superficial de la muestra CuCrx2, medida por AFM

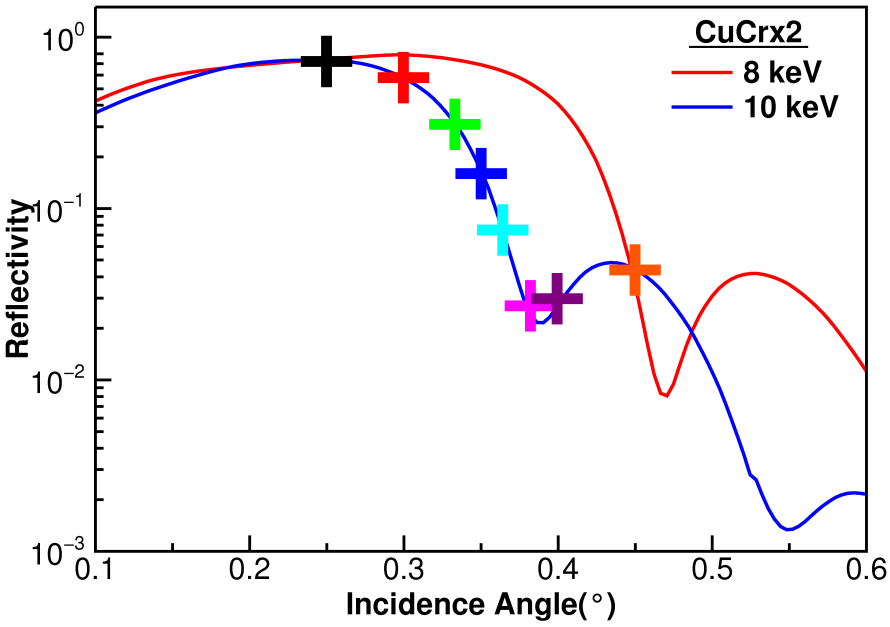

Figura A.8: Diagrama XRR experimental mostrando los ángulos escogidos para los espectros ReflEXAFS, para la muestra CuCrx2

crítico (que, en este caso, está alrededor de 0.320°). Asimismo, se pueden observar los patrones de interferencia producidos por las multicapas de la muestra.

Superpuesto al fondo de reflectividad, se puede ver claramente el borde de absorción K del Cu (8.979 keV), y de la estructura fina justo a continuación, extendido hacia alta energía.

A.4.1.3 Análisis

Usando la *aproximación de reflexión total* [18], podemos extraer la estructura fina del ángulo más bajo. Debido a que el espectro a 0.250° tiene muy mala relación señal-ruido, se escogió el de 0.300° para este análisis.

La función EXAFS obtenida se ajustó con los programas FEFF 6.0 y FEFFIT 2.54 [45, 46]. Se usó un modelo de Cu metálico, tomando las cinco primeras esferas de coordinación con los números de coordinación fijos e iguales a los cristalinos. Se tomo un parámetro Δa, que variara el parámetro de red del cristal, de forma que todas las distancias de coordinación variaran coherentemente. Los factores de Debye-Waller se consideraron parámetros independientes para cada esfera.

Los resultados del ajuste se pueden ver en la Tabla A.3. Las Figuras A.10 y A.11 muestran la comparación de los espectros EXAFS experimentales con las curvas de mejor ajuste tanto en el espacio k como en el espacio R.

Tabla A.3: Parámetros de ajuste EXAFS para el ángulo 0.300° en la muestra CuCrx2

a (Δa)	3.61 Å (+0.00 Å)				
Esfera	**1**^{a}	**2**^{a}	**3**^{a}	**4**^{a}	**5**^{a}
N	8	6	12	24	8
R (Å)	2.56	3.61	4.43	5.11	5.72
σ^2 **(Å^2)**	0.010	0.014	0.017	0.018	0.020

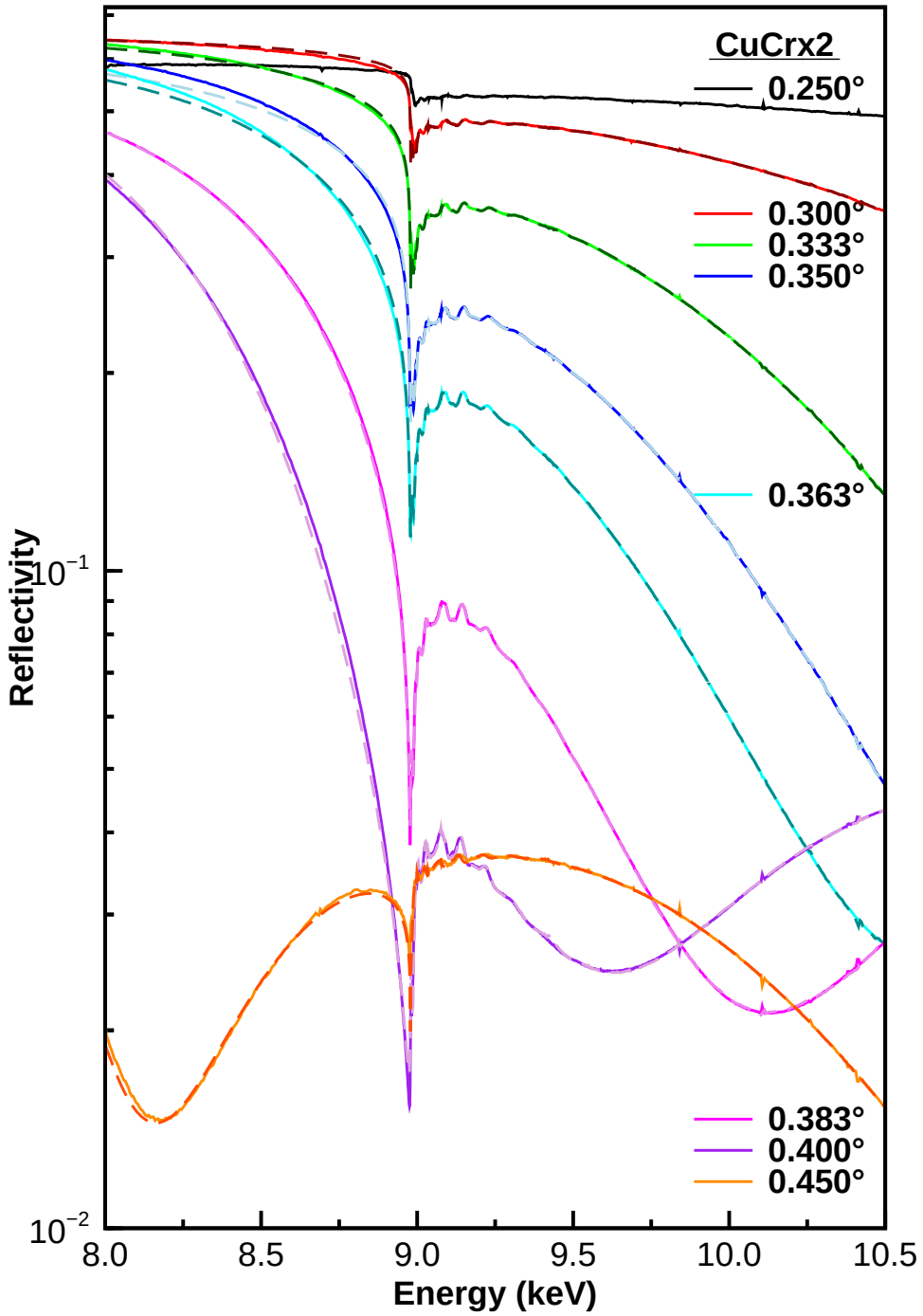

Figura A.9: Espectros experimentales ReflEXAFS (continuo) y mejor ajuste (discontinuo) para la muestra CuCrx2

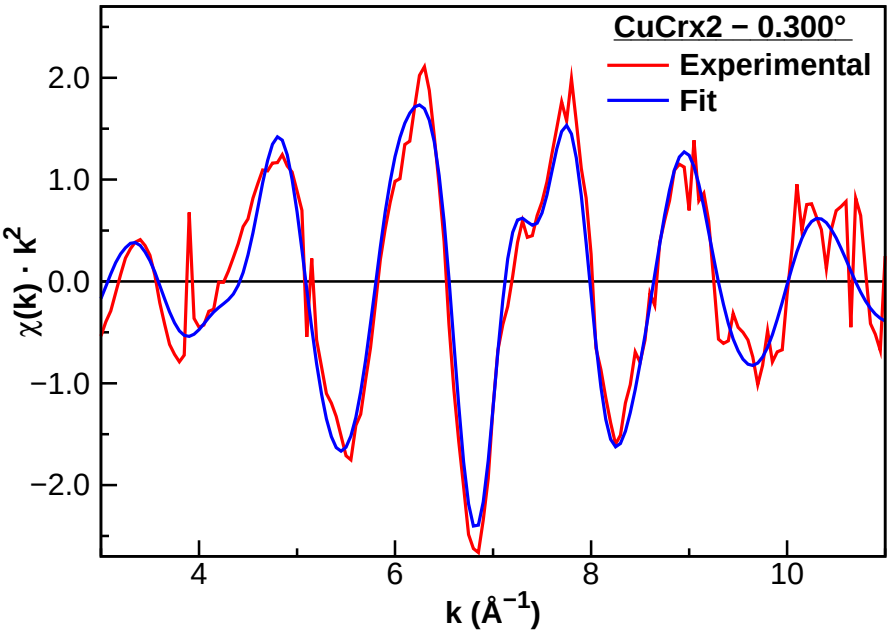

Figura A.10: χ(k) EXAFS experimental y mejor ajuste para la muestra CuCrx2

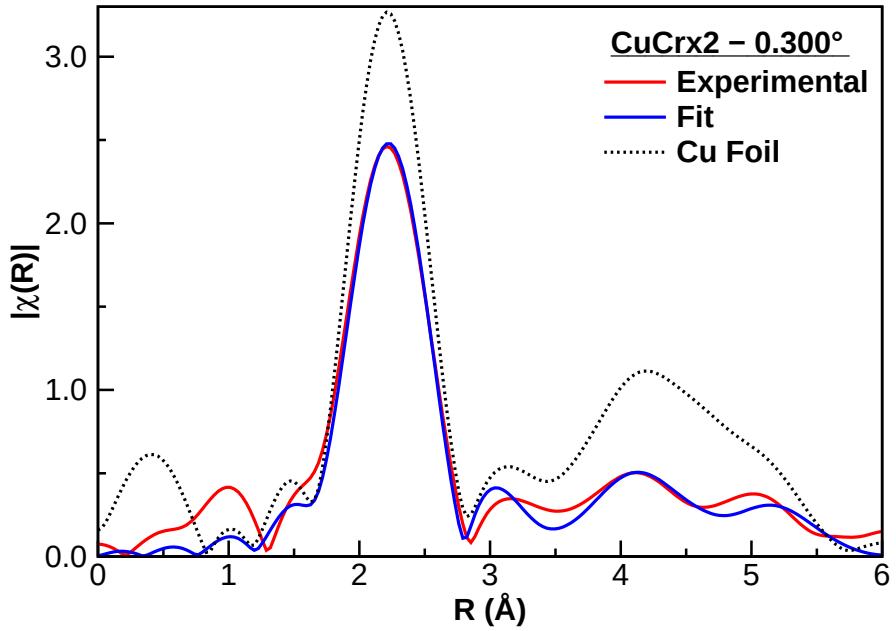

Figura A.11: χ(R) EXAFS experimental y mejor ajuste para la muestra CuCrx2

La estructura del Cu en estas capas es análoga a la que presenta en fase cristalina en lo que a distancias y números de coordinación se refiere, pero mucho más desordenada, como se refleja en los valores de los parámetros de Debye-Waller.

Para analizar los espectros ReflEXAFS de forma *global*, se usó el programa desarrollado expresamente para este fin. Primero se simuló el fondo de reflectividad (sin la estructura fina) dando como resultado los parámetros de mejor ajuste de espesor, densidad y rugosidad de las capas, además de los ángulos concretos de los espectros y el desplazamiento en energía. Estos se muestran en las Tablas A.4 (parámetros de la muestra) y A.5 (ángulos de mejor ajuste). El desplazamiento en energía de los espectros fue de -2.8 eV.

Tabla A.4: Resultados de la simulación de espectros ReflEXAFS (muestra)

Muestra	**Espesor (Å)**		**Densidad (at/Å^3)**		**Rugosidad (Å)**		
	Cu	Cr	Cu	Cr	Subst.	Interf.	Sup.
CuCrx2	50	32	0.085	0.075	18	17	10

Tabla A.5: Resultados de la simulación de espectros ReflEXAFS (ángulos)

CuCrx2	
Angle	**Fit**
0.250	0.254
0.300	0.302
0.333	0.331
0.350	0.347
0.363	0.358
0.383	0.376
0.400	0.395
0.450	0.458

Posteriormente, se extrajo la estructura fina suponiendo que todas las capas de Cu tienen la misma función EXAFS. Así, el ajuste completo se puede apreciar en la Figura A.9 (discontinuo).

Una vez que se extrajo la función EXAFS global a partir de los espectros medidos a todos los ángulos, fue analizada de la misma forma que la de ángulo de reflexión total. En la Tabla A.6 se resumen los parámetros de mejor ajuste del análisis. En las Figuras A.12 y A.13 se muestran la función EXAFS y su mejor ajuste en los espacios k y R.

Como ya se vio en el ajuste del espectro del ángulo de reflexión total, puede observarse cómo el desorden estructural en el entorno local del Cu en las capas de esta muestra es notable comparado con un entorno cristalino. Esto es producido porque el sistema de deposición de capas empleado no permite la relajación de la estructura de las capas a la estructura cristalina, ya que la condensación de los átomos sobre el sustrato se produce rápidamente, y no se ha aplicado un calentamiento al mismo. Además, el pequeño espesor de estas capas tiene el mismo efecto inhibiendo el orden a largo alcance en una de las direcciones del espacio.

Tal como es esperable, los resultados del análisis global (que analiza la muestra completa) difieren poco del análisis de ángulo de reflexión total (que solo analiza las primeras decenas de Ångströms). Esto se debe a que la capa más superficial de Cr que recubre la muestra ha evitado la oxidación de la capa superior de Cu, que debe tener una estructura muy parecida a la inferior, pues están sintetizadas en las mismas condiciones.

Tabla A.6: Resultados globales EXAFS para la muestra CuCrx2

a (Δa)	3.61 Å (+0.00 Å)				
Esfera	**1**^{a}	**2**^{a}	**3**^{a}	**4**^{a}	**5**^{a}
N	8	6	12	24	8
R (Å)	2.56	3.61	4.43	5.11	5.72
σ^2 (Å^2)	0.011	0.017	0.019	0.020	0.030

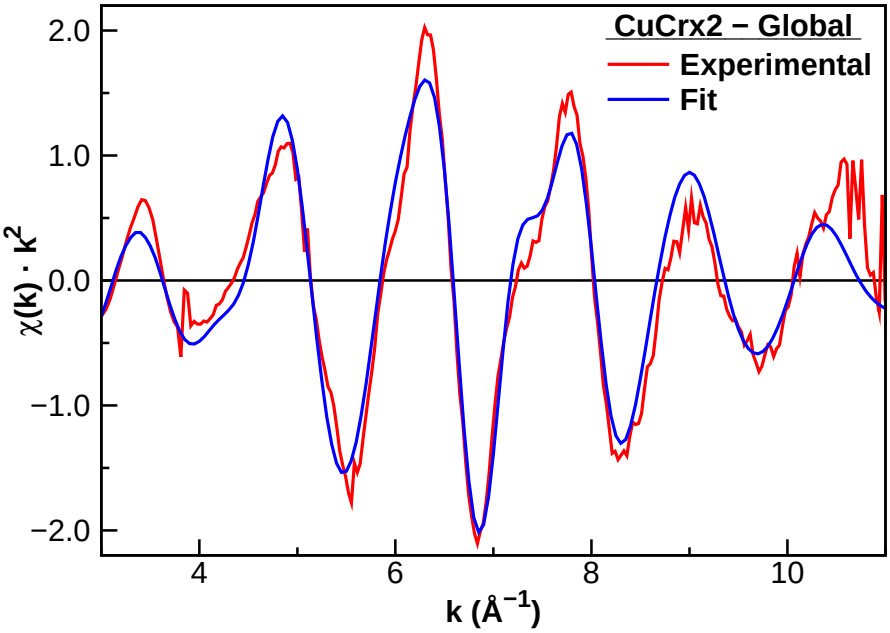

Figura A.12: χ(k) EXAFS experimental del análisis global, y mejor ajuste para la muestra CuCrx2

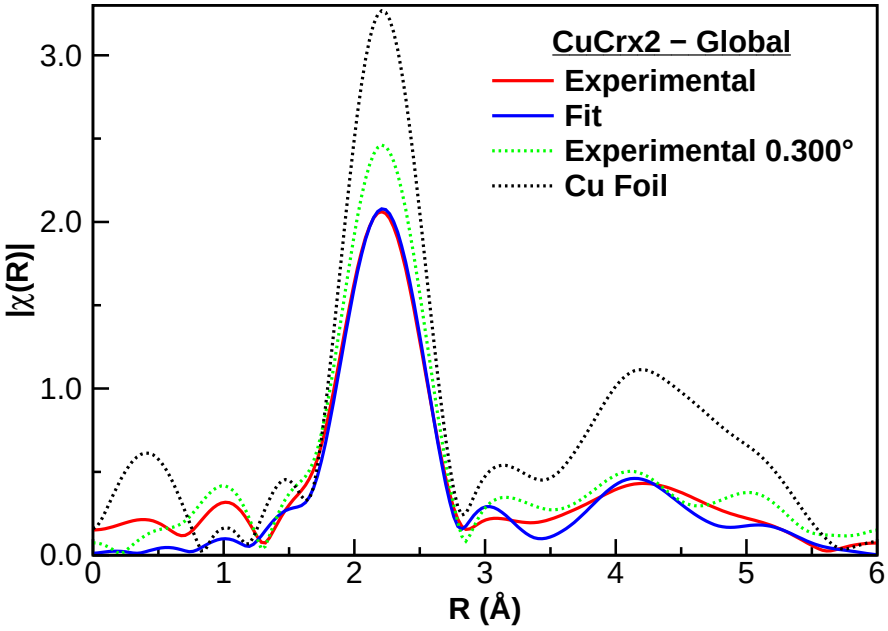

Figura A.13: χ(R) EXAFS experimental del ángulo de reflexión total, global, y mejor ajuste del global para la muestra CuCrx2

A.4.2 Aceros modificados superficialmente

Se estudiaron dos muestras del mismo acero de herramientas, ferrítico, con una composición de 3 % Cr, 0.8 % Mo, 0.3 % V, 0.3 % C y resto de Fe, una nitrurada y la otra sin nitrurar.

A.4.2.1 Caracterización

Se registraron diagramas de difracción de rayos X a bajo ángulo para ambas muestras. Así se aumenta la señal de las especies presentes en la zona más superficial.Estos diagramas se tomaron tras pulir las muestras, para estudiar el desorden de la matriz de Fe eliminando los compuestos FeN_x, ya que tienen poca adherencia y no mejoran las propiedades mecánicas (Figura A.14).

Los picos del Fe-*bcc* en la muestra nitrurada son más anchos y están desplazados hacia ángulos de difracción menores que en la muestra no nitrurada.

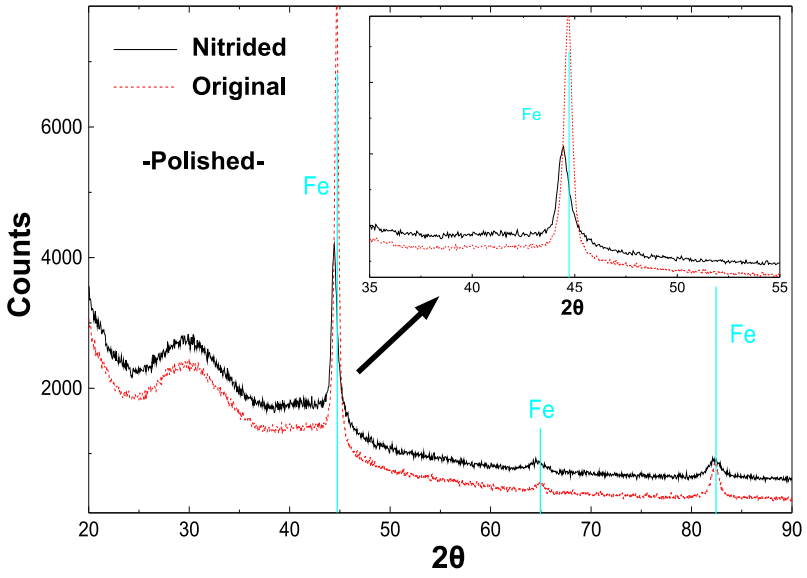

Figura A.14: Diagrama XRD para el acero nitrurado y no nitrurado tras el pulido

Esto indica que la nitruración produce una deformación y expansión de la estructura.

Se tomaron micrografías SEM tras tratar la superficie de las muestras con ácido nítrico y etanol para revelar su estructura de granos.

La micrografía (Figura A.15) muestra la estructura de agujas típica de la precipitación de la ferrita en la fabricación del acero.

A.4.2.2 Experimentos ReflEXAFS

Se obtivieron diagramas XRR a 8 keV para ver el comportamiento de la reflectividad a diferente ángulo para una energía cercana al borde K de absorción del Fe, y así escoger los ángulos más convenientes para las medidas ReflEXAFS.

Los espectros ReflEXAFS se registraron a distintos ángulos en torno al borde K de absorción del Fe, para ambas muestras (Figuras A.16 y A.17).

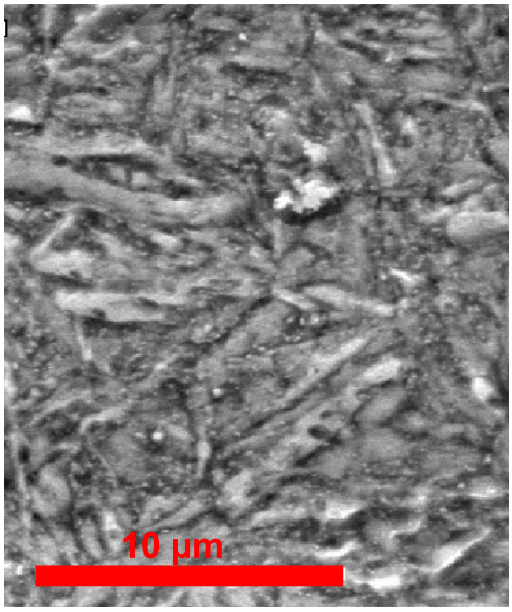

Figura A.15: Micrografía SEM de la superficie del acero nitrurado

A primera vista, los espectros de ambas muestras parecen iguales. Sin embargo, al extraer los espectros para ángulo de reflexión total, se puede ver que existe una diferencia notable entre ambos (Figura A.18)

Las transformadas de Fourier de los espectros EXAFS (Figura A.19) revelan que, mientras que la muestra sin nitrurar tiene un entorno típico de la estructura Fe-*bcc*, la muestra nitrurada presenta una contribución a bajo R que puede deberse a una esfera de coordinación con un retrodispersor ligero, como el N.

A.5 Conclusiones

El objetivo principal de este proyecto consistió en el diseño de protocolos para el registro y el análisis de espectros ReflEXAFS en un amplio rango de ángulos, incluidos aquellos superiores al ángulo crítico cuya medida y análisis

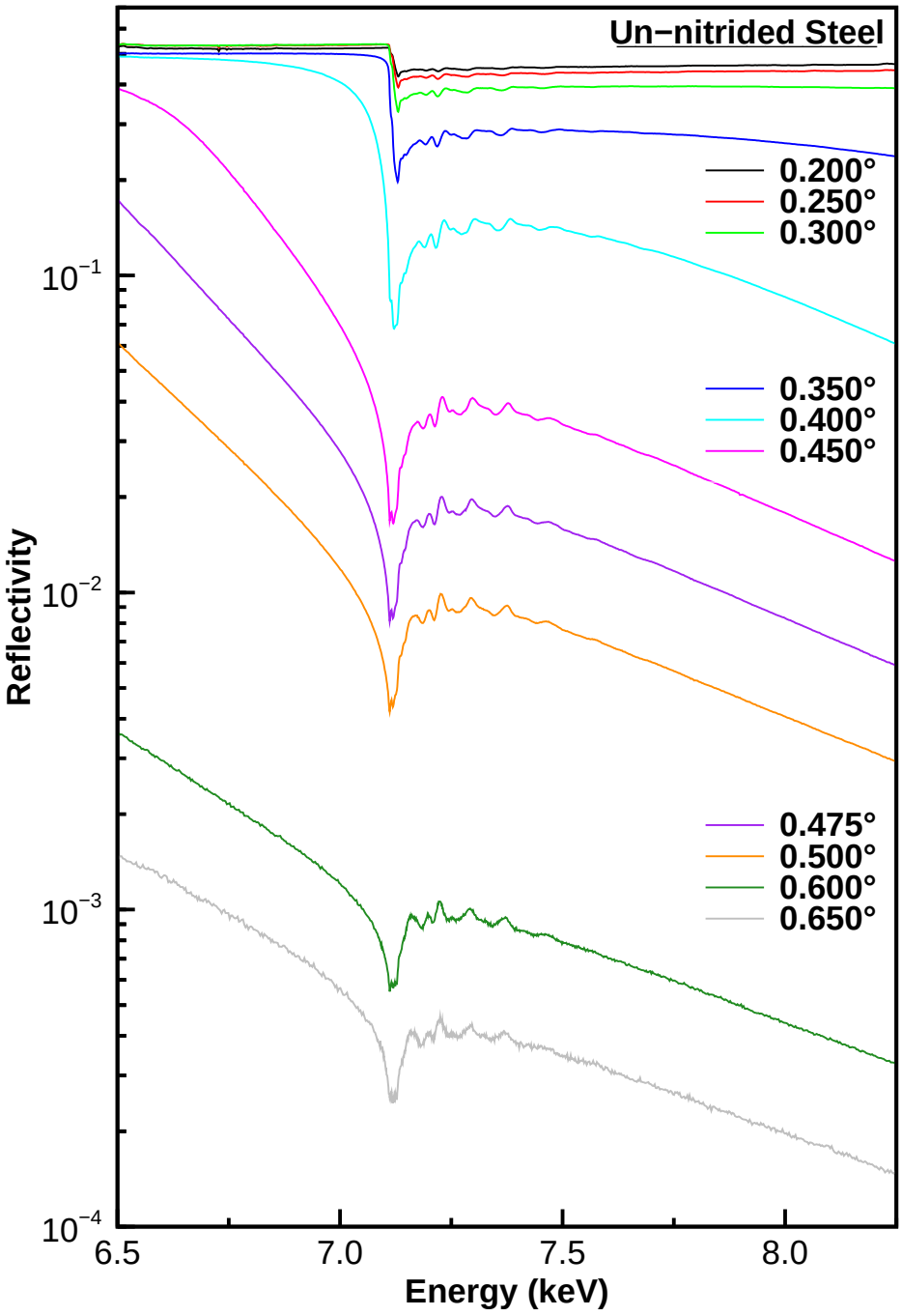

Figura A.16: Espectros ReflEXAFS normalizados para el acero no nitrurado

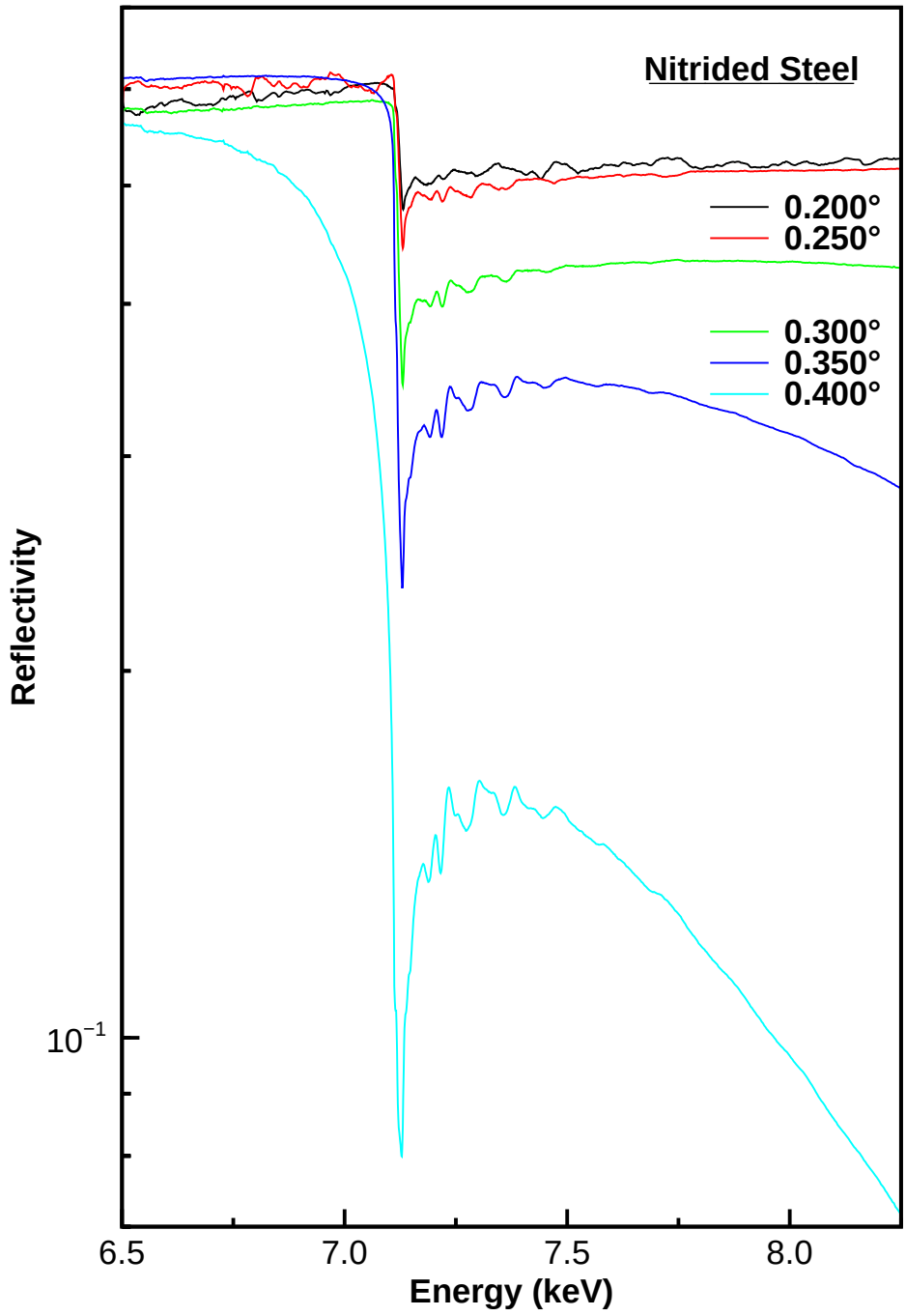

Figura A.17: Espectros ReflEXAFS normalizados para el acero nitrurado

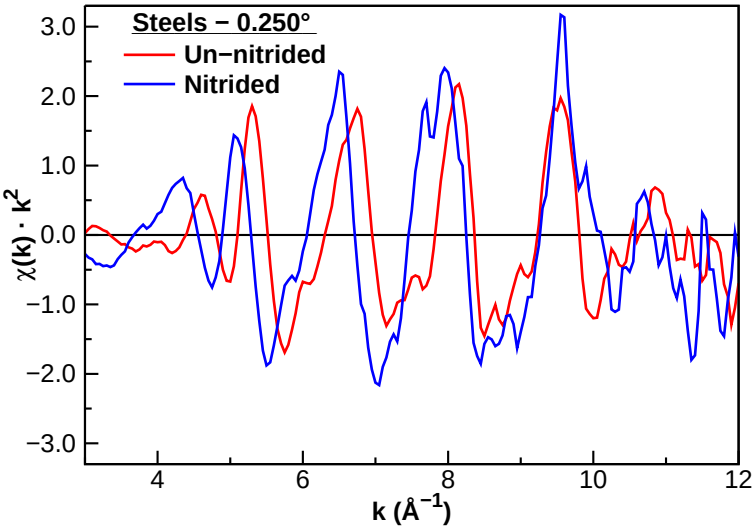

Figura A.18: χ(k) EXAFS experimental para el ángulo de reflexión total para los aceros no nitrurado y nitrurado

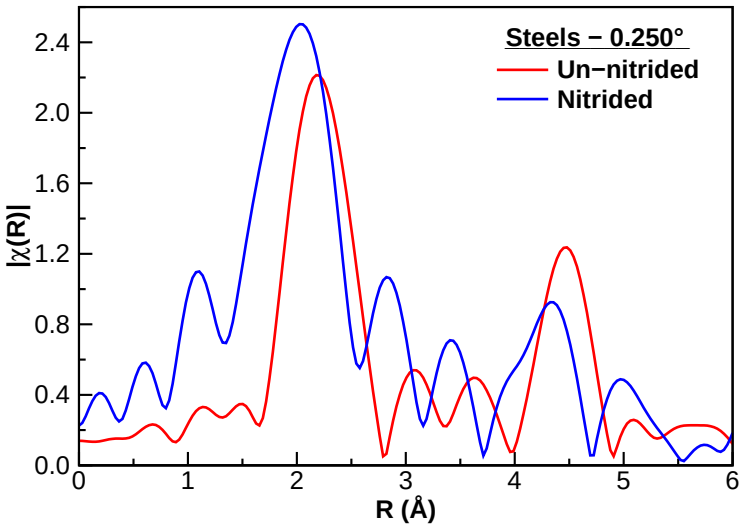

Figura A.19: χ(R) EXAFS experimental para el ángulo de reflexión total para los aceros no nitrurado y nitrurado

no se había abordado hasta ahora.

Esto ha permitido la obtención de información estructural no sólo a la parte más superficial de las muestras (decenas de Å desde la superficie) sino de regiones más profundas, a centenares de Å.

Para ello, se trabajó en dos frentes. En el frente experimental se desarrollaron, en la estación BM29 de la Fuente Europea de Radiación Sincrotrón (ESRF), los protocolos de medida optimizados para obtener datos de forma eficiente, automática y de suficiente calidad como para ser analizados.

En el frente teórico, se desarrolló un método de análisis de datos específico para estas medidas. Este método toma todos los datos de forma global para obtener la función EXAFS de la muestra.

Las muestras estudiadas se seleccionaron no sólo para que sirvieran para probar la técnica en diferentes condiciones, partiendo desde las más sencillas a las más complicadas de estudiar, sino que también se tuvo en cuenta su interés desde el punto de vista de la ciencia de materiales.

La primera serie de muestras fueron multicapas CuCrxN que sólo tenían un entorno local en toda la muestra, Cu metálico. Se vio cómo al reducir el espesor de las capas de cobre, aumentando número de repeticiones de la multicapa manteniendo su espesor total, éstas aumentaban su desorden estructural y reducían su parámetro reticular, pero mantenían las distancias y números de coordinacion del Cu metálico.

La segunda serie fueron multicapas de CrCux3, donde se expuso la capa de Cu más superficial al aire. Se encontró cómo ésta capa se oxida parcialmente dando tanto óxido de Cu(I) como óxido de Cu(II)

También se estudiaron multicapas de Mo y MoN, con las cuales se demostró que el protocolo experimental desarrollado es suficientemente robusto como para poder obtener espectros de alta calidad en condiciones adversas de rango angular limitado provocado por la alta energía estudiada, llegando a medir espectros con una diferencia de intensidad reflejada de 4 órdenes de magnitud.

Finalmente, se estudiaron aceros nitrurados en fase gaseosa. De estas muestras se obtuvieron buenos espectros a pesar de que no reunían las características óptimas para su medida por esta técnica, lo que demostró la robustez del método desarrollado. Se encontró que existen cambios en el entorno local del Fe a muy baja profundidad desde la superficie, cosa que no se ha detectado en los espectros EXAFS de fluorescencia [2], donde la profundidad de penetración de la técnica es del orden de los miles de Å.

Appendix B

The Laws of synchrotron radiation experiments

Law 1 *If a motor has two possible ways of movement, the experimentalists will always move it in the wrong one first.*

> **Theorem 1.1** *The experimentalists will not realize this until this wrong movement has been done completely.*

Law 2 *Once the experimentalists have checked everything in the sample room, left the room, closed the door, checked the security issues and sit in front of the computer in the control room, they will find out what is missing or wrong in the sample room.*

Law 3 *An experiment will only run properly if there is someone watching and checking constantly.*

> **Theorem 3.1** *Any attempt to program a macro to let the experimentalists do something different than watching or checking the experiment has a high probability to fail.*
>
> > **Corollary 3.1.1** *The probability of a macro to fail is proportional to the amount of sleep the experimentalists are enjoying.*

Corollary 3.1.2 *The probability of a macro to fail is proportional to the amount and quality of the food the experimentalists are eating.*

Corollary 3.1.3 *The probability of a macro to fail is proportional to the amount of amusement the experimentalists are enjoying.*

Law 4 *The most interesting sample will be measured the last, so the data will be incomplete or useless.*

Theorem 4.1 *This is independent of the amount of planning done before and during the experiment.*

Theorem 4.2 *The experimentalists will realize which was the most interesting sample once they have returned home.*

Corollary 4.2.1 *Any attempt to bring the most interesting sample to the synchrotron to be measured again will be impossible due to either sample destruction or no more beamtime allocation or beamline/synchrotron closure.*

Law 5 *The probability of missing breakfast/lunch/dinner for some more sleep is proportional to the quality of the food involved.*

Law 6 *The experimentalists will only need the local contact when he/she is unavailable.*

Theorem 6.1 *The probability of having a problem is proportional to the unavailability of the local contact.*

Theorem 6.2 *The seriousness of the problem is proportional to the unavailability of the local contact.*

Bibliography

[1] M. Ohring. *The materials science of thin films* (Academic Press, London, 2002), 2^{nd} edn. 1

[2] A. Muñoz-Páez, J. I. F. Peruchena, J. P. Espinós, A. Justo, F. Castañeda, S. Díaz-Moreno and D. T. Bowron. Experimental evidences of new nitrogen-containing phases in nitrided steels. *Chem. Mat.* **14**, 3220 (2002). 1, 8, A.5

[3] M. Vila, C. Prieto, J. García-Lopez and M. A. Respaldiza. Influence of the target and working gas on the composition of silicon nitride thin films prepared by reactive RF-sputtering. *Nuc. Instr. Meth. B* **211**, 199–205 (2003). 1, 2.1.1, 2.1.1.1

[4] S. K. Sinha. Application of synchrotron radiation techniques to nanoscience. *Rad. Phys. Chem.* **70**, 633–640 (2004). 1

[5] T. Hayes and J. Boyce. Extended X-ray Absorption Fine-Structure spectroscopy. *Sol. St. Phys.* **37**, 173–351 (1982). 1

[6] A. Erbil, G. S. Cargill, R. Frahm and R. F. Boehme. Total-Electron-Yield current measurements for near-surface Extended X-ray-Absorption Fine-Structure. *Phys. Rev. B* **37**, 2450–2464 (1988). 1

[7] G. Martens and P. Rabe. EXAFS studies on superficial regions by means of total reflection. *Phys. Stat. Sol. A* **58**, 415–424 (1980). 1, 4.2.1, 9, A, A.3.2.1

[8] S. M. Heald, H. Chen and J. M. Tranquada. Glancing-angle extended x-ray-absorption fine-structure and reflectivity studies of interfacial regions. *Phys. Rev. B* **38**, 1016–1026 (1988). 1, A

[9] S. Pizzini, K. J. Roberts, I. S. Dring, R. J. Oldman and G. N. Greaves. Applications of glancing-angle X-ray absorption-spectroscopy to the structural characterization of copper film surfaces. *Physica B* **150**, 676–678 (1989). 1, A

[10] N. T. Barrett, G. N. Greaves, S. Pizzini and K. J. Roberts. The local atomic-structure of the oxide coating on polished GaAs(100). *Surf. Sci.* **227**, 337–346 (1990). 1

[11] K. E. R. England, J. M. Charnock, R. A. D. Pattrick and D. J. Vaughan. Surface oxidation studies of chalcopyrite and pyrite by glancing-angle X-ray absorption spectroscopy (REFLEXAFS). *Min. Mag.* **63**, 559–566 (1999). 1

[12] F. d'Acapito, S. Mobilio, P. Cikmacs, V. Merlo and I. Davoli. Temperature modification of the Nb oxidation at the Nb/Al interface studied by reflEXAFS. *Surf. Sci.* **468**, 77–84 (2000). 1, A

[13] F. d'Acapito, M. de Seta, G. Capellini, L. di Gaspare and F. Evangelisti. Relaxed state of GexSi1-x islands embedded in Si. *Nuc. Instr. Meth. B* **246**, 64–68 (2006). 1, A

[14] G. Agostini *et al.* Reactivity of Cr species grafted on SiO2/Si(100) surface: A reflection extended X-ray absorption fine structure study down to the submonolayer regime. *J. Phys. Chem. C* **111**, 16437–16444 (2007). 1

[15] S. Pizzini, K. J. Roberts, G. N. Greaves, N. Harris, P. Moore, E. Pantos and R. J. Oldman. Instrumentation for glancing angle X-ray absorption-spectroscopy on the synchrotron radiation source. *Rev. Sci. Instrum.* **60**, 2525–2528 (1989). 1, 3, A

[16] F. d'Acapito, I. Davoli, P. Ghigna and S. Mobilio. The ReflEXAFS station at the GILDA beamline (BM08) of ESRF. *J. Synchr. Rad.* **10**, 260–264 (2003). 1, 3, A

[17] G. Martens and P. Rabe. EXAFS of a thin-film of Cu measured by total reflection. *Phys. Stat. Sol. A* **57**, K31–K34 (1980). 1, 4.2.1, 9, A

[18] G. Martens and P. Rabe. The extended X-ray absorption fine-structure in the reflectivity at the K edge of Cu. *J. Phys. C* **14**, 1523–1534 (1981). 1, 4.2.1, 5.3.1, 6.3.1, 7.3.1, 8.3.1, 9, A, A.3.2.1, A.4.1.3

[19] P. Borthen and H.-H. Strehblow. X-ray reflectivity fine-structure from homogeneous materials in the hard-energy range. *J. Phys.: Condens. Matter* **7**, 3779–3787 (1995). 1, 4.2.2, 4.2.2, 9, A

[20] P. Borthen and H.-H. Strehblow. X-ray-reflectivity fine-structure and EXAFS. *Phys. Rev. B* **52**, 3017–3019 (1995). 1, 4.2.2, 9, A

[21] U. Pietsch, V. Holỳ and T. Baumbach. *High-Resolution X-Ray Scattering: From Thin Films to Lateral Nanostructures* (Springer, 2004), 2^{nd} edn. 1, 3.2.2

[22] J. M. Albella (ed.) *Láminas delgadas y recubrimientos: preparación, propiedades y aplicaciones* (Ed. CSIC, Madrid, Spain, 2003). 2.1.1, 2.1.1.1

[23] D. Martinez-Martinez. *Recubrimientos protectores autolubricantes con estructura "nanocomposite" TIC/a-C y derivados nitrogenados preparados por pulverización catódica.* Ph.D. thesis, Institure of Materials Science of Seville (CSIC-University of Seville) (2007). 2.1.1, 2.1.1.1

[24] M. Vila, D. Cáceres and C. Prieto. Mechanical properties of sputtered silicon nitride thin films. *J. App. Phys.* **94**, 7868–7873 (2003). 2.1.1, 2.1.1.1

[25] J. Als-Nielsen and D. McMorrow. *Elements of modern X ray physics* (Wiley, New York, 2001), 1^{st} edn. 2.2.2

[26] M. Björck and G. Andersson. GenX: an extensible X-ray reflectivity refinement program utilizing differential evolution. *J. App. Cryst.* **40**, 1174–1178 (2007). 2.2.2, 4.3.1, 5.1.1, 5.1.1, 6.1.1, A.4.1.1

[27] W. K. Chu, J. W. Mayer and M. A. Nicolet. *Backscattering Spectrometry* (Academic Press, 1978). 2.2.3

[28] M. Mayer. SIMNRA User's Guide, Report IPP 9/113. Tech. Rep., Max-Planck-Institut fur Plasmaphysik, Garching, Germany (1997). 2.2.3

[29] W. D. Ehmann and D. E. Vance. *Radiochemistry and Nuclear Methods of Analysis* (Wiley-Interscience, 1993), 1^{st} edn. 2.2.4

[30] V. López-Flores, S. Ansell, D. T. Bowron, S. Díaz-Moreno, S. Ramos and A. Muñoz-Páez. Optimized end station and operating protocols for reflection extended x-ray absorption fine structure (ReflEXAFS) investigations of surface structure at the European Synchrotron Radiation Facility beamline BM29. *Rev. Sci. Instrum.* **78**, 013109–(1–12) (2007). 3

[31] D. C. Koningsberger and R. Prins (eds.) *X-Ray Absorption: Principles, Applications, Techniques of EXAFS, SEXAFS and XANES* (Wiley-Interscience, New York, 1988). 3.1, 4.1.5

[32] M. Borowski, D. T. Bowron and S. De Panfilis. High-energy X-ray absorption spectroscopy at ESRF BM29. *J. Synch. Rad.* **6**, 179–181 (1999). 3.1.1

[33] A. Filipponi, M. Borowski, D. T. Bowron, S. Ansell, A. Di Cicco, S. De Panfilis and J. P. Itié. An experimental station for advanced research on condensed matter under extreme conditions at the European Synchrotron Radiation Facility-BM29 beamline. *Rev. Sci. Instrum.* **71**, 2422–2432 (2000). 3.1.1

[34] SPEC is a trademark of Certified Scientific Software. 3.3

[35] D. T. Cromer and L. D. Relativistic calculation of anomalous scattering factors for x rays. *J. Chem. Phys.* 1891 (1970). 4.1.1, 4.3.1, A.3.1.1

[36] M. Born and E. Wolf. *Principles of Optics: Electromagnetic Theory of Propagation, Interference and Diffraction of Light* (Cambridge University Press, England, 1999), 7^{th} edn. 4.1.1, 4.1.2, 4.1.2, 4.1.2.1, 4.1.2.2

[37] L. G. Parratt. Surface studies of solids by total reflection of X-rays. *Phys. Rev.* **95**, 359–369 (1954). 4.1.1, 4.1.2, 4.1.2.1, 4.1.2.1, 4.3.1, A.3.1.1, A.3.1.1, A.3.1.1

[38] B. L. Henke, E. M. Gullikson and J. C. Davis. X-Ray interactions - photoabsorption, scattering, transmission and reflection at E=50-30,000 eV, Z=1-92 . *Atom. Data Nuc. Data Tab.* **55**, 349 (1993). 4.1.1, 4.1.1, 4.3.1, 4.3.1.1, A.3.1.1, A.3.1.1

[39] J. Bremer. Anomalous scattering of X-Ray photons at the K absorption-edge of free atoms and molecules, calculated by means of the modified Kramers-Heisenberg dispersion formula. *J. Phys. B* **12**, 2797–2807 (1979). 4.1.1

[40] I. W. Hamley and J. S. Pedersen. Analysis of neutron and X-ray reflectivity data. 1. Theory. *J. Appl. Cryst.* **27**, 29–35 (1994). 4.1.2.2

[41] L. Nevot and P. Croce. Characterization of surfaces by grazing X-Ray reflection - Application to study of polishing of some silicate-glasses. *Rev. Phys. App.* **15**, 761–779 (1980). 4.1.3, 4.3.1, 5.1.1, A.3.1.2

[42] D. Bahr, W. Press, R. Jebasinski and S. Mantl. X-ray reflectivity and diffuse-scattering study of *cosi*2 layers in si produced by ion-beam synthesis. *Phys. Rev. B* **47**, 4385–4393 (1993). 4.1.3, 4.1.3, 4.3.1, A.3.1.2

[43] J. P. Schlomka, M. Tolan, L. Schwalowsky, O. H. Seeck, J. Stettner and W. Press. X-Ray-diffraction from Si/Ge layers - Diffuse-scattering in the

region of total external reflection. *Phys. Rev. B* **51**, 2311–2321 (1995). 4.1.3

[44] B. K. Teo. *EXAFS: Basic principles and data analysis* (Springer, Berlin, 1986). 4.1.5

[45] J. J. Rehr, J. M. De Leon, S. I. Zabinsky and R. C. Albers. Theoretical X-ray absorption fine-structure standards. *J. Am. Chem. Soc.* **113**, 5135–5140 (1991). 4.1.5, 4.3.2, A, A.4.1.3

[46] M. Newville, B. Ravel, D. Haskel, J. J. Rehr, E. A. Stern and Y. Yacoby. Analysis of multiple-scattering XAFS data using theoretical standards. *Physica B* **209**, 154–156 (1995). 4.1.5, 4.3.2, 5.3.1, 6.3.2.2, A, A.4.1.3

[47] G. Martens and P. Rabe. The anomalous dispersion of the refractive-index and the extended X-ray absorption fine-structure at the K edge of Cu. *J. Phys. C* **13**, L913–L918 (1980). 4.2.1, 6.3.1, 7.3.1

[48] N. Hansen, S. D. Müller and P. Koumoutsakos. Reducing the time complexity of the derandomized Evolution Strategy with Covariance Matrix Adaptation (CMA-ES). *Evol.Comp.* **11**, 1–18 (2003). 4.3.1.1, A.3.2.2

[49] R. Penrose. A generalized inverse for matrices. *Proc. Cambr. Phil. Soc.* **51**, 406–413 (1955). 4.3.2, A.3.2.2

[50] R. Penrose. On best approximate solution of linear matrix equations. *Proc. Cambr. Phil. Soc.* **52**, 17–19 (1956). 4.3.2, A.3.2.2

[51] S. Díaz-Moreno, A. Muñoz-Páez and E. Sánchez-Marcos. X-ray Absorption Spectroscopy Study of the In-Solution Structure of Ni2+, Co2+, and Ag+ Solvates in Acetonitrile Including Multiple Scattering Contributions. *J. Phys. Chem. B* **104**, 11794–11800 (2000). 5.3.1

[52] P. A. O'Day, J. J. Rehr, S. I. Zabinsky and G. E. J. Brown. Extended X-ray Absorption Fine Structure (EXAFS) Analysis of Disorder and

Multiple-Scattering in Complex Crystalline Solids. *J. Am. Chem. Soc.* **116**, 2938–2949 (1994). 5.3.1, 6.3.2.2

[53] A. L. Ankudinov, B. Ravel, J. J. Rehr and S. D. Conradson. Real-space multiple-scattering calculation and interpretation of x-ray-absorption near-edge structure. *Phys. Rev. B* **58**, 7565–7576 (1998). 5.3.1, 6.3.2.2

[54] M. Newville. IFEFFIT: interactive XAFS analysis and FEFF fitting. *J. Sync. Rad.* **8**, 322–324 (2001). 5.3.1, 6.3.2.2

[55] The EXAFS database is a service provided by The International X-ray Absorption Society (IXAS). 5.3.1, 5.3.2.2, 6.3.1, 6.3.2.2, 6.3.2.2, 7.3.1

[56] S. F. Cheng, A. N. Mansour, J. P. Teter, K. B. Hathaway and L. T. Kabacoff. Structure and magnetic properties of magnetron-sputtered Fe/Cu multilayered thin films. *Phys. Rev. B* **47**, 206–216 (1993). 5.3.1

[57] G. A. Somorjai and M. A. Van Hove. Adsorbed monolayers on solid surfaces. In *Structure and bonding*, vol. 38 (Springer-Verlag, Berlin, 1979). 5.3.1

[58] A. Borrás, A. Yanguas-Gil, A. Barranco, J. Cotrino and A. R. González-Elipe. Relationship between scaling behavior and porosity of plasma-deposited TiO_2 thin films. *Phys. Rev. B* **76** (2007). 5.3.2.1

[59] A. Yanguas-Gil, J. Cotrino, A. Barranco and A. R. Gonzalez-Elipe. Influence of the angular distribution function of incident particles on the microstructure and anomalous scaling behavior of thin films. *Phys. Rev. Lett.* **96** (2006). 5.3.2.1

[60] N. Cabrera and N. F. Mott. Theory of the oxidation of metals. *Rep. Progr. Phys.* **12**, 163–184 (1949). 6.3.2.1, 6.3.2.2

[61] M. C. Snead, J. L. Maynard and R. C. Brasted. *Comprehensive inorganic chemistry*, vol. 2 (Van Nostrand, Princeton, 1954). 6.3.2.1

[62] J. C. Bailar, H. J. Emeleus, R. Nyholm and A. F. Trotman-Dickenson. *Comprehensive Inorganic Chemistry* (Pergamon Press Ltd., Oxford, England, 1973). 6.3.2.2

[63] V. P. Anitha, S. Major, D. Chandrashekharam and M. Bhatnagar. Deposition of molybdenum nitride thin films by rf reactive magnetron sputtering. *Surf. Coat. Tech.* **79**, 50–54 (1996). 7

[64] A. F. Wells. *Structural Inorganic Chemistry* (Oxford University Press, 1984), 5^{th} edn. 7

[65] H. Jehn and P. Ettmayer. Molybdenum-nitrogen phase-diagram. *J. Less-Common Met.* **58**, 85–98 (1978). 7

[66] A. Gomathi, A. Sundaresan and C. N. R. Rao. Nanoparticles of superconducting gamma-Mo2N and delta-MoN. *J. Sol. St. Chem.* **180**, 291–295 (2007). 7

[67] D. A. Papaconstantopoulos, W. E. Pickett, B. M. Klein and L. L. Boyer. Electronic-properties of transition-metal nitrides - The group-V and group-VI nitrides VN, NbN, TaN, CrN, MoN, and WN. *Phys. Rev. B* **31**, 752–761 (1985). 7

[68] Y. M. Wang and R. Y. Lin. Amorphous molybdenum nitride thin films prepared by reactive sputter deposition. *Mat. Sci. Eng. B* **112**, 42–49 (2004). 7

[69] T. Suszko, W. Gulbinski and J. Jagielski. Mo2N/Cu thin films - the structure, mechanical and tribological properties. *Surf. Coat. Tech.* **200**, 6288–6292 (2006). 7

[70] R. Barchewitz, M. Cremonese-Visicato and G. Onori. X-ray photoabsorption of solids by specular reflection. *J. Phys. C* **11**, 4439–4445 (1978). A

[71] S. Pizzini, K. J. Roberts, W. J. Phythian, C. A. English and G. N. Greaves. A fluorescence EXAFS study of the structure of copper-rich precipitates in Fe-Cu and Fe-Cu-Ni alloys. *Phil. Mag. Lett.* **61**, 223–229 (1990). A

[72] S. Pizzini, K. J. Roberts, G. N. Greaves, N. T. Barrett, I. Dring and R. J. Oldman. X-ray absorption-spectroscopy under conditions of total external reflection - Application to the structural characterization of the Cu/GaAs(100) interface. *Far. Disc.* 51+ (1990). A